

602738

RTD TDR-63-3116

2 of 3

RTD
TDR
63-3116

A STUDY OF THE BEHAVIOR OF A CLAY UNDER RAPID AND DYNAMIC
LOADING IN THE ONE-DIMENSIONAL AND TRIAXIAL TESTS

Final Report

June 1964

296-P

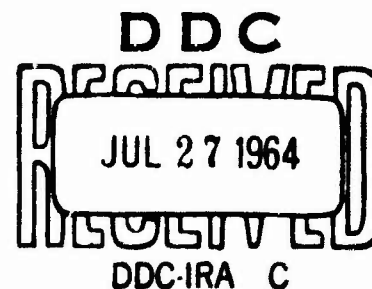
HC \$ 6.00

MF \$ 1.50

TECHNICAL DOCUMENTARY REPORT NO. RTD TDR-63-3116



Research and Technology Division
AIR FORCE WEAPONS LABORATORY
Air Force Systems Command
Kirtland Air Force Base
New Mexico



Project No. 1080, Task No. 108003

This research has been funded by the
Defense Atomic Support Agency under WEB No. 13.125

(Prepared under AF 29(601)-5535 by Kane, H.,
Davisson, M. T., Oleson, R. E., and Sinnamon,
G. K., Dept of Civil Engineering, University
of Illinois, Urbana, Illinois.)

**Research and Technology Division
Air Force Systems Command
AIR FORCE WEAPONS LABORATORY
Kirtland Air Force Base
New Mexico**

When Government drawings, specifications, or other data are used for any purpose other than in connection with a definitely related Government procurement operation, the United States Government thereby incurs no responsibility nor any obligation whatsoever; and the fact that the Government may have formulated, furnished, or in any way supplied the said drawings, specifications, or other data, is not to be regarded by implication or otherwise as in any manner licensing the holder or any other person or corporation, or conveying any rights or permission to manufacture, use, or sell any patented invention that may in any way be related thereto.

This report is made available for study upon the understanding that the Government's proprietary interests in and relating thereto shall not be impaired. In case of apparent conflict between the Government's proprietary interests and those of others, notify the Staff Judge Advocate, Air Force Systems Command, Andrews AF Base, Washington 25, DC.

This report is published for the exchange and stimulation of ideas; it does not necessarily express the intent or policy of any higher headquarters.

DDC AVAILABILITY NOTICE

Qualified requesters may obtain copies of this report from DDC.

FOREWORD

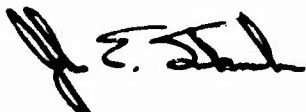
This report has been prepared as part of the work performed in the Department of Civil Engineering at the University of Illinois under contract AF 29(601)-5535 with the Air Force Weapons Laboratory, Kirtland Air Force Base, New Mexico. An advisory committee which included Dr. R. B. Peck, Professor of Foundation Engineering, and Mr. Stanley D. Wilson, of the firm Shannon and Wilson, Seattle, Washington, provided guidance for the experimental phase of the work. Professor R. E. Olson directed the triaxial shear strength studies; Professor M. T. Davisson directed the one-dimensional compression studies; and Professor G. K. Sinnamon supervised the construction of the dynamic loading equipment. The theoretical interpretation of the test results was the responsibility of Professor H. Kane, who was also designated as the project supervisor. The principal investigators were assisted by Mr. Dennis J. Leary and Mr. James L. Smith, Research Assistants in Civil Engineering.

ABSTRACT

The behavior of soil under dynamic loading is an important factor in the soil-structure interaction problem. To study this behavior, a series of dynamic, high-pressure triaxial and one-dimensional compression tests has been conducted. Special testing devices developed for this research are described. In the one-dimensional tests, the peak pressures ranged from 620 psi to 11,300 psi with rise times to the peak pressure of 1.9 milliseconds to 1,625 milliseconds. In the triaxial tests, cell pressures from 100 psi to 1,010 psi were used with times-to-failure varying from 3 milliseconds to 100 seconds. In addition, partial loading triaxial tests were run in which the applied axial stress was 20 percent to 60 percent of the failure stress. The soil used was a compacted silty clay of low plasticity. The test results are presented and the influence of rate of loading and pressure level on compressive strength, ratio of lateral to axial pressures, stress-strain relations, residual strains, and creep under constant load are evaluated.

PUBLICATION REVIEW

This report has been reviewed and is approved.



JOHN E. SEKNICKA
Lt USAF
Project Officer



THOMAS J. LOWRY, JR.
Colonel USAF
Chief, Structures Branch



PERRY L. HUIE
Colonel USAF
Chief, Research Division

CONTENTS

| | Page |
|--|------|
| FOREWORD | |
| CHAPTER 1. INTRODUCTION | |
| 1.1 General..... | 1 |
| 1.2 General Aspects of the Problem..... | 2 |
| 1.3 Scope of Study..... | 3 |
| FIGURE..... | 6 |
| CHAPTER 2. SELECTION OF SOIL AND MEASUREMENT OF STATIC PROPERTIES | |
| 2.1 Selection of Soil..... | 7 |
| 2.2 Index Properties of the Goose Lake Clay..... | 8 |
| 2.3 Compaction Studies..... | 9 |
| 2.4 Static Triaxial Compression Tests..... | 11 |
| 2.5 Static One-Dimensional Compression Test..... | 12 |
| REFERENCES..... | 14 |
| TABLES..... | 15 |
| FIGURES..... | 19 |
| CHAPTER 3. ONE-DIMENSIONAL TESTS | |
| 3.1 General..... | 28 |
| 3.2 Description of Apparatus..... | 29 |
| 3.3 Test Procedures..... | 37 |
| 3.4 Data Reduction..... | 42 |
| 3.5 Test Results..... | 44 |
| 3.6 Summary of Test Results..... | 46 |
| REFERENCES..... | 50 |
| TABLES..... | 51 |
| FIGURES..... | 54 |
| CHAPTER 4. DYNAMIC TRIAXIAL TESTS | |
| 4.1 Equipment..... | 76 |
| 4.2 Experimental Procedures..... | 85 |
| 4.3 Analysis of Experimental Errors..... | 89 |
| 4.4 Dynamic Triaxial Compression Tests..... | 97 |
| REFERENCES..... | 112 |
| TABLES..... | 113 |
| FIGURES..... | 118 |

| | Page |
|---|------------|
| CHAPTER 5. INTERPRETATION OF ONE-DIMENSIONAL AND TRIAXIAL TEST RESULTS | |
| 5.1 Horizontal Pressures..... | 153 |
| 5.2 Stress-Strain Relations..... | 157 |
| 5.3 Design Implications for High Pressure Levels..... | 159 |
| REFERENCES..... | 162 |
| TABLES..... | 163 |
| FIGURES..... | 165 |
| CHAPTER 6. SUMMARY, CONCLUSIONS, AND RECOMMENDATIONS | |
| 6.1 Summary of Testing Program..... | 169 |
| 6.2 Conclusions..... | 170 |
| 6.3 Recommendations for Future Research Efforts..... | 173 |
| APPENDIX A. ONE-DIMENSIONAL TEST DATA..... | 175 |
| APPENDIX B. SYMBOLS..... | 251 |
| DISTRIBUTION..... | 253 |

ILLUSTRATIONS

| <u>Number</u> | | <u>Page</u> |
|---------------|--|-------------|
| 1.1 | Blast Loading Effects on Underground Structures..... | 6 |
| 2.1 | Grain Size Curve of Goose Lake Clay..... | 19 |
| 2.2 | Dynamic Compaction Curves for Goose Lake Clay..... | 20 |
| 2.3 | Kneading Compaction Tests..... | 21 |
| 2.4 | Moisture-Density Data for Samples Used in Triaxial Tests..... | 22 |
| 2.5 | Mohr-Coulomb Diagram for Static Triaxial Tests on Goose Lake Clay..... | 23 |
| 2.6 | Mohr-Coulomb Diagram for Static Triaxial Tests on Goose Lake Clay..... | 24 |
| 2.7 | Mohr-Coulomb Diagram for Static Triaxial Tests on Goose Lake Clay..... | 25 |
| 2.8 | Mohr-Coulomb Diagram for Static Triaxial Tests on Goose Lake Clay..... | 26 |
| 2.9 | Total Stress Shearing Parameters from Static Unconsolidated-Undrained Triaxial Tests on Goose Lake Clay..... | 27 |
| 3.1 | One-Dimensional Test Requirements..... | 54 |
| 3.2 | Confining Ring Data..... | 55 |
| 3.3 | Schematic of Ring Calibrator..... | 56 |
| 3.4 | Schematic of Rapid Loading Machine..... | 57 |
| 3.5 | Rapid Test Data..... | 58 |
| 3.6 | Schematic of Dynamic Loading Machine..... | 59 |
| 3.7 | Dynamic Test Data..... | 60 |
| 3.8 | Instrumentation of Confining Rings..... | 61 |
| 3.9 | Instrumentation of Load Cell For Rapid Loading Machine..... | 62 |
| 3.10 | Instrumentation of Load Cell For Dynamic Loading Machine..... | 63 |

| <u>Number</u> | | <u>Page</u> |
|---------------|---|-------------|
| 3.11 | Instrumentation for Axial Strain..... | 64 |
| 3.12 | Schematic Cross Section of Ring Retainer For Compaction of One-Dimensional Test Specimens..... | 65 |
| 3.13 | Confining Ring Assembly..... | 66 |
| 3.14 | Confining Ring Assembly in Rapid Test Machine..... | 67 |
| 3.15 | Confining Ring Assembly in Dynamic Test Machine..... | 67 |
| 3.16 | Rapid Test Machine..... | 68 |
| 3.17 | Dynamic Test Machine..... | 68 |
| 3.18 | Stress-Strain Curve for Goose Lake Clay in One-Dimensional Compression..... | 69 |
| 3.19 | Stress-Strain Curve for Goose Lake Clay in One-Dimensional Compression..... | 70 |
| 3.20 | Stress-Strain Curve for Playa Silt in One-Dimensional Compression..... | 71 |
| 3.21 | Peak Axial Stress vs. Residual Strain..... | 72 |
| 3.22 | Relationship Between Constrained Modulus and Axial Stress For Goose Lake Clay in One-Dimensional Compression..... | 73 |
| 3.23 | Relationship Between Axial and Radial Stress For Goose Lake Clay in One-Dimensional Compression..... | 74 |
| 3.24 | Relationship Between Axial and Radial Stress For Goose Lake Clay in One-Dimensional Compression..... | 75 |
| 4.1 | Triaxial Cell..... | 118 |
| 4.2 | Calibration Curve for the Load Cell..... | 119 |
| 4.3 | Cell Pressure Panel Board Circuit..... | 120 |
| 4.4 | Dynamic Testing Frame..... | 121 |
| 4.5 | Hydraulic System..... | 122 |
| 4.6 | Rates of Deformation in Oil Valve Tests..... | 123 |
| 4.7a | Calibration Marks for the Deflection Trace on the Oscillograph Tape of Test No. 39..... | 124 |

| <u>Number</u> | | <u>Page</u> |
|---------------|--|-------------|
| 4.7b | Calibration Marks for the Axial Load and Cell Pressure Traces on the Oscillograph Tape of Test No. 39..... | 125 |
| 4.7c | Oscillograph Traces for Application of Cell Pressure and Seating Load, and for Shearing Sample No. 39..... | 126 |
| 4.8 | Data Reduction Form..... | 127 |
| 4.9 | Nitrogen Leakage Through Membranes..... | 128 |
| 4.10 | Influence of Time to Failure on Shearing Strength, Confining Pressure = 114 psi..... | 129 |
| 4.11 | Influence of Time to Failure on Shearing Strength, Confining Pressure = 1010 psi..... | 130 |
| 4.12 | Modified Mohr-Coulomb Diagram for Dynamic Unconsolidated-Undrained Triaxial Compression Tests on Goose Lake Clay..... | 131 |
| 4.13 | Semi-logarithmic Modified Mohr-Coulomb Diagram for Dynamic Unconsolidated-Undrained Triaxial Compression Tests on Goose Lake Clay..... | 132 |
| 4.14 | Dimensionless Stress-Strain Relationships for Triaxial Tests to Failure with $\sigma_3 = 114$ psi..... | 133 |
| 4.15 | Dimensionless Stress-Strain Relationships for Tests to Failure with $\sigma_3 = 210$ psi to 328 psi..... | 134 |
| 4.16 | Dimensionless Stress-Strain Relationship for Tests to Failure with $\sigma_3 = 498$ psi..... | 135 |
| 4.17 | Dimensionless Stress-Strain Relationships for Tests to Failure with $\sigma_3 = 705$ psi & 735 psi..... | 136 |
| 4.18 | Dimensionless Stress-Strain Relationships for Tests to Failure with $\sigma_3 = 1010$ psi..... | 137 |
| 4.19 | Hyperbolic Curve-Fitting Diagram for Tests to Failure with $\sigma_3 = 114$ psi..... | 138 |
| 4.20 | Alternate Hyperbolic Stress-Strain Curve for Tests to Failure with $\sigma_3 = 114$ psi..... | 139 |
| 4.21 | Parabolic Stress-Strain Curve for Tests to Failure with $\sigma_3 = 114$ psi..... | 140 |

| <u>Number</u> | | <u>Page</u> |
|---------------|--|-------------|
| 4.22 | Logrithmic Stress-Strain Curve for Tests to Failure with $\sigma_3 = 114$ psi..... | 141 |
| 4.23 | Influence of Confining Pressure on the Secant Modulus at 1 Percent Strain for Tests with Times to Failure of 3 or 4 Milliseconds..... | 142 |
| 4.24 | Influence of Confining Pressure on the Secant Modulus Defined at Half the Failure Stress for Tests with Times to Failure of 3 to 4 Milliseconds..... | 143 |
| 4.25 | Influence of the Rate of Deformation on the Secant Modulus Defined at 1 Percent Strain in Tests at Confining Pressure of 114 psi and 1010 psi..... | 144 |
| 4.26 | "Dynamic" Triaxial Compression Tests at a Cell Pressure of 117 psi..... | 145 |
| 4.27 | "Dynamic" Triaxial Compression Tests at a Cell Pressure of 1010 psi..... | 146 |
| 4.28 | Triaxial Compression Tests at a Cell Pressure of 117 psi and an Oil Valve Setting of 10..... | 147 |
| 4.29 | Triaxial Compression Tests at a Cell Pressure of 208 psi and an Oil Valve Setting of 10..... | 148 |
| 4.30 | Triaxial Compression Tests at a Cell Pressure of 498 psi and an Oil Valve Setting of 10..... | 149 |
| 4.31 | Triaxial Compression Tests at a Cell Pressure of 705 psi and an Oil Valve Setting of 10..... | 150 |
| 4.32 | Triaxial Compression Tests at a Cell Pressure of 1000 psi and an Oil Valve Setting of 10..... | 151 |
| 4.33 | Creep Rates for Times Between 0.1 sec. and 0.4 sec., Triaxial Compression Tests..... | 152 |
| 5.1 | Relationship Between K and $\Delta\sigma_v$ for One-Dimensional and Triaxial Tests on Goose Lake Clay..... | 165 |
| 5.2 | Relationship Among K, $\Delta\sigma_v$, and Axial Strain for Triaxial Tests on Goose Lake Clay..... | 166 |
| 5.3 | Comparison of One-Dimensional and Triaxial Stress-Strain Curves..... | 167 |
| 5.4 | Relation Between K_o and M_{ct}/E_s | 168 |

CHAPTER 1

INTRODUCTION

1.1 GENERAL

Conventional underground structures have been successfully designed for many years with only a limited knowledge of the properties of the surrounding soil. These design procedures have been developed largely from field observations of successful and unsuccessful structures and, therefore, they are useful only for conventional loadings and types of structures. Underground structures which are intended to survive the effects of a nuclear blast must resist dynamic loads of great intensity which are well beyond the normal range of experience. These loads are transmitted to the structure through the soil and the load acting on the structure is a function of the behavior of both the soil and the structure under the dynamic loading. To fill the void resulting from the lack of experience with this type of loading, the study of the dynamic soil-structure problem has been undertaken by many investigators. Much of the theoretical work has been based on assumed simplified soil properties with the primary interest directed towards the structure. In other cases, model structures buried in soil have been tested in the laboratory. Here, the behavior of soil under dynamic loading is complicated by the complex boundary conditions which result from the interaction between the soil and the structure.

It is apparent that a full understanding of soil-structure interaction demands a knowledge of the effect of the loading and of the boundary

conditions on the behavior of the soil. This research is directed to this end. Since the soil properties will depend to a large extent on the character of the loading, a brief review of the ground shock phenomena resulting from a nuclear blast follows. This will serve to define the nature of the loads which are of interest.

1.2 GENERAL ASPECTS OF THE PROBLEM

Figure 1.1 shows three structures embedded in the soil overburden at three different distances from ground zero. The structure nearest ground zero is assumed to be close enough for direct induced loading to be of major concern. The remaining two structures are assumed to be far enough away from ground zero for the direct induced loading to be of minor importance compared to the air-blast loading. For purposes of discussion, three zones of differing blast load character will be defined, namely, close-in, superseismic and subseismic.

Close-in structures quite likely will receive a major direct induced load with both vertical and horizontal components; an instant later, similar loading will be received from the air induced ground shock. Very little field information is available on underground structures that were subjected to significant pressures in the close-in zone.

The air induced loading in the superseismic zone has both vertical and horizontal components. However, for structures over which the transit time of the peak pressure is very small (relatively compact structures parallel to the direction of wave propagation), the principal phenomena involved appear to be vertical motions; this conclusion is

based on interpretations of field test results. For this reason, compact structures may be treated by one-dimensional techniques. However the two-dimensional aspects become increasingly important for longer or taller structures, in which cases the transit time of the wave front and the relative horizontal displacements of the soil at different depths are significant.

Finally, structures in the subseismic zone will receive first a load from the seismic wave propagating through the soil; at a later time the air-blast loading will arrive. The first motion of the structure may actually be upwards because of reflection of the wave propagated through the soil.

The overpressure levels of interest in the close-in zone may exceed 10,000 psi, those in the intermediate zone may be in the range of several thousand down to several hundred psi. In the subseismic zone, pressures on the order of a few hundred psi in rock, or considerable less in soil, will be of interest. The general problem is to find the magnitude, direction, and time dependency of the loads transmitted onto buried structures by the soil surrounding them. The loads transmitted to the structure depend not only on the physical properties of the soil, but also on the physical properties of the structure. This is the interaction problem. The area of interest in this research is the role of the soil medium in the dynamic interaction problem.

1.3 SCOPE OF STUDY

The purpose of this work was to define the dynamic stress-strain relations for a particular soil throughout a range of loading conditions.

The emphasis on a single soil was necessary to limit the number of variables to that which could be thoroughly investigated within the time limits available. The static properties of the soil selected for study are given in Chapter 2.

One-dimensional compression tests, which provide stress-strain relations under the condition of zero lateral strain, were conducted on specimens 1 inch thick and 4 inches in diameter using a range of pressures up to 11,000 psi with rise times, i.e. the time required to apply the peak pressure, as short as 2 milliseconds. A specially designed apparatus was required for these tests. A description of the apparatus, the test results, and an interpretation of the test results are presented in Chapter 3.

The stress-strain relations and the strength of the soil under the condition of constant lateral stress were investigated using a tri-axial testing apparatus developed for this purpose. Specimens 1.5 inches in diameter and 3 inches high were used with cell pressures up to 1000 psi. The axial load was applied with times-to-failure varying from 3 milliseconds to approximately a minute. Chapter 4 contains a description of the apparatus and a presentation of the test results with their interpretation.

An attempt to formulate a theory which could relate the dynamic one-dimensional and triaxial stress-strain relations proved to be unsuccessful. The reason for this is that a theory, if it is indeed possible to formulate one, must reflect the test results and the empirical relationships among the variables. Because the time required to develop the testing equipment greatly exceeded the original estimates, it was not possible to accomplish this. It would also appear that, in light of the

test results, the development of a general theory for stress-strain relations of soil under dynamic loads will require data on effective stresses and volume changes. Techniques for measuring these during a dynamic test are not yet available. The triaxial and one-dimensional tests results are compared in Chapter 5 to study relationships which are of interest in soil-structure interaction problems.

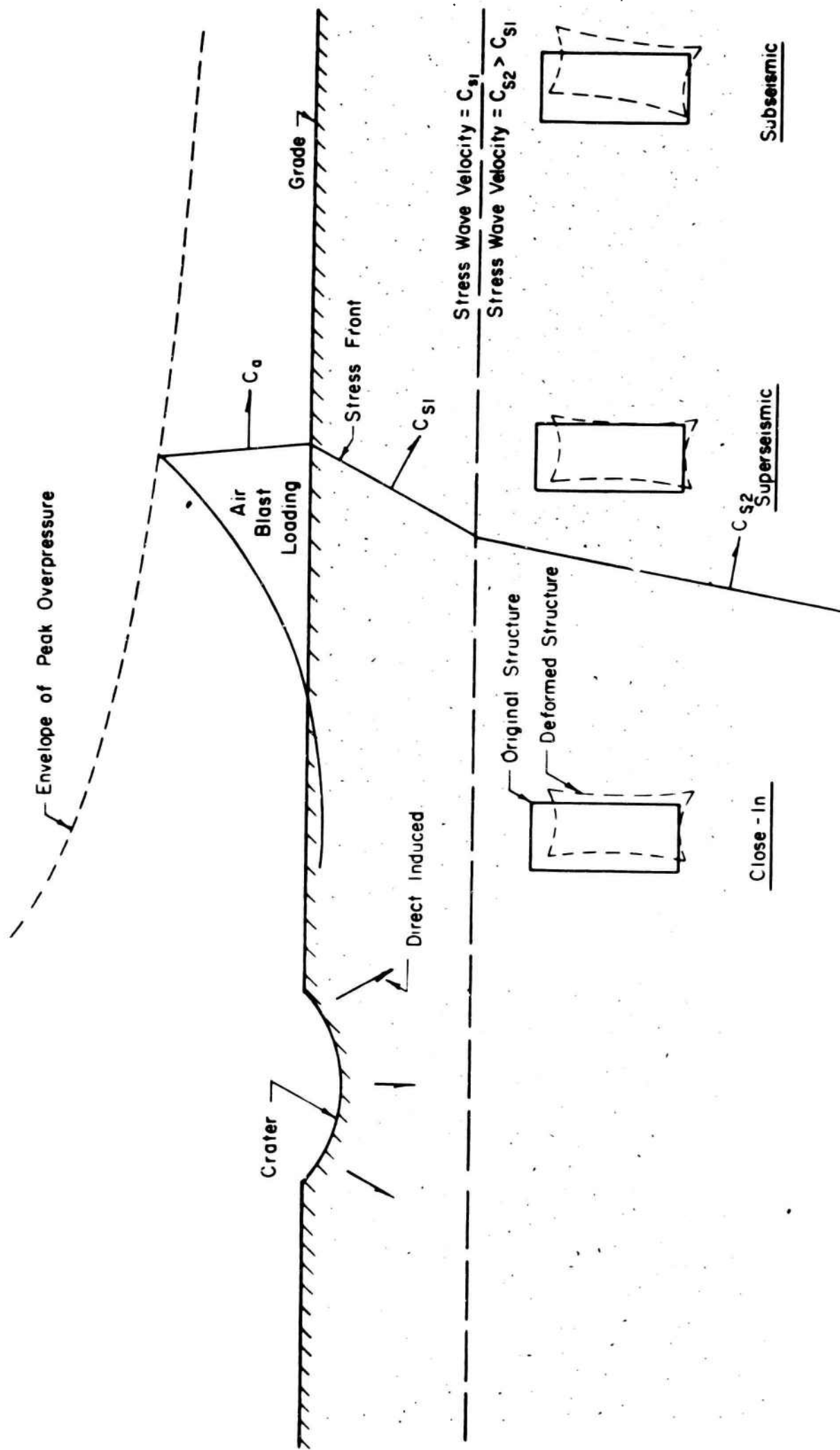


FIGURE 1.1. BLAST LOADING EFFECTS ON UNDERGROUND STRUCTURES.

CHAPTER 2

SELECTION OF SOIL AND MEASUREMENT OF STATIC PROPERTIES

2.1 SELECTION OF SOIL

Considering the limited time available to perform this investigation and the fact that most of the experimental apparatus had to be designed and constructed during the contract period, it was necessary to restrict the investigation to a single soil. The ranges in properties of this soil were restricted by various practical considerations. Tests on sands were not considered since tests by Whitman and Healy¹ indicated that dynamic effects of major importance were associated only with dense saturated sands. Saturated soils, of all types, were eliminated since one of the major aspects of the investigation was to investigate the dynamic one-dimensional compression characteristics of a soil. In a saturated soil, the dynamic one-dimensional properties would be dominated by the properties of the relatively incompressible water and useful soil data would not result. Natural soils were eliminated because of the problem of obtaining a large number of essentially identical specimens. Hence, the project was restricted to the study of the dynamic compression characteristics of a compacted unsaturated cohesive soil.

A clay of low plasticity was selected since highly plastic clays are not commonly used in compacted fills. The desired maximum particle size was set at about the #40 sieve (0.42 mm) since the triaxial tests were to be performed using 1.5-inch diameter samples. A clay of low plasticity with a liquid limit of about 35 percent was considered to meet the requirements most satisfactorily.

In investigating sources of commercially processed clay, samples of "Goose Lake Flour" and "Grundite" were obtained from the Illinois Clay Products Co., Joliet, Illinois. The Goose Lake Flour had most of the desired properties and a large quantity of this soil was obtained. To avoid confusion, this soil will be called "Goose Lake Clay" in this report.

2.2 INDEX PROPERTIES OF THE GOOSE LAKE CLAY

Tests on several samples from the shipment revealed that the clay was quite uniform in physical properties. The index properties of the soil include:

| | |
|-----------------------|------------|
| liquid limit..... | 31 percent |
| plastic limit..... | 17 percent |
| shrinkage limit..... | 15 percent |
| specific gravity..... | 2.72 |

A grain-size distribution curve is presented in Fig. 2.1, which reveals that the soil is 9 percent sand (coarser than 0.06 mm), 57 percent silt (0.06 mm to 0.002 mm) and 34 percent clay (finer than 0.002 mm). Hence, the activity² is 0.41.

The standard and modified Proctor moisture-density curves for Goose Lake Clay are shown in Fig. 2.2. The maximum dry densities and optimum water contents are:

| <u>Test</u> | <u>Maximum Dry Density, pcf</u> | <u>Optimum Water Content, percent</u> |
|------------------------|-------------------------------------|---|
| Standard Proctor | 112.7 | 14.5 |
| Modified Proctor | 124.5 | 11.3 |

Professor R. E. Grim (Geology Department, University of Illinois) indicated that the dominate clay mineral in the Goose Lake Clay is illite. Mineral analyses were performed on the soil used in this investigation.

2.3 COMPACTION STUDIES

To produce a large number of essentially identical samples, it was necessary to select a specific method of compaction to be followed throughout the study. Since the problems associated with the preparation of the triaxial specimens were considered to be more severe than the problems associated with the preparation of the specimens for the one-dimensional tests, the preliminary compaction studies were performed simultaneously with the development of the compaction techniques for the triaxial specimens.

A study of the various compaction methods in common use suggested that the most uniform samples would probably be obtained by static compaction of very large specimens followed by trimming out small specimens for testing. However, economic considerations indicated that such a procedure would not be feasible on this project. Instead, a kneading compaction procedure, developed on another research project, was adapted for this project. The soil was compacted into a 1.5-inch diameter by 3.0-inch high 3-part split compaction mold using a compaction foot shaped like a sector of a circle. Moisture-density curves for Goose Lake Clay using a range in water content between 7 percent and 16 percent and using foot pressures of 100 psi, 200 psi and 400 psi are shown in Fig. 2.3. For this series of tests, the soil was compacted in ten layers using 8 blows per layer and using a 30-degree compaction foot.

A series of samples was compacted and miniature penetration tests were performed on the soil at various locations in an attempt to develop

a compaction procedure that would produce reasonably homogeneous samples. The procedure that seemed to give the most satisfactory results was to compact the soil in ten layers using eight blows per layer from a wedge-shaped foot having a 30-degree apex angle. Each layer was scarified with an pick before the soil for the next layer was added. A nominal foot pressure of 200 psi was used. All samples were compacted at water contents slightly lower than the optimum water content.

After completion of a series of preliminary tests involved with equipment development, the main series of triaxial compression tests were performed using soil from six batches. The dry densities and water contents of all these specimens are shown in Table 2.1. The mean water contents and dry densities for samples compacted from each batch of soil, together with the standard deviations, are presented in Table 2.2. Considering that normal weighing accuracy and variations in oven temperature can produce errors in measuring the water content of at least 0.1 percent, the standard deviations of the water contents within each batch are about as small as possible. The largest source of error in controlling the dry density is the dwell time of the compaction foot. Wide variations in dwell time can alter the compacted dry density by several pounds per cubic foot. Thus the standard deviations in dry density are also considered to be about the minimum that can be expected without engaging in elaborate, and expensive, compaction procedures. A comparison between the initial water contents or dry densities and the scatter in the shear data reveals no correlation. Thus the samples are considered to be essentially identical.

2.4 STATIC TRIAXIAL COMPRESSION TESTS

No static triaxial compression tests were performed by project personnel except during very early stages of the project when attempts were being made to develop a suitable instrumentation system. The data obtained from these tests are not reported since these preliminary tests experienced a number of experimental difficulties. However, four series of unconsolidated-undrained triaxial compression tests were performed by students in a graduate laboratory course, using cell pressures between 0 psi and 120 psi. These tests are not in the same range of cell pressure used in the subsequent dynamic tests but they provide the only data on the static shearing characteristics of this soil and are reported for that reason.

These samples were compacted using the same procedures used to prepare samples for the subsequent dynamic tests. The dry density - water content data are plotted in Fig. 2.4 together with the data obtained from the samples prepared for the dynamic tests.

Modified Mohr-Coulomb failure envelopes, expressed in total stresses, are presented in Fig. 2.5 through 2.8. The minimal scatter of the individual points from the failure envelopes indicates the high level of reproducibility of the soil properties. The total stress angles of internal friction and cohesion intercepts are plotted against the compaction water content in Fig. 2.9. The samples used for the dynamic triaxial tests probably had an angle of internal friction of about 22.5 deg. and a cohesion intercept of about 38 psi for pressures less than about 120 psi.

Unfortunately, these static tests were performed before the performance of the dynamic tests; thus the water content and dry density for

the dynamic specimens had not been chosen. None of the static tests was performed on specimens with water contents or densities close enough to those of the subsequent dynamic tests to yield accurate information on volume change properties. However, a very approximate interpolation between the available static tests indicates that the application of a cell pressure of 120 psi to the samples used in the dynamic tests probably resulted in a decrease in volume of about 1.0 percent and that another 3.5-percent volume change occurred during shear.

2.5 STATIC ONE-DIMENSIONAL COMPRESSION TEST

The procedure used to prepare and compact the specimen of Goose Lake Clay for the static one-dimensional test was the same as that used for the rapid and dynamic one-dimensional tests as described in Section 3.3. The water content and dry density of the specimen were 11.5 percent and 120.9 pcf, respectively. The specimen was set in the rapid loading machine and subjected to a seating pressure of 10 psi. A deformation of 0.0004 inch occurred under the seating load, as measured by a pair of dial indicators recording to 0.0001 inch per dial division.

Because it was not known precisely when extrusion of the soil would occur, a continuously decreasing pressure-increment ratio was used in an attempt to define a possible point of inflection in the stress-strain curve at a critical extrusion pressure. The pressure-increment ratio was decreased from 5 to 16/15 over 16 increments; each pressure increment was applied rapidly, (within 0.1 second). For the duration of each load increment the axial stress, radial stress, and axial strain were recorded on an oscillograph at a paper speed of one-quarter inch per second. The instrumentation is described in Chapter 3.

The duration of the pressure increment required for the rate of specimen deformation to be undiscernable on the oscillograph trace and the dial indicators was approximately one minute. At a pressure of 1140 psi, small droplets of water could be seen forming at the contact of the lucite piston guide and the piston. The saturation of the specimen at the time the droplets of water were observed was calculated to be 98 percent. The maximum applied pressure was 3100 psi. At this pressure it was evident that the specimen was undergoing continuous extrusion. The specimen was rebounded at decreasing pressure-increment ratios varying from 7/8 to 1/2 through eight increments. The specimen continued to extrude during unloading until the pressure was below 2500 psi. After the test the specimen assembly was removed from the loading machine and a final dial comparator reading was obtained. When the lucite guide rings were removed, a thin smear of extruded material was observed between the lucite piston guide and the top of the ring.

The test specimen was removed from the ring for a final water-content determination. The difference between the initial water content, determined from small samples taken during compaction, and the final water content was one percent. The test was completed within approximately 30 minutes. Figures A.25, A.50 and A.75 in Appendix A show the results of the test.

REFERENCES

1. Whitman, Robert V. and Kent A. Healy (1962), "Shear Strength of Sands During Rapid Loading," Proc. A.S.C.E., vol. 82, No. SM2, April, pp. 99-132.
2. Skempton, A. W. (1948), "The Colloidal Activity of Clays," Proc. Third Intern. Conf. on Soil Mech. and Found. Engr., vol. 1, pp. 57-61.

TABLE 2.1
DENSITY-WATER CONTENT DATA FOR SPECIMENS
USED FOR TRIAXIAL TESTS

| Specimen No. | Dry Density pcf | Water Content % | Batch No. |
|-----------------|--------------------|--------------------|--------------|
| 1 | 117.6 | 11.5 | 1 |
| 2 | 118.2 | 11.6 | 1 |
| 3 | 117.8 | 11.9 | 1 |
| 4 | 118.3 | 11.5 | 1 |
| 5 | 117.7 | 11.5 | 1 |
| 6 | 117.7 | 11.6 | 1 |
| 7 | 117.4 | 11.5 | 1 |
| 8 | 117.8 | 11.6 | 1 |
| 9 | 117.8 | 11.6 | 1 |
| 10 | 117.1 | 11.5 | 1 |
| 11 | 117.8 | 11.6 | 1 |
| 12 | 117.3 | 11.5 | 1 |
| 13 | 116.9 | 11.5 | 1 |
| 14 | (115.4) | 11.5 | 1 |
| 15 | 117.1 | 11.5 | 2 |
| 16 | 116.5 | 11.6 | 2 |
| 17 | 116.6 | 11.2 | 2 |
| 18 | 116.5 | 11.5 | 2 |
| 19 | 116.6 | 11.6 | 2 |
| 20 | 116.4 | 11.2 | 2 |
| 21 | 117.3 | 11.3 | 2 |
| 22 | 117.1 | 11.5 | 2 |
| 23 | 116.5 | 11.3 | 2 |
| 24 | 116.7 | 11.4 | 2 |
| 25 | 116.9 | 11.3 | 2 |
| 26 | 117.1 | 11.4 | 2 |
| 27 | 117.0 | 11.2 | 2 |
| 28 | 117.1 | 11.4 | 2 |
| 29 | 117.1 | 11.3 | 3 |

TABLE 2.1 (continued)

| Specimen No. | Dry Density pcf | Water Content % | Batch No. |
|-----------------|--------------------|--------------------|--------------|
| 30 | 117.2 | 11.3 | 3 |
| 31 | 117.5 | 11.4 | 3 |
| 32 | 116.7 | 11.4 | 3 |
| 33 | 116.8 | 11.4 | 3 |
| 34 | 117.3 | 11.3 | 3 |
| 35 | 117.5 | 11.4 | 3 |
| 36 | 117.3 | 11.2 | 3 |
| 37 | 117.6 | 11.2 | 3 |
| 38 | 117.8 | 11.1 | 3 |
| 39 | 117.2 | 11.1 | 3 |
| 40 | 117.3 | 11.1 | 3 |
| 41 | 117.3 | 11.1 | 3 |
| 42 | 117.3 | 11.3 | 4 |
| 43 | 117.8 | 11.2 | 4 |
| 44 | 117.3 | 11.2 | 4 |
| 45 | 117.3 | 11.2 | 4 |
| 46 | 117.4 | 11.3 | 4 |
| 47 | 117.0 | 11.2 | 4 |
| 48 | 118.0 | 11.1 | 4 |
| 49 | 117.1 | 11.2 | 4 |
| 50 | 117.2 | 11.2 | 4 |
| 51 | 117.5 | 11.2 | 4 |
| 52 | 117.4 | 11.0 | 5 |
| 53 | 117.6 | 11.0 | 5 |
| 54 | 117.6 | 11.0 | 5 |
| 55 | 117.6 | 11.0 | 5 |
| 56 | 117.4 | 11.0 | 5 |
| 57 | 117.7 | 11.0 | 5 |
| 58 | 117.6 | 11.0 | 5 |
| 59 | 117.8 | 11.0 | 5 |
| 60 | 117.4 | 11.0 | 5 |
| 61 | 117.8 | 11.0 | 5 |
| 62 | 117.8 | 10.9 | 5 |

TABLE 2.1 (continued)

| Specimen No. | Dry Density pcf | Water Content % | Batch No. |
|-----------------|--------------------|--------------------|--------------|
| 63 | 117.4 | 11.2 | 6 |
| 64 | 117.2 | 11.1 | 6 |
| 65 | 117.1 | 11.1 | 6 |
| 66 | 117.6 | 11.2 | 6 |
| 67 | 117.4 | 11.2 | 6 |
| 68 | 117.7 | 11.4 | 6 |
| 69 | 117.6 | 11.2 | 6 |
| 70 | 117.8 | 11.2 | 6 |
| 71 | 117.3 | 11.2 | 6 |
| 72 | 116.9 | 11.0 | 7 |
| 73 | 117.2 | 10.9 | 7 |
| 74 | 117.5 | 10.9 | 7 |

TABLE 2.2

AVERAGE DRY DENSITIES AND WATER CONTENTS
OF SAMPLES USED FOR TRIAXIAL SHEAR TESTS

| Batch No. | Number of Samples | Mean γ_d pcf | σ γ_d pcf | Mean w % | σ w % |
|--------------|----------------------|---------------------------|-------------------------------|----------------|--------------------|
| 1 | 15 | 117.6 | .4 | 11.6 | .1 |
| 2 | 14 | 116.8 | .3 | 11.4 | .1 |
| 3 | 13 | 117.3 | .3 | 11.2 | .1 |
| 4 | 10 | 117.4 | .3 | 11.2 | .1 |
| 5 | 11 | 117.6 | .2 | 11.0 | .0 |
| 6 | 9 | 117.5 | .2 | 11.2 | .1 |
| 7 | 3 | 117.2 | -- | 10.9 | -- |

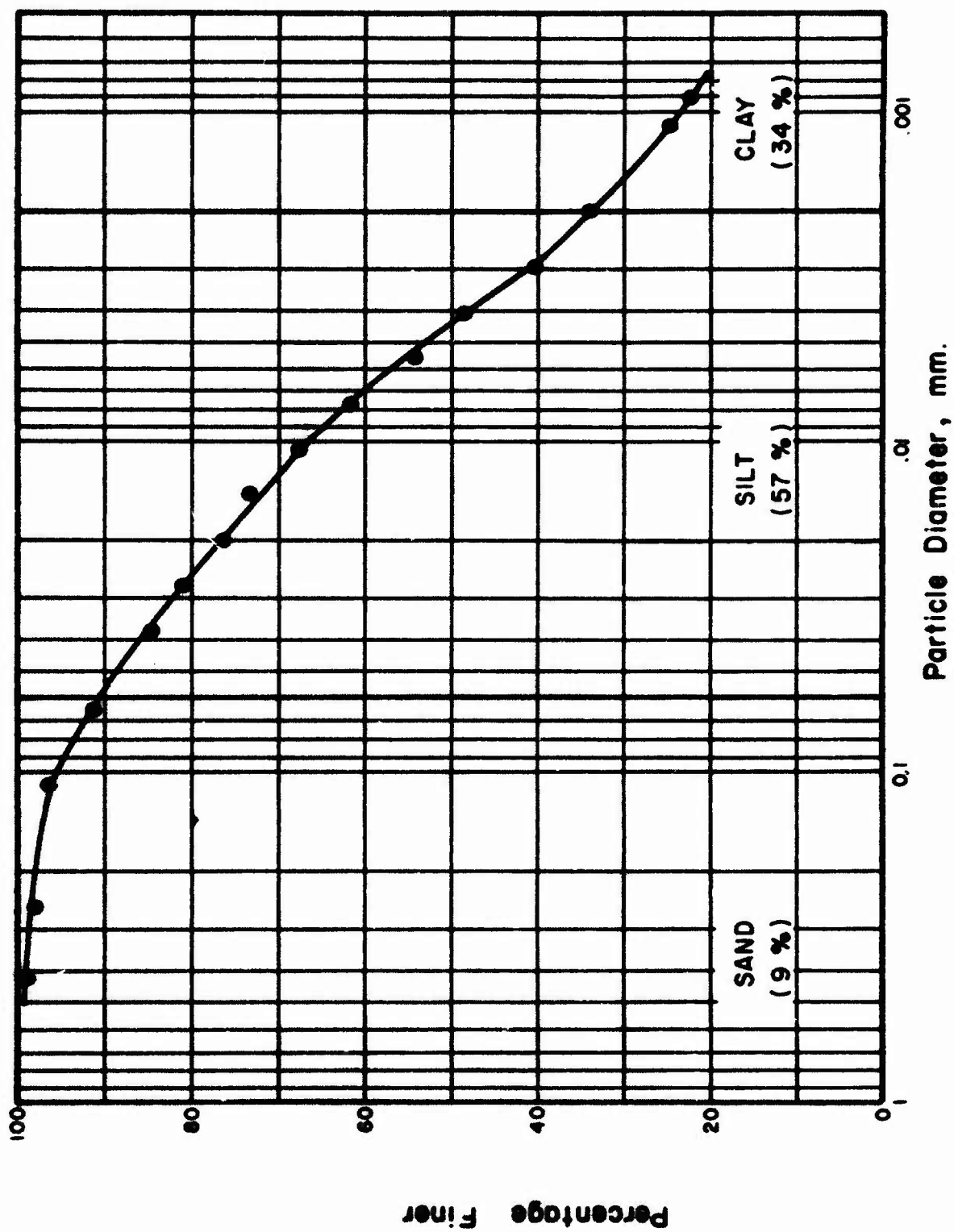


Figure 2.1. Grain Size Curve of Goose Lake Clay .

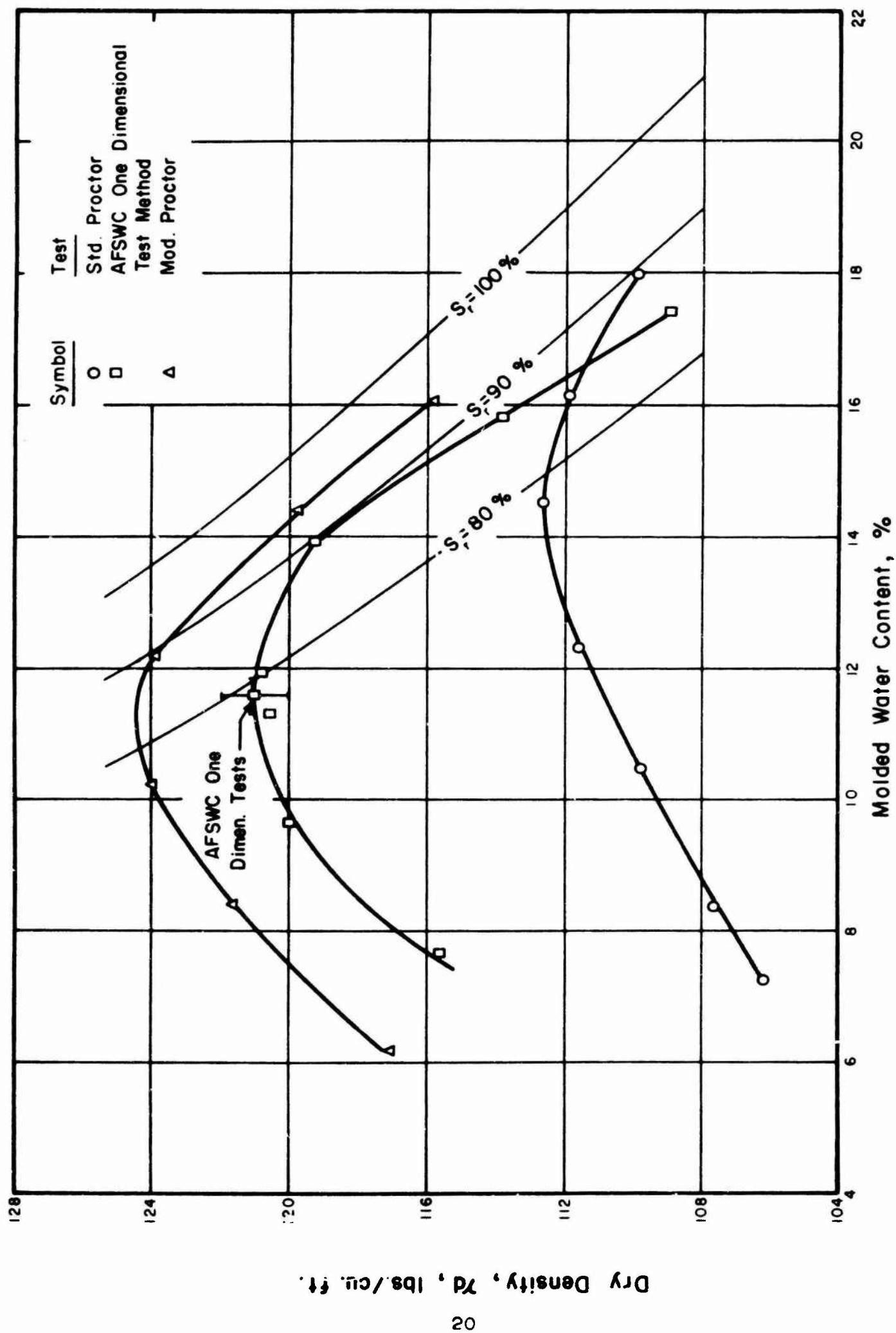


Figure 2.2. Dynamic Compaction Curves for Goose Lake Clay .

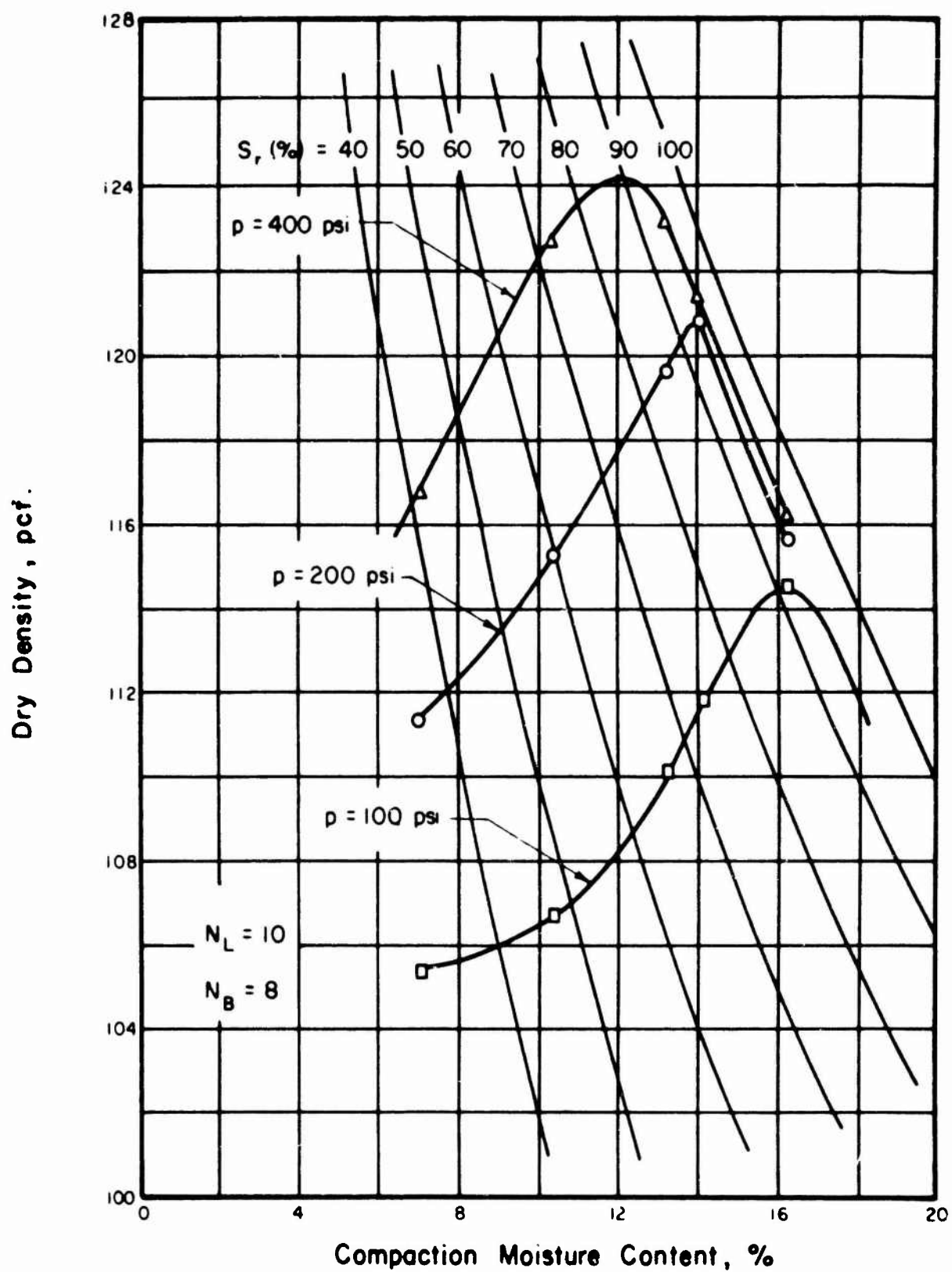


Figure 2.3. Kneading Compaction Tests .

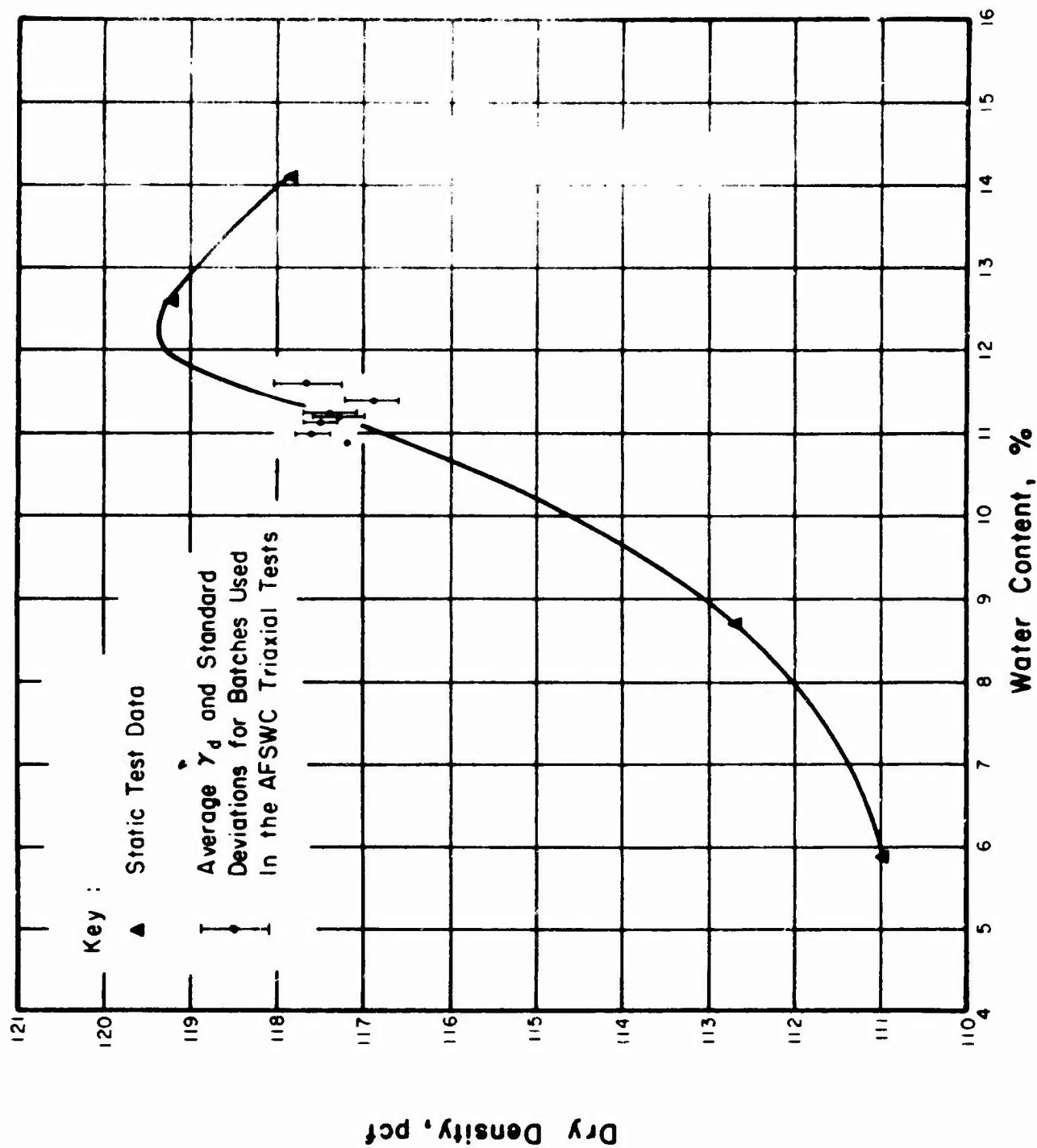


Figure 2.4. Moisture - Density Data for Samples Used in Triaxial Tests.

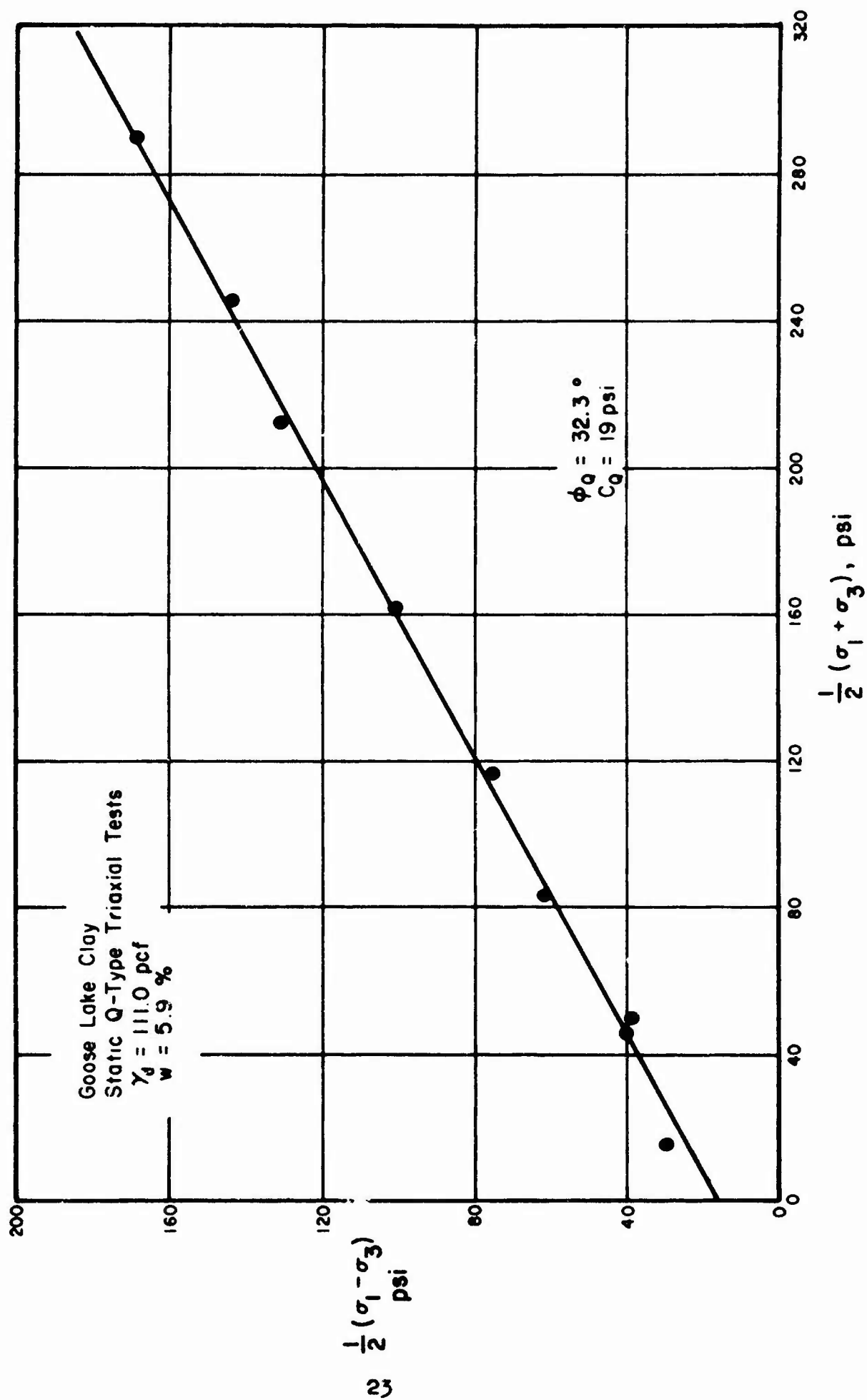


Figure 2.5. Mohr-Coulomb Diagram for Static Triaxial Tests on Goose Lake Clay .

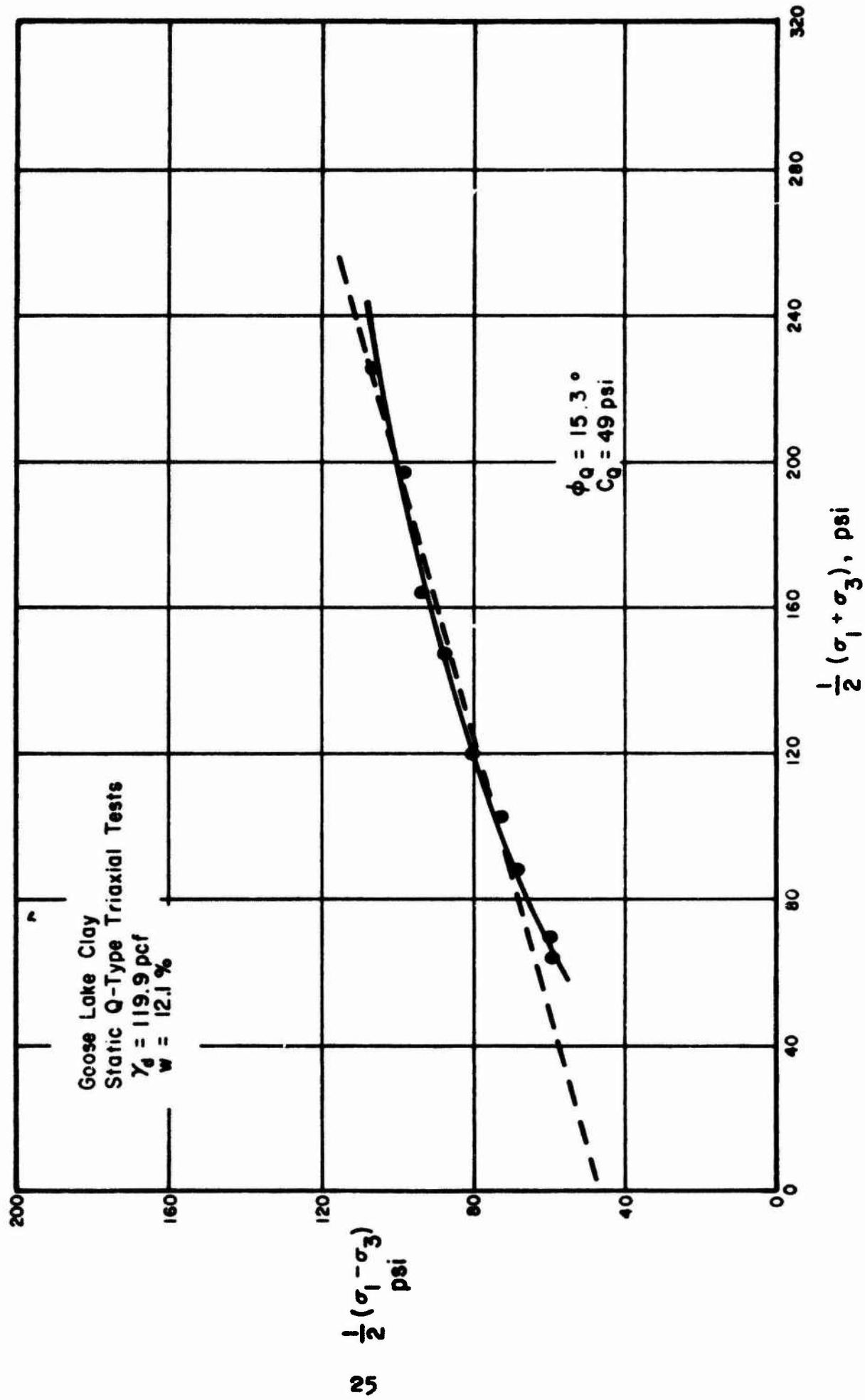


Figure 2.7. Mohr-Coulomb Diagram for Static Triaxial Tests on Goose Lake Clay .

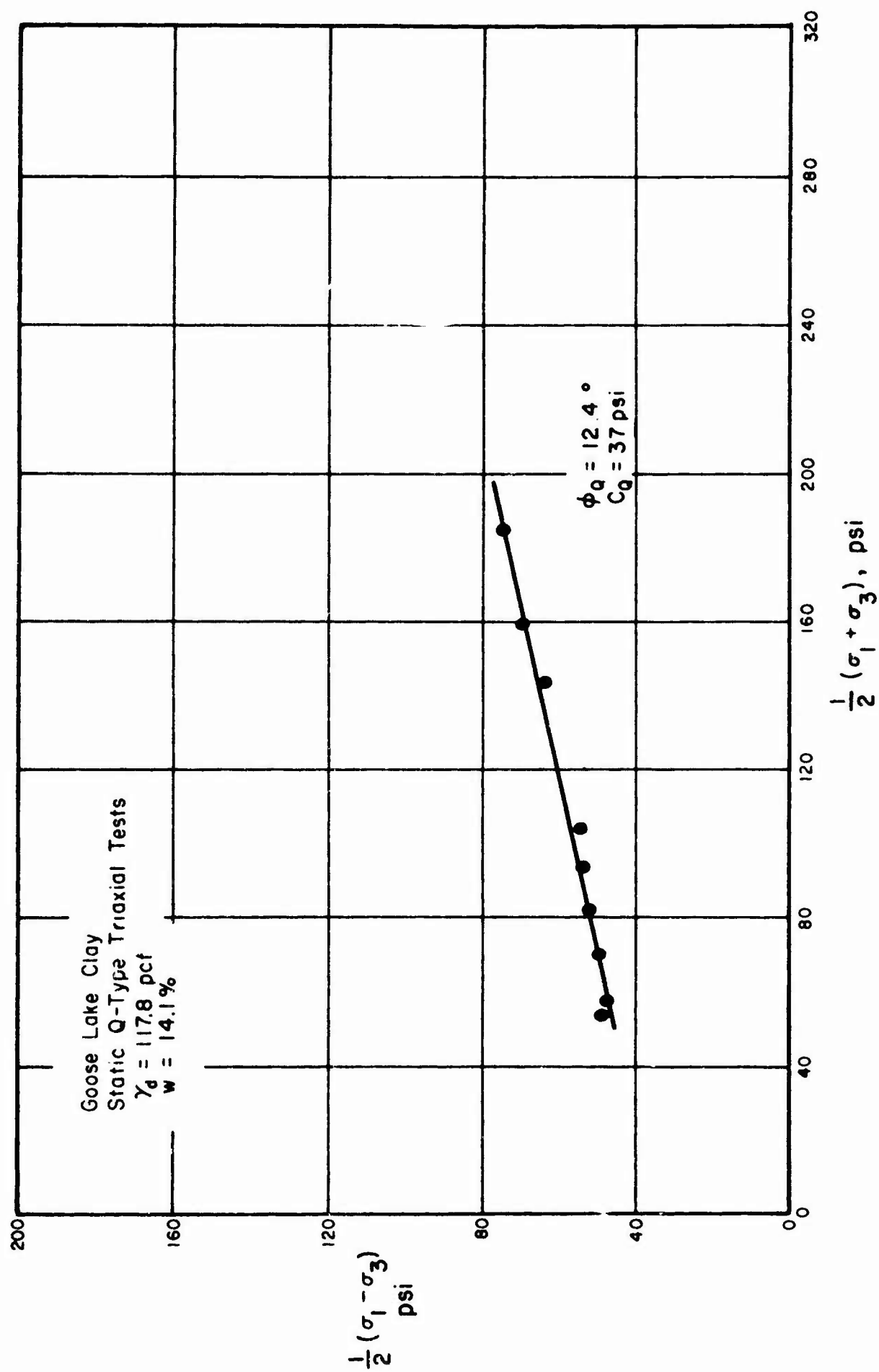


Figure 2.8. Mohr-Coulomb Diagram for Static Triaxial Tests on Goose Lake Clay .

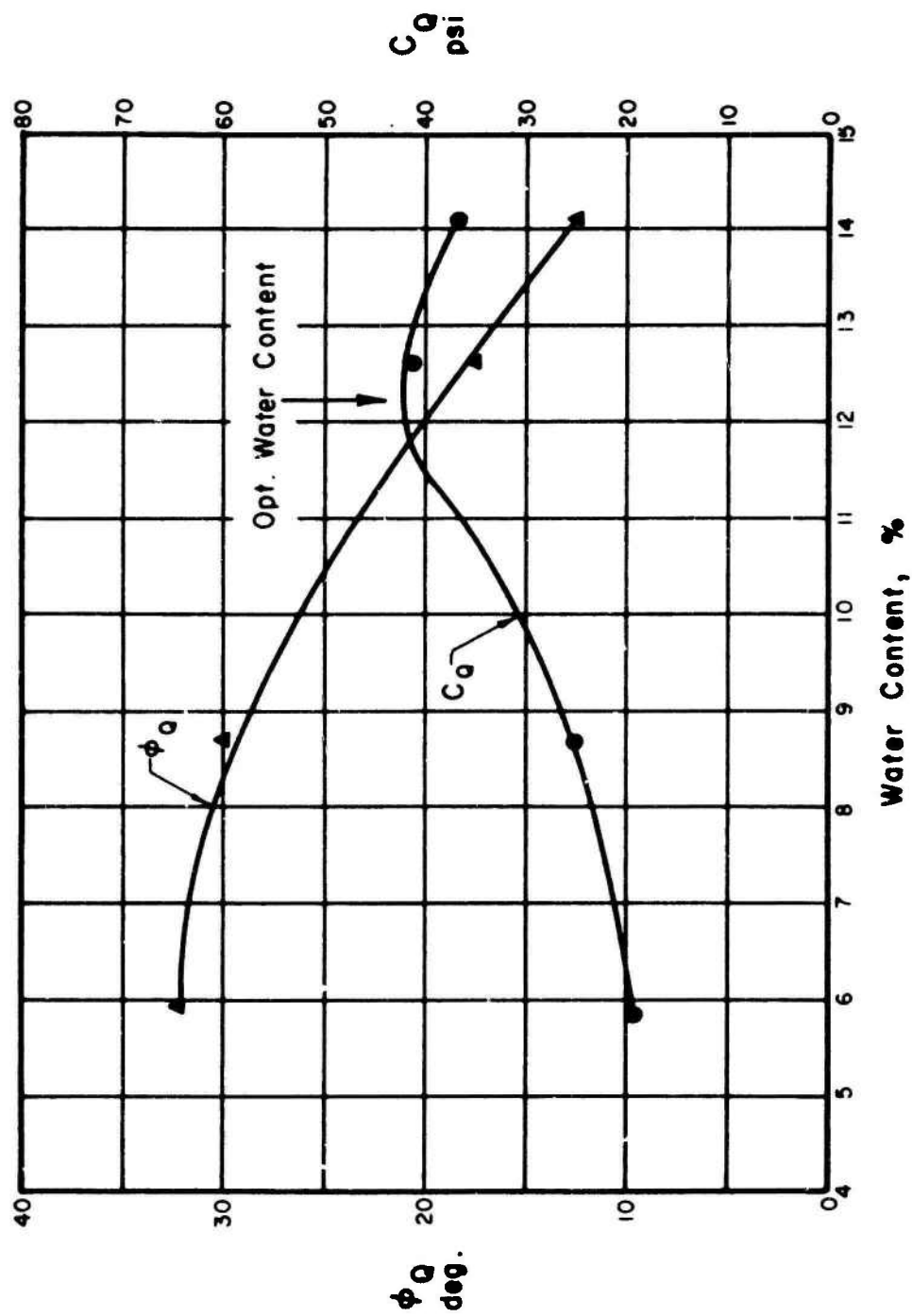


Figure 2.9. Total Stress Shearing Parameters from Static Unconsolidated - Undrained Triaxial Tests on Goose Lake Clay .

CHAPTER 3

ONE-DIMENSIONAL TESTS

3.1 GENERAL

To perform the one-dimensional compression tests it was necessary to develop machines capable of applying dynamic compressive loads. The governing criterion was that the full load should be applied within five milliseconds; control over the rate of load application was also considered desirable. Other requirements were that the machine be capable of maintaining the load for a controlled period of time, and that the load could be decayed rapidly. Consequently, the strain measuring equipment had to be capable of responding to the strain rates involved. A peak stress of 10,000 psi was to be obtained on the soil specimen.

One-dimensional compression implies that no lateral strains are allowed to occur. Although this restraint is possible in static tests¹, economical means are not available at present for controlling lateral strains in dynamic tests. Consequently thick steel rings were used in this investigation to confine the soil specimens; the thickness of the ring was controlled to keep the radial strains to a minimum. For reasons presented later it is believed that the occurrence of limited radial strains had a very minor influence on the test results.

Figure 3.1 illustrates schematically the problems and requirements of dynamic one-dimensional compression tests. It is desirable to measure the axial stress σ_a , the radial stress σ_r , and the axial strain ϵ_a , when the radial strain, ϵ_r , is kept to a minimum. Further, simultaneous values of these measurements are desired, but such measurements are not

feasible with the present state of the art of instrumenting soil tests. Therefore, indirect measurements are made that must be interpreted with considerable judgment to account for the influence of stress wave propagation on the time relationship of the measured functions.

For example, the peak axial stress wave passes through the SR-4 load cell before the soil specimen is stressed to this level. Furthermore, after the peak stress reaches the soil, there is a delay before the concomitant radial stress in the soil is indicated by the SR-4 gages on the periphery of the confining ring that were used to measure radial stresses.

Several other problems also exist even for static tests. The axial deformation is measured between two points remote from the soil specimen; therefore, the deflections of the equipment must be determined and subtracted from the recorded deflections. The usual problems of seating errors and ring wall friction are also present and must be minimized. The following section describes the details of the test apparatus along with the solutions, and compromises, to the foregoing problems.

3.2 DESCRIPTION OF APPARATUS

Confining Rings

A thick steel ring one-inch high with a four-inch inside diameter was used to confine the test specimens. To limit the amount of radial strain induced by an applied axial stress, the thickness of the ring in a radial direction was adjusted for the range of radial stresses that would be imposed. An attempt was made to limit the radial

strains to only those required to facilitate accurate recording by the use of SR-4 gages. As the ring thickness in a radial direction was increased, the amount of strain that could be recorded on the periphery decreased; therefore, thicker rings were used for the higher stress levels. A wall thickness of 0.3 inch was used for the 2,500-psi stress level, whereas the thicknesses ranged up to one inch for the 10,000-psi stress level. The details of the instrumentation are discussed in a later section. Figure 3.2 shows the dimensions of the rings, the pressure ranges in which they were used, the theoretical radial strain of the soil per psi of radial stress, and the number of microinches output per psi of radial stress, as determined by calibration.

Figure 3.3 is a schematic of the equipment that was used to calibrate the confining rings. The equipment consists essentially of a base and an upper cap having a chamber with a diameter equal to that of the inside diameter of the ring. The ring was inserted between the upper and lower parts and a clearance was maintained between them. The clearance was just sufficient for the ring to expand radially without inducing frictional forces against the upper and lower parts of the calibration device. A rubber diaphragm was used to contain the hydraulic fluid and prevent it from leaking out from between the clearances. Calibrations were carried out by inducing a pressure in the hydraulic fluid which was recorded by a calibrated Bourdon gage. The output of the SR-4 gages was monitored with an SR-4 indicator; the calibrations were linear.

Rapid Loading Machine

It was found convenient to use hydraulic loading equipment for rise times in excess of 35 milliseconds. To distinguish this from the

dynamic loading equipment that is described in the following section, the hydraulic machine has been denoted as the "rapid-loading machine." The schematic of the rapid-loading machine is shown on Fig. 3.4; it is essentially a hydraulic ram mounted in a frame. The load is applied to the soil specimen by vigorously operating a three-way lever valve that connects the hydraulic ram to a reservoir of oil subjected to high pressure from a pneumatic source.

As shown in Fig. 3.4 the pressure source is commercial nitrogen that is connected to a pressure manifold. Gas from the pressure manifold is supplied to the pneumatic control panel. The pneumatic controls are divided into two ranges, one for high pressure and one for low pressure. The controlled nitrogen pressure is then supplied to a transfer barrier in which the nitrogen pressure is converted to oil pressure. No pressure loss occurs in the transfer barrier because the nitrogen is enclosed in a neoprene bag. This also is a safety precaution. The oil from the transfer barrier is connected to the hydraulic ram after passing through a solenoid-operated valve and a three-way manual valve. An oil reservoir is shown connected to the third position of the three-way valve and to the outlet of the solenoid-operated valve. Oil may be exhausted from the ram into the reservoir, or in reverse, oil may be supplied from the reservoir to either the transfer barrier or to the ram. The solenoid-operated valve is a safety precaution; a microswitch placed above the ram causes the solenoid-operated valve to close when the switch contacts the ram, thereby preventing further ram motion. The essential feature of the three-way valve is that it has relatively large port openings, but may be easily operated by a 45-degree movement of the lever, even

under a 30,000-psi pressure. The solenoid-operated valve also has a relatively large port, and when coupled with the 1/2-inch extra-heavy pipe this allows a relatively unobstructed flow of the hydraulic fluid and a rapid application of the load by the hydraulic ram.

The operation of the machine proceeds as follows: the three-way valve is placed in the off position and a nitrogen pressure sufficient to produce the desired load in the hydraulic ram is introduced into the transfer barrier. When the three-way valve is moved to the position connecting the transfer barrier to the hydraulic ram, the load is applied. The third valve position connects the ram to the oil reservoir. Oil from the ram may then escape into the reservoir, thereby providing a decay of the load. The ram has a diameter of 8 1/2 inches for which a pressure of 2,210 psi is required to produce a load of 125.6 kips which is equal to 10,000 psi on the soil specimen. This is essentially the upper limit of the equipment because commercial nitrogen is normally supplied at a guaranteed minimum pressure of 2,300 psi.

Figure 3.5 shows an example of test data obtained in the rapid test machine. The axial and radial stresses and the axial strain are shown plotted against time for Test No. 13. The initial portion of the axial stress-time diagram is concave upwards for which approximately 30 percent of the rise time is required to apply 10 percent of the load. Beyond the early portion of the curve the load time relationship is essentially linear to within 10 percent of the first peak. For the first peak an overshoot of approximately 9 percent of the steady-state stress level occurs. The radial stresses are essentially in phase with the axial stresses, but the stress oscillations are damped considerably.

The axial strain-time relationship is not in phase with the stress relationships, indicating that some strain rate effects are present. The peak strain lags slightly behind the peak stress, but after the peak strain is reached there is essentially no increase in strain with time. The traces on Fig. 3.5 are taken directly from an FM tape recording made with equipment having a frequency response of 10,000 cycles per second. The characteristics of the recording equipment will be described in a following section.

Dynamic Loading Machine

The essential feature of the dynamic loader is the mechanism that produces the dynamic load. It is a pneumatic valve that will release gas at 1,000 psi from a reservoir in times approaching 2 milliseconds. The details of the pneumatic loader are given by Sinnamon and McVinnie². Figure 3.6 is a schematic of the dynamic loading machine. The equipment shown on the lower portion of the schematic is the auxiliary equipment designed especially for this project. Essentially, the pneumatic valve supplies a gas pressure which is collected on top of a control piston within an expansion chamber. The load applied on the control piston is carried through the load cell to the soil specimen. The entire machine is mounted in a reaction frame which is not shown on the schematic.

The operation of the machine is initiated by placing the main valve in the closed position. The chamber is then charged with nitrogen to a pre-determined pressure level. A charge pressure as high as 1,000 psi may be used. The valve is operated by a trigger assembly, which in itself is a pneumatic loading device. A pressure of 400 psi is introduced into the trigger assembly; the trigger assembly is connected

to the rod that operates the main valve. A mechanical device holds the main piston in the off position. To fire the machine a solenoid-operated device is used to electrically trip the mechanical stop holding the main piston in the off position. The gas in the trigger assembly chamber then moves the piston at a very high speed, on the order of 400 inches per second, which in turn rapidly opens the main valve and allows the gas to expand into the expansion chamber. A feature of the pneumatic valve is that the main piston travels a distance sufficient to achieve a very high speed before the valve ports begin to open. The rise time is adjusted by controlling the size of the ports on the main valve. The decay time is controlled by adjusting the port size on the decay valves. Because the entire system is enclosed, and is controlled by valves, the machine is capable of holding a constant load (dwell). Over long periods of time the increase in the temperature of the gas accompanying the expansion will cause an increase in load with time. This is not significant except for dwell-times exceeding several seconds.

Figure 3.7 shows test data obtained in the dynamic loading machine; the axial and radial stresses and the axial strains have been plotted versus time for Test No. 2. In this test the steady state pressure during the dwell portion was 8,700 psi whereas the initial peak was at 9,350 psi. Thus an overshoot of less than 10 percent of the steady state stress was observed; however, the percentage of overshoot increases as the pressure level decreases. For example, in Test No. 6 an overshoot of approximately 291 percent of the steady state stress was observed. Generally the radial stress lags the axial stress by approximately 0.1 millisecond and the oscillations are damped considerably. The axial

to the rod that operates the main valve. A mechanical device holds the main piston in the off position. To fire the machine a solenoid-operated device is used to electrically trip the mechanical stop holding the main piston in the off position. The gas in the trigger assembly chamber then moves the piston at a very high speed, on the order of 400 inches per second, which in turn rapidly opens the main valve and allows the gas to expand into the expansion chamber. A feature of the pneumatic valve is that the main piston travels a distance sufficient to achieve a very high speed before the valve ports begin to open. The rise time is adjusted by controlling the size of the ports on the main valve. The decay time is controlled by adjusting the port size on the decay valves. Because the entire system is enclosed, and is controlled by valves, the machine is capable of holding a constant load (dwell). Over long periods of time the increase in the temperature of the gas accompanying the expansion will cause an increase in load with time. This is not significant except for dwell-times exceeding several seconds.

Figure 3.7 shows test data obtained in the dynamic loading machine; the axial and radial stresses and the axial strains have been plotted versus time for Test No. 2. In this test the steady state pressure during the dwell portion was 8,700 psi whereas the initial peak was at 9,350 psi. Thus an overshoot of less than 10 percent of the steady state stress was observed; however, the percentage of overshoot increases as the pressure level decreases. For example, in Test No. 6 an overshoot of approximately 291 percent of the steady state stress was observed. Generally the radial stress lags the axial stress by approximately 0.1 millisecond and the oscillations are damped considerably. The axial

strains tend to lag the axial stress somewhat; they reach their maximum value a few milliseconds after the application of the initial peak stress. Afterwards, there is essentially no increase in strain with time while the steady state stress is applied.

The operating characteristics of the machine are such that an initial stress peak tends to occur within three milliseconds regardless of the time at which the peak stress is obtained. This is believed to be due primarily to the physical characteristics of the reaction frame, and to a certain extent, the control piston that collects the gas from the pneumatic valve. Therefore, a load time relationship uninterrupted by an oscillation before the peak stress is obtained requires that the rise time be less than approximately 4 milliseconds. These operating characteristics could be changed by a change in the mounting system. Figure 3.7 is an example of dynamic test data showing a stress oscillation before the initial peak stress has been observed.

Instrumentation

The confining ring and the load cell were instrumented with SR-4 gages connected in a standard four arm bridge. The strains were measured with a linear variable differential transformer (LVDT). These sensors were monitored with a CEC type 5-124 oscillograph and a Minneapolis-Honeywell model 8100 FM tape recording system. The amplifiers used to drive the equipment were in a CEC type 1-127 20-kc 4-channel carrier amplifier system; the output of the system was used to drive the oscillograph directly. The output from the CEC carrier system was also carried through a model 2000 Dana OC amplifier to provide a signal for the FM tape system. CEC type 7-363 galvanometers (1000 cycle response)

were used throughout the testing program: a paper speed of 128 inches per second was used for the dynamic tests, whereas a speed of 60 inches per second was used for the rapid tests. A timing signal of 500 cycles per second was used on the oscillograph, whereas a 10-kc signal was used for the tape system.

Figure 3.8 is a schematic of the electrical hookup for the SR-4 gages on the confining ring. Four active gages were mounted on the periphery of the confining ring at 90-degree intervals. They record circumferential strains. Unstressed external dummy gages are used to complete the four-arm bridge.

Figures 3.9 and 3.10 present schematics of the SR-4 gage hookup for the load cells used in the rapid and dynamic machines, respectively. Different load cells were used, according to the required load, in order to provide maximum sensitivity at the low stress levels. The hookup was a standard four arm bridge. The tables on Figs. 3.9 and 3.10 list the load cell capacities and the sensitivities in terms of stress on the soil specimen per microinch of output on the recorder.

A Schaevitz model No. 040 MS-L LVDT with a linear range of plus or minus 0.020 inch was used to monitor the strains. Figure 3.11 is a schematic of the micrometer depth gage system that was used to calibrate the core movement of the LVDT. An electrical null position was found before calibration of the LVDT. The LVDT was calibrated by moving the LVDT core both up and down from the null position in increments of 0.020 inch as determined from the micrometer. For slow tests in the rapid test machine it is possible to use dial indicators to monitor the deflection as shown on Fig. 3.11.

3.3 TEST PROCEDURES

The Goose Lake Clay was stored in a covered 33-gallon galvanized can at room temperature. The water content of the soil before sample preparation was approximately one percent. Batches of 1000 gms. of soil plus 105 ml. of water were hand mixed, placed in sealed glass containers, and stored for twenty-four hours to allow the molding water to distribute itself equally throughout the soil. Two test specimens could be compacted from each batch.

Before compaction, the empty consolidation ring was weighed to the nearest gram and the combined height of the base plate and piston measured with a dial-comparator device. After storage the soil was spooned into the instrumented consolidation ring which was held in a clamping device, designed specifically for the large diameter consolidation rings (Fig. 3.12). The soil was compacted in two layers, each layer receiving twenty-two evenly distributed blows from a 5.5 lb. hammer falling twelve inches. The top of the bottom layer was scarified to ensure a bond between it and the top layer. Before the soil for the bottom and top layer were placed in the ring, small representative samples were taken for water-content determinations. After compacting the top layer, a steel disc having a diameter slightly less than four inches was set in the collar and held in position as the collar was lifted off; this prevented removing some of the compacted soil as the collar was removed. The soil was then trimmed to the top of the consolidation ring with a laboratory knife and steel straight edge. After all loose soil was cleaned from the outside of the ring, the ring and specimen were weighed to the nearest gram. The compacted specimen,

base plate, piston, and lucite guide were assembled and set in the dial-comparator device to determine the combined height of the base plate, specimen and piston. The specimen height was determined to the nearest 0.001 inch by subtracting the initial dial-comparator reading from the final reading. It should be noted that the soil used in these tests was used only once, i.e., test specimens were not dried and ground for subsequent use.

After testing, the assembly was set in the dial-comparator to determine the change in specimen height. The specimen was extruded from the ring, placed in a container, weighed, and oven-dried at 110°C for twenty-four hours to determine the as-tested water contents. Table 3.1 lists the initial dry density, water content, void ratio, and degree of saturation for each of the 24 test specimens. The mean value of the initial dry densities was 121.1 pcf with a standard deviation of 0.87 pcf. Similarly, the initial water contents averaged 11.57 percent with a standard deviation of 0.30 percent; this amounts to 97.3 percent of the modified Proctor density. It should be noted that the density control maintained in this program exceeds that normally achieved in soil compaction research.

After preparation the soil specimen assembly was placed in the testing machine. In the dynamic loading machine a seating stress on the order of 135 psi was required to ensure that a compressive stress was always on the test specimen. Referring to Fig. 3.6 it is seen that the upward motion of the main piston increases the volume of the expansion chamber. This will cause a vacuum which can produce an upward motion of the piston immediately upon opening of the valve. A pressure of 12 psi

was introduced into the expansion chamber to prevent an upward motion. After application of the preload the LVDT core was put in the null position and its movement calibrated as mentioned in section 3.2 on instrumentation. Electrical calibration steps were used to simulate the effects of strain for both the load cell and confining ring. Generally, four or five calibration steps were used.

The actual test was performed by charging the chamber in the pneumatic valve with nitrogen to the pressure that would produce the desired steady state stress on the soil specimen. A timing device was utilized to delay the firing of the valve assembly 0.4 second until the recording equipment had an opportunity to attain its operating speed. A second timing unit was employed to trip the decay valve after the steady state stress had been applied for a designated period of time. A third timing device was used to turn off the recording equipment. After the test the oscillograph trace was developed by exposing it to light; the results were inspected to be sure that all recording systems had performed satisfactorily.

In the rapid test machine the test procedure was essentially the same as for the dynamic machine, except that a preload on the order of 10 psi was applied. The instrumentation was precisely the same, but the operation of the machine was manual and was not programmed electrically as was the dynamic machine. The loading operation was carried out by placing the three-way valve in the off position and then charging the transfer barrier with a predetermined nitrogen pressure. The three-way valve was then opened vigorously to apply the load to the hydraulic ram.

By vigorously reversing the position of the three-way valve it was placed in the exhaust position and the load was decayed.

Figure 3.13 shows a photo of the confining ring assembly. Close-ups of the confining ring assembly in the rapid and dynamic loading machine are shown on Fig. 3.14 and 3.15 respectively. Photographs of the rapid and dynamic machines are shown in Figs. 3.16 and 3.17 respectively.

In general it is believed that the accuracy of the measurements, and other factors associated with the measurements, are within the five-percent limits usually considered adequate for dynamic testing. Because of the initial strain due to the preload in the dynamic testing machine, the recorded strains are not the total strains, but are those relative to the preload. Fortunately, the preload was constant for all tests. A strain of approximately one percent occurred under the preload stress; this fact must be considered when comparing the dynamic tests to the rapid tests for which the preload stress and strain were negligible.

The initial height of the specimen was determined within plus or minus 0.0005 inch with the dial-comparztor. The LVDT measurements are believed to be accurate within plus or minus 0.001 inch. Because of the many calibration steps that were used on the LVDT, and considering the possible electrical and mechanical errors, the total error involved in the strain measurement is likely to be on the order of plus or minus two percent of the peak strain. A large signal was available from the load cells, and it is believed that the load measurements are accurate within plus or minus one percent of the peak load. The ring, however, was purposely limited in strain so that only a sufficient signal for accurate

recording was obtained. The measurements on the ring are believed to be accurate within plus or minus two percent.

A possibility of error exists for the seating of the base plate and the piston onto the soil specimen. In the preparation of the soil specimens the lower face of the soil was in contact with the ground steel base plate. The upper surface was smoothed with a straight edge. Considering these sources, it is not likely that a seating error of more than 0.002 inch is involved.

Because of the friction of the soil on the sides of the confining ring some of the load is carried through the ring to the base. For this reason a very light coat of lubricant was applied to the inside of the confining rings before the soil was placed in it. Another possible loss of load occurs if the piston binds when entering the ring. It was observed, however, that the piston did not bind in the ring because at high pressures a very thin film of soil was observed extruding around the entire piston. The magnitude of the friction loss is one of the factors that entered into the design of the test assembly. To keep the effects of ring wall friction to a minimum, it is desirable to have the diameter of the soil specimen very large with respect to the height of the soil specimen. In fact, the thickness should be zero for the optimum effect. By contrast, the thickness of the specimen should be very great to decrease the importance of seating errors. Because artificial samples were used, and because their surfaces could be trimmed accurately, the seating error was given relatively little weight in the choice of the ring height-diameter ratio. It was desirable to have a sufficient amount of sample thickness so that an accurate measurement of total deformation could be

made. At the same time it was necessary to restrict the diameter of the specimen to four inches to achieve a 10,000-psi pressure with the 130-kip load that is available in the dynamic loading machine. An estimate of the possible ring friction error involved was made in a manner similar to that used by Taylor³; the effect is believed to be less than five percent.

Another source of error may occur in the measurement of radial strains. Because the ring is being forced downward against the base plate, and at the same time is straining radially, there is a possibility of friction of the ring on the base. The base has been lubricated to keep this effect to a minimum. The error involved is unknown, but it is not believed to be significant due to the very small radial strains involved.

3.4 DATA REDUCTION

The FM tape records shown on Figs. 3.5 and 3.7 are typical of those obtained throughout the testing program. Because of the high-frequency response of the tape recording system (10,000 cps) and the 20-kc carrier amplifier system, it is possible to see the large number of minor oscillations that actually occur. By contrast, the oscillograph records were smooth curves with the high-frequency oscillations effectively filtered out by the galvanometer. In order to select data from the FM tape records an average line through the minor oscillations was assumed.

Generally the FM tape records were relied on for the data reported herein. With the tape data reduction equipment now available in the Department of Civil Engineering at the University of Illinois, it is possible to plot point by point data digitized from the FM tape; the interval of time between the points may be made as small as desired.

Generally, for the dynamic tests, the first 15 milliseconds of the record were plotted; this was divided into 400 intervals by the automatic data reduction equipment. The data were then plotted, along with the calibrations, and the plotter was attenuated so that the traces were to a convenient scale in terms of psi or percent strain. This greatly reduced the amount of labor in reducing data from an oscillograph record. The values of the rise times and the peak stresses as well as the total time for the test were checked against the oscillograph record for consistency; the records generally were in agreement.

The magnification of the early portion of the data makes it possible to study the soil behavior in detail. The FM tape records were also reduced for the entire length of the test. In this case the test, which may be on the order of 0.5 second to 1 second long, was divided into 400 intervals and the points were plotted. These records were useful for determining the length of the dwell time and also gave an estimate of the decay time; the value of the steady state stress was also obtained very accurately. The reduced FM tape records represent the raw data from which all of the test results reported herein were obtained. It should be noted, however, that on the axial strain record a correction was made for the machine deflections. This correction was made by attenuating the axial strain record on the plotter to bring the peak value of the axial strain to the value determined by subtracting the machine deflection. Therefore, the correction applied at the peak strain was applied proportionately throughout the record.

3.5 TEST RESULTS

The reduced data from the FM tape records have been used to obtain the data plots presented in Appendix A. Figures A.1 - A.25 show the axial stress plotted versus the axial strain; Fig. A.1 - A.12 are for the dynamic tests, Fig. A.13 - A.24 are for the rapid tests, and Fig. A.25 is for the static test. In a similar manner the constrained secant modulus, M_{cs} , and the constrained tangent modulus, M_{ct} , have been plotted on Figs. A.26 - A.50, whereas the radial stress has been plotted versus the axial stress on Figs. A.51 through A.75.

In Tables 3.2 and 3.3 a summary of the test data is presented for both the dynamic tests (Nos. 1-12) and the rapid tests (Nos. 13-24). The time from the start of loading to the first stress peak (rise time), the time between the first stress peak and the beginning of unloading (dwell time), and the time from the beginning of unloading to zero load (decay time) have been tabulated; the sum of these three time intervals equals the total elapsed time for the test. In addition the axial stress, axial strain, degree of saturation, and the ratio of the radial stress to the axial stress, K_o , have been tabulated at the initial peak axial stress. The value of K_o for the initial part of the test has been tabulated along with the stress level up to which it is valid. After the first few load oscillations the axial stress and strain assume essentially constant values (steady state); these values have also been tabulated. Finally, the recorded residual strain at the end of the test has been tabulated. The residual strain determined by the dial-comparator did not agree with that determined electrically for the dynamic tests because of the strain that occurred during the application of the preload.

In the dynamic stress-strain plots on Figs. A.1 - A.12 the dashed line from the origin to the 135-psi stress level indicates the strain that occurred under the preload stress. The dynamic data are represented by a solid line that is generally concave upwards. At a stress level of 4,000 psi a flattening of the curve is detected which is caused by extrusion of the soil from the confining ring. After reaching the initial stress peak several oscillations occur which are not shown. A dashed line is shown from the initial peak stress to the unload portion of the stress-strain relationship. In those tests wherein significant extrusion took place the rebound curve has been omitted because it has no meaning. The same procedures have been used in Figs. A.13 - A.25 except that the stress and strain under the seating load are negligible and have been ignored.

On Figs. A.26 - A.50 the secant modulus has been taken as the stress divided by the corresponding strain. It should be noted that for the dynamic tests in Figs. A.26 - A.37 the stress-strain axes have been shifted to the preload position because only the dynamic effects were desired. The tangent modulus was determined as the slope of the chord between two points on the stress-strain curve. Data points were not always used to obtain the slope; in many cases the modulus was taken as the slope of a smooth curve fitted through the data points. The moduli have been presented only for the initial loading portion of the stress-strain curve.

The axial stress-radial stress relationships shown on Figs. A.51 - A.62 for the dynamic tests again refer to the preload stress and strain as the origin. Curves are presented for the initial loading and for the

unloading portion of the test. In many cases a dashed line has been used to connect the two parts to indicate that several load oscillations occur in between. For the tests wherein extrusion occurred, the rebound curve has been omitted because it is meaningless.

3.6 SUMMARY OF TEST RESULTS

The initial loading portion of the stress strain curves for the dynamic tests have been summarized on Fig. 3.18. If the soil specimens had been absolutely identical and if the testing machine had performed in the same manner for each test, then all the curves should be identical. In an attempt to determine the reason for the relatively wide range of strain that was observed at high pressures the initial degree of saturation and the strain rate stand out as the prime suspects. No definite conclusions could be drawn regarding the strain rate, but in general, the initial degree of saturation was higher for those tests in which a high modulus was observed. A similar study has been made of the rapid test data on Fig. 3.19. In this case the results are much more uniform and no correlation could be made with either degree of saturation or strain rate.

The foregoing data have been compared with the one-dimensional compression tests now available in the literature¹ in Fig. 3.20. Tests Nos. 7 and 13 have been eliminated because they are probably not representative of the remaining tests. It is seen that the band of rapid test data falls within the band of the dynamic test data but is offset in the direction of higher strains. The results of the static tests fall to the right of both the dynamic and the rapid tests. It should be noted

that relatively small strains were observed for the Goose Lake clay in comparison to the strains observed for the playa silt from the Nevada Test Site.

As noted on the stress strain curve on Figs. A.1 - A.25 in Appendix A, the unloading portion of the curve is very steep except at stress levels below a few hundred psi. Because of the importance of residual strains in the design of protective construction, an attempt was made to correlate the residual strain with the peak axial stress that occurred during the test. This plot is shown on Fig. 3.21; if the axes were rearranged, it is essentially a stress strain curve as shown for Test Nos. 1 to 25. For stress levels below approximately 1,000 psi but greater than 500 psi a residual strain on the order of 3 percent occurs. For stress levels beyond 1,000 psi but less than approximately 10,000 psi the residual strain is, for the most part, between 3 percent and 5 percent. In terms of degree of saturation a strain of 3 percent amounts to approximately 87 percent saturation whereas a strain of 6 percent is required for 100 percent saturation; these figures are based on the average moisture content and dry density for the test series. It is significant that an increase in the stress level from 1,000 psi to 10,000 psi will cause an increase of approximately 50 percent in the residual strain. It should also be noted that there is essentially no difference between the dynamic and the rapid test data. As noticed on the strain versus time records there is essentially no increase in strain with respect to time after a period of several milliseconds from the time the peak stress was applied. For this reason there should be essentially no difference between the residual strains observed for the static and

the dynamic tests. Note, however, that the residual strain from the static test is more than twice as high as that observed in the rapid or dynamic tests. This test was performed in a period of 15 minutes to 30 minutes and there was time for drainage (consolidation) as well as some extrusion to occur.

Because the tangent moduli are extremely difficult to determine (in that they depend on the slope of the stress strain diagram), no attempt has been made to correlate them. By contrast, the secant modulus is not as sensitive as the tangent modulus to small changes in the stress strain curve. Figure 3.22 shows the zones occupied by the secant moduli from the dynamic and the rapid tests. Again it is noted that the rapid test data fall within the zone of the dynamic test data, but they generally have somewhat lower values. In the stress range from zero to 1,000 psi the secant modulus decreases to a minimum at approximately 50 psi and then increases in a nearly linear relationship with the axial stress level. It should be noted that if the data were to be used to predict ground motions, relatively accurate predictions could be made for stress levels beyond 1,000 psi, but for stresses below 1,000 psi the problem becomes much more difficult.

The relationship between the axial stresses and radial stresses have been summarized in Fig. 3.23 for the dynamic tests. The ratio of the radial stress to the axial stress has been defined as K_0 ; it varies from 0.4 at the low stress levels to unity at the high stress levels. For axial stress levels beyond approximately 1,500 psi the axial stress-radial stress relationship is essentially parallel to the line $K_0 = 1$. At the lower stress levels, below 1,500 psi, the soil is not saturated

and the K_0 -value is less than unity. However, as the stress level is increased the additional stresses are essentially transmitted to the pore water; this stress is distributed equally in all directions and accounts for the fact that the relationship becomes parallel to the line $K_0 = 1$. The rapid test data are shown on Fig. 3.24; they will fall within the zone for the dynamic data. For practical purposes, when dealing with high pressures, the value of K_0 may be assumed equal to unity although a more precise value may be on the order of 0.9. If the soil were saturated initially, a value of unity would be appropriate in all cases. It should be noted for the high stress levels, when the applied stress is essentially carried by the pore water, that the rebound relationship should be very similar to that for the loading. The test data presented in Figs. A.51 to A.75 confirm the anticipated behavior.

REFERENCES

1. Hendron, A. J., Jr., and Davisson, M. T., (1963), "Static & Dynamic Behavior of a Playa Silt in One-Dimensional Compression," Technical Documentary Report No. RTD TDR-63-3078 AFWL, Kirtland Air Force Base, New Mexico, September.
2. Sinnamon, G. K., and McVinnie, W. W., (1963), "Operation Manual & Fabrication Information for Gas Operated 90 kip Dynamic Loading Machine," Report to AFWL, Kirtland Air Force Base, New Mexico on Contract AF 29(601)-2876, August.
3. Taylor, D. W., (1942), "Research on Consolidation of Clays," Publication No. 82, Publications of the Department of Civil Engineering, Massachusetts Institute of Technology, Cambridge, Massachusetts.

TABLE 3.1
INITIAL SPECIMEN DATA

Specific gravity of soil solids, S_s , equals 2.72

| Test No. | Dry Density γ_{di} , pcf | Water Content w_i , % | Void Ratio e_i | Degree of Saturation S_{ri} , % |
|----------|------------------------------------|----------------------------|---------------------|--------------------------------------|
| 1 | 122.9 | 11.40 | 0.381 | 81.50 |
| 2 | 121.0 | 11.39 | 0.401 | 77.40 |
| 3 | 121.0 | 11.80 | 0.401 | 80.10 |
| 4 | 121.1 | 11.53 | 0.403 | 78.30 |
| 5 | 121.1 | 11.52 | 0.403 | 78.00 |
| 6 | 122.2 | 10.92 | 0.384 | 77.50 |
| 7 | 121.1 | 11.14 | 0.398 | 76.00 |
| 8 | 121.9 | 11.51 | 0.393 | 78.90 |
| 9 | 122.2 | 11.00 | 0.384 | 77.80 |
| 10 | 120.2 | 11.69 | 0.408 | 75.50 |
| 11 | 121.4 | 11.20 | 0.396 | 76.80 |
| 12 | 120.8 | 12.01 | 0.405 | 80.80 |
| 13 | 119.7 | 12.09 | 0.418 | 78.60 |
| 14 | 121.0 | 11.59 | 0.401 | 78.50 |
| 15 | 119.6 | 11.68 | 0.418 | 76.00 |
| 16 | 121.1 | 11.84 | 0.398 | 80.70 |
| 17 | 120.4 | 11.70 | 0.408 | 77.90 |
| 18 | 121.4 | 11.57 | 0.386 | 79.40 |
| 19 | 123.0 | 11.42 | 0.380 | 82.40 |
| 20 | 121.0 | 11.76 | 0.401 | 79.80 |
| 21 | 119.9 | 11.94 | 0.416 | 77.70 |
| 22 | 120.9 | 11.79 | 0.405 | 79.20 |
| 23 | 120.6 | 11.49 | 0.406 | 76.80 |
| 24 | 120.9 | 11.79 | 0.405 | 79.20 |
| | 121.1 | 11.57 | Mean Value | |
| | 0.87 | 0.30 | Standard Deviation | |

TABLE 3.2

SUMMARY OF DYNAMIC TEST DATA

| Sample Number | Time, milliseconds | | | Initial Peak | | | Ko | Initial Value | Steady State | | Residual | Residual by Dial Comparator | |
|---------------|--------------------|-------|-------|------------------|-----------|------------------|-------|---------------|------------------|-----------|----------|-----------------------------|-----------|
| | Rise | Dwell | Decay | σa , psi | ea, in/in | Saturation Sr, % | | | σa , psi | ea, in/in | | ea, in/in | ea, in/in |
| 1 E | 1.90 | ---- | ---- | 7,850 | 0.020 | 87.6 | 0.995 | 0.60/300 | ----- | ----- | ----- | ----- | ----- |
| 2 | 2.50 | 1150 | 180 | 9,350 | 0.050 | 94.1 | 0.895 | 0.50/700 | 8,700 | 0.030 | 0.022 | 0.040 | 0.040 |
| 3 | 3.30 | 410 | 105 | 6,900 | 0.038 | 92.6 | 0.920 | 0.30/500 | 4,380 | 0.038 | 0.029 | 0.038 | 0.038 |
| 4 | 2.85 | 970 | 80 | 6,710 | 0.036 | 93.2 | 0.834 | 0.55/800 | 4,200 | 0.034 | 0.026 | 0.039 | 0.039 |
| 5 | 3.95 | 415 | 65 | 1,840 | 0.036 | 89.3 | 0.945 | 0.67/400 | 740 | 0.034 | 0.026 | 0.032 | 0.032 |
| 6 | 4.40 | 960 | 90 | 2,930 | 0.029 | 86.2 | 1.000 | 0.74/400 | 750 | 0.035 | 0.027 | 0.031 | 0.031 |
| 7 | 4.28 | 425 | 295 | 11,300 | 0.083 | 100.0 | 0.975 | 0.25/600 | 8,800 | 0.105 | 0.097 | 0.047 | 0.047 |
| 8 E | 2.20 | 800 | ---- | 7,300 | 0.028 | 88.6 | 0.930 | 0.63/700 | ----- | ----- | ----- | ----- | ----- |
| 9 | 3.00 | 428 | 205 | 8,430 | 0.074 | 100.0 | 0.806 | 0.40/900 | 4,400 | 0.066 | 0.060 | 0.046 | 0.046 |
| 10 | 2.40 | 1000 | 100 | 4,420 | 0.035 | 85.8 | 0.865 | 0.48/600 | 4,060 | 0.044 | 0.034 | 0.043 | 0.043 |
| 11 | 5.60 | 310 | 620 | 1,550 | 0.049 | 92.8 | 0.858 | 0.75/700 | 680 | 0.043 | 0.034 | 0.044 | 0.044 |
| 12 | 4.40 | 1025 | 40 | 770 | 0.029 | 90.2 | 1.000 | 0.92/800 | 650 | 0.030 | 0.022 | 0.029 | 0.029 |

TABLE 3.3

SUMMARY OF RAPID TEST DATA

| Sample Number | Time, milliseconds | | | Initial Peak | | | Ko | Initial Value | Steady State | | Residual | Residual by Dial Comparator | |
|---------------|--------------------|-------|-------|------------------|-----------|------------------|-------|---------------|------------------|-----------|----------|-----------------------------|-----------|
| | Rise | Dwell | Decay | σ_a , psi | ea, in/in | Saturation Sr, % | | | σ_a , psi | ea, in/in | | ea, in/in | ea, in/in |
| 13 | 40 | 370 | 53 | 9,670 | 0.056 | 97.3 | 0.914 | 1.0/9,700 | 9,200 | 0.062 | 0.049 | 0.044 | 0.044 |
| 14 E | 68 | 180 | ---- | 9,700 | 0.057 | 98.1 | 0.981 | 0.57/500 | 8,300 | ----- | ----- | ----- | ----- |
| 15 | 83 | 151 | 53 | 4,900 | 0.064 | 99.7 | 0.888 | 0.52/600 | 4,400 | 0.063 | 0.052 | 0.045 | 0.045 |
| 16 | 48 | 725 | 75 | 5,070 | 0.054 | 99.4 | 0.925 | 0.44/400 | 4,650 | 0.050 | 0.032 | 0.036 | 0.036 |
| 17 | 85 | 160 | 50 | 860 | 0.045 | 92.3 | 0.720 | 0.53/600 | 760 | 0.046 | 0.023 | 0.033 | 0.033 |
| 18 | 77 | 750 | 65 | 850 | 0.041 | 92.8 | 0.711 | ---/--- | 750 | 0.049 | 0.034 | 0.031 | 0.031 |
| 19 | 1,250 | 900 | 100 | 8,350 | 0.063 | 100.0 | 0.977 | 1.0/8,300 | 8,300 | 0.063 | 0.048 | 0.044 | 0.044 |
| 20 | 1,375 | 340 | 360 | 8,450 | 0.052 | 97.5 | 1.000 | 1.0/8,500 | 8,500 | 0.052 | 0.034 | 0.044 | 0.044 |
| 21 | 800 | 975 | 65 | 4,200 | 0.055 | 96.3 | 0.905 | 0.53/700 | 4,250 | 0.055 | 0.034 | 0.036 | 0.036 |
| 22 | 460 | 0 | 180 | 2,660 | 0.051 | 96.1 | 0.910 | 0.68/900 | ----- | ----- | 0.035 | 0.034 | 0.034 |
| 23 | 1,625 | 115 | 85 | 6,900 | 0.043 | 90.5 | 0.638 | 0.44/400 | 6,900 | 0.043 | 0.025 | 0.026 | 0.026 |
| 24 | 925 | 0 | 115 | 620 | 0.040 | 92.1 | 0.360 | 0.57/500 | 620 | 0.040 | 0.020 | 0.024 | 0.024 |

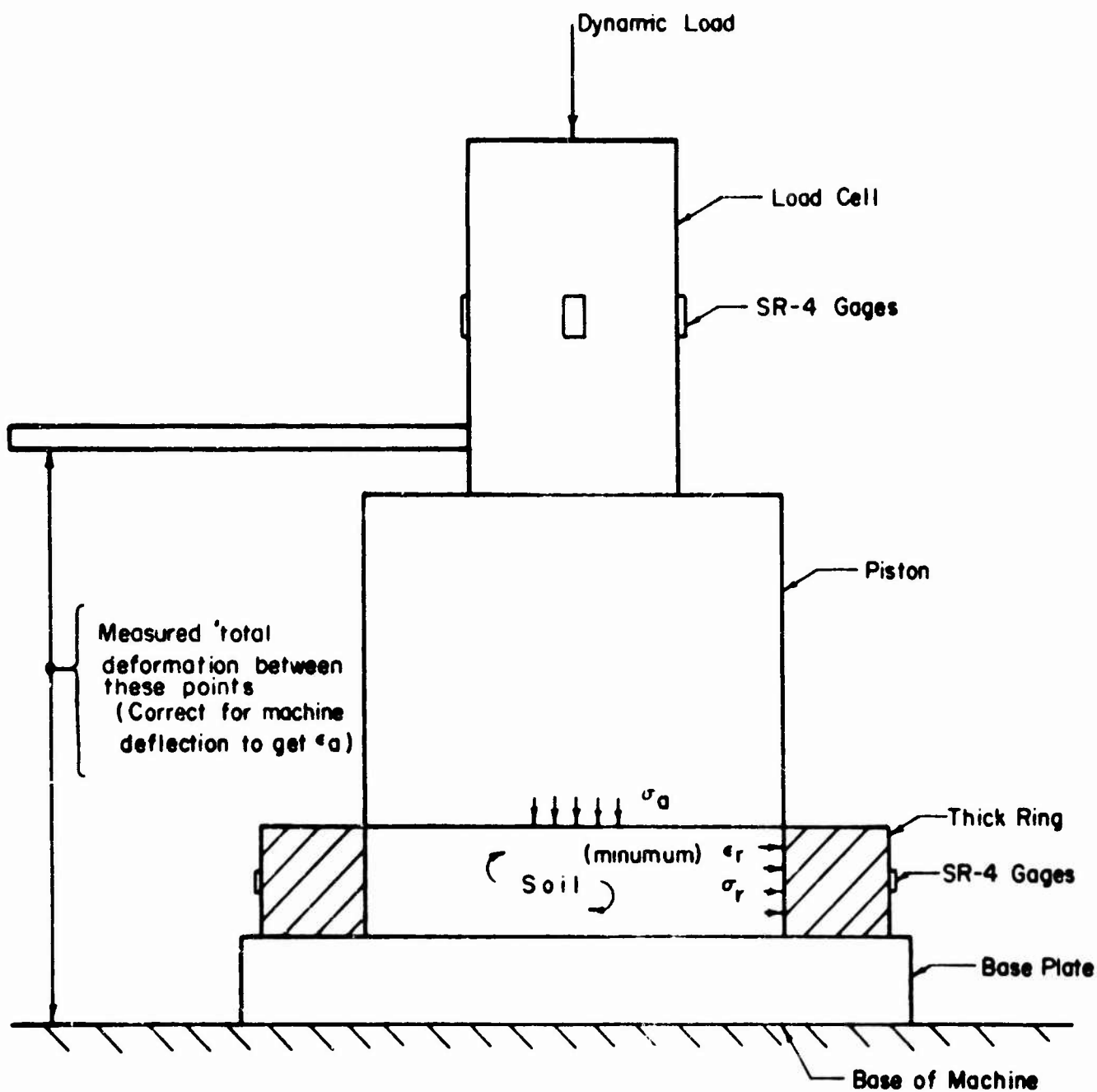
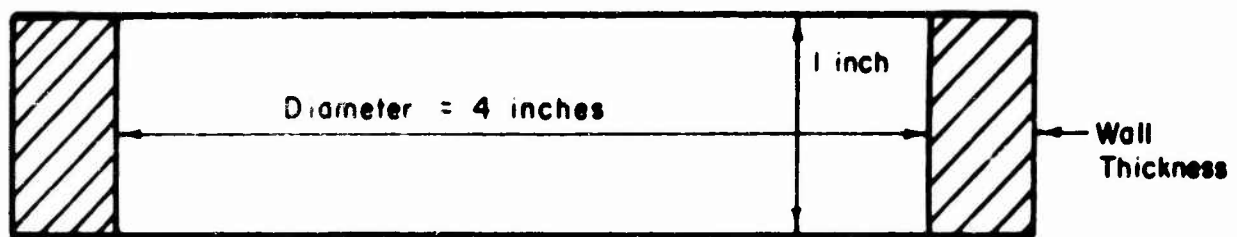


FIGURE 3.1. ONE-DIMENSIONAL TEST REQUIREMENTS .



| Ring Number | Wall Thickness, inches | Theoretical Strain μ in/in/psi | Recorded External Strain μ in/in/psi | Maximum Design Internal Pressure, psi |
|-------------|------------------------|------------------------------------|--|---------------------------------------|
| 1 | 0.100 | 0.6460 | 1.281 | 1,000 |
| 2 | 0.100 | 0.6460 | 1.300 | 1,000 |
| 3 | 0.300 | 0.2460 | 0.416 | 2,500 |
| 4 | 0.300 | 0.2460 | 0.408 | 2,500 |
| 5 | 0.500 | 0.1620 | 0.243 | 5,000 |
| 6 | 0.500 | 0.1620 | 0.236 | 5,000 |
| 7 | 1.000 | 0.0965 | 0.104 | 10,000 |
| 8 | 1.000 | 0.0965 | 0.1075 | 10,000 |
| 9 | 1.000 | 0.0965 | 0.1088 | 10,000 |

FIGURE 3.2. CONFINING RING DATA .

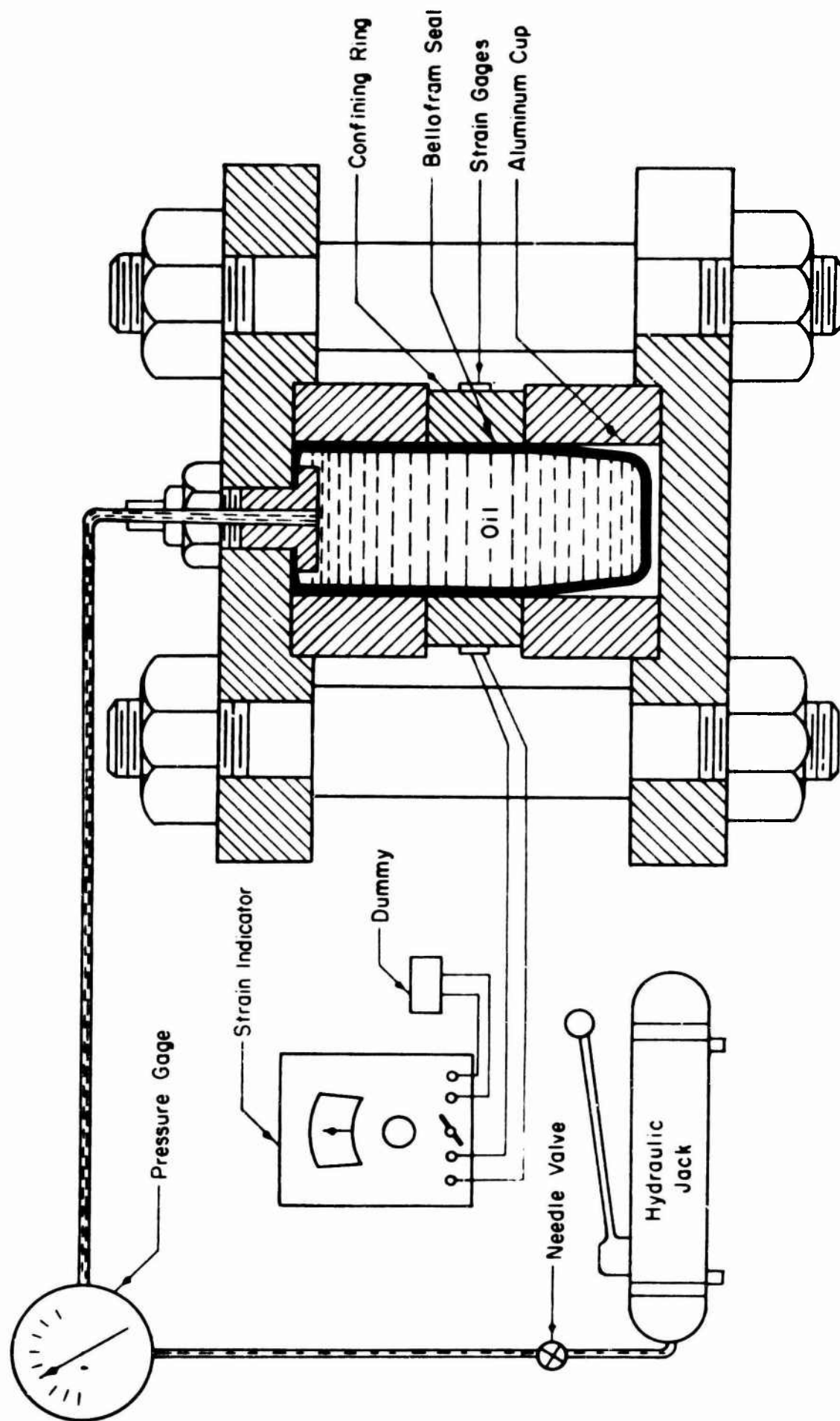


FIGURE 3.3. SCHEMATIC OF RING CALIBRATOR .

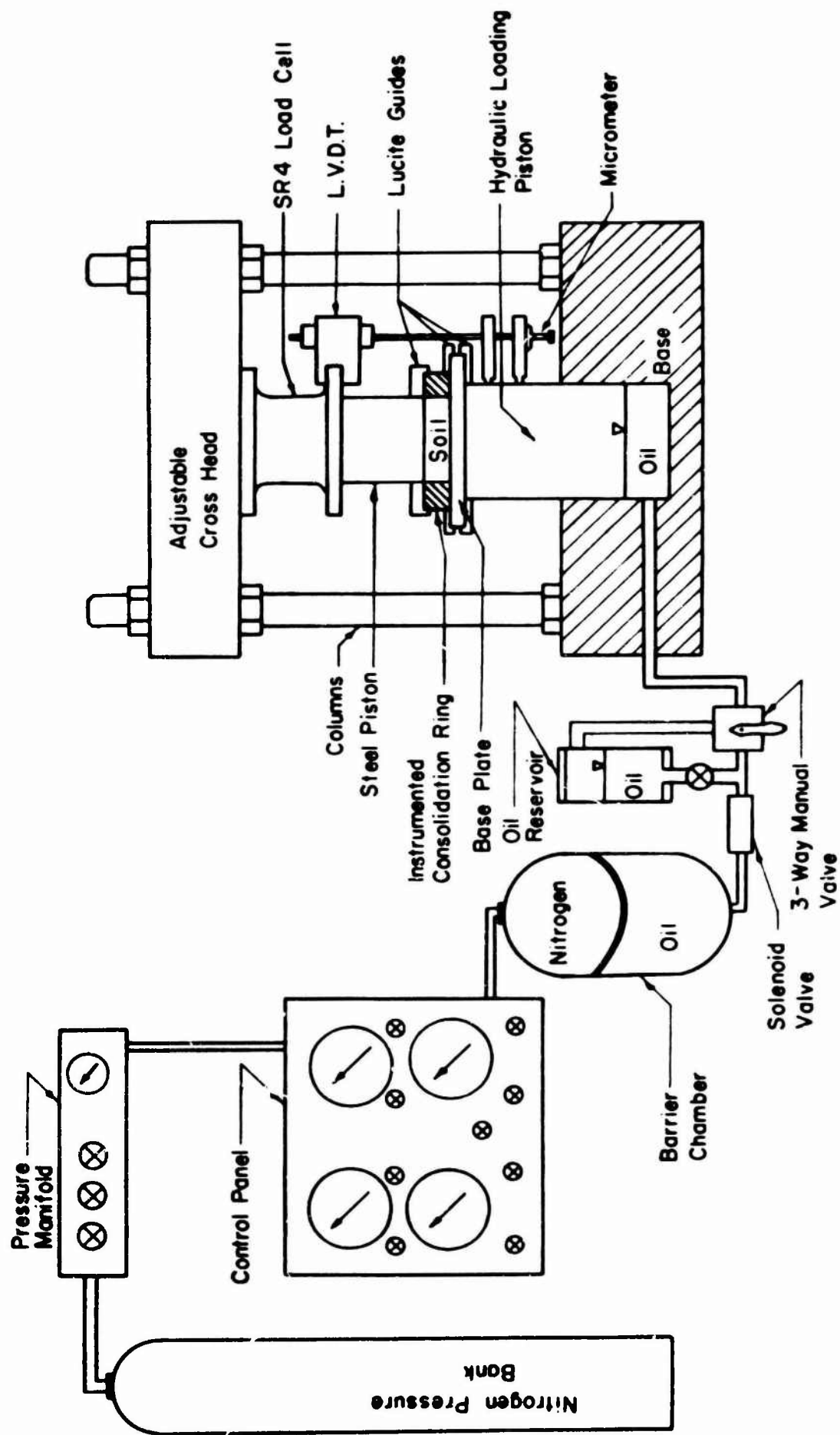


FIGURE 3.4. SCHEMATIC OF RAPID LOADING MACHINE .

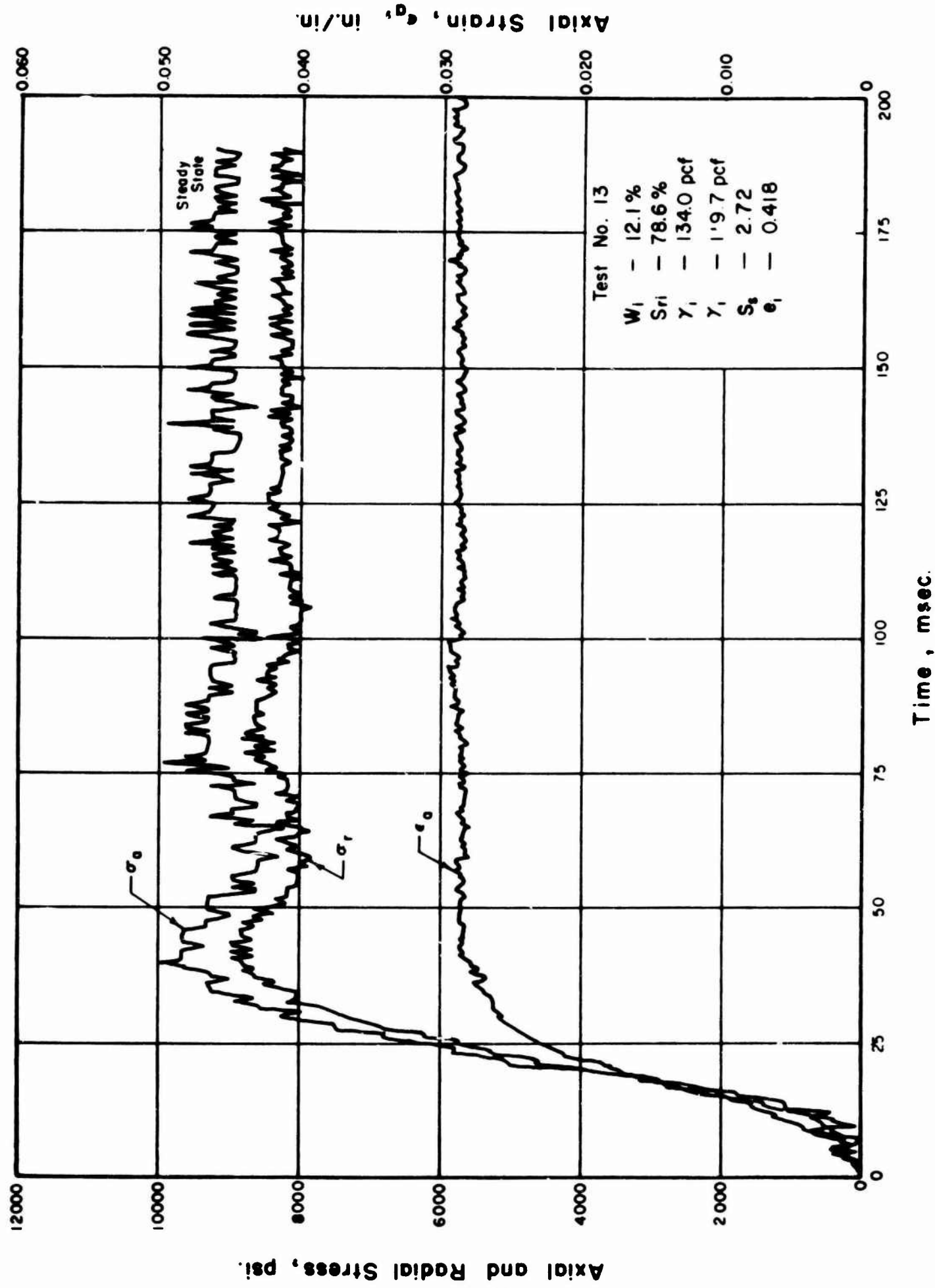


FIG. 3.5. RAPID TEST DATA

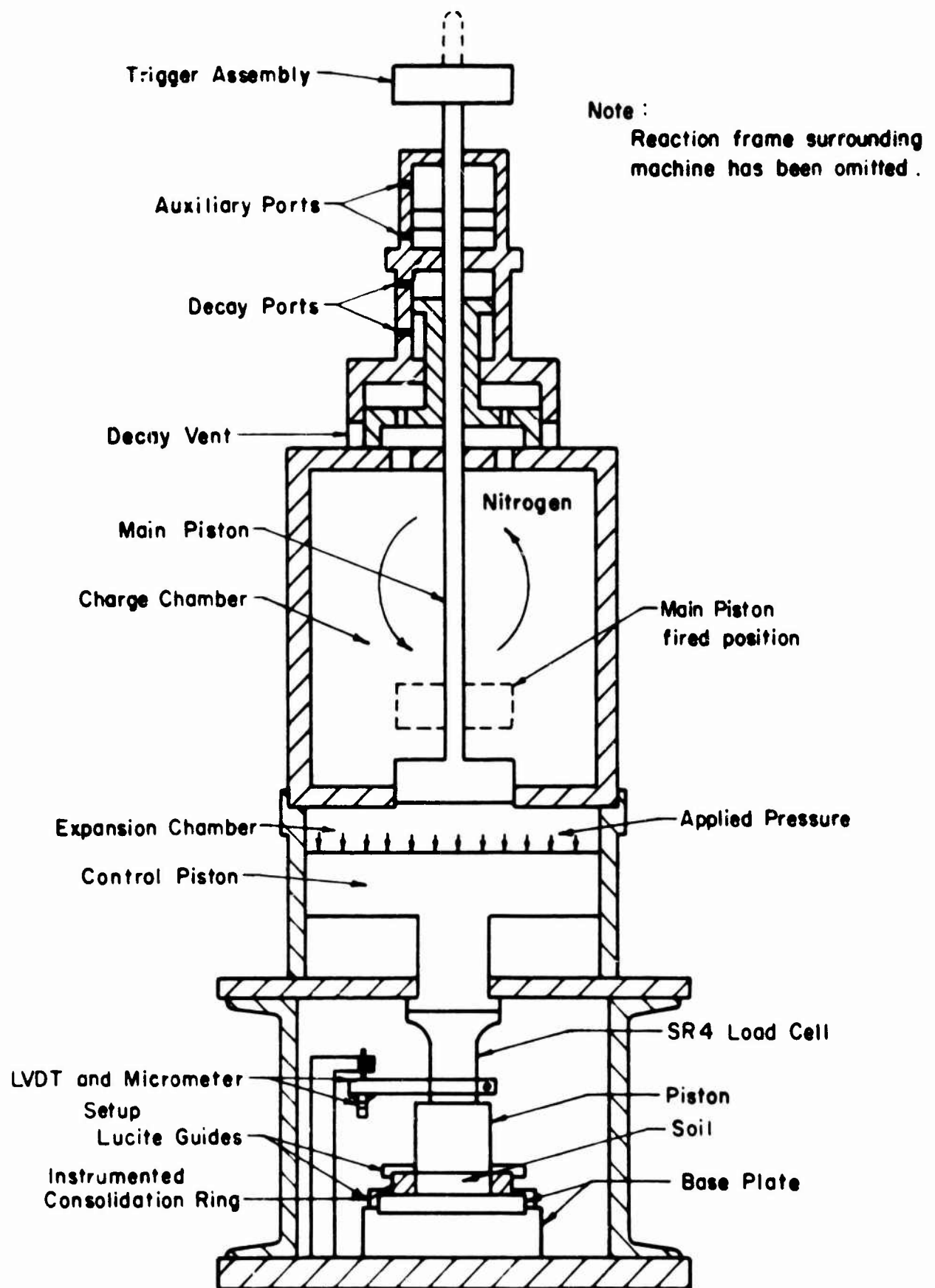


FIG. 3.6. SCHEMATIC OF DYNAMIC LOADING MACHINE

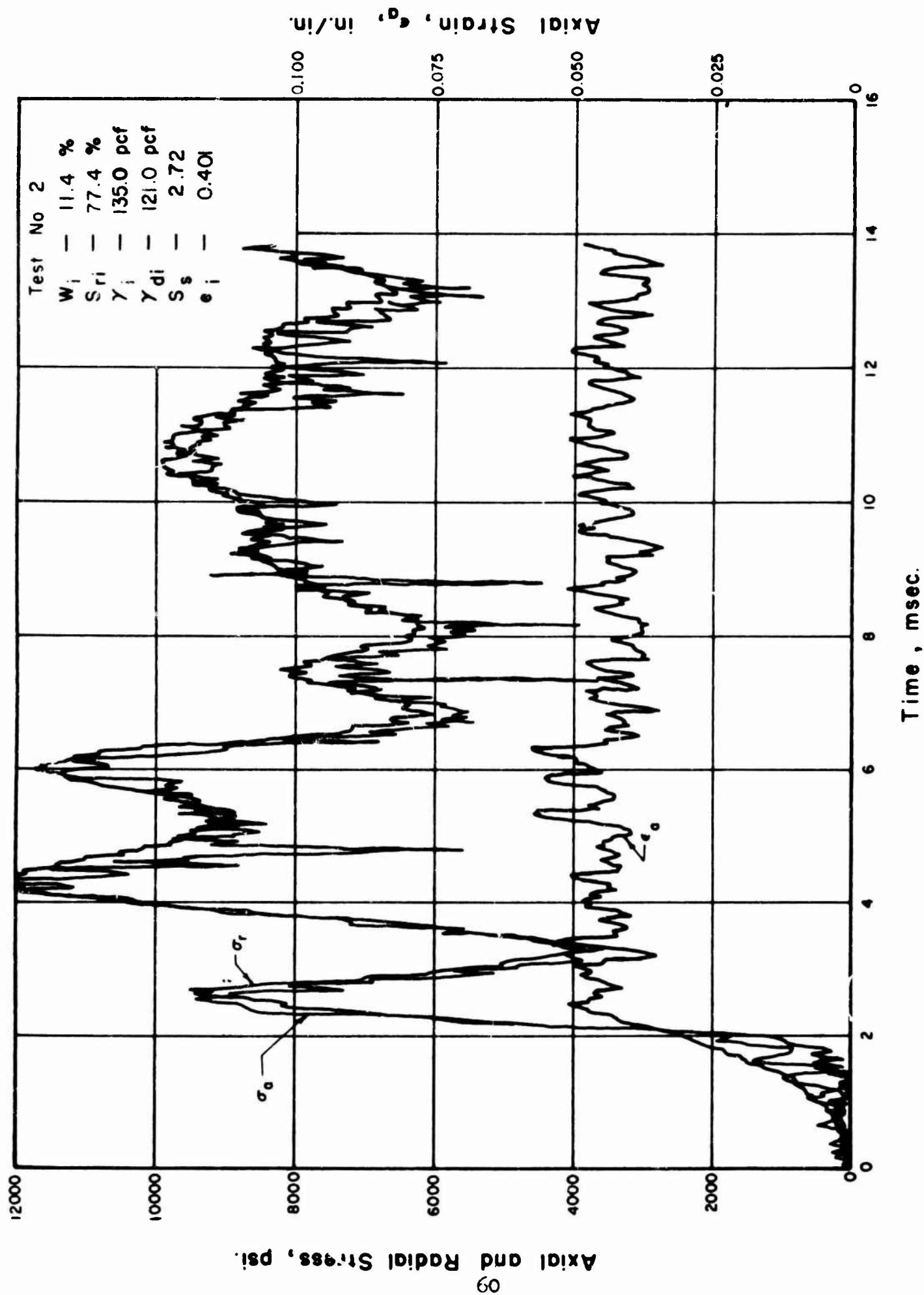
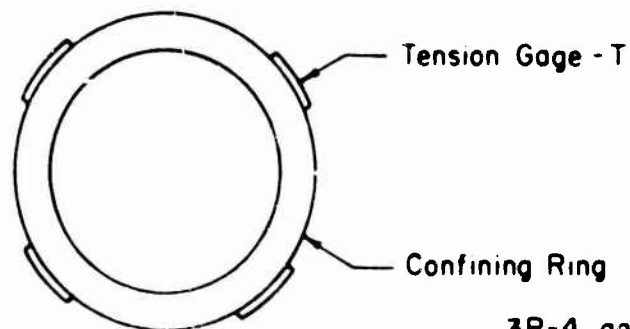


FIG. 3.7. DYNAMIC TEST DATA



3R-4 gages, Baldwin Type A-3
 Resistance : 120 ± 0.2
 Gage Factor : 2.06

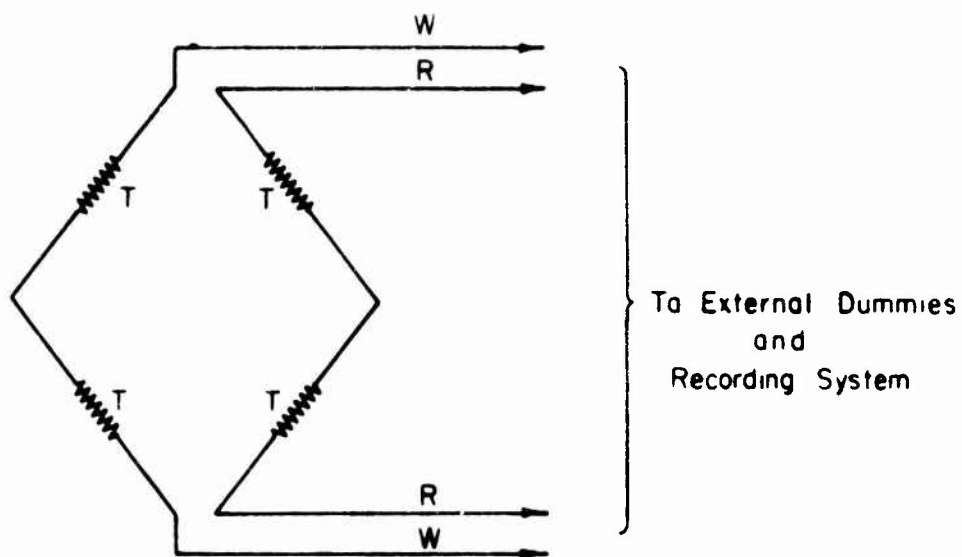
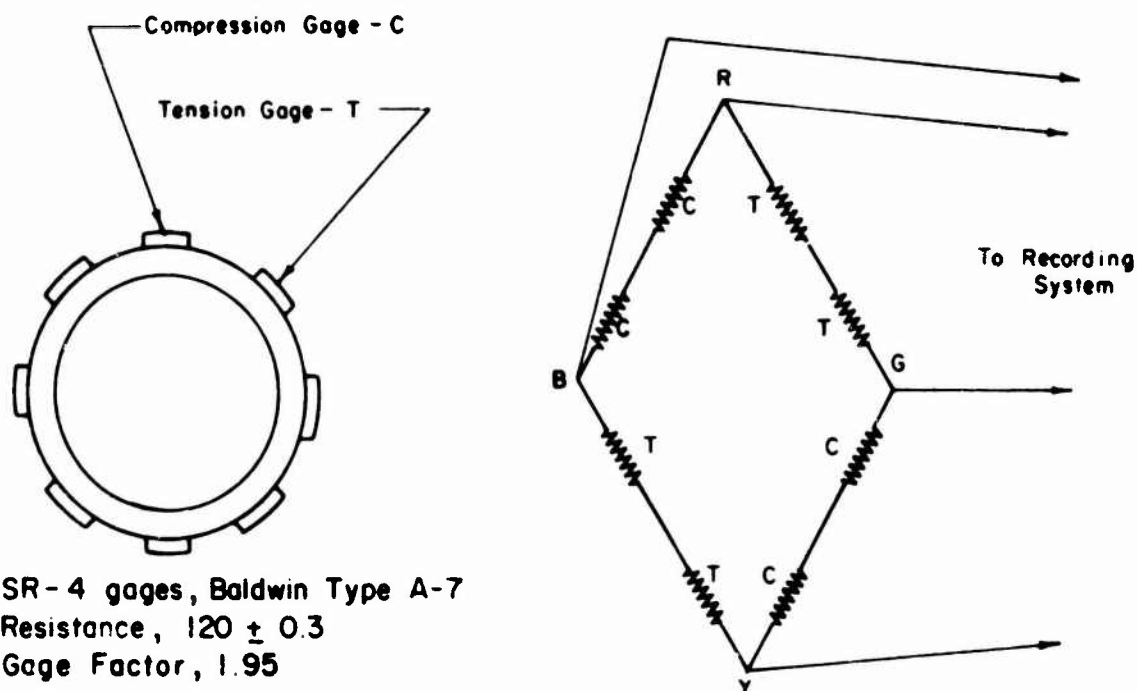
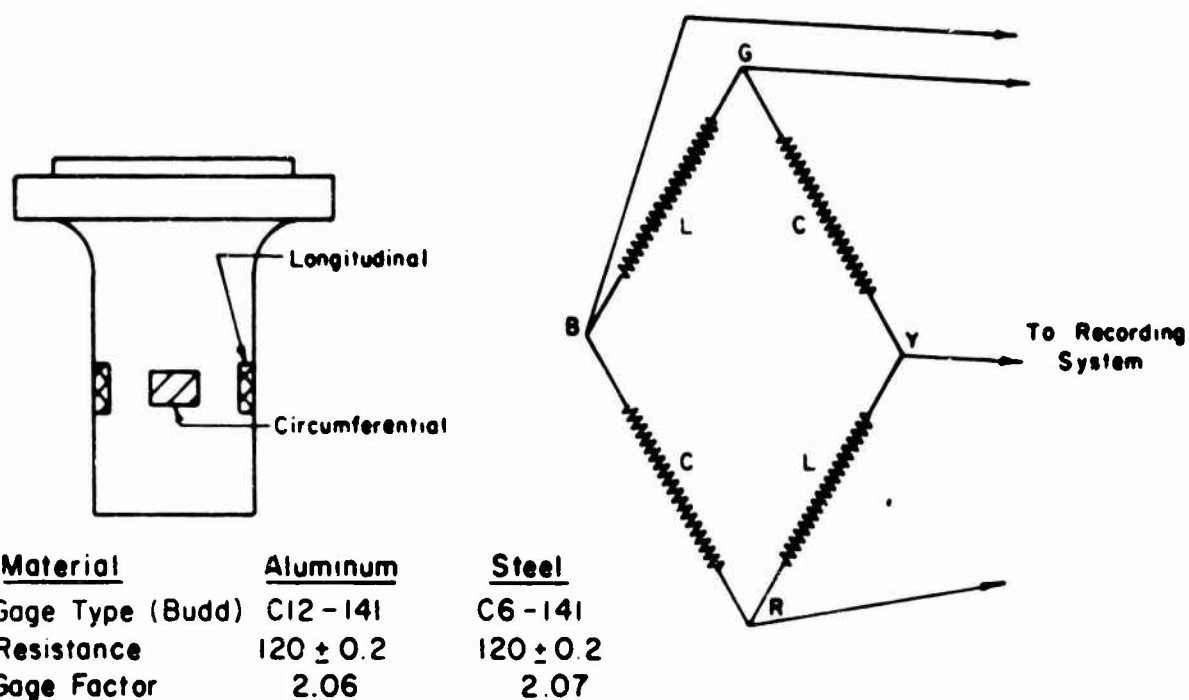


FIGURE 3.8. INSTRUMENTATION OF CONFINING RINGS.



| CELL NO. | MATERIAL | Stress on Specimen psi / u in. | CAPACITY |
|----------|----------|-----------------------------------|----------|
| 1 | Steel | | 30 kips |
| 2 | Steel | 2.77 | 90 kips |
| 3 | Steel | 7.55 | 150 kips |

FIGURE 3.9. INSTRUMENTATION OF LOAD CELL FOR RAPID LOADING MACHINE .



| CELL NO. | MATERIAL | STRESS ON SPECIMEN, $\frac{\text{psi}}{\text{u in.}}$ | CAPACITY |
|----------|--------------------|---|----------|
| 4 | Aluminum 2024-T351 | 0.56 | 30 kips |
| 5 | Steel, T-1 | 2.04 | 150 kips |
| 6 | Steel, T-1 | 3.72 | 300 kips |

FIGURE 3.10. INSTRUMENTATION OF LOAD CELL FOR DYNAMIC LOADING MACHINE.

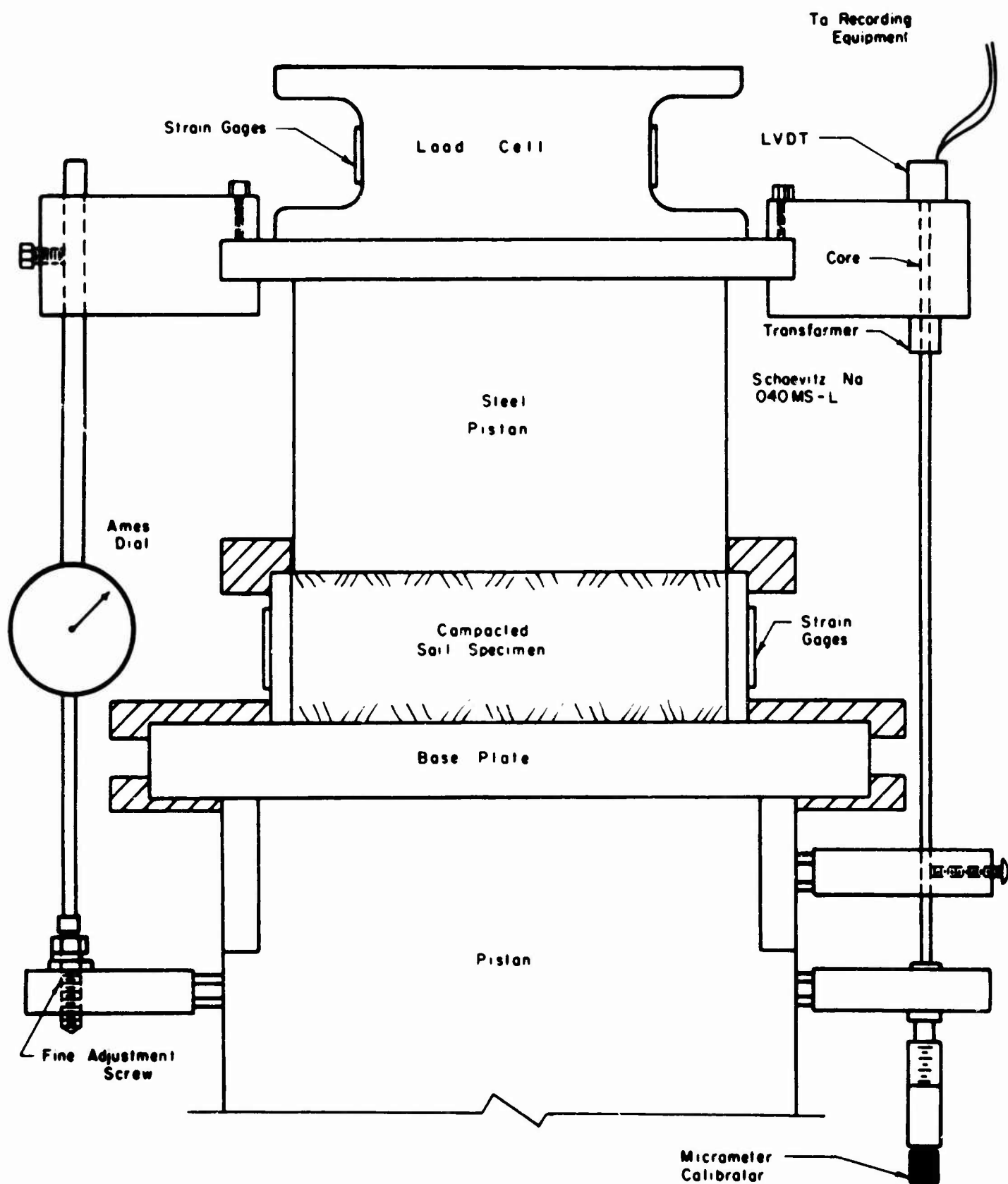


FIGURE 3.11. INSTRUMENTATION FOR AXIAL STRAIN.

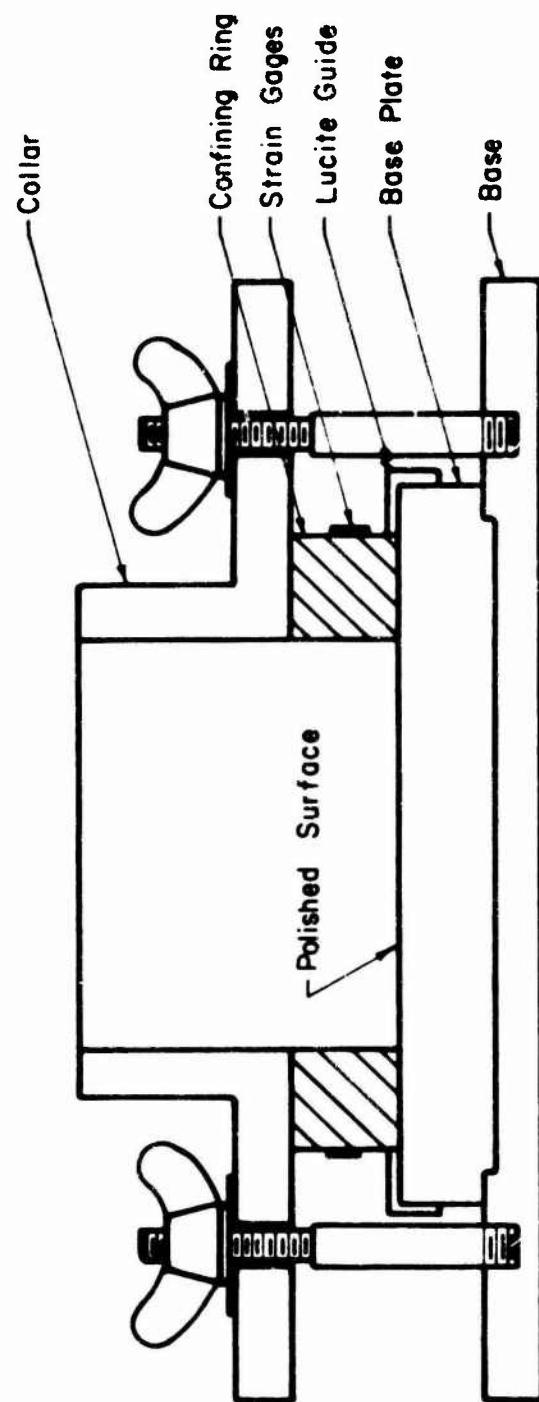


FIGURE 3.12. SCHEMATIC CROSS SECTION OF RING RETAINER FOR COMPACTION OF ONE-DIMENSIONAL TEST SPECIMENS.

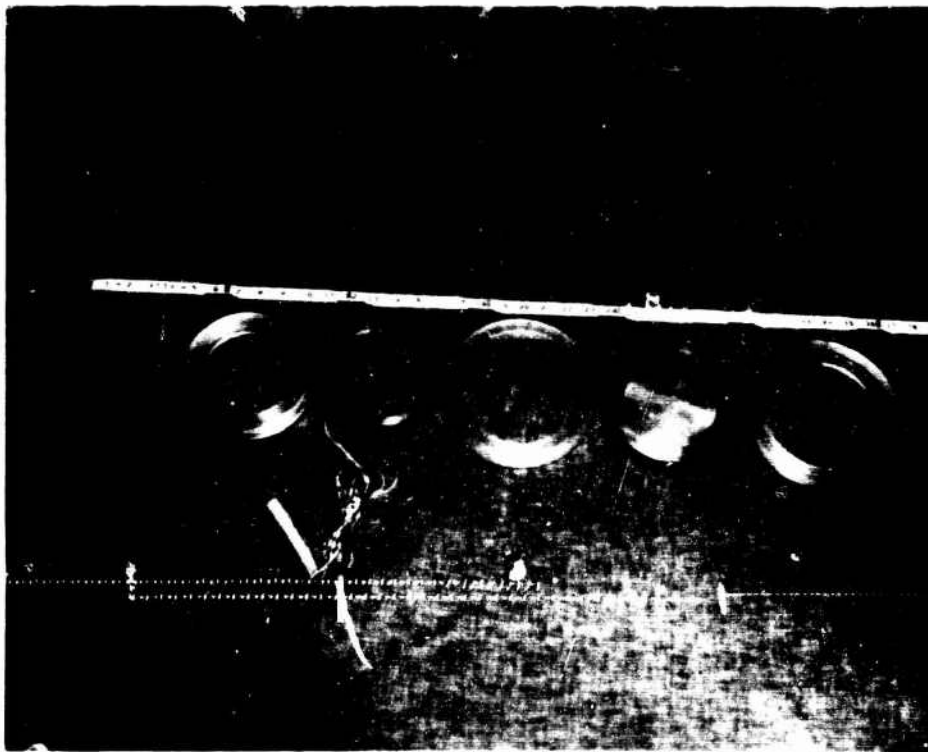


FIGURE 3.13. CONFINING RING ASSEMBLY .

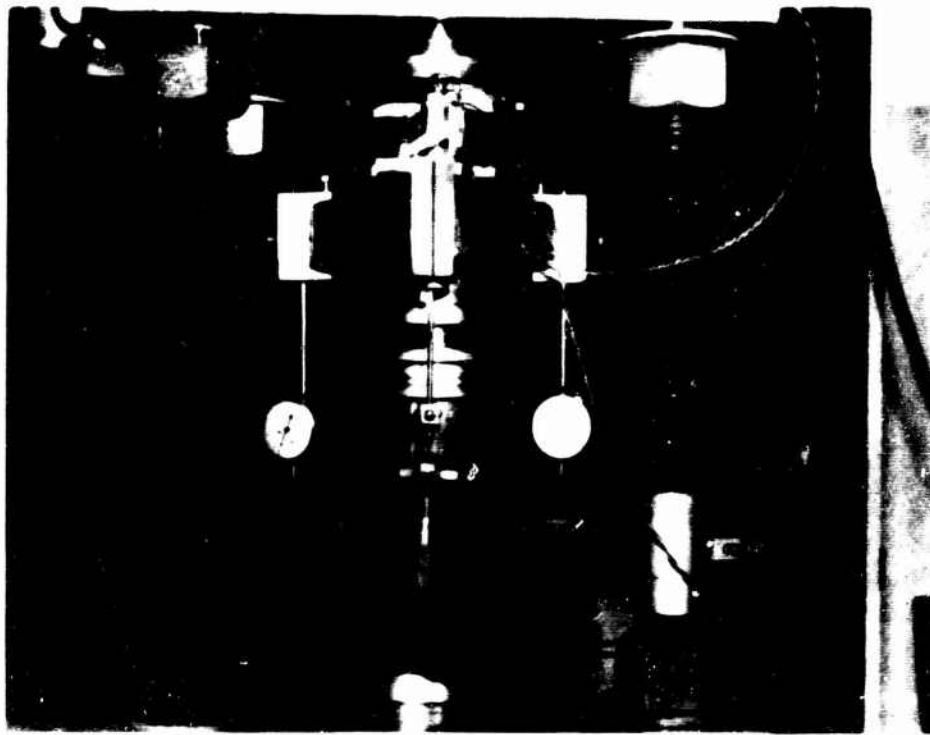


FIGURE 3.14 . CONFINING RING ASSEMBLY IN RAPID TEST MACHINE .

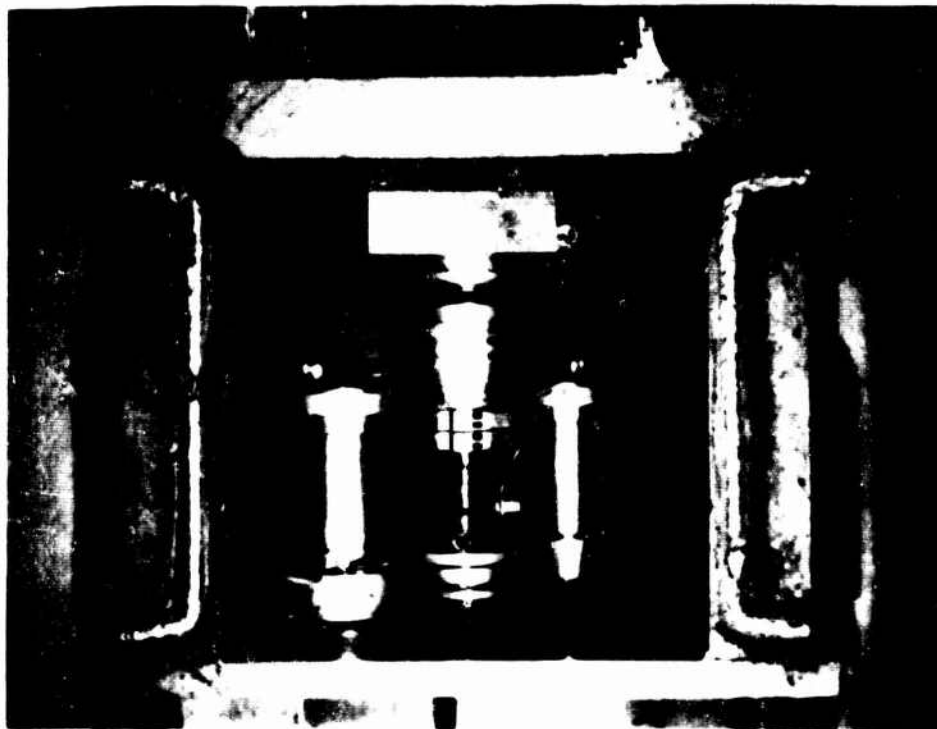


FIGURE 3.15 . CONFINING RING ASSEMBLY IN DYNAMIC TEST MACHINE .

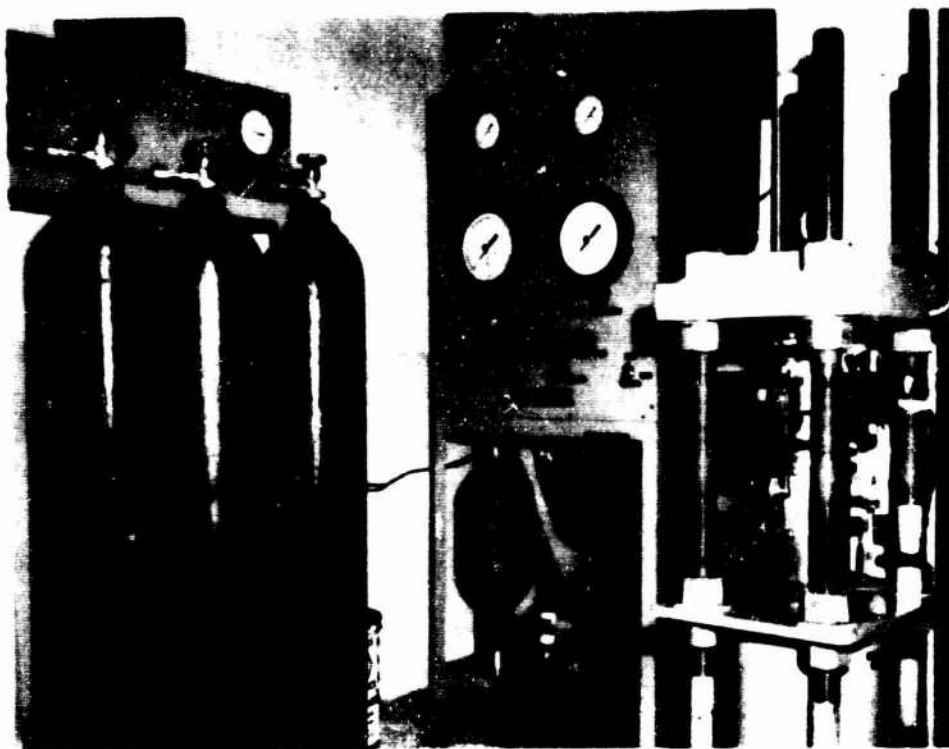


FIGURE 3.16. RAPID TEST MACHINE .

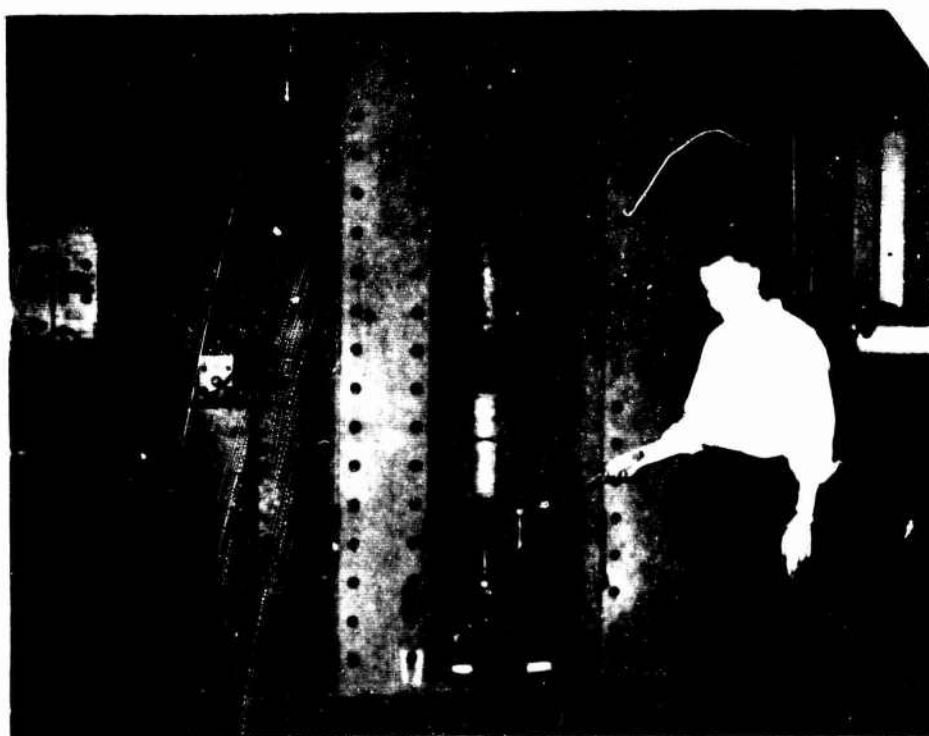


FIGURE 3.17. DYNAMIC TEST MACHINE .

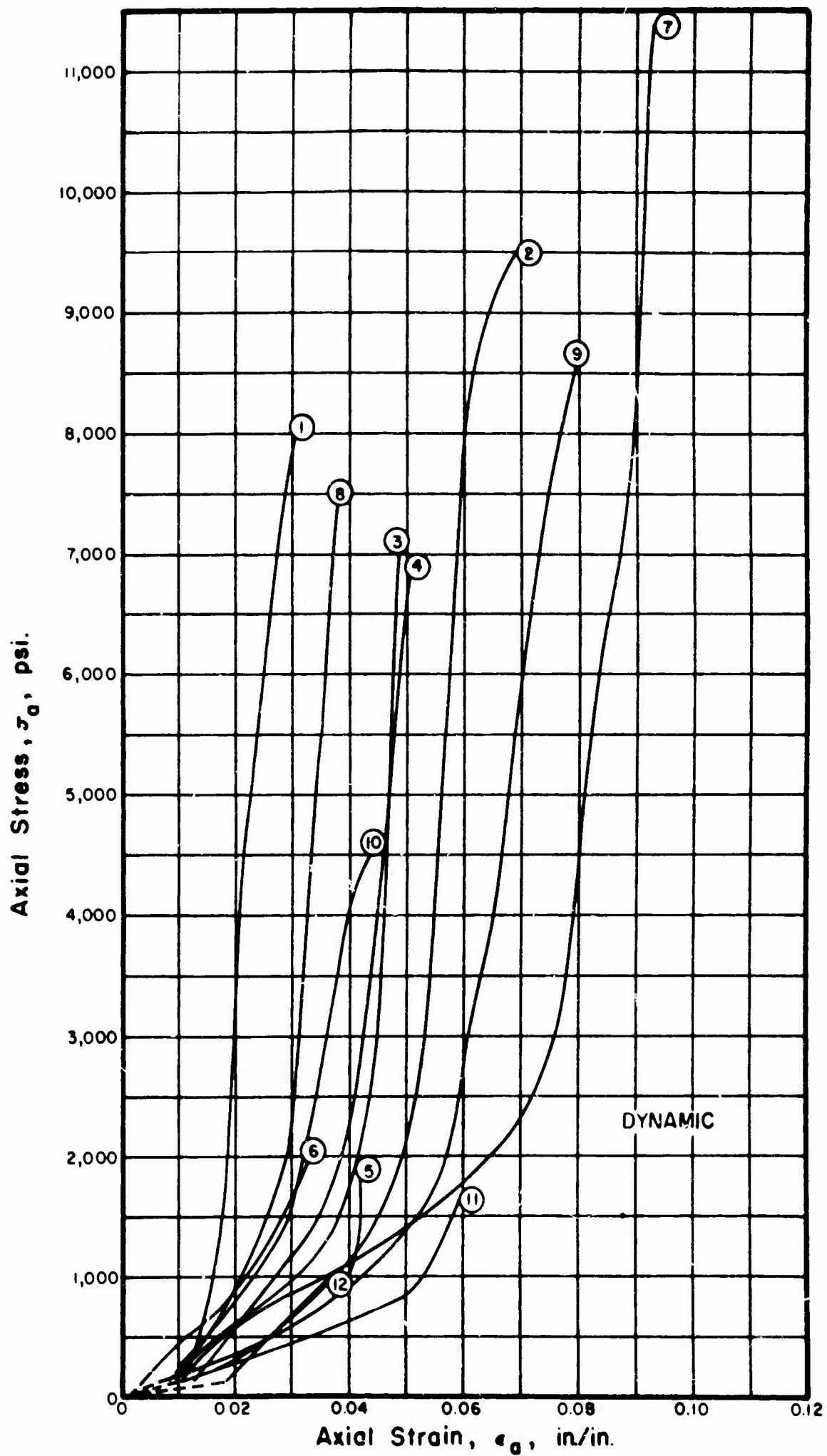


FIGURE 3.18. STRESS-STRAIN CURVE FOR GOOSE LAKE CLAY IN ONE-DIMENSIONAL COMPRESSION.

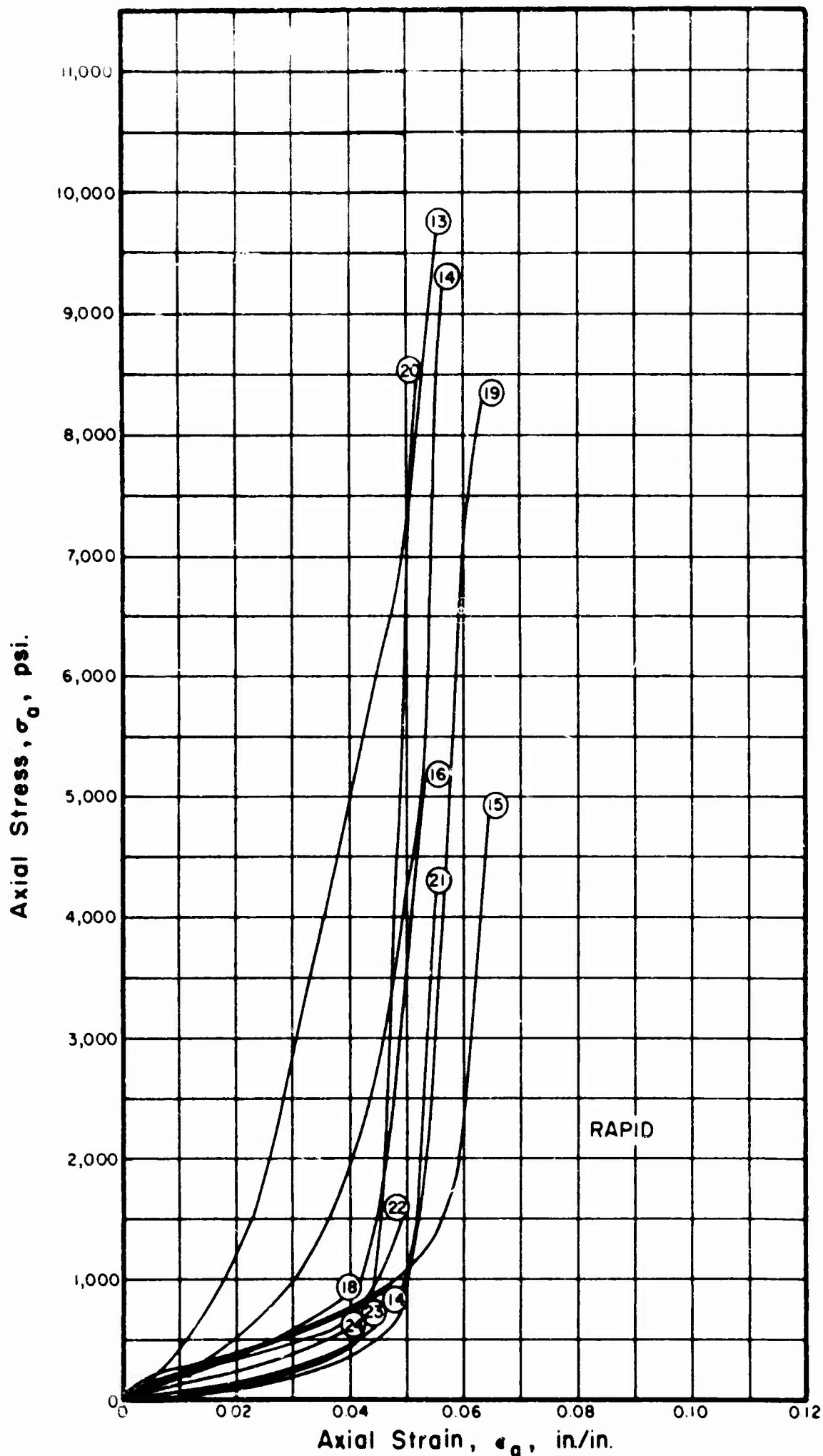


FIGURE 3.19. STRESS-STRAIN CURVE FOR GOOSE LAKE CLAY IN ONE-DIMENSIONAL COMPRESSION.

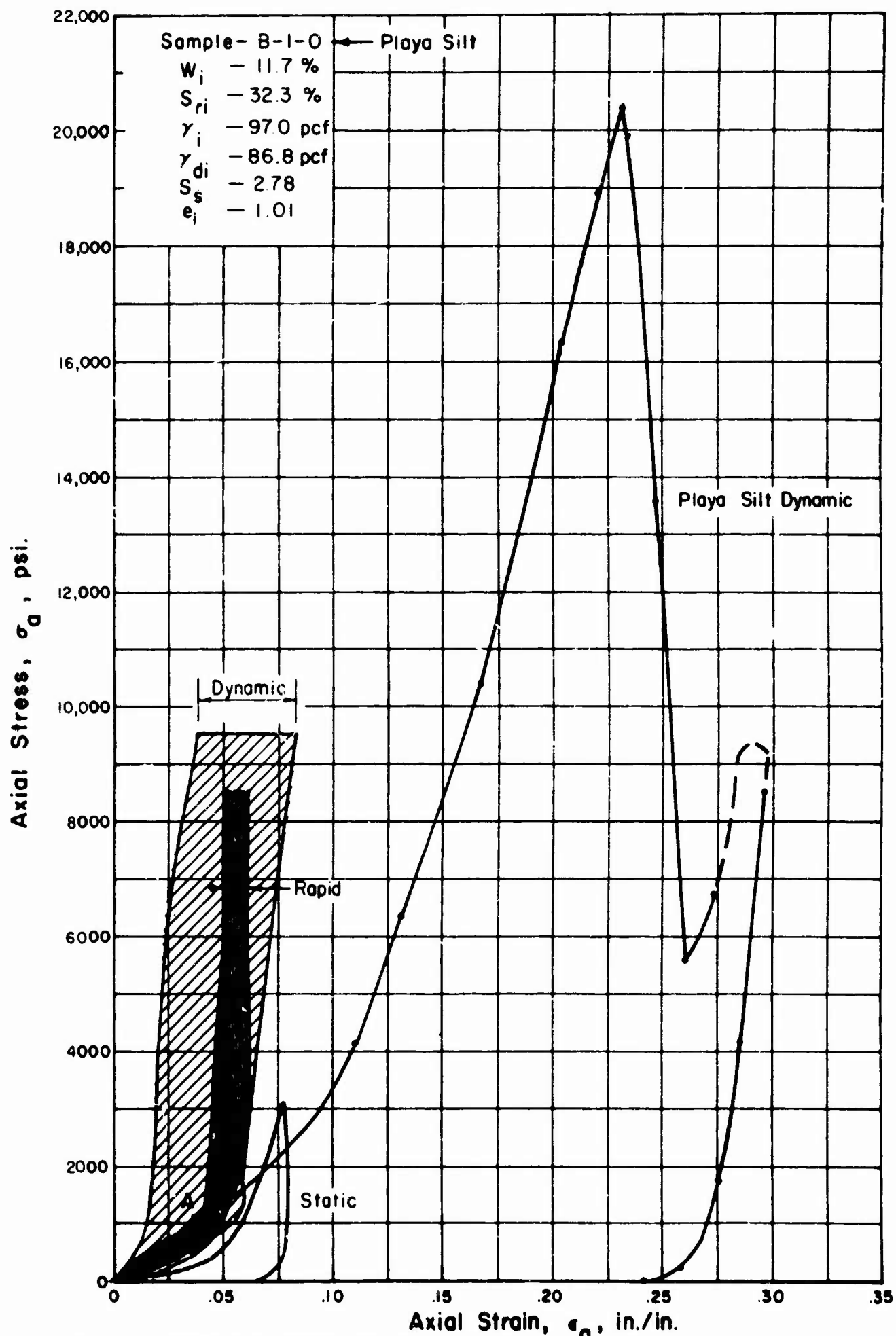


FIG. 3.20 STRESS-STRAIN CURVE FOR PLAYA SILT IN ONE-DIMENSIONAL COMPRESSION.

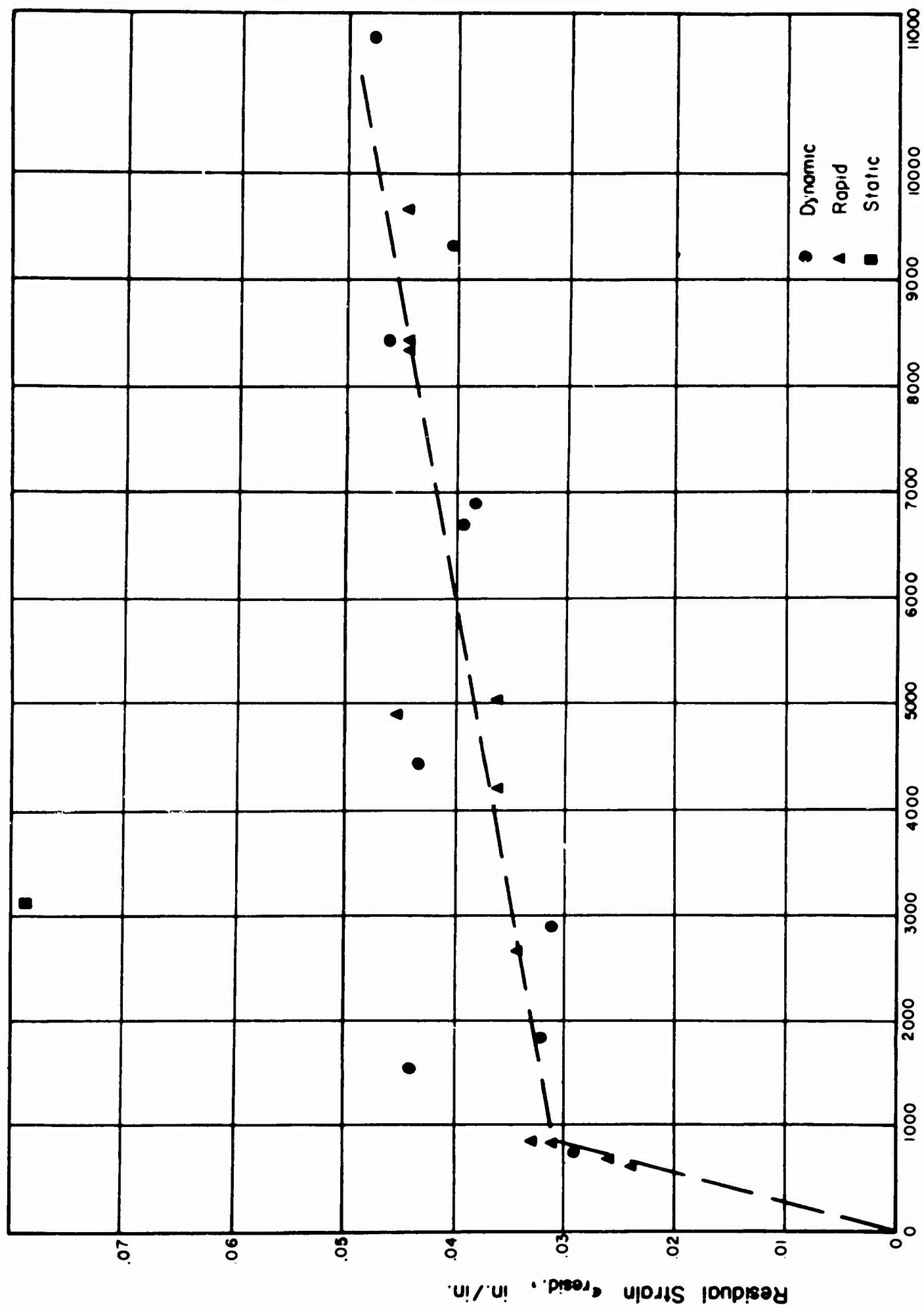


FIGURE 3.21 PEAK AXIAL STRESS vs. RESIDUAL STRAIN

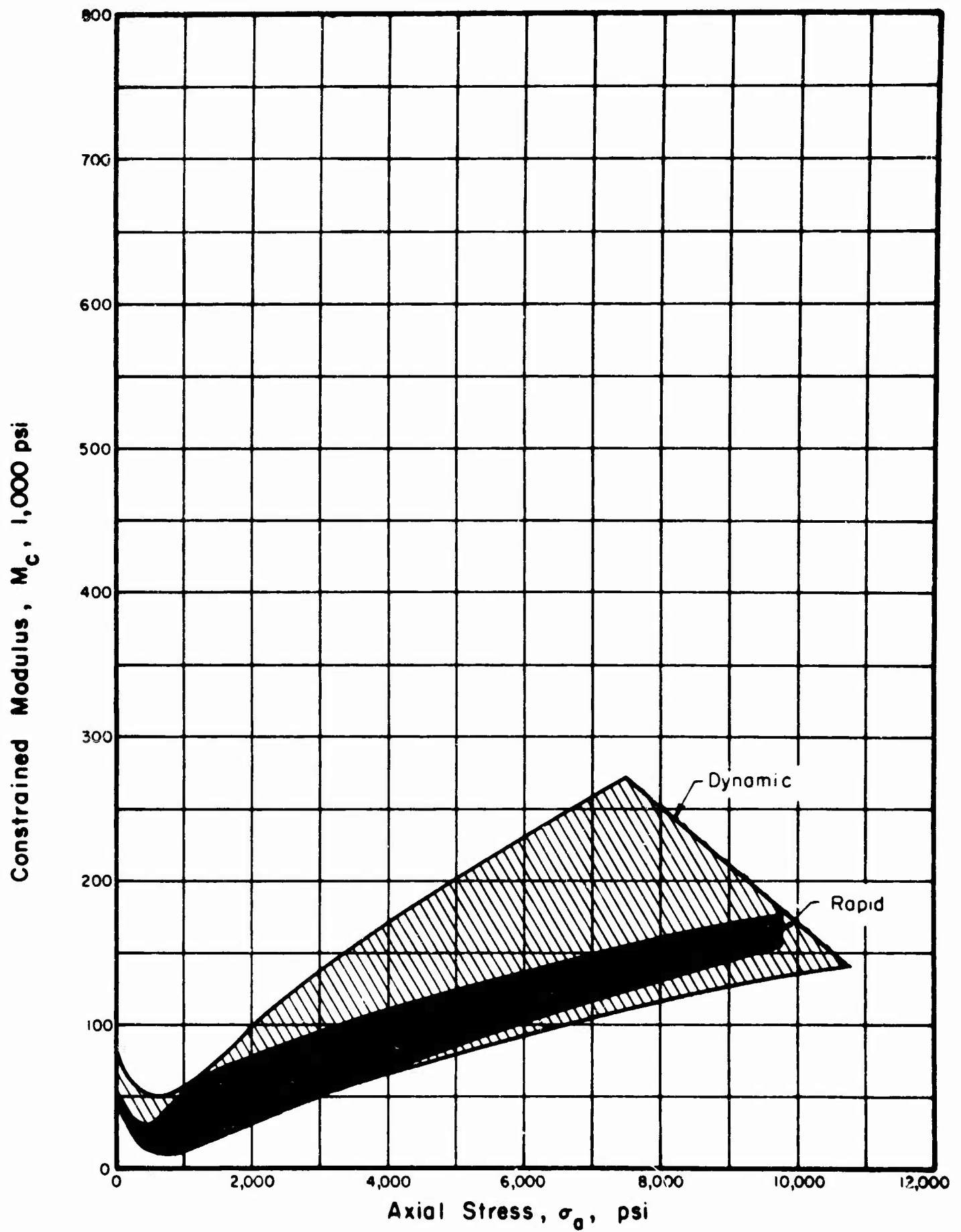


FIGURE 3.22. RELATIONSHIP BETWEEN CONSTRAINED MODULUS AND AXIAL STRESS FOR GOOSE LAKE CLAY IN ONE DIMENSIONAL COMPRESSION.

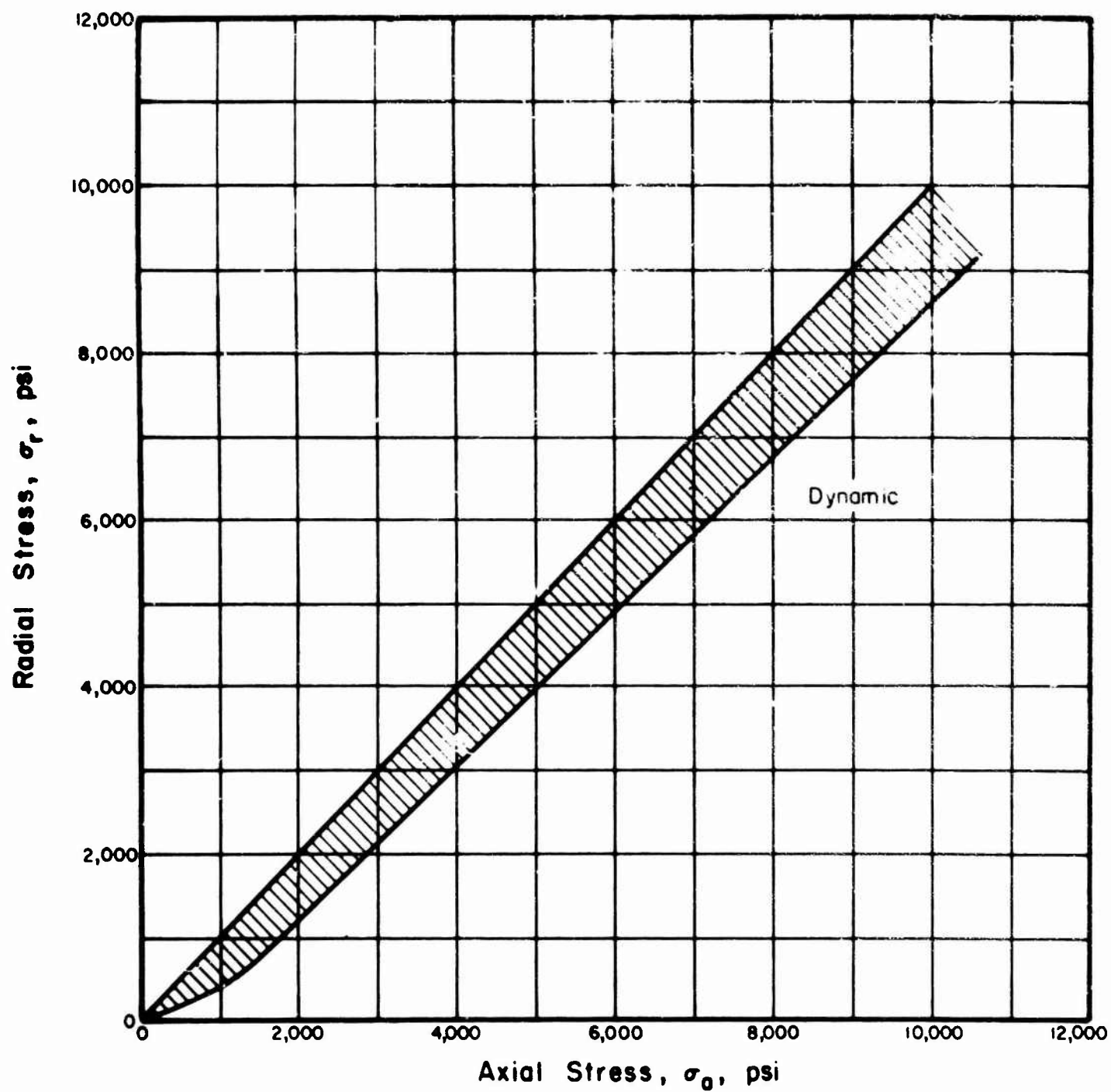


FIGURE 3.23. RELATIONSHIP BETWEEN AXIAL AND RADIAL STRESS FOR GOOSE LAKE CLAY IN ONE-DIMENSIONAL COMPRESSION .

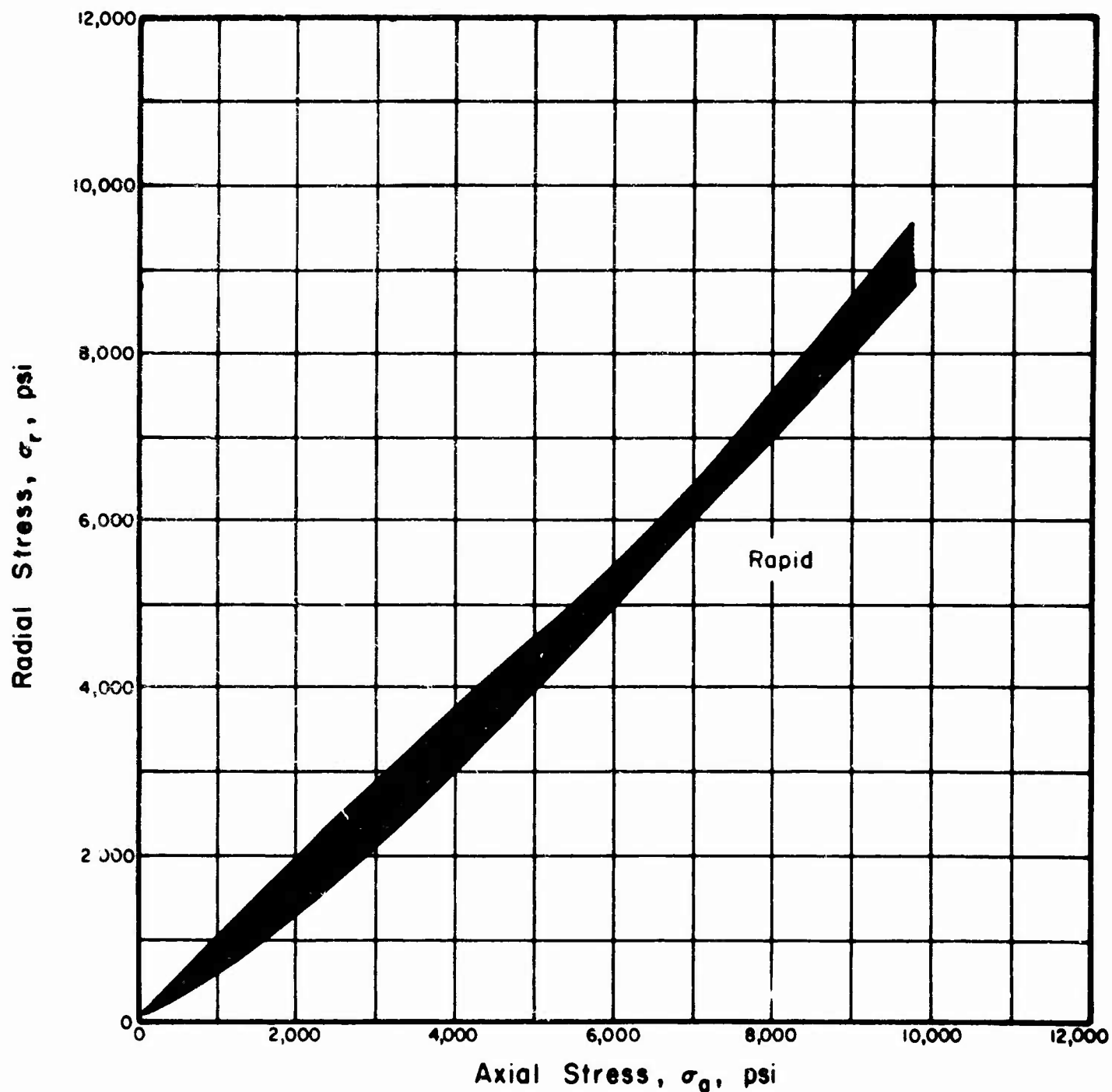


FIGURE 3.24. RELATIONSHIP BETWEEN AXIAL AND RADIAL STRESS FOR GOOSE LAKE CLAY IN ONE-DIMENSIONAL COMPRESSION.

CHAPTER 4

DYNAMIC TRIAXIAL TESTS

4.1 EQUIPMENT

Triaxial Cell

The triaxial cell was designed specifically for dynamic triaxial tests but provisions were made to allow the performance of static triaxial tests. A cross section through the cell is shown in Fig. 4.1.

Since most of the specimens were to be subjected to the cell pressure for very short periods of time, it was possible to use direct gas pressure for confinement of the sample (see section 4.3 on gas leakage through the membranes). Provisions were made for using mercury as the cell fluid in tests where the sample was to be subjected to the cell pressure for prolonged periods of time. Since water was not used as a cell fluid, corrosion became a relatively minor problem, so the cell was made of steel. Steel was needed to provide an adequate factor of safety against failure, the consequences of failure being especially severe since the cell was to be filled with gas. Regular steel was chosen over stainless steel as an economic expediency. The structural members of the cell were designed for operating pressures of 2000 psi. However, the seals were designed for only 1500 psi since major changes in seal design were required for significantly higher pressures.

The high rates of movement of the loading piston during dynamic tests dictated the use of Thomson ball bushings where the loading piston passes through the top of the cell. These bushings can withstand relatively large lateral loads during dynamic tests without developing significant

amounts of piston friction. Two Thomson bushings were used in the top of the cell to provide adequate resistance to lateral forces. A 0.750-inch-diameter loading piston was used (Thomson steel shaft, hardness 60C). A quad-ring seal was used beneath the lower bushing (Fig. 4.1). Problems associated with the starting friction of the seal were avoided by measuring the axial stress in the soil sample with an interior load cell.

The load cell was mounted beneath the soil sample (Fig. 4.1). The inside of the load cell was fitted with four vertical strain gages with opposite gages connected in series to reduce the effects of bending moments. The load cell was designed for a maximum axial force of 7000 pounds. The load cell was calibrated for axial loads up to 5300 pounds using a Tinius Olsen proving ring. The calibration curve is shown in Fig. 4.2

The signal from the load cell was amplified and recorded on an oscillograph tape. To account for variable amplification, a series of resistors were inserted into the circuit at the time of calibration and the output from the resistor circuit was recorded on the same oscillograph tape. The output from the resistors could then be read off the load calibration curve as equivalent to some axial load on the load cell. A series of resistors was permanently installed in the instrumentation system and was used to calibrate the oscillograph tape before each test. The four resistors used for calibration corresponded to axial pressures of 580, 977, 1951 and 2995 psi (see Fig. 4.2).

The deformation of the soil sample was measured with a CEC LVDT having a travel of $\pm 3/4$ inch (Fig. 4.1). The coil of the LVDT was mounted in the top of the triaxial cell. The core was attached to the cross arm, which, in turn, was rigidly connected to the loading piston. Thus relative

movements between the piston and the top of the cell were measured. However, since the load cell was relatively incompressible, the LVDT also measured the sample deformation. The upper end of the LVDT core was threaded into the cross arm thus allowing adjustment of the core prior to each test. The core could be locked in place by a set screw.

Calculations indicated that the deformations of the original cross arm, which was a 3/8-inch thick steel plate, as a result of rapid accelerations, would be too small to be of consequence. Nevertheless, in all the early dynamic tests, the oscillograph records indicated that the sample started taking stress before there was any detectable deformation. This implied either a nearly infinite initial tangent modulus for the soil, or that the cross arm was deforming under rapid accelerations. Difficulties were also experienced in keeping the cross arm securely fixed to the loading piston. Hence, a much thicker aluminum cross arm was designed with tapered ends (Fig. 4.1). On subsequent tests the load and deformation traces started simultaneously.

To prevent rotation of the loading piston, the side of the cross arm opposite from the LVDT mounting was equipped with a nylon guide and allowed to slide vertically on a rigid rod.

Four spacers, with lengths of 3/8 inch, 3/4 inch, 1-1/8 inch, and 1-1/2 inch, were made so that the spacing between the cross arm and the top of the cell could be set at predetermined values. Prior to setting-up each test, the LVDT trace on the oscillograph tape was calibrated by inserting the various spacers and recording the output from the LVDT. Thus, the deflections of the LVDT trace for known deformations could be measured and the appropriate constant (expressed as inches of sample deformation per inch

of trace deflection) could be determined. Since the LVDT calibration curve was nonlinear, it was necessary to select the constant to represent the range in deformation experienced by the sample.

The gas pressure in the cell was read from a calibrated Marsh Bourdon gage on the cell pressure panel board during the time that the cell pressure was statically maintained. However, it seemed wise to monitor the cell pressure during the dynamic tests. Hence, a CEC pressure transducer with a capacity of 1000 psi was mounted in the base of the triaxial cell (Fig. 4.1). This transducer was calibrated against the Bourdon gages and appropriate resistors were inserted into the instrumentation circuits so that the deflection of the cell pressure trace on the oscillograph tape could be calibrated prior to each test.

All tests performed under this contract were of the unconsolidated-undrained type where the cell pressure was applied just prior to the performance of the test. If consolidated-undrained tests had been performed, it would have been necessary to apply the cell pressure for extended periods of time and gas leakage through the rubber membranes would have been a very serious problem. For such tests, the apparatus was designed to allow mercury to be used as a cell fluid. A cushion of several inches of air would be left above the mercury to provide system flexibility for dynamic tests.

The load cell was fitted with a solid stainless steel cap for the unconsolidated-undrained tests. A separate cap was made with a porous stone and provisions for the insertion of drainage lines, to allow the sample to consolidate for consolidated-undrained tests.

Cell Pressure Panel Board

The cell pressure was supplied from nitrogen bottles using a panel board to measure and regulate the pressure. A circuit diagram for the panel board is shown in Fig. 4.3. In order to provide adequate pressure capacity with accuracy in the low pressure range, the panel board was equipped with three Bourdon gages with capacities of 100 psi, 600 psi and 3000 psi. The nitrogen pressure was regulated with a Hoke No. 920 A 01 regulator for higher pressures and a Conoflow model H-10 regulator for pressures less than about 125 psi. The Marsh gages were calibrated and found to be accurate within 1 percent; hence, the gage readings were used without correction.

Loading Press

The characteristics that were considered desirable in the loading press included (1) adequate capacity to shear 1.5-inch diameter samples at cell pressures of at least 2000 psi, (2) ability to shear 3-inch high samples to failure at relatively constant rates of strain in up to two minutes, and (3) ability to apply stresses to soil samples dynamically, hold the stress for a predetermined period of time, and decay the stress. The loading press developed during this contract met all of these characteristics.

The general layout of the press is shown in Fig. 4.4. The press is approximately 7 feet tall and 30 inches wide. The various parts of the press are held in position by two 2-inch diameter steel posts (item 7, Fig. 4.4) which also withstand the force applied by the press. The posts are connected to a heavy base assembly (item 14, Fig. 4.4) which rests directly on the floor. The triaxial cell rests on this base plate. The cell is precisely centered through use of a steel guide, (item 13, Fig. 4.4)

which is permanently attached to the base plate. The loading machine (item 8, Fig. 4.4) is suspended from a frame (items 4 and 6, Fig. 4.4) connected to a cross head (item 1, Fig. 4.4) via a screw jack (item 2, Fig. 4.4). The jack is used to raise or lower the frame and thus raise and lower the loading machine. To provide adequate rigidity during a test, the loading machine is welded to a heavy cross arm (item 10, Fig. 4.4) which slides vertically on the two posts and which can be tightly clamped to the two posts. This cross arm also acts as a guide to center the loading machine. Thus, in operation, the cross arm connected directly to the loading machine is unclamped, the screw jack is used to position the loading machine, and then the cross arm is reclamped to the posts.

The essential part of the loading press is the "loading machine" (item 8, Fig. 4.4), which operates hydraulically. The hydraulic system is shown, schematically, in Fig. 4.5. The soil samples are loaded by applying a pressure to the "main piston" of the loading machine (Fig. 4.5) and forcing this piston to move downward. There are two modes of operation depending on whether high or low loading rates are desired. For the fastest loading rates, the loading machine is operated in the following manner: The oil beneath the main piston (Fig. 4.5) is exhausted into the "upper oil container" (Fig. 4.5) so that the space beneath the main piston is occupied only by air. The main piston is raised to near the upper extremity of its travel and the main valve is lowered to the position shown in Fig. 4.5. A mechanical force (the trigger mechanism) is applied to the top of the main valve to hold it in place. The decay valve is also closed. Nitrogen is then let into the main chamber until some predetermined pressure is attained. This pressure is unable to act on the main piston since the main valve is

closed. The nitrogen pressure acts through the "Auxillary Port" (Fig. 4.5) and applies an upwards force on the main valve, movement of which is resisted by the trigger. When the trigger is released, the chamber pressure, acting through the auxillary port, drives the main valve upwards and opens the main ports. The main valve accelerates to a velocity of about 400 inches per second within about 0.5 inch of travel and has attained this terminal velocity before the main ports start to open. Thus, the main ports open very rapidly. The nitrogen from the main chamber rushes through the main ports and applies a pressure to the main piston which moves downwards to load the sample. By using a 400-psi chamber pressure, it was possible to strain a 3-inch sample by 25 percent within 3 to 4 milliseconds. Higher loading rates could be obtained by using higher chamber pressures and by using helium in place of nitrogen but special damping mechanisms would be needed to stop the main piston at the end of its travel; in the present apparatus the main piston just bottoms-out on the base of the loading machine. In the remainder of the report, samples loaded in this manner are designated as "dynamic" tests.

Constant load tests, with rapid rise times, were performed by using chamber pressures that were not sufficient to fail the soil sample. Thus, the piston applied a rapid load to the soil sample and then maintained the load. After the elapse of some predetermined dwell time, the decay valve was "fired," following the same general procedure as used with the main valve, and the pressure in the chamber was exhausted.

Tests with slower rise times are performed in a slightly different manner. In these tests, the main valve is raised, the space beneath the main piston is filled with oil, the decay valve and the oil valves are

closed, valves 3 and 1 (Fig. 4.5) are closed, valve 2 is opened, and a gas pressure is applied to the main piston. Thus the oil is subjected to a pressure in a closed system. When the oil valve is "fired," the oil can escape through the regulating valve (no. 4) and through valve 2 into the lower oil container. The rate of loading of the soil sample is controlled by the nitrogen pressure applied to the main piston, by the viscosity of the oil, and by the setting of the regulating valve. Tests performed under this contract utilized no. 10 oil. Figure 4.6 shows the relationship between the setting of the oil regulating valve and the deformation rate for a 400 psi chamber pressure. These data were obtained from actual tests performed on Goose Lake Clay at cell pressures of 114 psi and 1010 psi. Times to failure as low as 40 milliseconds were obtained in this manner. Lower times to failure could have been obtained by using an oil of lower viscosity.

Electrical Instrumentation

The instrumentation system utilized a 4-channel 20-kc CEC carrier amplifier to activate the sensing elements which consisted of four vertically mounted type C6-141 Budd foil gages with a length of 1/4 inch each. Opposing gages were connected in series to reduce the influence of bending moments and the two pairs of two gages each were connected in parallel as one arm of a four arm bridge circuit. The output signal was recorded with a CEC type 5-124 oscillograph using paper speeds up to 128 inches per second. On a few tests, a model 8100 Minneapolis-Honeywell 8-channel FM tape recorder, supplied by the Department of Civil Engineering, was used to record data. This system had a much faster response time than the oscillograph but, unfortunately, was not available until near the end of this contract. When the magnetic tape system was used, it was necessary to insert a model

2000 Dana DC amplifier just ahead of the recorder to obtain an adequate signal. The same system was used to record the sample deflection and the cell pressure.

A second part of the electrical instrumentation system was the timing unit that set off the solenoid valves at the proper time and also provided a timing signal to be recorded on the oscillograph tape. A Hewlett-Packard model 202A function generator was used to generate a square timing trace on the oscillograph tape and to provide a timing signal to a dual preset counter timing unit. When the switch was closed to start a test, the timing unit provided a 400-millisecond delay to allow the oscillograph paper to attain constant velocity, then closed a circuit to discharge a bank of condensers to activate the solenoid that released the main valve in the loading machine, and then, at some predetermined later time, closed another circuit to discharge another bank of condensers to activate the solenoid to release the decay valve.

A typical oscillograph tape from one of the tests is copied in Fig. 4.7 with the superfluous parts of the tape left out, e.g., the part used during the 400 millisecond delay after the oscillograph is started but before the first solenoid is fired. The first five marks on the tape are the LVDT calibration marks which were obtained before the top of the tri-axial cell was bolted to the base. The next two marks are the load cell calibration marks resulting from inserting the 580-psi and 977-psi resistors into the system. The next set of twelve marks are the CEC pressure transducer calibration marks. A section of the tape was then removed. The next section of the tape shows the application of the cell pressure which is recorded on both the axial load trace and the CEC transducer. The

LVDT moved in jerks as the cell pressure overcame the force of static O-ring friction and moved the loading piston slightly. Then another section of the tape was removed. The instrumentation technician was unable to see the traces at the time they were generated since the tape must be exposed to sunlight to be developed. Hence, he made a mark on the tape showing the location of the axial load trace just prior to the application of the seating load. This mark was used to make sure that only a very small seating load was applied. The seating load on this trace was 6 psi which was about 2 percent of the load required to fail this sample. A section of the tape was again removed. The next part of Fig. 4.7 shows the actual test complete with the square timing trace at the bottom. For this test, the rate of deformation was almost linearly a function of time up until failure.

4.2 EXPERIMENTAL PROCEDURES

Sample Preparation

The 3000 grams of soil needed for each batch was mixed with 300 ml of water in a Lancaster model PC mixer until uniform. The soil was then stored in a double plastic bag for one week to allow hydration to occur. The soil was remixed by hand in the bag before compaction of the samples. The samples were subjected to kneading compaction using a nominal foot pressure of 200 psi, 10 layers and 8 blows per layer. After compaction, the mold was disassembled and the soil sample weighed with an accuracy of about 0.03 gram. The sample was then placed on a solid 1.5-inch-diameter plastic disc, another plastic disc was placed on top of the sample, and a single rubber membrane was rolled over the sample. The edges of the plastic discs had been coated with silicone high-vacuum grease to reduce the danger

of evaporation during storage. The samples were stored under water for one week before shearing.

Set-up of Samples in the Triaxial Cell

The wet weight and dimensions of each soil sample were determined immediately after removal from the water bath. The final wet weight was usually within 0.1 gram of the initial wet weight and varied (plus and minus) randomly. The sample was placed on the pedestal of the triaxial cell and surrounded by a double thickness of thin paper towel. The paper was slit vertically to avoid the development of hoop stresses and the second layer of paper was rotated from the first so that the slits in the two sheets of paper did not coincide. The paper towel was used to protect the thin membranes from any sharp projections on the surface of the soil samples. Both the pedestal and the stainless steel top cap were greased and two membranes were rolled down over the soil sample. The membranes were sealed to the pedestal using a rubber band and to the top cap using a rubber O-ring. The top (closed) end of the membrane was trimmed away to allow the loading piston to enter the top cap.

Instrument Calibration and Preparation of the Loading Machine

Before the cell was assembled, the loading piston was moved up and down through increments of $3/8$ inch each and the core of the LVDT and the recording equipment were adjusted to obtain the electrical null point. Calibration marks were then placed on the oscillograph tape for piston movements of 0, $3/8$, $3/4$, $1-1/8$, and $1-1/2$ inches. The cell was then assembled and centered in the loading press.

The main piston of the loading machine was raised to its starting position and the trigger cocked. The cell was centered in the loading

machine, and the loading machine was then lowered, using the screw jack, until the loading cap of the press was almost in contact with the loading piston of the triaxial cell. The oscillograph was turned on and the triaxial cell pressure applied. The movement of paper through the oscillograph was stopped and a mark made by the instrumentation technician indicating the location of the axial load trace for no stress difference applied to the sample. The loading machine was then lowered until the trace was seen to deflect slightly, indicating contact of the loading piston with the soil sample, and the loading machine was locked in position.

All personnel then left the room in which the test was to be performed. The apparatus for applying the pressure in the main chamber of the loading machine together with the instrumentation equipment were in a separate room for the protection of the personnel. The main chamber was pressurized and final checks were made to determine that the timing trace was of the correct frequency and that all the instrumentation equipment was ready.

Shearing the Sample

Essentially the only function of the operator in the actual performance of the shear test was to close the switch that activated the instrumentation system. When the switch was closed, the oscillograph and magnetic tape units started. Four hundred milliseconds later the preset counter unit closed another circuit to discharge a bank of condensers and to activate the solenoid valve that set off the main piston. The piston flew upwards, thus opening the main ports and allowing the chamber pressure to act on the main piston. At some predetermined time later, the preset counter closed another circuit to discharge the chamber pressure (for constant load tests). The recording equipment was turned off.

Conclusion of the Test

The main chamber pressure was discharged (in tests to failure) and the triaxial cell pressure was reduced to zero. The cell was removed from the press and dismantled. The sample was removed and used to determine the final water content.

The oscillograph tape was exposed briefly to sunlight to develop the traces and show if the test was successful. The tape was then subjected to a chemical treatment to fix the traces.

Data Reduction

Several procedures were used in data reduction on this contract. On the triaxial tests, the magnetic tape unit was not used extensively so reduction of the magnetic tapes will not be discussed. Most of the oscillograph tapes were reduced using a model E-2, Benson-Lehner decimal converter. This machine operates in the following manner: The paper oscillograph tape is aligned on an underlit frosted-glass surface. The machine has a frame that can be moved along the tape parallel to the time scale, i.e., lengthwise on the tape, and a cross feed device that can be moved at right angles to the time scale. The cross feed has a transparent plastic scale with a fine inscribed line. The electrical system of the converter is calibrated for each test so that the movement of the cross feed through one inch results in an electrical signal of one unit. The signal is typed out by an IBM electric typewriter on a data form when the operator presses a button. Thus, the operator selects a base line from which all trace deflections are read and zeros the machine on this base line. He then reads the deflections of all the calibration traces, i.e., he sets the cross hair on each trace in turn and presses the read button.

The timing pulse on each tape provides the time scale which is also automatically typed out. The operator reads each trace at a series of times and types the data on a standard form. Such a form is reproduced in Fig. 4.8.

The remainder of the calculations are performed by hand since early attempts at machine reduction indicated that hand reduction would be more convenient and less expensive. The operator first calculates the constants. The two constants required are the inches of sample deformation per inch of trace deflection and the uncorrected axial stress in psi per inch of trace deflection. The operator then calculates the trace deflections using the deflections at time zero as base lines and uses the constants to determine sample deformation and uncorrected axial pressure. The sample deformation is converted to strain assuming all samples to be 3.00 inches long. Area corrections were made assuming that the samples deform as right cylinders without volume change. Errors in these assumptions are discussed in the next section.

The corrected stress difference, strain, and time are then plotted in some suitable fashion and numerical data are taken from the average curves.

4.3 ANALYSIS OF EXPERIMENTAL ERRORS

Volume Changes

A knowledge of the volume changes of the soil samples under ambient stresses up to 1000 psi and during both static and dynamic shear tests would be of considerable interest. Besides being of direct interest these data are needed to allow precise calculation of the stresses in the soil samples during shear.

The usual way of measuring such volume changes is to fill the cell with a relatively incompressible fluid, usually water, apply cell pressure, and measure the quantity of fluid entering the cell to maintain constant pressure. The volume change of the soil sample is obtained as the difference between the measured gross volume change and the volume change of the cell fittings. Similar measurements are made during shear with an additional correction applied for the volume of the loading piston as it enters the cell. This procedure was used with the static triaxial compression tests performed at pressures up to 120 psi. Unfortunately, the static volume change apparatus that was available was not designed for higher pressures and could not be used within the pressure range used for the dynamic tests on this project. Further, this technique of measurement could not be adapted conveniently for this project since filling the cell with an incompressible fluid would certainly have resulted in rupture of the cell during dynamic tests.

An attempt was made to fill the cell with mercury up to the center of the top cap and to measure the change in mercury elevation using an LVDT in which the core would be attached to a float. The method did not operate satisfactorily and was abandoned. Other methods under consideration did not appear sufficiently accurate and attempts to measure volume changes were abandoned when it became apparent that the time lost in developing a procedure for determining the volume changes would not be compensated for by the value of the data obtained since the number of tests performed on this contract would be reduced significantly. Assuming a dry density of 117.4 pcf, a specific gravity of 2.72 and an average water content of 11.3 percent, the air content of the samples was about 9.7 percent of the total volume. The

static tests at low pressures indicated that the total volume change at failure at 120 psi was about 4.5 percent. Thus, the error involved in ignoring volume changes would only be 5.2 percent (of total volume) greater at 1000 psi than at 120 psi. Such an error would result in a slight rotation of the failure envelope in a Mohr-Coulomb diagram but the rotation would be small. It is recommended that such volume change data be obtained in future research.

Errors in Determination of Strain

Strain calculations were all based on an assumed initial length of 3.00 inches. Actual measurements of the length, under conditions of zero total stress, indicated random scatter of up to 0.3 percent.

Assuming an isotropic sample, the 9.7 percent maximum possible error in volume determination would lead to a maximum possible error in determination of the initial length of about + 3.2 percent (the plus sign indicating that the assumed value is larger than the real value).

Errors in determination of strain also result from calibration problems with the LVDT. As a result of mechanical limitations, it was not possible to make use of only the relatively linear part of the output-core movement curve in the vicinity of the electrical null point. Electrical adjustments were used to make the calibration curve as linear as possible but the trace deflection per 3/8-inch movement of the loading piston varied from about 1.2 inches to 1.4 inches within the range of piston movements actually encountered in the tests (trace deflections as small as about 1.06 inches were encountered at the extreme ends of core travel). Thus an error in using an average trace deflection of 1.3 inches per 3/8-inch piston travel would involve an error of about plus and minus 7.7 percent. Attempts

were made to select an LVDT constant for the range in deformations actually encountered on each test; thus, the probable maximum error is about 5 percent. Thus, a sample that apparently failed at 23 percent strain could actually have failed between limits of about 22 percent to 24 percent.

Errors are also involved in recording the data and reading the tape. The maximum error in reading the tape is estimated at 0.02 inch which is an error of about 0.2 percent of the sample length. Instrumental errors associated with the response of the oscillograph are very difficult to access. However, the fastest rise times encountered with these tests was about 3 ms. If the stress-time curve is taken as the first quarter of a sine wave, then the period becomes 12 ms or the frequency about 80 cps. The galvanometer in the oscillograph had at least a 500 cps response. Thus, the response time of the galvanometer was a problem only for very small strains on the fastest tests. Seating problems and other mechanical problems are also severe at small strains.

Based on this discussion, it appears that the largest errors in determination of strain are associated with the unknown initial length of the sample and with the use of a linear calibration of the LVDT. Both of these errors are systematic errors and do not result in scatter of the points from the stress-strain curves. Both errors can be reduced considerably by further refinements in the apparatus and analytical procedures. Such refinements were not made during this contract since they would have resulted in a substantial reduction in the number of tests that could have been performed and interpreted and since the errors are small compared to the dynamic effects under investigation.

Error in Stress Measurement

The load cell was calibrated to read stress on a 1.5-inch-diameter specimen. The errors involved in assuming a linear calibration curve for the load cell are too small to warrant consideration. The load cell was calibrated statically. The difference between the static and dynamic calibrations is assumed negligible.

All samples were assumed to have an initial diameter of 1.5 inches. The diameters of the samples after compaction varied from about 1.500 inches to 1.506 inches, a range of 0.4 percent. The assumption of no volume change when the ambient and shearing stresses are applied results in a maximum error of about minus 6.5 percent in stress, i.e., the calculated stresses are smaller than the actual stresses.

The errors in determination of strain cause a second order error in determination of stress since an area correction is made to account for bulging of the samples during compression. This error probably does not exceed plus and minus 1 percent.

Instrumental recording errors for both the axial stress and the cell pressure are similar to those previously discussed for the strain measurements.

The errors involved in the determination of cell pressure are very small since a calibration of the Bourdon gages indicated they were within 1 percent and since pressure changes within the cell during dynamic tests were not detectable with the CEC pressure transducer.

In some of the early tests, the data were recorded in such a way that the seating loads could not be determined. The estimates of the seating loads could be in error by up to 10 psi but this error was eliminated after the first series of tests.

The main error associated with the determination of stress, based on the above discussion, is involved with the assumption of no volume change. This error should have a negligible effect on the strain rate investigations where all samples in the series were subjected to the same cell pressure. The effect on the Mohr-Coulomb diagrams should vary systematically with cell pressure.

A problem involved in the measurement of stresses at small strains is that of applying a sufficiently small seating load. If too large a seating load is applied, the soil undergoes creep under the static seating load. Such creep may affect the shape of the stress strain curve at small strains in subsequent dynamic tests. This problem may have influenced the results of some of the early tests where seating loads of up to about 15 percent of the compressive strength of the sample were accidentally applied. Improvements in the experimental techniques reduced the seating loads down to about 5 percent of the compressive strength of the samples. The plastic strains associated with such small seating loads are probably negligible.

Membrane Leakage Experiments

One of the experimental problems that warrants attention is the problem of nitrogen leakage through the rubber membranes surrounding the soil samples. Leakage of nitrogen through the membranes, or under the bindings, will result in an increase in the pore air pressure in the soil and, under constant total stress, a reduction in effective stress. The decrease in effective stress results in a loss of strength. On this project, the problem of membrane leakage was set aside during the early stages of the testing program because of the preponderant problems in instrumentation and mechanical design. An analysis of some of the early experimental results

indicated the presence of a random experimental error that could not be attributed to any of the sources of error previously discussed. In a meeting of the project advisory committee in June 1963, Mr. Stanley Wilson, consultant on this contract, brought up the subject of membrane leakage and suggested that measurements should be taken as soon as possible.

Measurements of membrane leakage were obtained by mounting a 1.5-inch-diameter by 3.0-inch-high porous stone (Norton, P2120) in a 1000-psi capacity Wykeham-Farrance triaxial cell, surrounding the stone with a solid filter paper drain and two membranes using the same set-up procedure as used with the soil tests, and then subjecting the membranes to direct nitrogen pressure. The drainage connection from the stone was connected to a buret system that allowed measurement of the volume of gas passing through the membrane. The gas volume was measured at atmospheric pressure. Measurements were made at a series of pressures between 100 psi and 1000 psi. A steady leakage rate was attained within the first minute. Enough measurements were taken at each pressure to assure reasonable reproducibility (about 2 percent scatter). The curve of leakage rate vs cell pressure is presented in Fig. 4.9. The leakage rate appears to be directly (though not linearly) related to the cell pressure and to approach 3 ml/min at a cell pressure of 1000 psi.

The outer surface of the second membrane was then coated with a thin layer of high-vacuum silicone grease and a third membrane was placed around the sample. Again leakage measurements were made at cell pressures between 100 and 1000 psi. As shown in Fig. 4.9, the rate of leakage was reduced by about 40 percent.

All of the triaxial tests performed on this project utilized two membranes without grease between them. The nitrogen leakage rates at cell pressures of 100 psi, 500 psi and 1000 psi should have been 0.4, 1.7 and

2.95 ml/min. Assuming an average dry density of 117.4 pcf, an average water content of 11.3 percent, a specific gravity of 2.72 and an unstressed (total stresses) volume of 87.1 cc, and assuming that all of the nitrogen leaking through the membrane became compressed into the same gas volume as the sample possessed prior to leakage, calculations based on the general gas law indicate that the pore air pressure should have changed by 0.7, 2.9 and 4.9 psi/min. for cell pressures of 100, 500 and 1000 psi. These pore air pressures act back against the inside of the rubber membranes and thus reduce the actual confining pressure. The change in confining pressure, expressed as a percentage of the confining pressure, are 0.7, 0.6 and 0.5 percent per minute. In some of the early triaxial tests, problems in the operation of the equipment led to appreciable delays between the time when the cell pressure was applied and when the shear test was actually performed. Nitrogen leakage through the membranes may explain some of the scatter obtained in these tests. Most of the triaxial tests were performed within several minutes after the cell pressure was applied, however, so the membrane leakage problem was probably of negligible importance. However, in tests lasting more than a few minutes, it would be necessary to make use of the mercury system discussed previously.

Summary

Based on the foregoing discussion, it appears that the important testing errors include (1) lack of data on the volume change characteristics of the samples, (2) nonlinearity of the LVDT calibration and (3) membrane leakage. The volume change data under static conditions can be obtained with comparatively minor additional amounts of work. The nonlinear LVDT calibration can be used in reducing the experimental data but a new data reduction system must be used in order to reduce the additional expense.

Membrane leakage was not a serious problem except where delays required subjecting the samples to the cell pressure for extended periods of time prior to testing. However, for longer term tests the cell should contain mercury up to the elevation of the center of the top cap.

4.4 DYNAMIC TRIAXIAL COMPRESSION TESTS

Introduction

All the dynamic triaxial compression tests were of the unconsolidated-undrained type at cell pressures between 114 psi and 1010 psi. Two types of tests were performed, tests to failure and partial loading tests. In the tests to failure, the samples were strained until the main piston of the loading machine reached the end of its travel, i.e., to about 40 percent strain. In the partial loading tests, an attempt was made to apply a predetermined pressure with a known rise time and to maintain this pressure for some predetermined dwell time.

A summary of the type of tests performed together with other miscellaneous data is presented in Table 4.1. Tests 3, 5, 12, 14, 25, 28, 36, 47 and 58 were defective in various ways and the stress data are not presented. Difficulties included loss of the trace on the oscillograph tape because of the very high trace velocity in some of the "dynamic" tests, burst membranes, excessive time periods under pressure with resulting gas leakage through the membranes, and running out of oscillograph paper for some of the tests with very long rise times.

In Table 4.1, the "Oil Valve" column designates the number of turns open of the oil valve. In tests where the space beneath the main piston of the loading machine was filled with gas (tests with 3 to 4 millisecond rise times) the Oil Valve column contains a hyphen.

Tests to Failure

Introduction. Excluding about twenty preliminary tests, forty-four triaxial compression tests to failure were performed. Considering the limited number of tests that were possible, an attempt was made to bracket the effects of confining pressure and loading rate by performing three series of tests: (1) a series of tests at a cell pressure of 100 psi with variable times to failure, (2) a series of tests at 1010 psi with variable times to failure, and (3) a series of tests with very short times to failure and with cell pressures ranging from 100 psi to 1000 psi. A series of only five tests was performed using the full range of cell pressures and relatively slow times to failure (about 70 seconds).

Effect of time-to-failure on compressive strength. The effect of time-to-failure on the compressive strength at a cell pressure of 114 psi is shown in Fig. 4.10. The compressive strength increased by about 50 percent when the time-to-failure was reduced from 100 seconds to 3 milliseconds; thus, the compressive strength increased about 10 percent for each ten-fold reduction in the time-to-failure.

A similar relationship for the series of tests at a cell pressure of 1010 psi is shown in Fig. 4.11. For these tests, the compressive strength increases by about 45 percent as the time-to-failure is reduced from 100 seconds to 3 milliseconds. Thus, the influence of deformation rate on the compressive strength is similar at the upper range of and the lower range of pressures used on this project.

For a range of times-to-failure where the strength vs log time-to-failure relationship is approximately linear, the strength can be expressed by an equation such as:

$$\frac{1}{2}(\sigma_1 - \sigma_3) = a - b \log t_f \dots \dots \dots (4.1)$$

where a and b are constants and t_f is the time-to-failure in seconds.

By approximating various parts of the strength-time relationships with strain lines, the appropriate values of a and b become:

| Cell Pressure psi | Range in Time-to-Failure | a | b |
|----------------------|--------------------------|-----|------|
| 114 | 3 ms to 10 ms | 99 | 32.7 |
| | 10 ms to 200 ms | 126 | 13.5 |
| | 0.2 s to 100 s | 128 | 8.0 |
| 1010 | 2 ms to 50 ms | 181 | 47.0 |
| | 0.05 s to 100 s | 227 | 7.5 |

An empirical relationship could be fitted to a curved strength vs log time-to-failure relationship, but the limited amount of data obtained to date does not warrant the more involved formulation.

Mohr-Coulomb diagrams. The influence of confining pressure on strength is shown in the modified Mohr-Coulomb diagram in Fig. 4.12. The curved failure envelopes are common for unconsolidated-undrained compression tests on unsaturated soils. When an increment of ambient total stress is applied to an unsaturated soil, the pore air pressure, pore water pressure and effective stress all increase. However, only the change in effective stress influences the shearing strength (by definition). When the total stress is increased, the increased pore air pressure results in a partial dissolution of the air in the pore water according to Henry's law.

Continued increases in the total stress will eventually cause all the pore air to dissolve in the pore water; thus, the soil is "pressure saturated." When the soil is unsaturated, an applied increment of total stress results in an increase in effective stress and an increase in shearing strength.

When the soil has been pressure saturated, nearly all of the increment of ambient total stress goes into the pore water and a negligible increase in effective stress results. Thus, for a saturated soil, the modified Mohr-Coulomb diagram, expressed in total stresses, becomes horizontal. Both dynamic failure envelopes in Fig. 4.12 (times-to-failure of 3.5 ms and 70 sec.) are concave downwards and approach a zero slope at high pressures.

Mr. Stanley Wilson suggested (personal communication) that a semi-logarithmic relationship might be used to formulate the failure envelope. The two dynamic failure envelopes have been plotted in semilogarithmic form in Fig. 4.13. The equations of the two failure envelopes are approximately:

$$\frac{1}{2}(\sigma_1 - \sigma_3) = -191 + 135 \log \frac{1}{2}(\sigma_1 + \sigma_3) \quad 70 \text{ sec. to failure}$$

$$\frac{1}{2}(\sigma_1 - \sigma_3) = -367 + 218 \log \frac{1}{2}(\sigma_1 + \sigma_3) \quad 3\frac{1}{2} \text{ ms. to failure}$$

These relationships are applicable to the range in confining pressure from 100 psi to 1000 psi. A more general equation could probably be derived to define the total stress failure envelope if the effective stress properties of the soil were known.

The failure envelope defined with the low-pressure static tests is also shown in Fig. 4.12. The times-to-failure for the static tests were about 700 seconds, ten times longer than the times-to-failure for the 70-second dynamic failure envelope. Thus, the extended 70-second dynamic envelope should be slightly above the static envelope. Actually, the two envelopes are almost perfectly coincident. The explanation is that the decreases in volume resulting from the application of both ambient and shearing stresses were taken into account with the static tests. The reduced areas of the samples could not be taken into account with the dynamic tests; thus, the assumed areas of the samples are slightly too

large for the dynamic tests and the calculated compression stresses are too low. An adjustment of the areas puts the two failure envelopes in proper relative positions. Thus, the static envelope provides evidence that there are no major errors in defining the stresses in the dynamic tests.

Stress-strain relationships. The stress-strain curves derived from the tests-to-failure show a remarkable uniformity. Examination of Table 4.1 demonstrates that the strains at failure are independent of both the confining pressure and the time-to-failure. Only three samples failed at strains outside of the range from 18 percent to 24 percent and those three samples failed at 17, 25 and 26 percent strain. Considering the uniformity of the stress-strain curves, there is little to be gained by presenting all the curves individually. Attempts were made to reduce the stress-strain data to dimensionless plots for condensed presentation.

The stress-strain data were normalized by plotting the ratio of the stress difference to the stress difference at failure, $(\sigma_1 - \sigma_3)/(\sigma_1 - \sigma_3)_f$, versus the ratio of the strain to the strain at failure, ϵ/ϵ_f . These ratios are designated as R_σ and R_ϵ respectively. The resulting plot is a dimensionless stress-strain curve with the stress and strain ratios varying between 0 and 1.

The most convenient method of grouping tests was to plot all tests subjected to the same confining pressure together. The dimensionless stress-strain diagrams for all tests performed at confining pressures of about 114, 210, 498, 705 and 1010 psi are presented in Figs. 4.14 through 4.18. Since the tests at each confining pressure were performed at a wide range of strain rates, much of the scatter in Figs. 4.14 through 4.18 represents strain rate effects. Some of the scatter represents experimental error.

It would be convenient if these dimensionless stress-strain diagrams could be represented by mathematically simple curves. Efforts were made to fit several types of curves to the data. The stress strain data obtained from tests at a confining pressure of 114 psi (Fig. 4.14) will be used to illustrate the methods used.

A hyperbola of the form:

$$R_{\sigma} = \frac{R_{\epsilon}}{a + b R_{\epsilon}} \dots \dots \dots (4.2)$$

has been suggested by Kondner¹ for the representation of the stress-strain relationship. The constants a and b are easily determined since a plot of R_{ϵ}/R_{σ} vs R_{ϵ} results in a straight line with an intercept of a and a slope of b. The data shown in Fig. 4.14 have been replotted in this form in Fig. 4.19. For values of R_{ϵ} greater than 0.2, the data define a straight line; thus the dimensionless stress-strain curve is approximately hyperbolic for R_{ϵ} greater than 0.2. The constants are $a = 0.09$ and $b = 0.91$. Similar diagrams were prepared for tests at other pressures and the following parameters were obtained:

| Confining Pressure psi | a | b |
|---------------------------|------|------|
| 114 | 0.09 | 0.91 |
| 210 to 328 | 0.09 | 0.91 |
| 477 to 453 | 0.07 | 0.93 |
| 705 to 735 | 0.05 | 0.95 |
| 1010 | 0.05 | 0.95 |

The decreasing value of a and increasing value of b indicate that the stress-strain curves rise more rapidly at low strains when the confining pressure is increased. The hyperbolas are drawn in Figs. 4.14 through

4.18 for comparison with the real data and it is evident that the fit is satisfactory at large strains but is not satisfactory at low strains.

Using the data obtained at a confining pressure of 114 psi, the simple hyperbolic relationship (Eq. 4.2) was also fitted to the data at low strains. The hyperbolic parameters were then $a = 0.07$ and $b = 0.93$. A comparison between this hyperbola and the real stress-strain data is shown in Fig. 4.20. As expected, the hyperbola fits the experimental data reasonably well at low strains but does not fit for $R_\sigma > 0.6$.

A curve obeying the equation (Brinch-Hansen²):

$$R_\sigma = \frac{\sqrt{R_\epsilon}}{a + b\epsilon} \quad \dots \dots \dots (4.3)$$

was fitted to the same experimental data with the provision that the curve must pass through the coordinate (1,1) with a horizontal tangent; thus a and b must be 0.5. The curve is shown in Fig. 4.21 together with the experimental data. The curve fits the data at small strains but deviates widely from the experimental data for $R_\epsilon > 0.2$.

Finally, a logarithmic curve of the form:

$$R_\epsilon = a 10^{nR_\sigma} \quad \dots \dots \dots (4.4)$$

was fitted to the data (Fig. 4.22). In this case, the constants a and n were 0.006 and 2.13 respectively. The fit is reasonably good up to $R_\epsilon = 0.8$ but the curve deviates widely from the experimental data at larger values of R_ϵ .

None of the simple mathematical equations fits the experimental data adequately throughout the range in strain up to failure but any of the equations can be fitted to the experimental data for limited ranges in strain.

In the soil-structure interaction problem, there is particular interest in the shape of the early part of the stress-strain curve. Since the curved form of the stress-strain curve introduces complexity into analytical work, it is common practice to define the early part of the stress-strain curve using the secant modulus (E_s), i.e., the ratio of the stress to the strain at some arbitrary point on the stress-strain curve. The arbitrary points are often either one percent strain or at half the failure stress, though any point on the stress-strain curve may be chosen.

Definition of the stress at low strains, and vice versa, was particularly difficult on this project because of the very rapid rise times. Since the rates of strain were approximately uniform during a single test, samples that failed in 3.5 milliseconds at 22 percent strain must have developed one percent strain in less than 0.2 milliseconds. The 500-cps (2 milliseconds per cycle) galvanometers in the oscillographs cannot give an accurate response to such rapid loadings. Since the stress-strain curve is very steep at such low strains, small variations in the deformation trace resulting from stray electric currents or from loosening of the cross arm holding the LVDT core could exert considerable influence on the secant modulus at low strains. An additional difficulty with some of the early tests was that appreciable seating loads were applied to the samples. The influence of these seating loads on the dynamic secant moduli is not known.

The influence of the confining pressure on the secant moduli defined at 1 percent strain in "dynamic" tests is shown in Fig. 4.23. The semi-logarithmic plot was used since the semi-logarithmic modified Mohr-Coulomb diagram yielded a straight line failure envelope. The data in Fig. 4.23 have a considerable amount of scatter but they suggest that,

within the range of pressure from 100 psi to 1000 psi, the secant modulus defined at 1 percent strain increases with the logarithm of the confining pressure. The secant modulus ranged from about 10,000 psi at a confining pressure of 100 psi to 21,000 psi at a confining pressure of 1000 psi. Similar data are plotted in Fig. 4.24 where the secant moduli are defined at half the failure strength. These secant moduli are somewhat lower, ranging from about 9000 psi to 15,000 psi for the range in confining pressure from 100 psi to 1000 psi.

The influence of the rate of loading on the secant moduli at 1 percent strain is shown in Fig. 4.25. Considering the difficulties associated with the definition of the secant modulus, the scatter is small. For samples subjected to a confining pressure of 114 psi, the secant modulus is independent of the loading rate within the range of 3 milliseconds to 70 seconds to failure. At a confining pressure of 1010 psi, the secant modulus increases linearly as the time-to-failure decreases logarithmically down to 50 milliseconds, the time-to-failure associated with the fastest setting of the oil valve. The fastest tests at 1010 psi yielded somewhat lower secant moduli. Within the range of times-to-failure of 50 milliseconds to 70 seconds, the secant modulus for the tests at 1010 psi is given by the equation:

$$E_s @ 1\% \text{ strain} = 24,000 - 2630 \log t_f$$

where the time-to-failure (t_f) is expressed in seconds.

Interpretation of the secant modulus data is complicated by lack of sufficient data and by uncertainties regarding the validity of the observations for the tests with times to failure around 3 milliseconds. Nevertheless, some preliminary interpretation seems necessary. The samples used

in this investigation were subjected to a kneading compaction procedure with nominal foot pressures of about 200 psi. The actual foot pressure was much larger for small foot penetrations since the bottom of the foot was slightly rounded. Thus, these samples were subjected to a prestress equivalent to at least 200 psi before they were inserted into the triaxial cell. It is assumed that sample deformation results from a combination of particle distortion (mainly bending of clay plates in cohesive soils) and interparticle displacements. The deformation resulting from particle distortion should largely be elastic, i.e., the deformations should be recoverable though the stress-strain curve may not be linear and may contain a hysteresis loop between the loading and unloading parts of the curve. Deformation resulting from particle displacements should be plastic and should exhibit a viscous effect, i.e., the resistance to displacement should be a function of the rate of deformation.

For the samples subjected to a confining pressure of 114 psi, the particles have been subjected to a prestress well in excess of the confining pressure and deformations up to perhaps one percent strain should be largely elastic. Elastic response is assumed to occur in less than a millisecond; thus, the secant modulus for an elastic response should be independent of the loading rate (Fig. 4.25) for times-to-failure in excess of 3 milliseconds. When the samples are subjected to a confining pressure of 1000 psi, much of the prestress resulting from compaction is exceeded and both the elastic and plastic deformation occur at strains less than one percent. Thus, the secant modulus at 1000 psi is somewhat strain rate dependent (Fig. 4.25). Since the effective stresses are greater in the samples with a confining pressure of 1010 psi than in those with 114 psi,

the soil structure is more rigid and a larger secant modulus results. The interpretation of the secant modulus data is complicated by the fact that the physical properties of soils are functions of the state of effective stress, not the state of total stress. On this project, only total stress data are available. If pore pressure data were available for these dynamic tests, it is probable that a much more quantitative explanation of the influence of confining pressure and loading rate on the secant modulus could be developed.

Partial Loading Tests

Introduction. At the first meeting of the Project Advisory Committee, Mr. Stanley Wilson expressed great interest in partial loading tests, i.e., tests in which some fraction of the load required to produce failure is applied dynamically and is maintained constant for some prescribed period of time with resulting strains being measured. It was recognized that difficulties would be experienced in such tests because of overshoot resulting from the inertia of the main piston in the loading machine but a series of tests were performed to study the feasibility of such tests and to determine if useful data could be obtained using the type of apparatus that was then under design.

With a limited amount of time available, it was decided to restrict the tests to two loading rates, the first using gas loading (such as in the 4-millisecond tests discussed previously) and the second using an oil valve setting of 10. The gas-loaded tests were performed at cell pressures of 117 psi and 1010 psi. The oil-valve tests were performed at cell pressures of 117 psi, 208 psi, 498 psi, 705 psi and 1000 psi.

Chamber pressures were selected such that the applied axial stress varied from about 20 percent to 60 percent of the stress required to cause

failure. The sum of the rise time and dwell time was restricted to about 400 milliseconds.

Equipment problems. As noted above, the most serious equipment problem was expected to be involved with reduction of the overshoot of stress to tolerable limits. Since the main piston of the loading machine does not strike the base of the loading machine in partial loading tests it would seem possible to replace the steel piston with a piston made of much lighter metal and thus to reduce the inertia of the loading system. Lack of time precluded attempts at such equipment refinements but it is recommended that attempts along these lines should be made on future research.

A second equipment problem involved the maintenance of a constant load over predetermined periods of time. The use of a controlled chamber pressure in the loading machine established that the stress applied to the main piston of the loading machine was essentially constant. However, there were rubber O-ring seals between this piston and its cylinder and between the loading piston of the triaxial cell and the top of the cell. Rubber O-rings seals exert approximately a constant frictional drag on a moving piston provided the piston velocity is constant. If the piston velocity decreases to almost zero, the O-rings often tend to freeze against the moving piston and, thus, increase the drag. The slight decrease in axial stress in some of the tests could have resulted from O-ring freezing.

Stress-time and strain-time relationships. The stress-time and strain-time relationships for all the partial loading tests are presented in Fig. 4.26 through 4.32.

The problem of overshoot of applied stress was particularly severe in the tests with very rapid rise times (Fig. 4.26 and 4.27). The

oscillograph was unable to respond accurately to such rapid stress pulses, so the actual magnitudes of the overshoot cannot be determined. Using the oscillograph data, the overshoot was from 21 percent to 34 percent except on test 60 where the oscillograph indicated only a 2 percent overshoot. As shown in Figs. 4.26 and 4.27, the applied stresses were maintained reasonably constant during the 400-millisecond dwell time. The samples underwent a rapid strain associated with the rise time of the load but continued to strain, in most tests, when the stress was decreasing from its peak value toward the constant value. As the stress approached the constant value, some of the samples underwent a slight re-expansion.

The tests with an oil-valve setting of 10 (Figs. 4.28 through 4.32) exhibit stress-time and strain-time curves that are very similar to those of the more rapid tests except that the rise time is longer (about 50 milliseconds as opposed to about 0.2 to 1.5 milliseconds for the fast tests) and the stress overshoot is smaller. The overshoot varied from 4 percent to 18 percent and averaged about 10 percent. In many of these tests the sample continues to compress during the time when the load is decreasing from its peak value back toward the constant value. Thus, the continued strain during decreasing stress on the very rapid tests is probably not caused by instrumentation errors but is a real occurrence. If the stress could be applied almost instantaneously and then held constant, it appears that the soil might undergo an almost instantaneous elastic strain followed by a plastic strain that occurs at a decreasing rate as the time increases.

Effect of stress level on creep rate. Examination of Figs. 4.26 through 4.32 indicates that the rate of creep, under approximately constant stress, is a function of the stress level, the higher the stress level the

higher the creep rate. As a first approximation, the strain occurring between 0.1 second and 0.4 second was expressed in units of percent per second and plotted against the constant axial stress expressed as a percentage of the axial stress required to produce failure, i.e., the stress ratio (Fig. 4.33 and Table 4.2).

Figure 4.33 shows that continued creep does not take place until the stress is about 35 percent of the failure stress. Considering only the oil valve tests, the applications of stresses beyond 35 percent of the failure stress results in deformation in the 0.1- to 0.4-second interval; this creep increases with the stress level and is greater, for a given stress ratio, at higher cell pressures. The influence of stress ratio on the creep rate is to be expected; at stress ratios approaching one the creep rate should become very large. The explanation of the influence of cell pressure on creep rate is essentially the same as the explanation of the influence of cell pressure on the secant modulus. These soil samples were compacted using a nominal foot pressure of 200 psi. Thus, samples subjected to cell pressures less than perhaps 200 psi are over-consolidated and should undergo very reduced amounts of creep. The creep should be very small for samples subjected to cell pressures less than 100 psi. The samples subjected to 1000 psi of cell pressure were compressed sufficiently so that they might approximate normally consolidated insensitive clays and increased creep rates are to be expected.

Only two cell pressures were used with the dynamic tests, 114 psi and 1000 psi. The 114 psi tests experienced the same creep rates as the 114 psi tests using the oil valve. However, the tests at 1000 psi experienced relatively small and erratic creep. As shown in Table 4.2, the stress overshoot in the dynamic tests ranged from 21 percent to 34 percent

(as noted previously, the overshoot of only 2 percent in test 60 is believed to indicate an inability of the oscillograph to respond to a very rapid stress pulse), whereas the overshoot in the oil-valve tests was always less than 18 percent. Even in the oil-valve tests, the samples subjected to a high stress overshoot underwent little creep; the samples that underwent creep had an average overshoot of only 6.7 percent. It appears that samples subjected to large stress overshoot, and associated elastic strains, are prestressed to such an extent that subsequent viscous straining is inhibited.

These partial-loading tests demonstrate that the rate of creep is a function of the stress level (expressed as a ratio of the stress required to cause failure) and the cell pressure (degree of overconsolidation) and that prestress caused by stress overshoot reduces the creep rate. The overshoot is believed to result from the inertia of the main piston of the loading machine and the piston and top cap of the triaxial cell, with perhaps a small inertial effect from the gas. Thus, reduction of overshoot will necessitate using either slower rise times or reduced mass in the loading system.

Since the strain-time curves were curved, consideration was given to fitting a visco-elastic model to the curves. However, the unknown magnitudes of the stress overshoot and the lack of sufficient data precluded a useful visco-elastic analysis.

REFERENCES

1. Kondner, Robert L. (1963), "Hyperbolic Stress-Strain Response: Cohesive Soils," Proc. A.S.C.E., vol. 89, SM-1, pp. 115-144.
2. Brinch-Hansen, J. (1963), Discussion, Proc. A.S.C.E., vol. 89, SM-4, pp. 241-242.

TABLE 4.1

SUMMARY OF TRIAXIAL TESTS

Note: All shear data were reduced from
oscillograph tape. Corrections
have been applied for the seating load.

| Batch No. | Sample No. | σ_3 psi | Seat Load psi | $\frac{\sigma_1 - \sigma_3}{2}$ psi | $\frac{\sigma_1 + \sigma_3}{2}$ psi | ϵ_f % | t_f | Chamber Pressure psi | Oil Valve |
|--------------|---------------|-------------------|---------------------|--|--|-------------------|-------------------|----------------------------|--------------|
| 1 | 1 | 1005 | (20) | 298 | 1303 | 21 | 3 ms | 320 | - |
| 1 | 2 | 790 | 18 | 275 | 1065 | 22 | 3 ms | 300 | - |
| 1 | 3 | 600 | - | - | - | - | - | - | - |
| 1 | 4 | 600 | (20) | 267 | 867 | 24 | $3\frac{1}{2}$ ms | 280 | - |
| 1 | 5 | 410 | - | - | - | - | - | - | - |
| 1 | 6 | 208 | 13 | 198 | 406 | 23 | 4 ms | 220 | - |
| 1 | 7 | 114 | 22 | 163 | 277 | 17 | 3 ms | 180 | - |
| 1 | 8 | 114 | 30 | 120 | 234 | 20 | 70 s | 400 | .1 |
| 1 | 9 | 114 | 15 | 112 | 226 | 18 | 29 s | 400 | .5 |
| 1 | 10 | 114 | 30 | 122 | 236 | 20 | 18 s | 400 | 1 |
| 1 | 11 | 114 | 11 | 119 | 233 | 20 | 6 s | 400 | 1.5 |
| 1 | 12 | 114 | 10 | - | - | - | - | - | - |
| 1 | 13 | 114 | 24 | 128 | 242 | 22 | 1.5 s | 400 | 3.0 |
| 1 | 14 | 114 | - | - | - | - | - | - | - |

TABLE 4.1 (continued)

| Batch No. | Sample No. | σ_3 psi | Seat Load psi | $\frac{\sigma_1 - \sigma_3}{2}$ psi | $\frac{\sigma_1 + \sigma_3}{2}$ psi | ϵ_f % | t_f | Chamber Pressure psi | Oil Valve |
|-----------|------------|-------------------|------------------|--|--|-------------------|--------|-------------------------|-----------|
| 2 | 15 | 1020 | 18 | 232 | 1252 | 21 | 50 ms | 400 | 11 |
| 2 | 16 | 1010 | 15 | 253 | 1263 | 21 | 50 ms | 400 | 10 |
| 2 | 17 | 1010 | 22 | 253 | 1263 | 22 | 125 ms | 400 | 9 |
| 2 | 18 | 1010 | 25 | 244 | 1254 | 20 | 130 ms | 400 | 8 |
| 2 | 19 | 1010 | 20 | 217 | 1227 | 21 | 280 ms | 400 | 7 |
| 2 | 20 | 1010 | 18 | 217 | 1227 | 22 | 400 ms | 400 | 6 |
| 2 | 21 | 1010 | 22 | 228 | 1238 | 22 | 600 ms | 400 | 5 |
| 2 | 22 | 1010 | 32 | 230 | 1240 | 21 | 1 s | 400 | 4 |
| 2 | 23 | 1010 | 35 | 239 | 1249 | 21 | 1.75 s | 400 | 3 |
| 2 | 24 | 1010 | 33 | 217 | 1227 | 21 | 4.4 s | 400 | 2 |
| 2 | 25 | 1010 | 37 | - | - | - | - | - | - |
| 2 | 26 | 1010 | 30 | 212 | 1222 | 18 | 85 s | 400 | .1 |
| 2 | 27 | 1010 | (30) | 305 | 1315 | 22 | 3.2 ms | 320 | - |
| 2 | 28 | 114 | - | - | - | - | - | - | - |
| 3 | 29 | 114 | 10 | 142 | 256 | 21 | 40 ms | 400 | 10 |
| 3 | 30 | 114 | 0 | 137 | 254 | 22 | 110 ms | 400 | 8 |
| 3 | 31 | 114 | 9 | 134 | 248 | 21 | 300 ms | 400 | 7 |
| 3 | 32 | 114 | 12 | 132 | 246 | 22 | 650 ms | 400 | 2 |
| 3 | 33 | 114 | 3 | 130 | 244 | 22 | 470 ms | 400 | 5 |
| 3 | 34 | 114 | 24 | 140 | 254 | 21 | 3.5 s | 400 | .5 |
| 3 | 35 | 113 | 8 | 120 | 234 | 22 | 14 s | 400 | 1 |
| 3 | 36 | 113 | - | - | - | - | - | 400 | .1 |
| 3 | 37 | 910 | 20 | 291 | 1201 | 25 | 4 ms | 310 | - |
| 3 | 38 | 705 | 14 | 293 | 998 | 19 | 4 ms | 270 | - |
| 3 | 39 | 498 | 16 | 279 | 777 | 22 | 4 ms | 270 | - |
| 3 | 40 | 498 | 16 | 283 | 781 | 24 | 5 ms | 250 | - |
| 3 | 41 | 328 | 12 | 245 | 573 | 22 | 4 ms | 230 | - |

TABLE 4.1 (continued)

| Batch No. | Sample No. | σ_3 psi | Seat Load psi | $\frac{\sigma_1 - \sigma_3}{2}$ psi | $\frac{\sigma_1 + \sigma_3}{2}$ psi | ϵ_f % | t_f | Chamber Pressure psi | Oil Valve |
|-----------|------------|-------------------|------------------|--|--|-------------------|-------|-------------------------|-----------|
| 4 | 42 | 1010 | 31 | 300 | 1310 | 26 | 4 ms | 320 | - |
| 4 | 43 | 1010 | 0 | 182 | 1192 | 22 | 75 s | 400 | .5 |
| 4 | 44 | 1010 | 33 | Partial Loading | | | | 155 | - |
| 4 | 45 | 1010 | 11 | " | " | | | 130 | - |
| 4 | 46 | 1010 | 33 | " | " | | | 105 | - |
| 4 | 47 | 1000 | 6 | - | - | - | - | 400 | 10 |
| 4 | 48 | 1000 | - | - | - | - | - | 155 | 10 |
| 4 | 49 | 1000 | 8 | Partial Loading | | | | 130 | 10 |
| 4 | 50 | 1000 | 6 | " | " | | | 105 | 10 |
| 4 | 51 | 1000 | 11 | " | " | | | 155 | 10 |
| 5 | 52 | 117 | 4 | 115 | 232 | 21 | 1.5 s | 400 | 3 |
| 5 | 53 | 293 | 2 | 153 | 446 | 22 | 1.5 s | 420 | 3 |
| 5 | 54 | 477 | 10 | 168 | 645 | 22 | 1.5 s | 440 | 3 |
| 5 | 55 | 735 | 4 | 180 | 915 | 22 | 1.6 s | 460 | 3 |
| 5 | 56 | 1010 | 2 | 190 | 1200 | 24 | 1.7 s | 480 | 3 |
| 5 | 57 | 117 | 6 | Partial Loading | | | | 35 | 10 |
| 5 | 58 | 117 | 4 | - | - | - | - | 45 | 10 |
| 5 | 59 | 117 | 2 | Partial Loading | | | | 55 | 10 |
| 5 | 60 | 117 | 4 | " | " | | | 35 | - |
| 5 | 61 | 117 | 8 | " | " | | | 45 | - |
| 5 | 62 | 117 | 2 | " | " | | | 55 | - |
| 6 | 63 | 208 | 6 | Partial Loading | | | | 45 | 10 |
| 6 | 64 | 208 | 4 | " | " | | | 55 | 10 |
| 6 | 65 | 208 | 4 | " | " | | | 65 | 10 |
| 6 | 66 | 498 | 8 | " | " | | | 55 | 10 |
| 6 | 67 | 498 | 8 | " | " | | | 80 | 10 |
| 6 | 68 | 498 | 12 | " | " | | | 100 | 10 |
| 6 | 69 | 705 | 14 | " | " | | | 65 | 10 |
| 6 | 70 | 705 | 10 | " | " | | | 90 | 10 |
| 6 | 71 | 705 | 14 | " | " | | | 114 | 10 |

TABLE 4.1 (continued)

| Batch No. | Sample No. | σ_3 psi | Seat Load psi | $\frac{\sigma_1 - \sigma_3}{2}$ psi | $\frac{\sigma_1 + \sigma_3}{2}$ psi | ϵ_f % | t_f | Chamber Pressure psi | Oil Valve |
|--------------|---------------|-------------------|---------------------|--|--|-------------------|-------|----------------------------|--------------|
| 7 | 72 | 210 | (10) | 164 | 374 | 23 | 70 s | 400 | .1 |
| 7 | 73 | 498 | (10) | 203 | 701 | 20 | 70 s | 400 | .1 |
| 7 | 74 | 705 | 20 | 215 | 920 | 18 | 63 s | 400 | .1 |

TABLE 4.2
SUMMARY OF PARTIAL LOADING TESTS

| Test No. | σ_3 psi | Oil Valve | $\frac{(\sigma_1 - \sigma_3)}{(\sigma_1 - \sigma_3)_f}$ % | Overshoot % | $\Delta\epsilon/\Delta t$ %/sec. |
|----------|-------------------|-----------|--|----------------|-------------------------------------|
| 57 | 114 | 10 | 38 | 5 | 0.3 |
| 59 | 114 | 10 | 62 | 8 | 3.3 |
| 63 | 208 | 10 | 37 | 11 | 0.0 |
| 64 | 208 | 10 | 44 | 9 | 1.0 |
| 65 | 208 | 10 | 56 | 5 | 5.3 |
| 66 | 498 | 10 | 17 | 15 | 0.0 |
| 67 | 498 | 10 | 39 | 13 | 1.3 |
| 68 | 498 | 10 | 51 | 7 | 5.7 |
| 69 | 705 | 10 | 19 | 18 | 0.0 |
| 70 | 705 | 10 | 41 | 12 | 0.7 |
| 71 | 705 | 10 | 54 | 4 | 4.3 |
| 49 | 1000 | 10 | 27 | 5 | 0.0 |
| 50 | 1000 | 10 | 39 | 1 | 3.0 |
| 51 | 1000 | 10 | 45 | 3 | 11.3 |
| 60 | 117 | - | 33 | (2) | 0.0 |
| 61 | 117 | - | 57 | 29 | 1.7 |
| 62 | 117 | - | 64 | 25 | 2.7 |
| 46 | 10 10 | - | 39 | 34 | 2.0 |
| 45 | 10 10 | - | 53 | 21 | 2.5 |
| 44 | 10 10 | - | 62 | 25 | 1.1 |

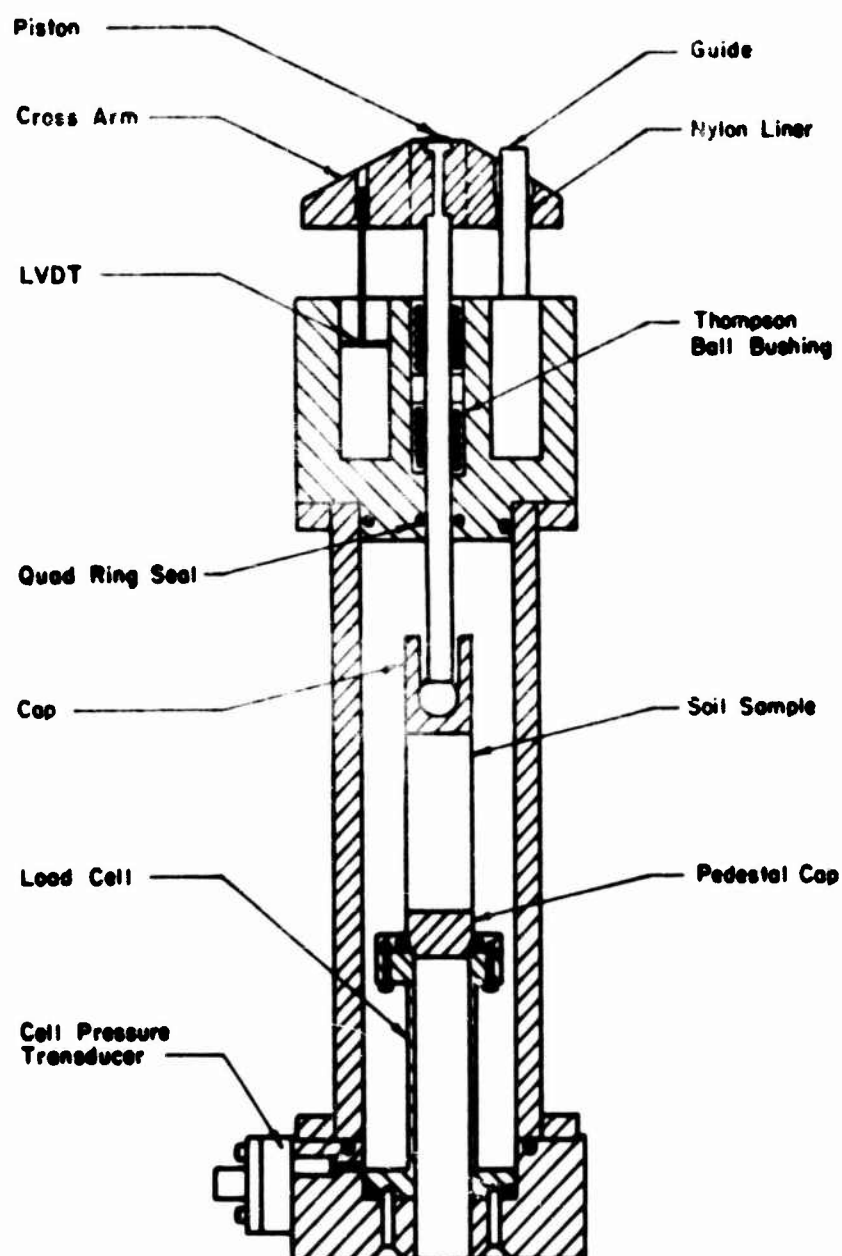


Figure 4.1. Triaxial Cell .

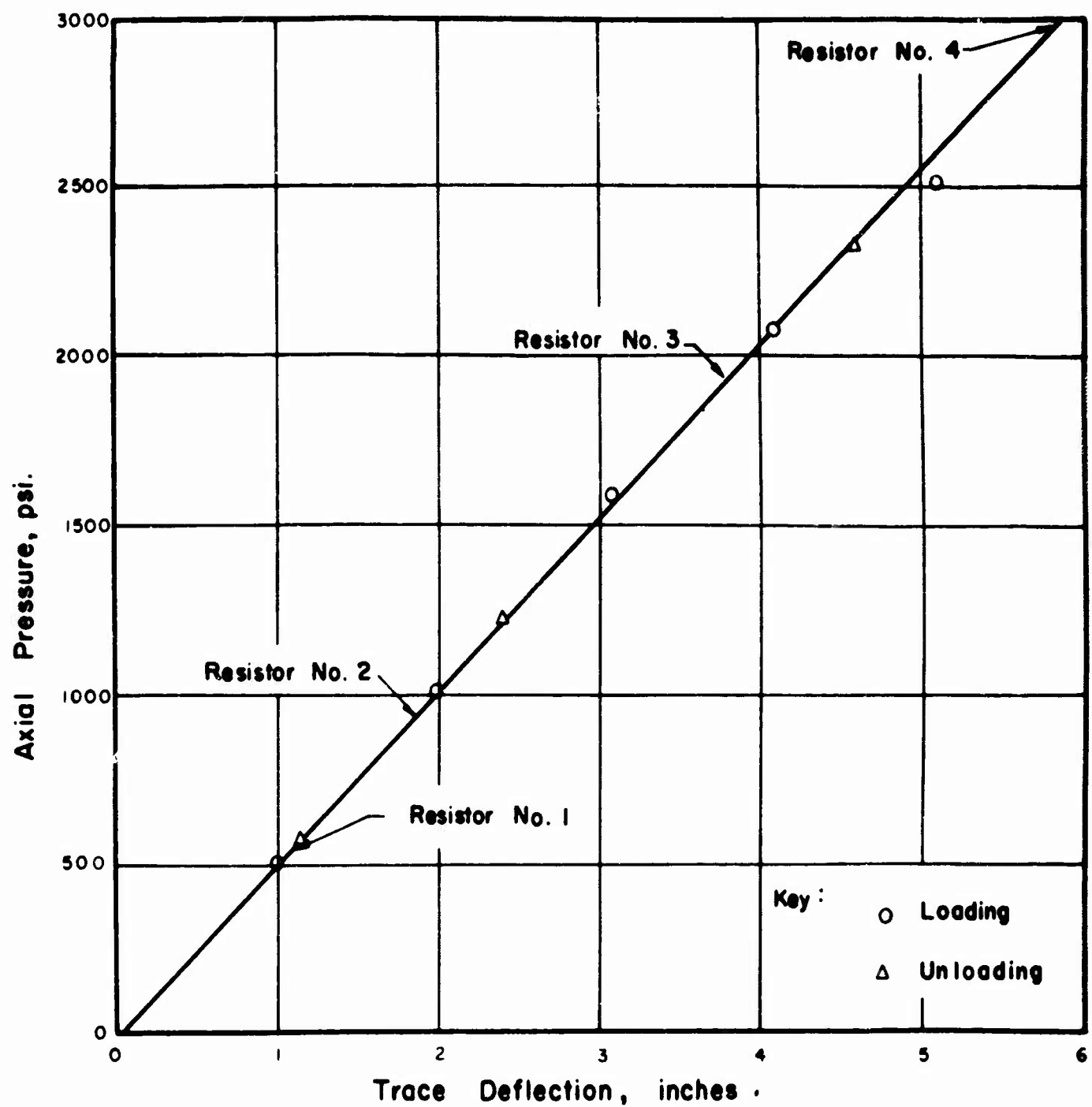


Figure 4.2. Calibration Curve For The Load Cell

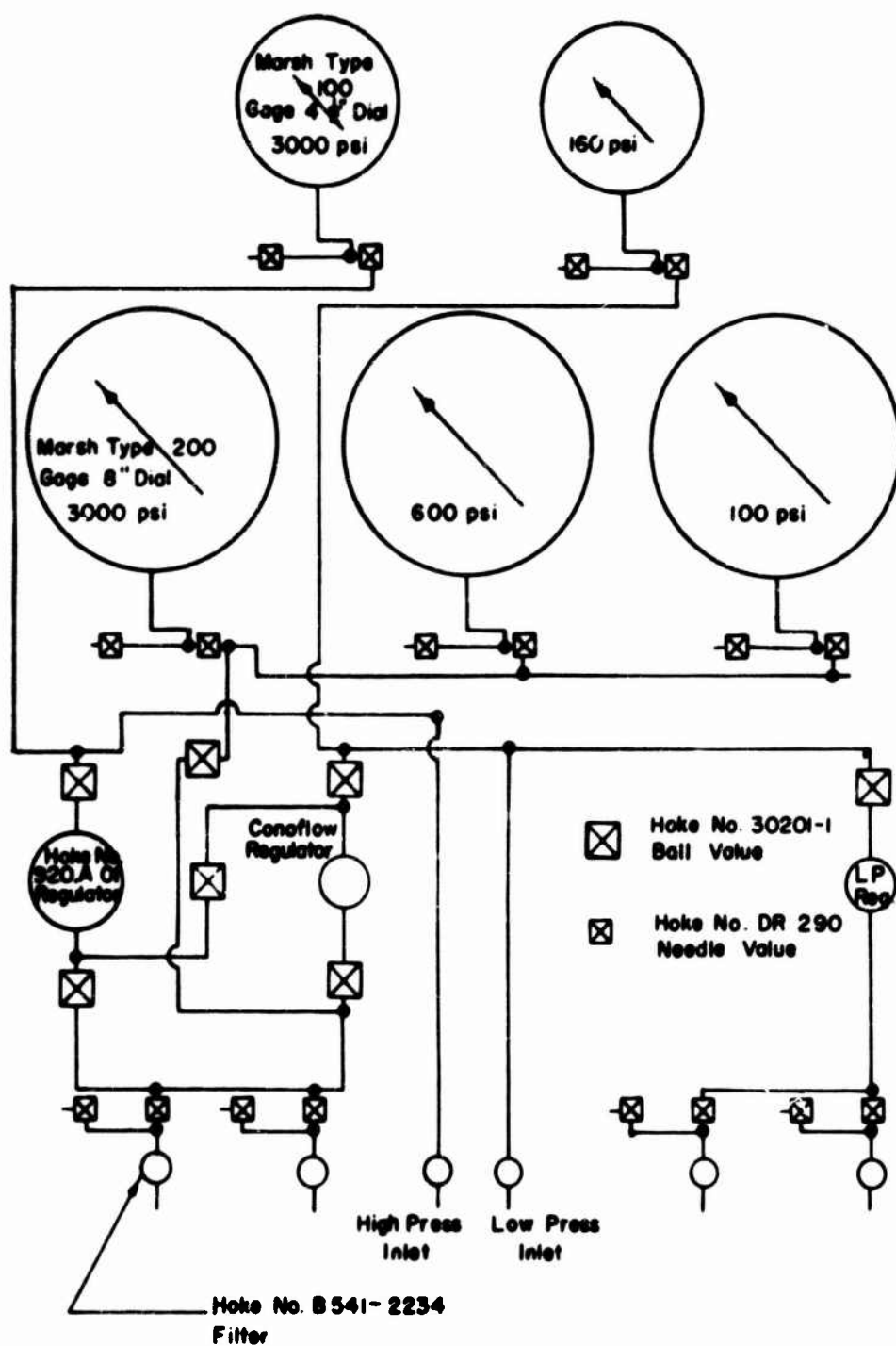


Figure 4.3. Cell Pressure Panel Board Circuit

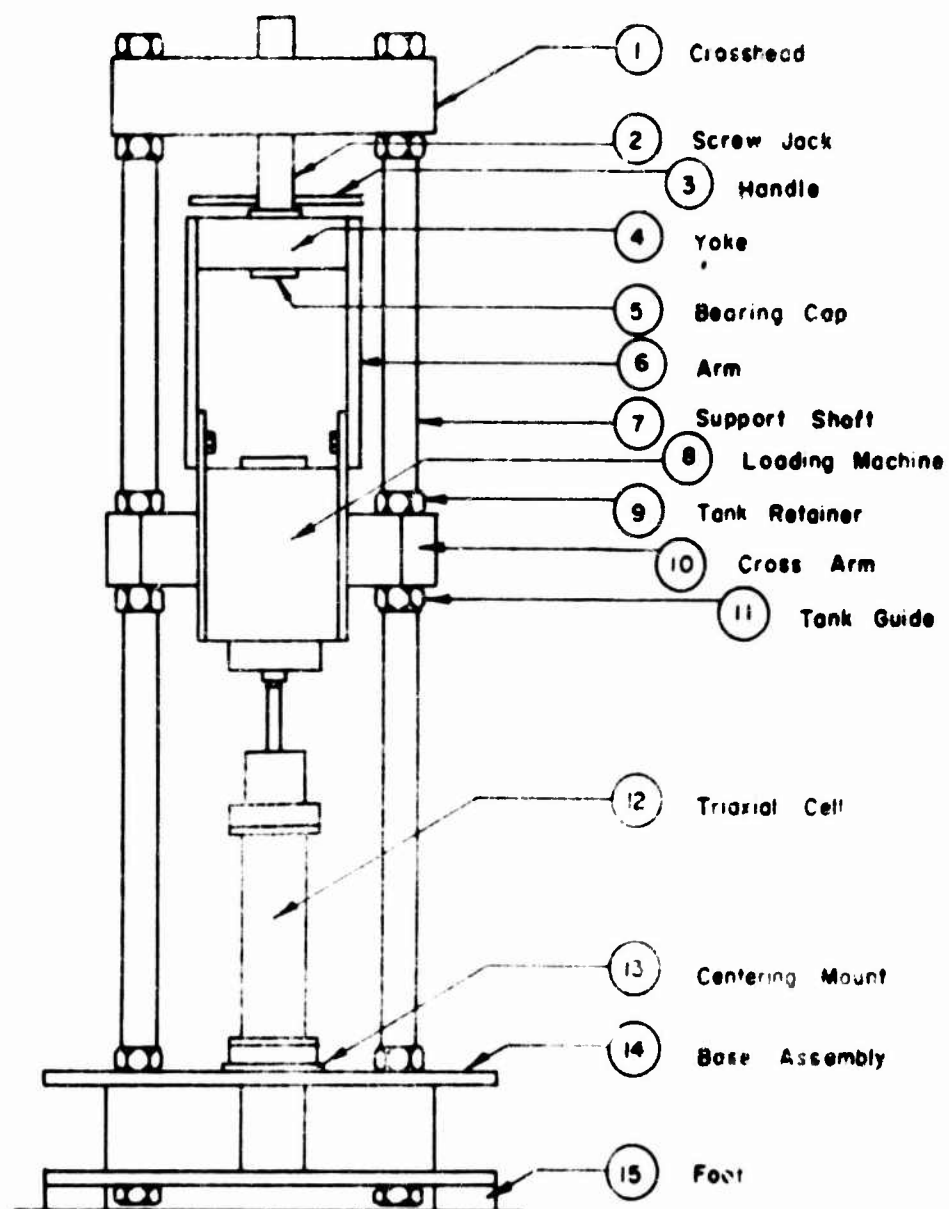


Figure 4.4 Dynamic Testing Frame

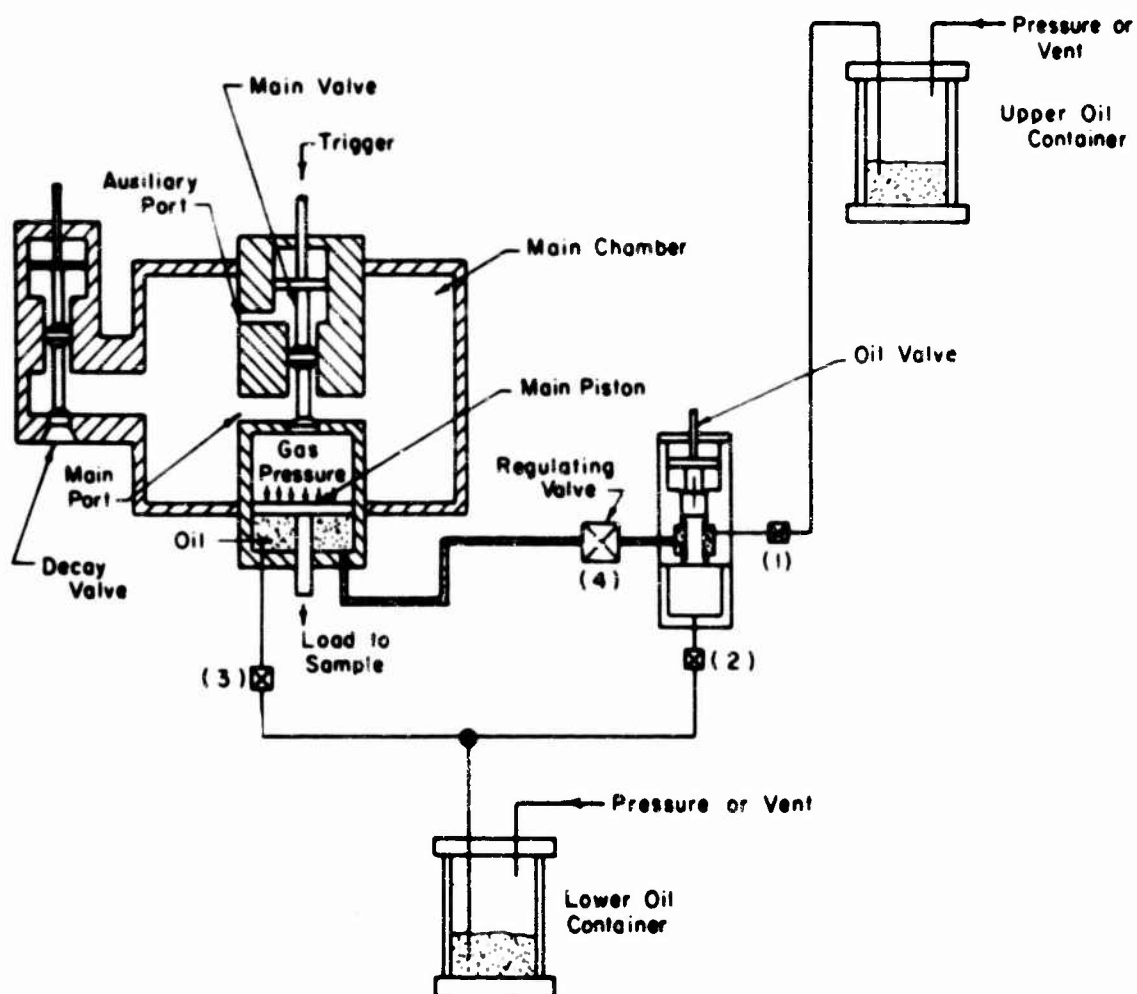


Figure 4.5. Hydraulic System

Rate of Deformation, inches per second

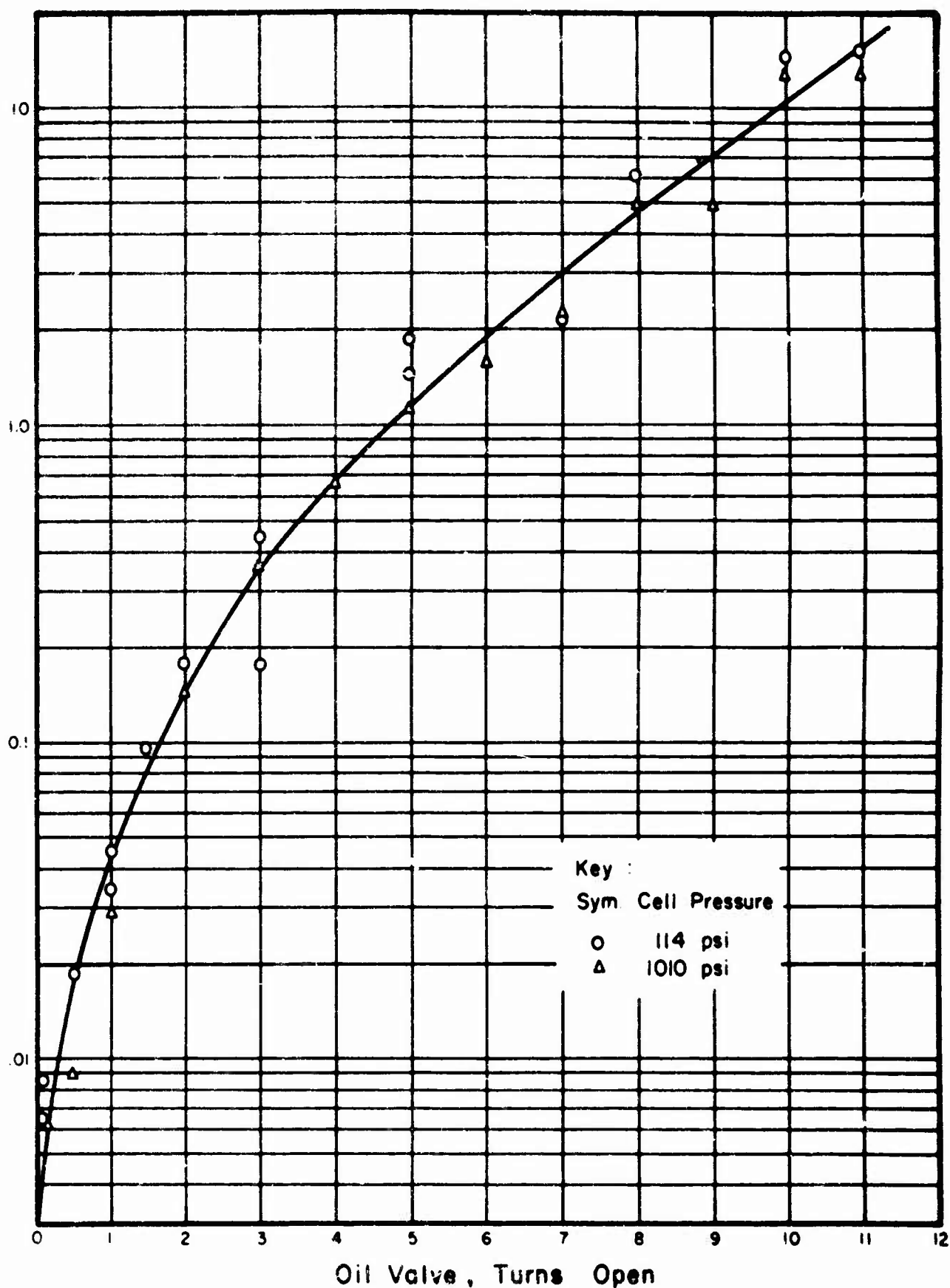


Figure 4.6. Rates of Deformation in Oil Valve Tests.

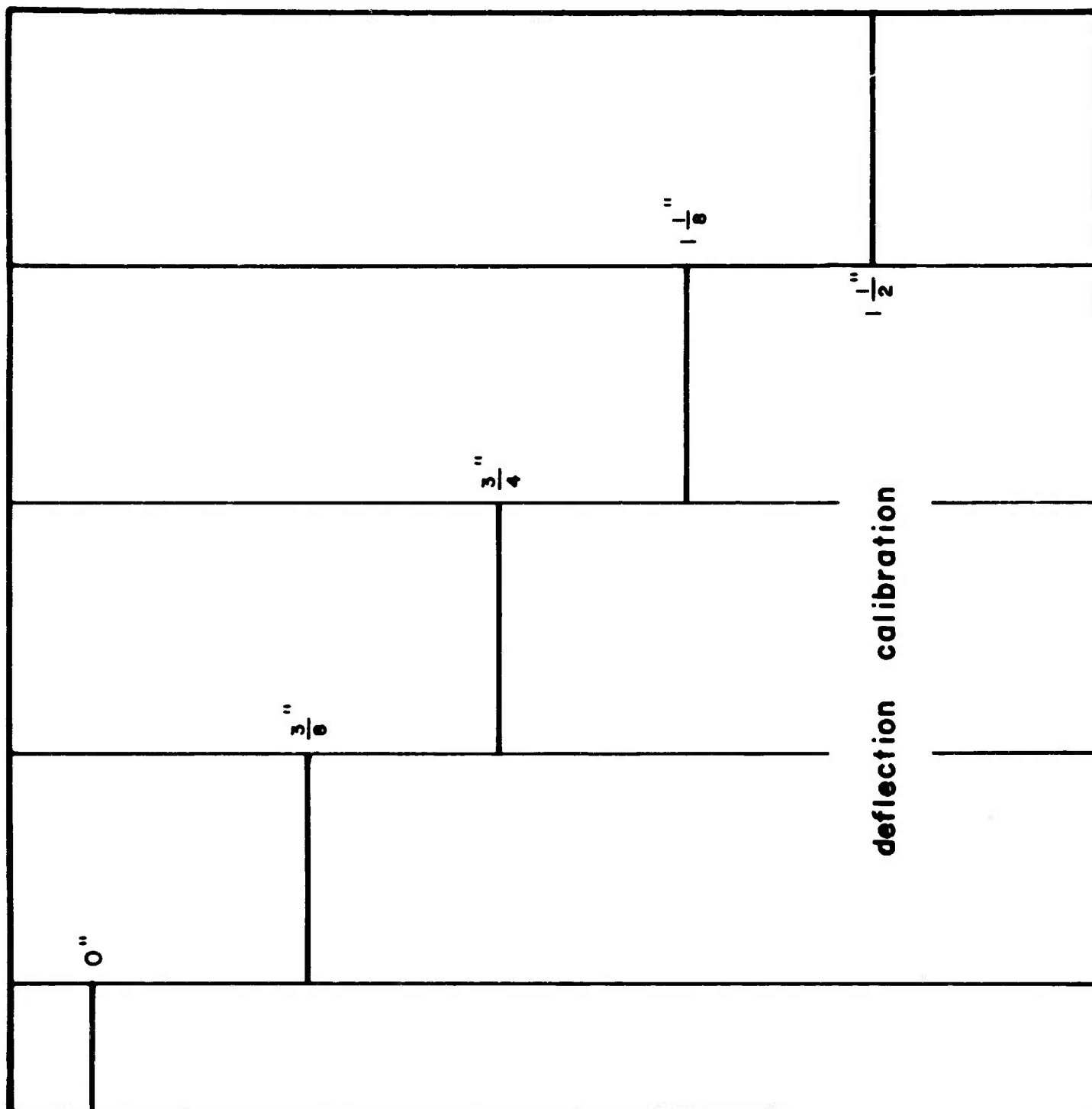


Figure 4.7a. Calibration Marks for the Deflection Trace on the Oscillograph Tape of Test No. 39.

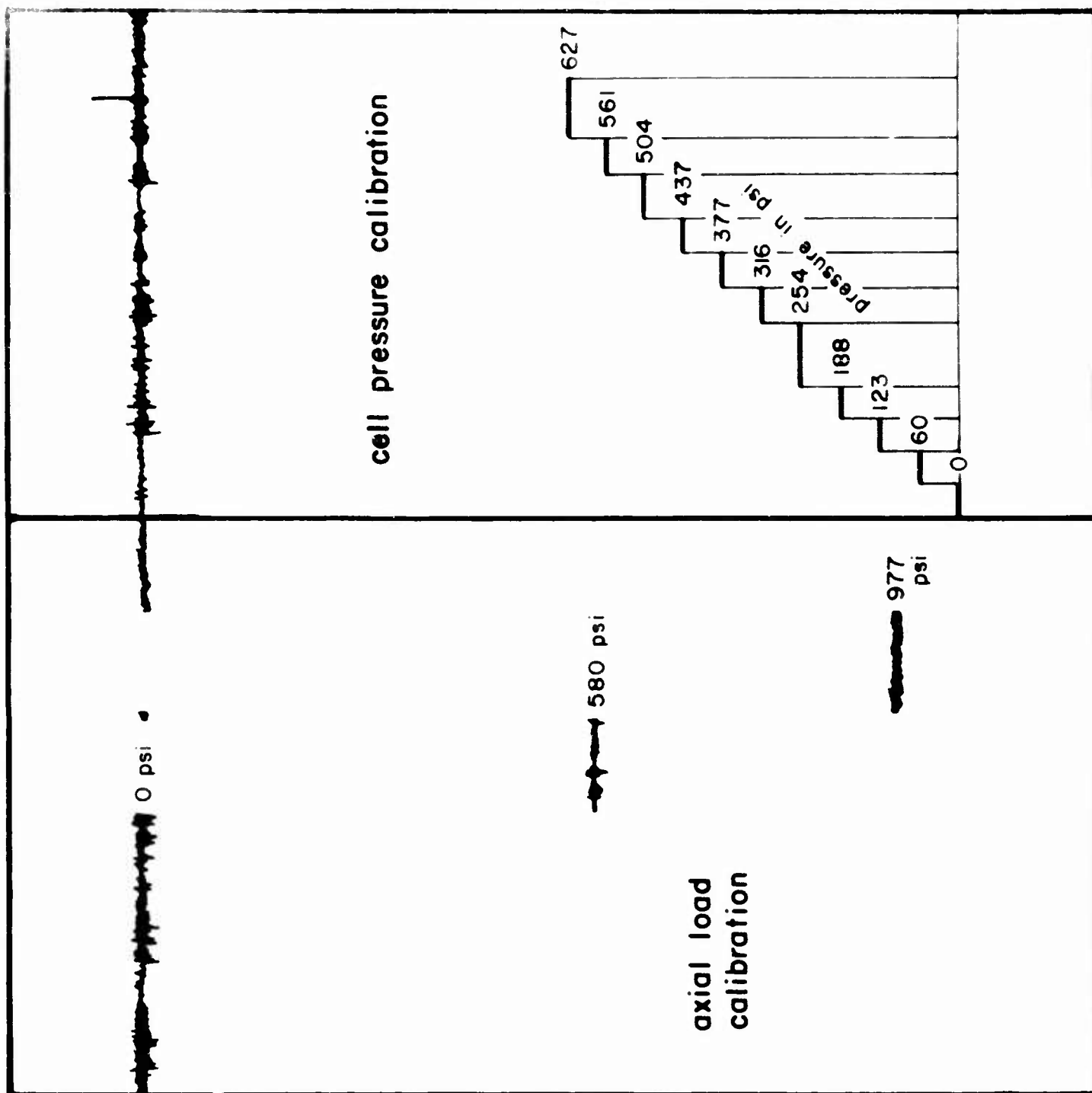


Figure 4.7b. Calibration Marks for the Axial Load and Cell Pressure Traces on the Oscilloscope Tape of Test No. 39.

AF 5535

DATA REDUCTION FORM

TRIAXIAL STRESS-STRAIN DATA

Test No. 49Date 8-1-63Operator Madden, L. O.Deformation: $C = \underline{.307}$ "sample/"tape, $\epsilon = \underline{10.22}$ %/"tapeStress Difference: $C = \underline{210}$ psi/"tape

| Time sec. | Deformation | | Stress Difference | | | | Strain % |
|--------------|--------------|------------|-------------------|------------|----------------|--------------|-------------|
| | Gross in. | Net in. | Gross in. | Net in. | Uncorr. psi | Corr. psi | |
| .000 | 4.04 | 0 | 1.87 | 0 | 0 | 0 | 0 |
| .002 | 4.03 | .01 | 2.06 | .19 | 40 | 40 | 0.1 |
| .004 | 4.00 | .04 | 2.24 | .37 | 78 | 78 | 0.4 |
| .006 | 3.99 | .05 | 2.38 | .51 | 107 | 107 | 0.5 |
| .009 | 3.96 | .08 | 2.47 | .60 | 126 | 125 | 0.8 |
| .014 | 3.94 | .10 | 2.58 | .71 | 149 | 148 | 1.0 |
| .020 | 3.88 | .16 | 2.68 | .81 | 170 | 168 | 1.6 |
| .034 | 3.78 | .26 | 2.80 | .93 | 195 | 190 | 2.7 |
| .049 | 3.69 | .35 | 2.83 | .96 | 202 | 195 | 3.6 |
| .080 | 3.63 | .41 | 2.84 | .97 | 204 | 196 | 4.2 |
| .120 | 3.59 | .45 | 2.83 | .96 | 202 | 193 | 4.6 |
| .181 | 3.56 | .48 | 2.84 | .97 | 204 | 194 | 4.9 |
| .252 | 3.55 | .49 | 2.85 | .98 | 206 | 196 | 5.0 |
| .396 | 3.51 | .53 | 2.84 | .97 | 204 | 193 | 5.4 |

seating load = $(1.76 - 1.72) 210 = 8$ psi

LVDT cal. steps 4.88 3.77 2.44 1.17 (0.30)

axial load cal. steps 0.61 3.42 5.17

FIG. 4.3 DATA REDUCTION FORM

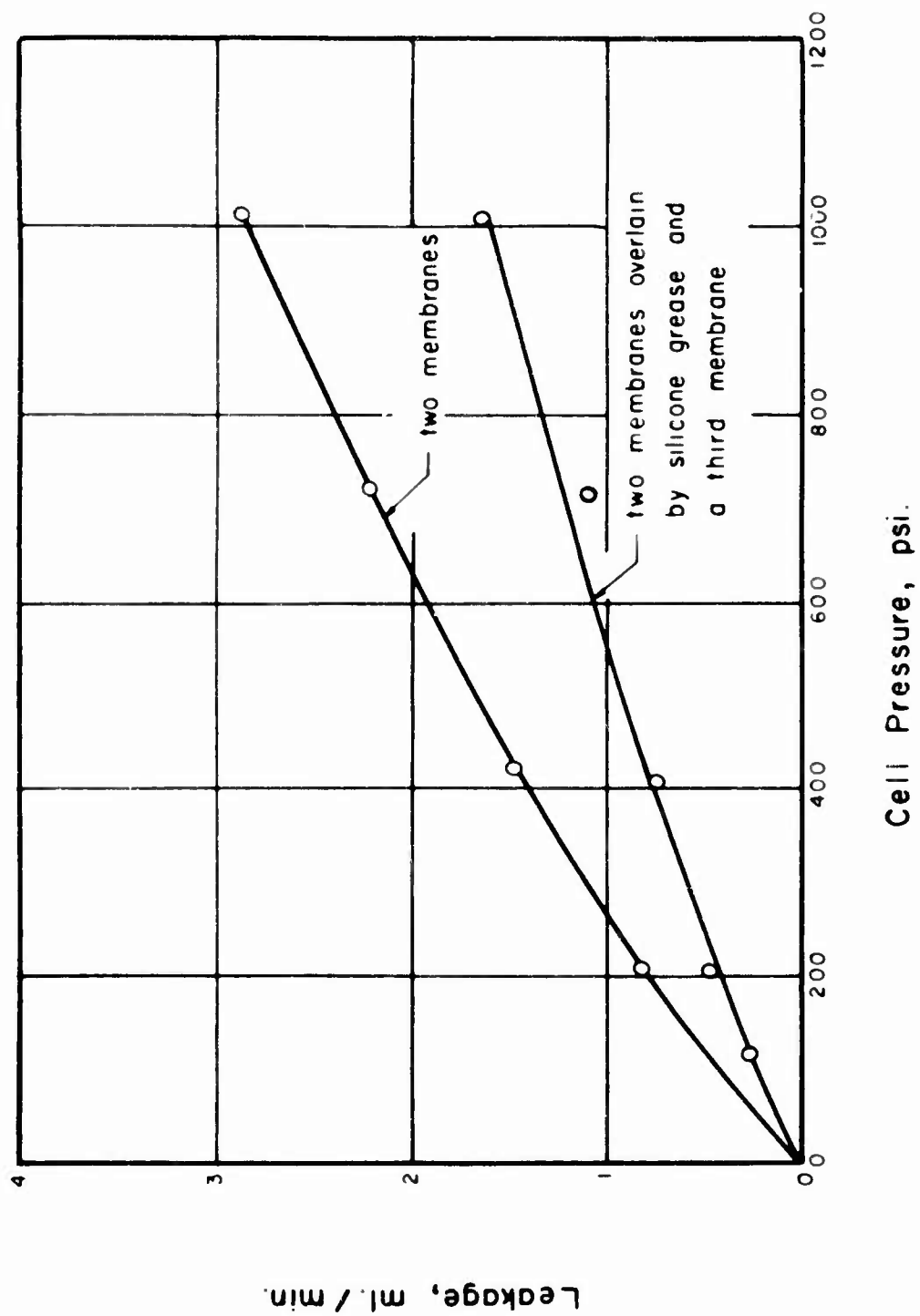


Figure 4.9. Nitrogen Leakage Through Membranes

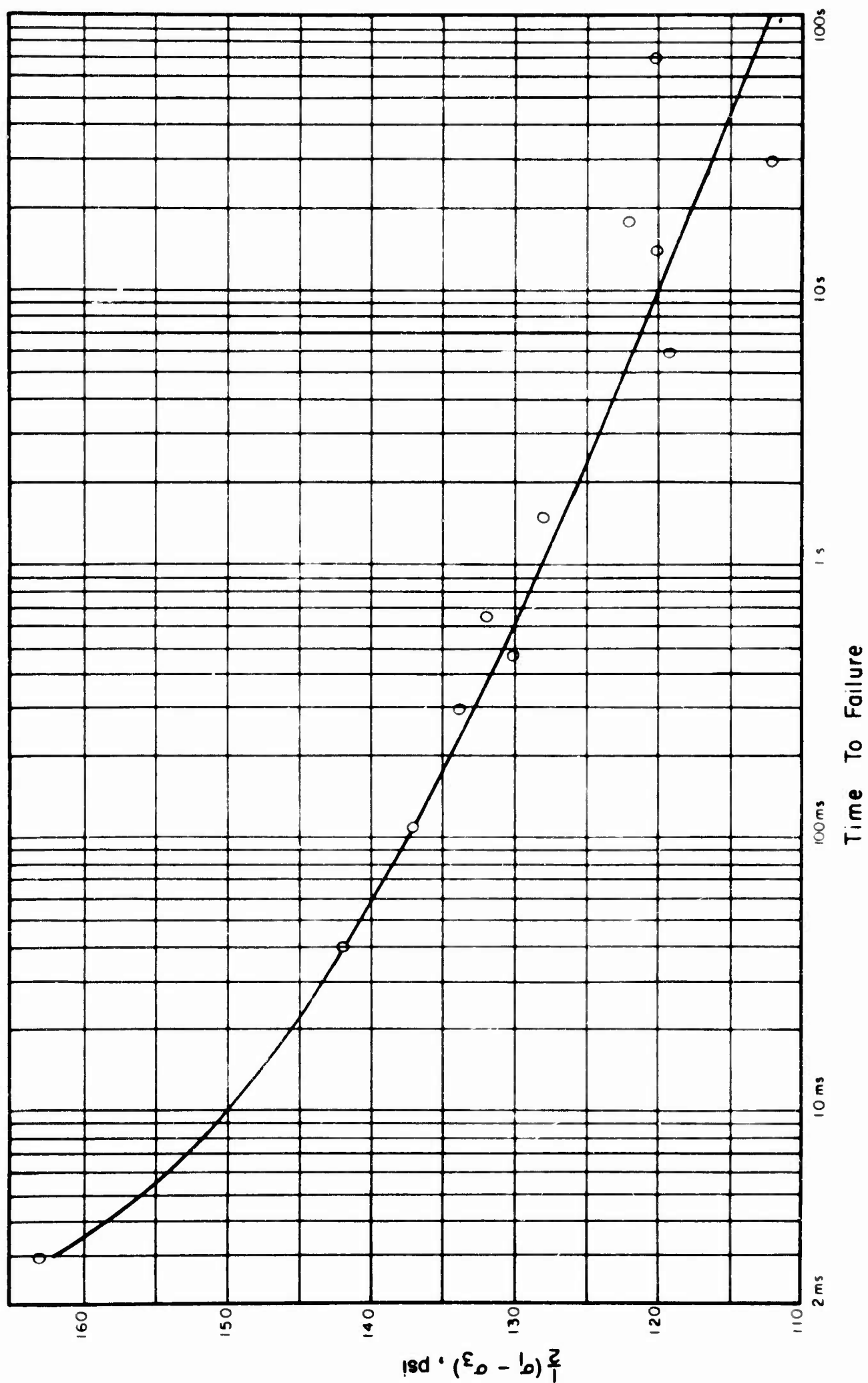


Figure 4.10. Influence Of Time To Failure On Shearing Strength, Confining Pressure – 114 psi.

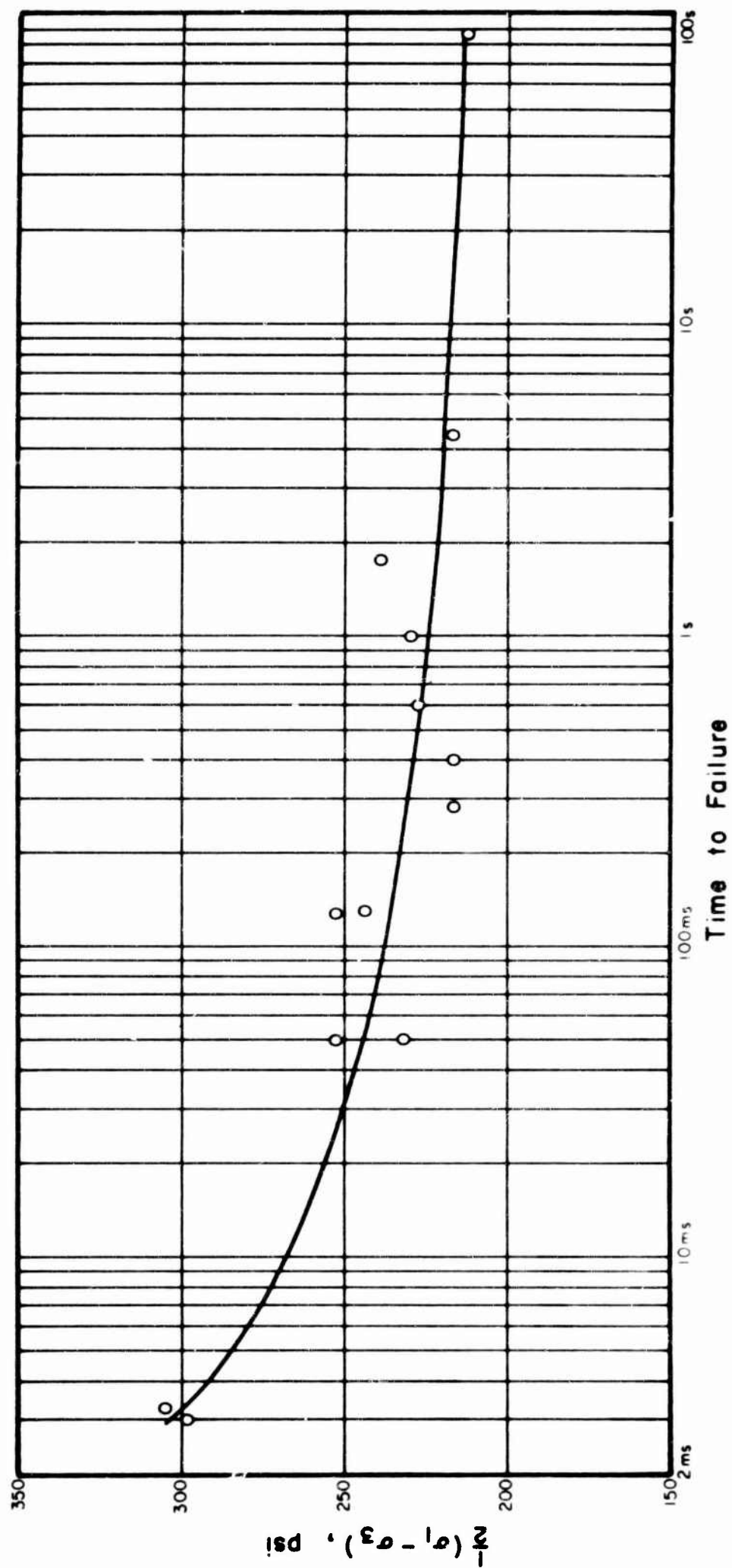


Figure 4.11. Influence of Time to Failure on Shearing Strength, Confining Pressure = 1010 psi.

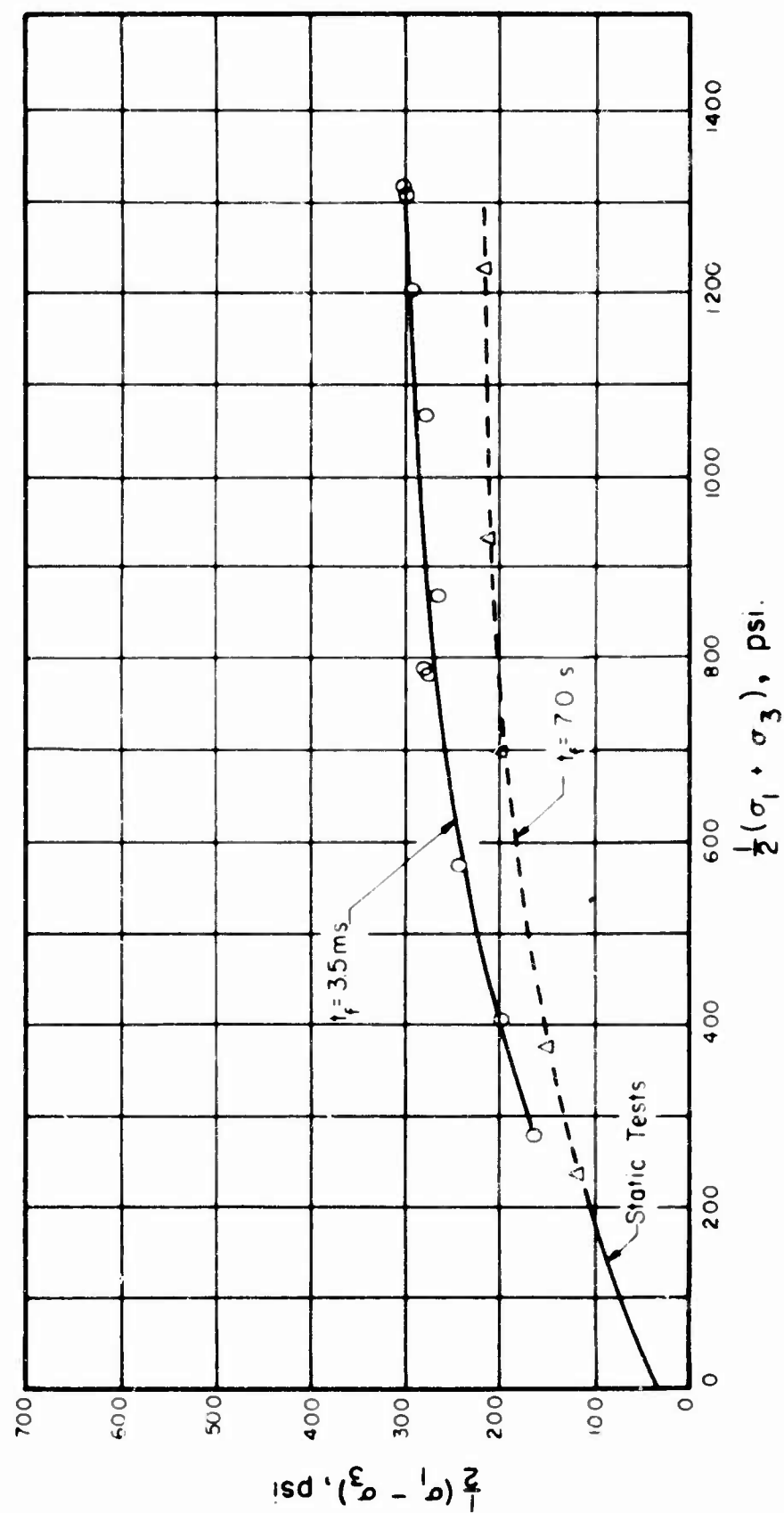


Figure 4.12. Modified Mohr - Coulomb Diagram For Dynamic Unconsolidated - Undrained Triaxial Compression Tests On Goose Lake Clay

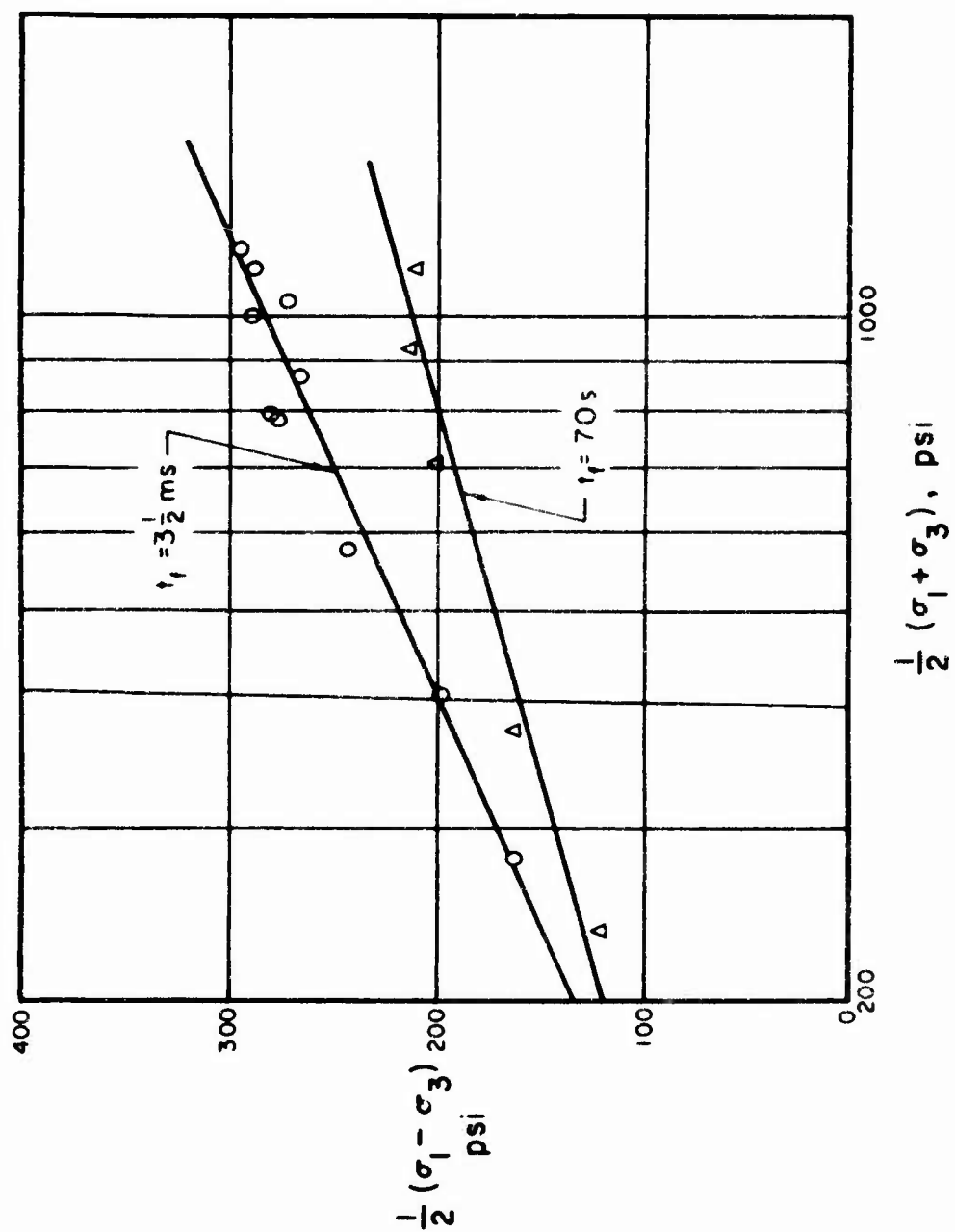


Figure 4.13 Semi-logarithmic Modified Mohr-Coulomb Diagram
For Dynamic Unconsolidated-Undrained Triaxial
Compression Tests On Goose Lake Clay

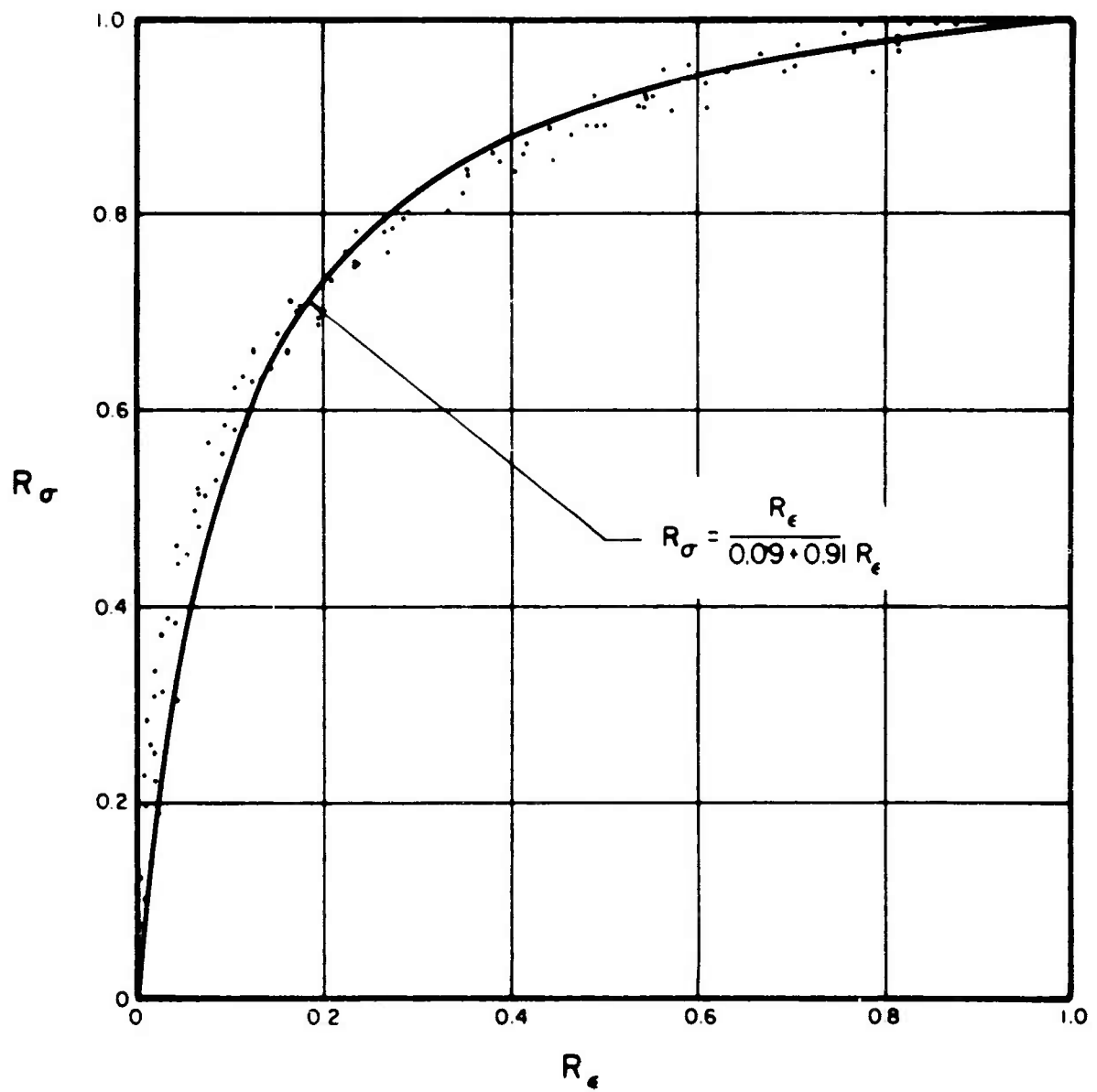


Figure 4.14. Dimensionless Stress-Strain Relationships for Triaxial Tests to Failure with $\sigma_3 = 114$ psi.

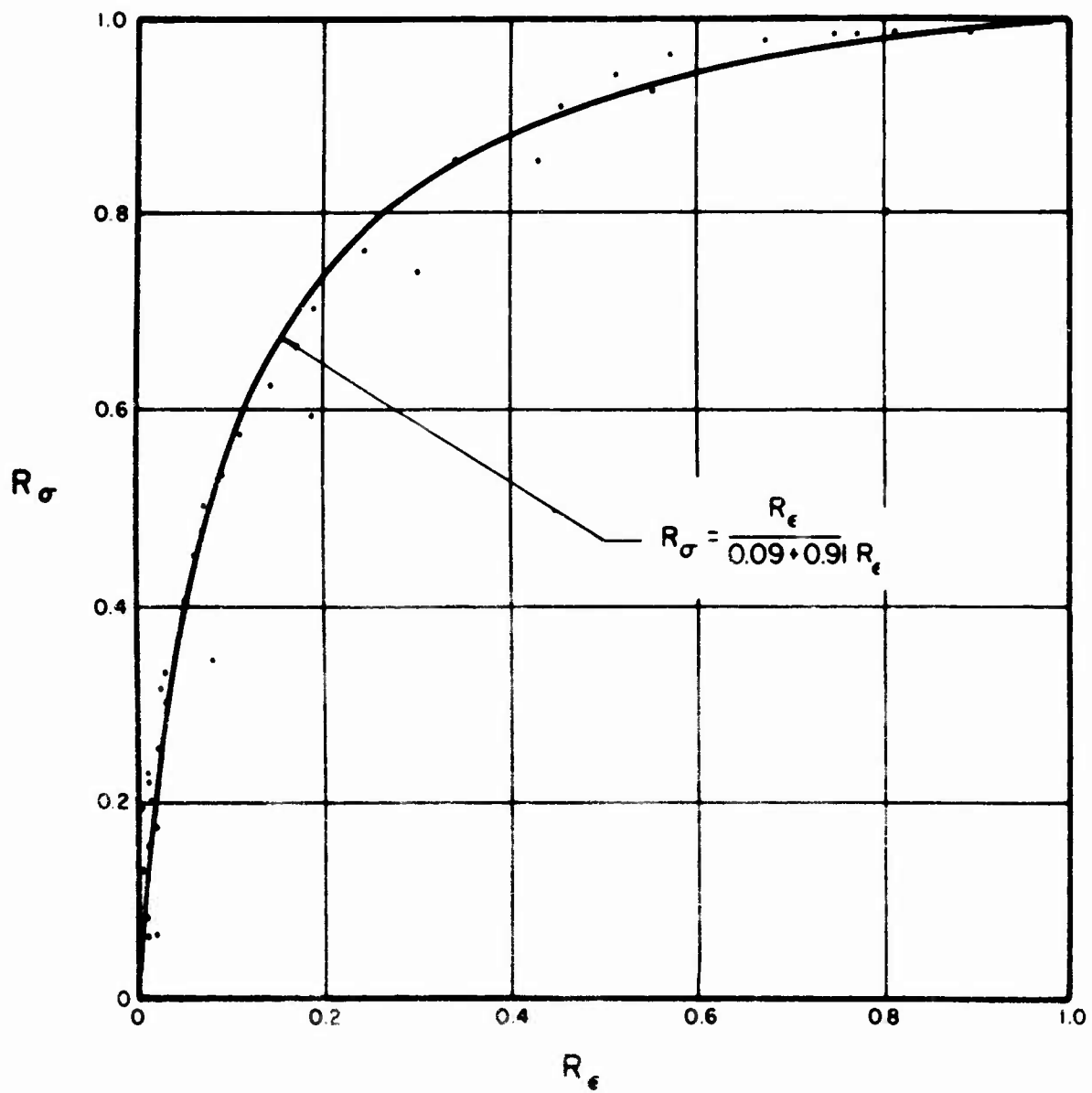


Figure 4.15. Dimensionless Stress-Strain Relationships for Tests to Failure with $\sigma_3 = 210$ psi to 328 psi.

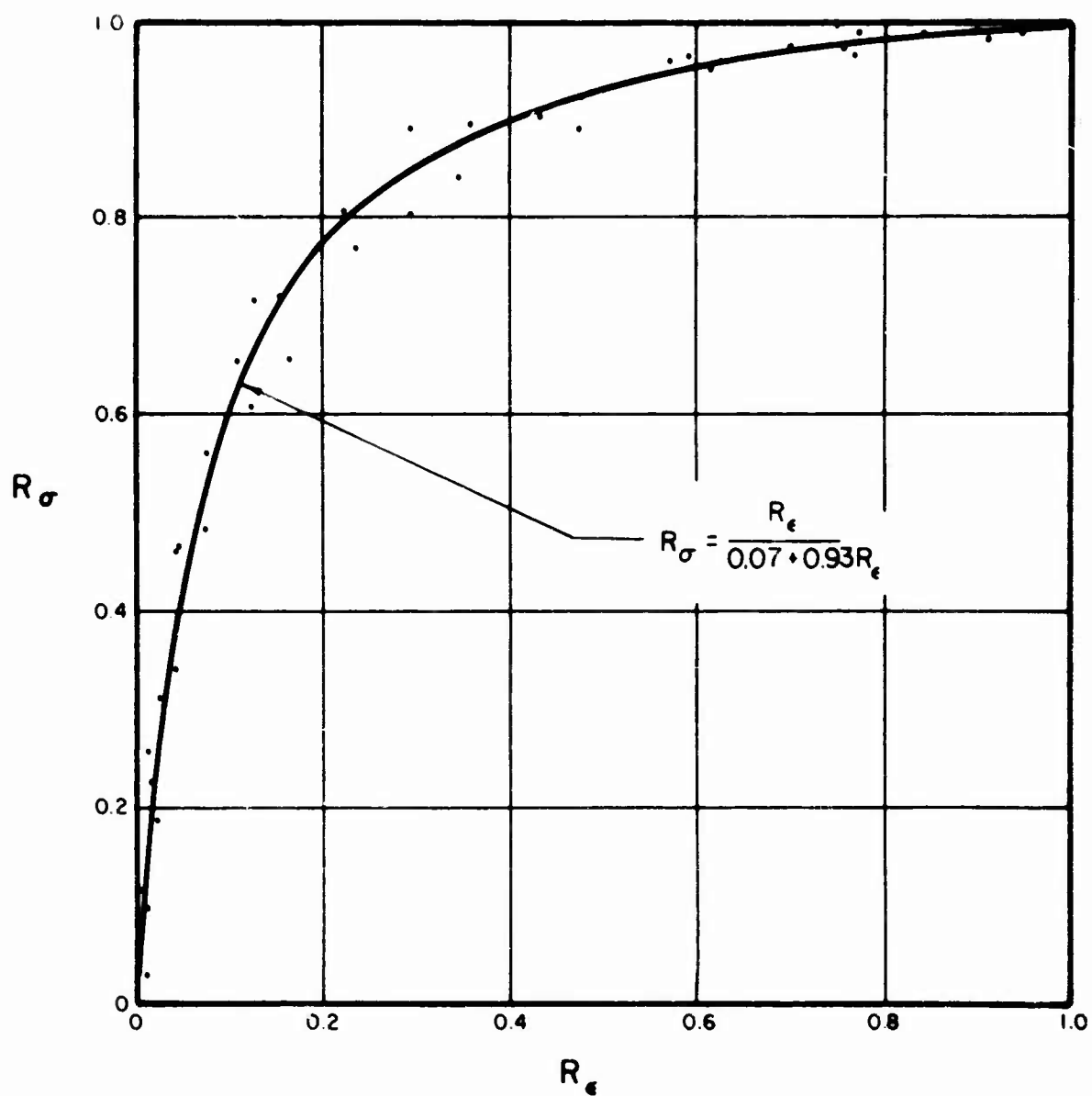


Figure 4.16. Dimensionless Stress-Strain Relationship for Tests to Failure with $\sigma_3 = 498$ psi.

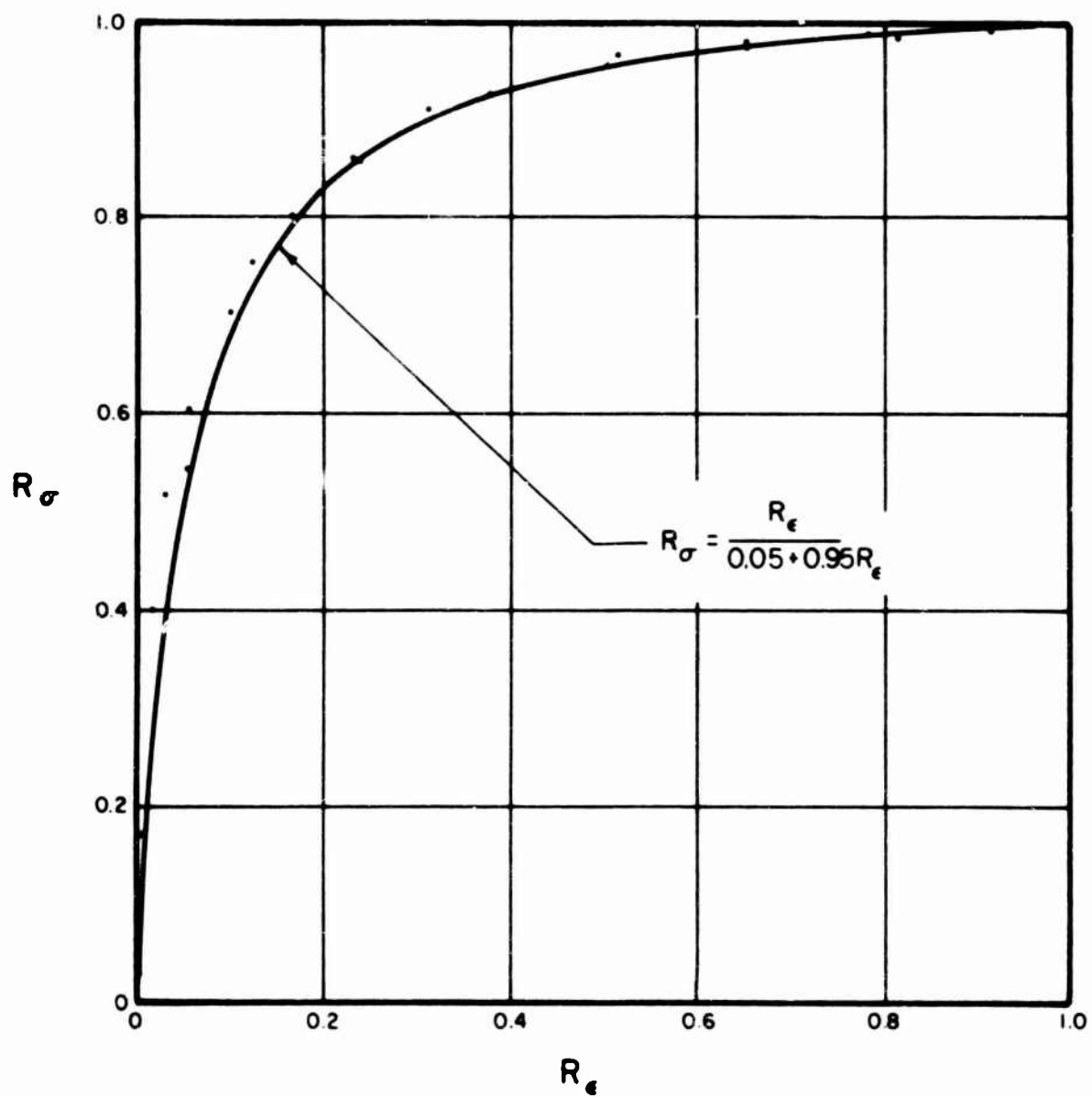


Figure 4.17. Dimensionless Stress-Strain Relationships for Tests to Failure with $\sigma_3 = 705$ psi & 735 psi.

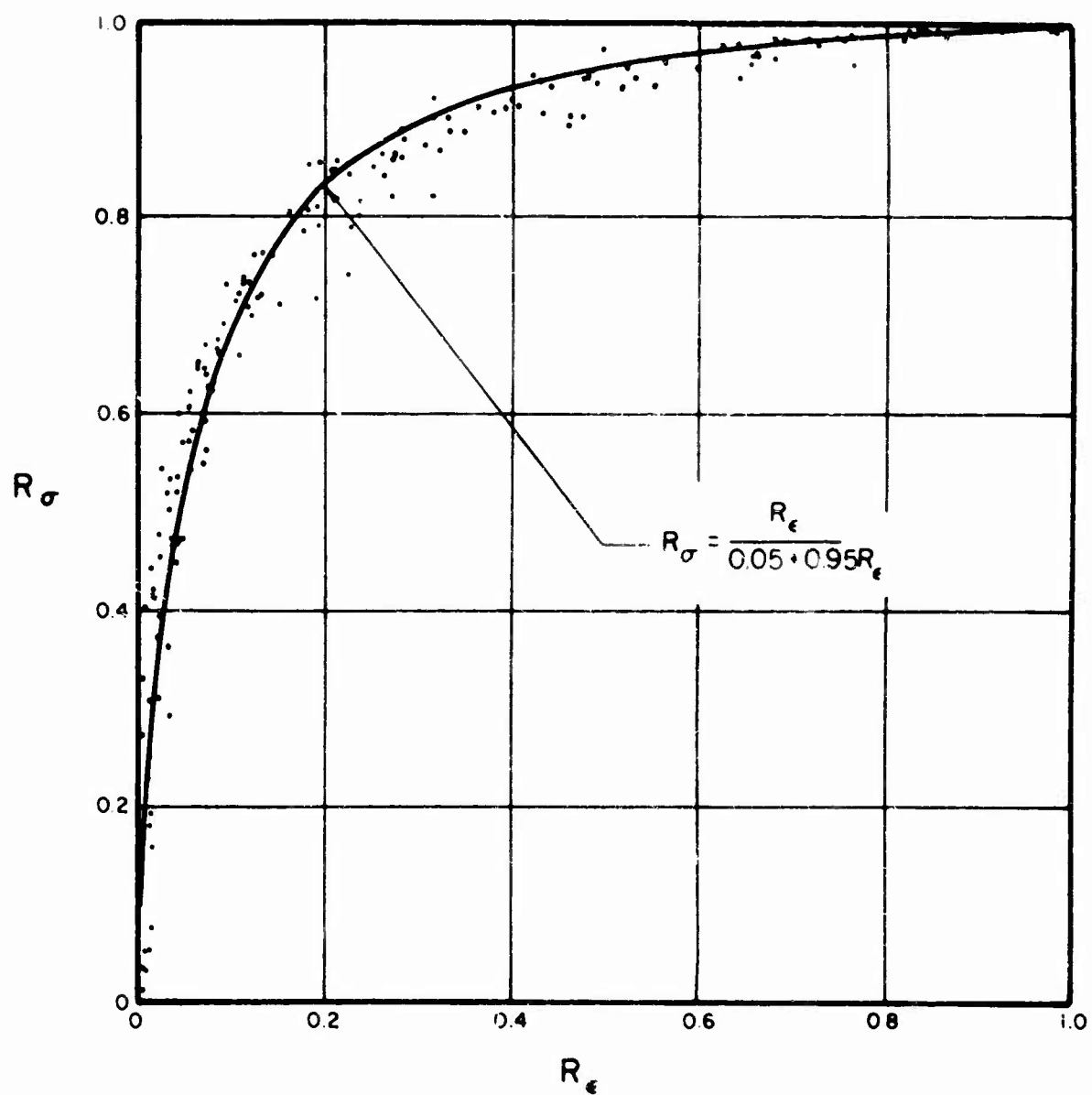


Figure 4.18 . Dimensionless Stress-Strain Relationships for Tests to Failure with $\sigma_3 = 1010$ psi.

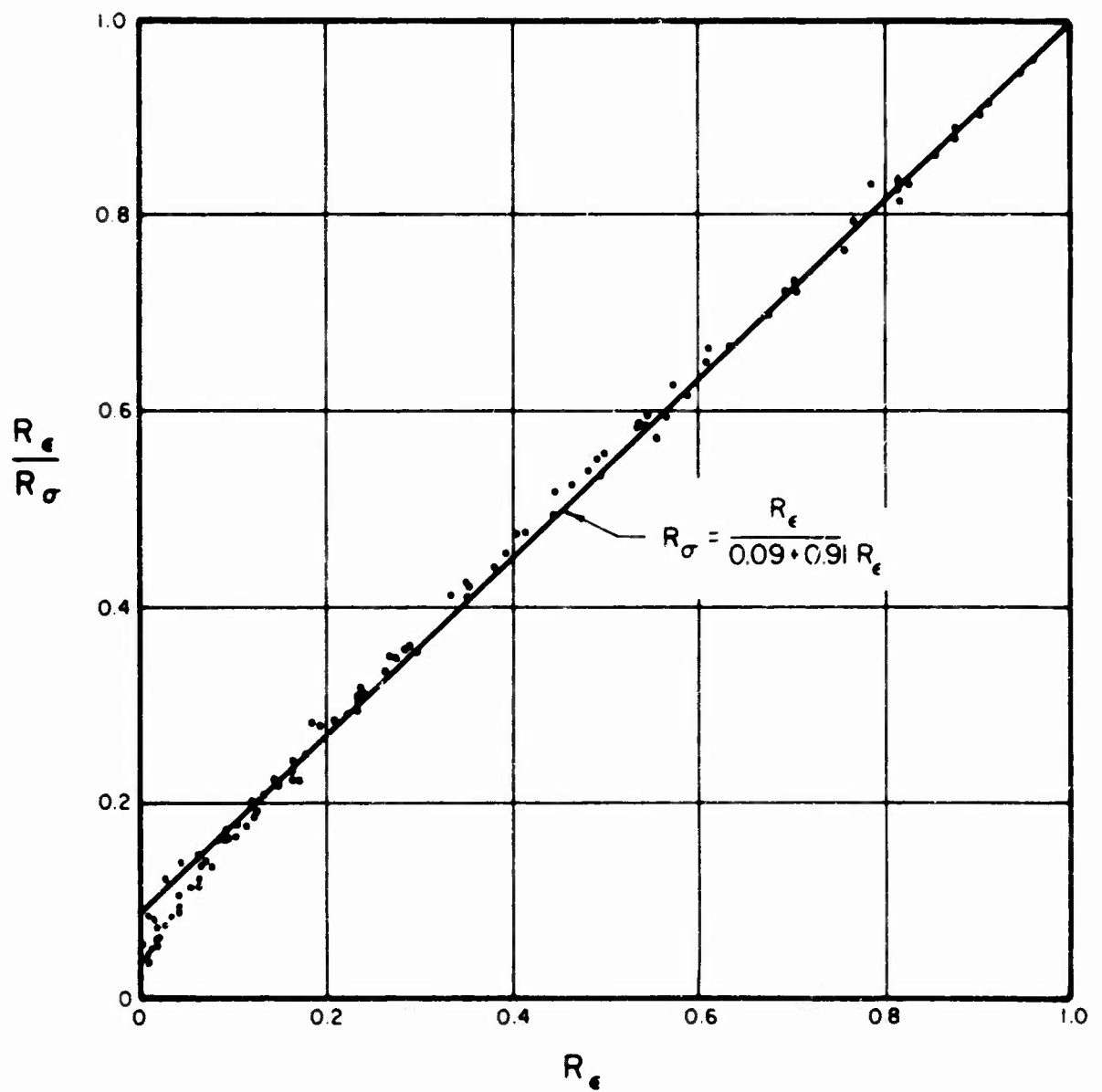


Figure 4.19. Hyperbolic Curve-Fitting Diagram for Tests to Failure with $\sigma_3 = 114$ psi.

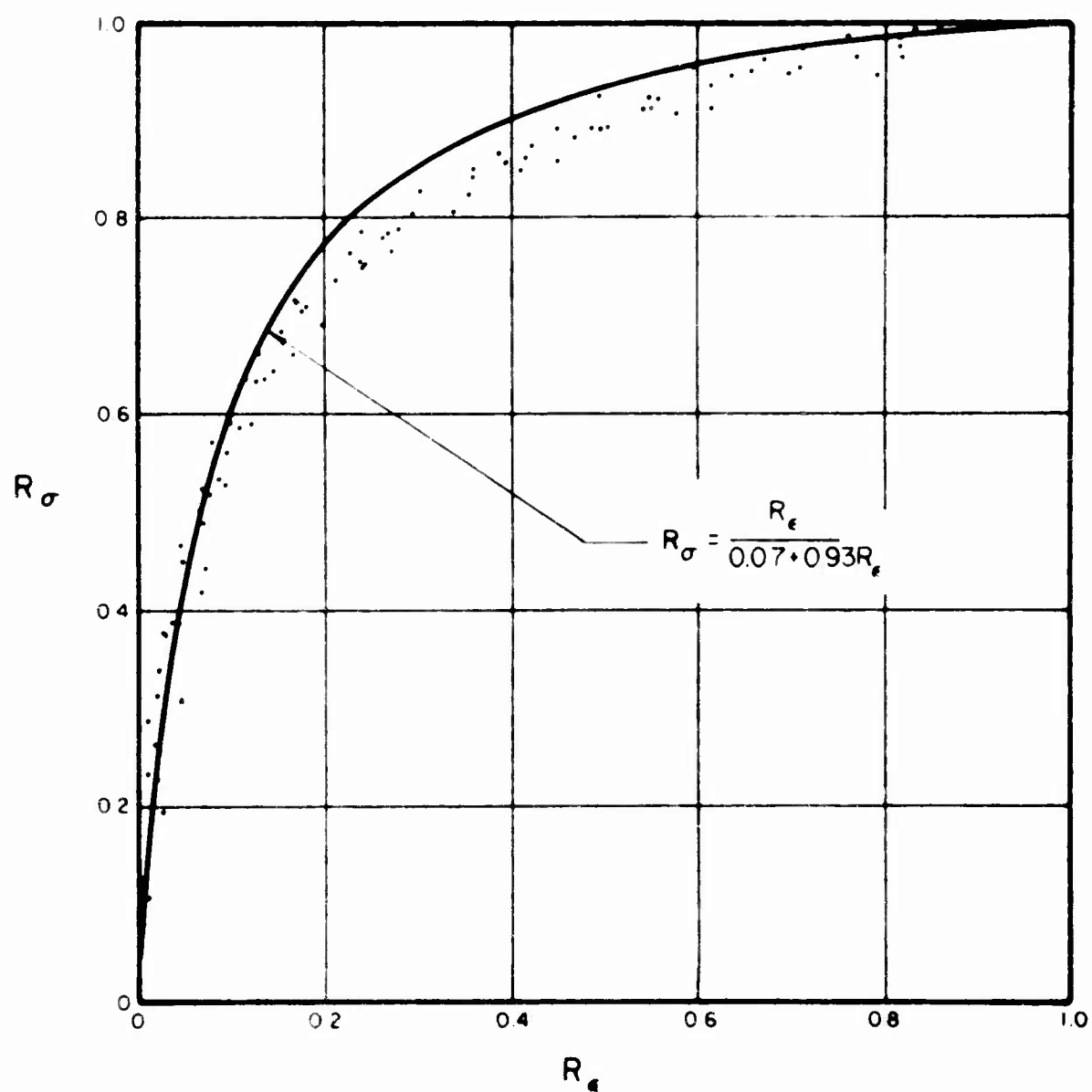


Figure 4.20. Alternate Hyperbolic Stress-Strain Curve for Tests to Failure with $\sigma_3 = 114$ psi.

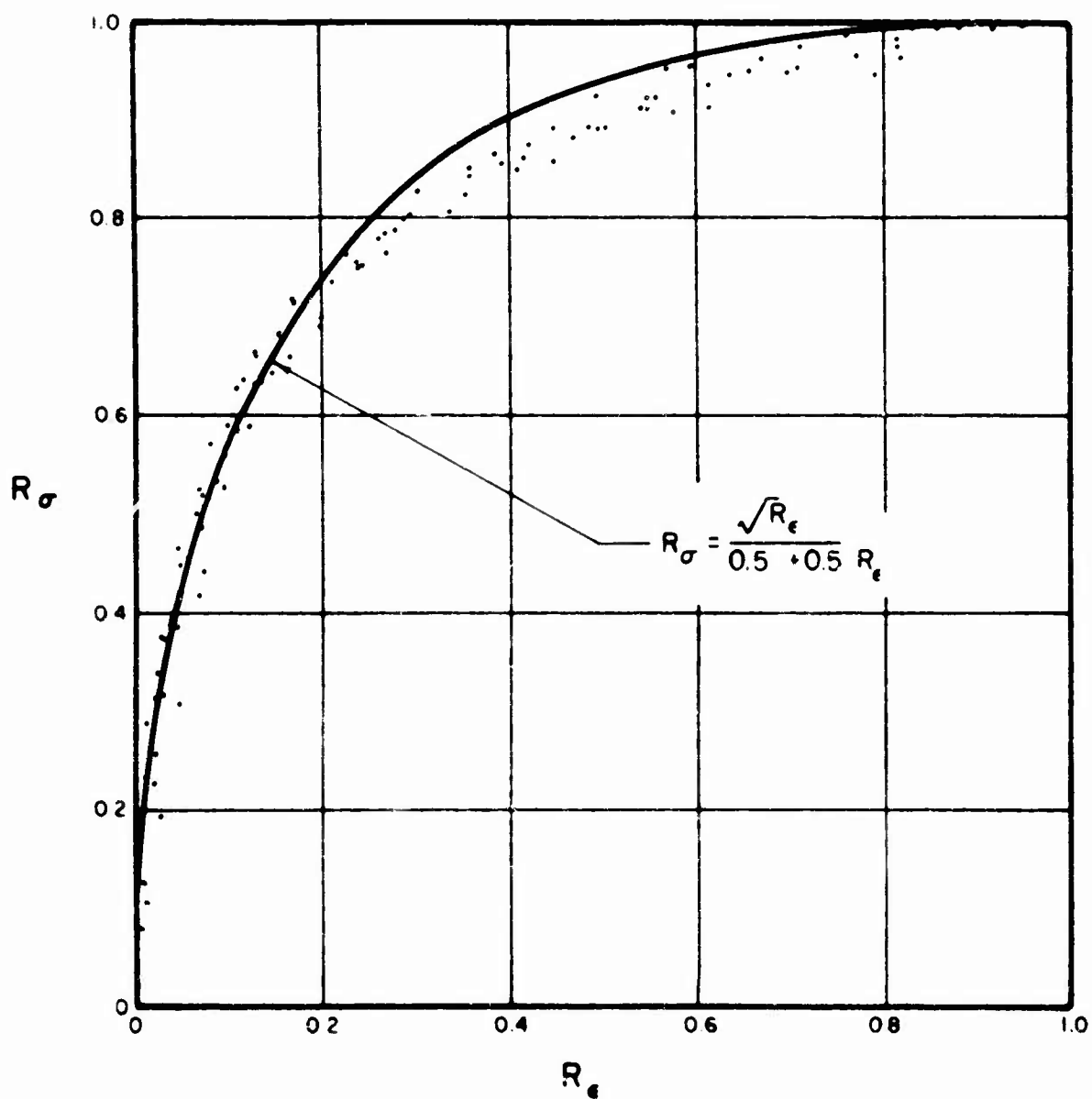


Figure 4.21. Parabolic Stress-Strain Curve for Tests to Failure with $\sigma_3 = 114$ psi.

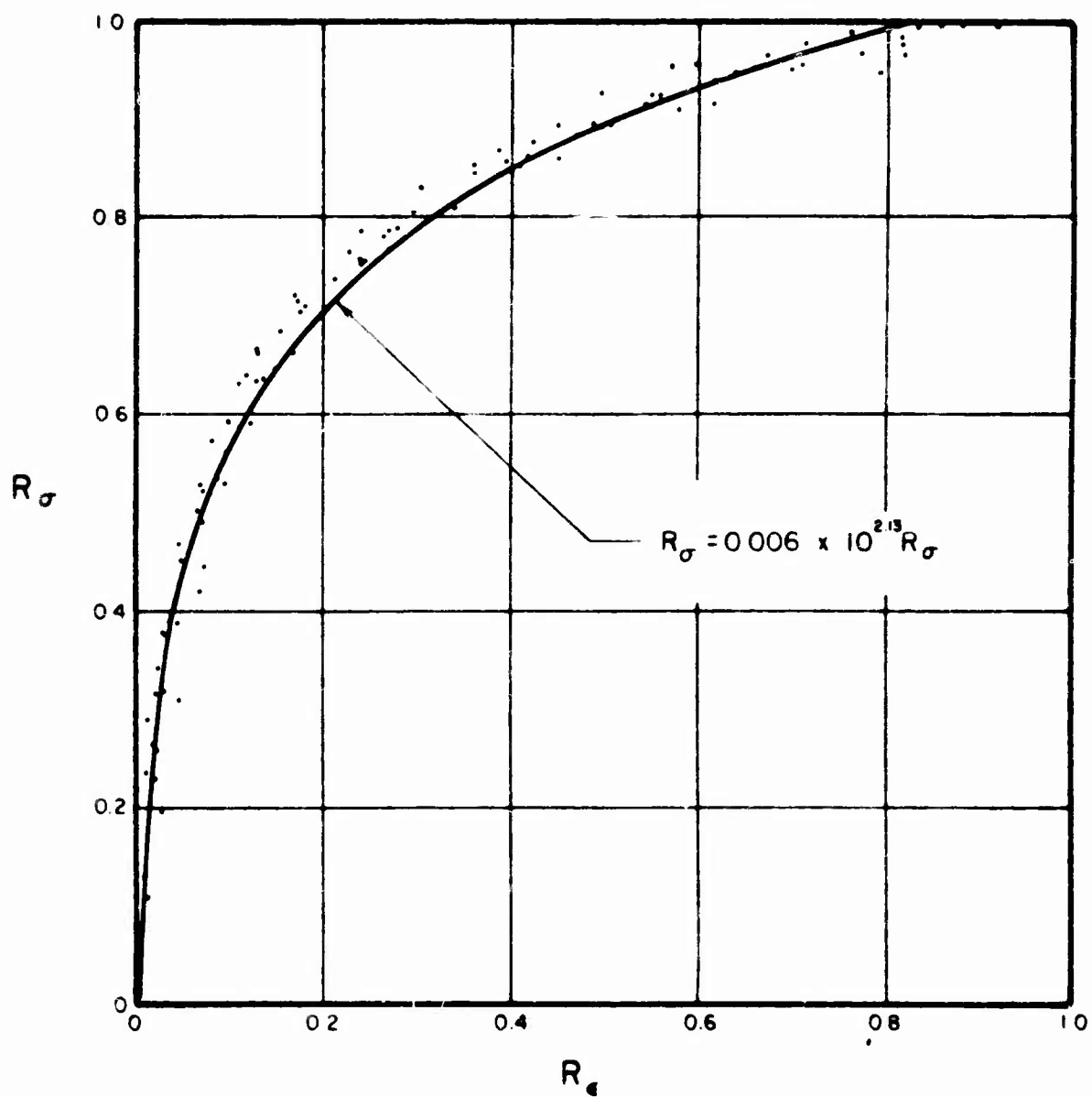


Figure 4.22. Logarithmic Stress-Strain Curve for Tests to Failure with $\sigma_3 = 114$ psi .

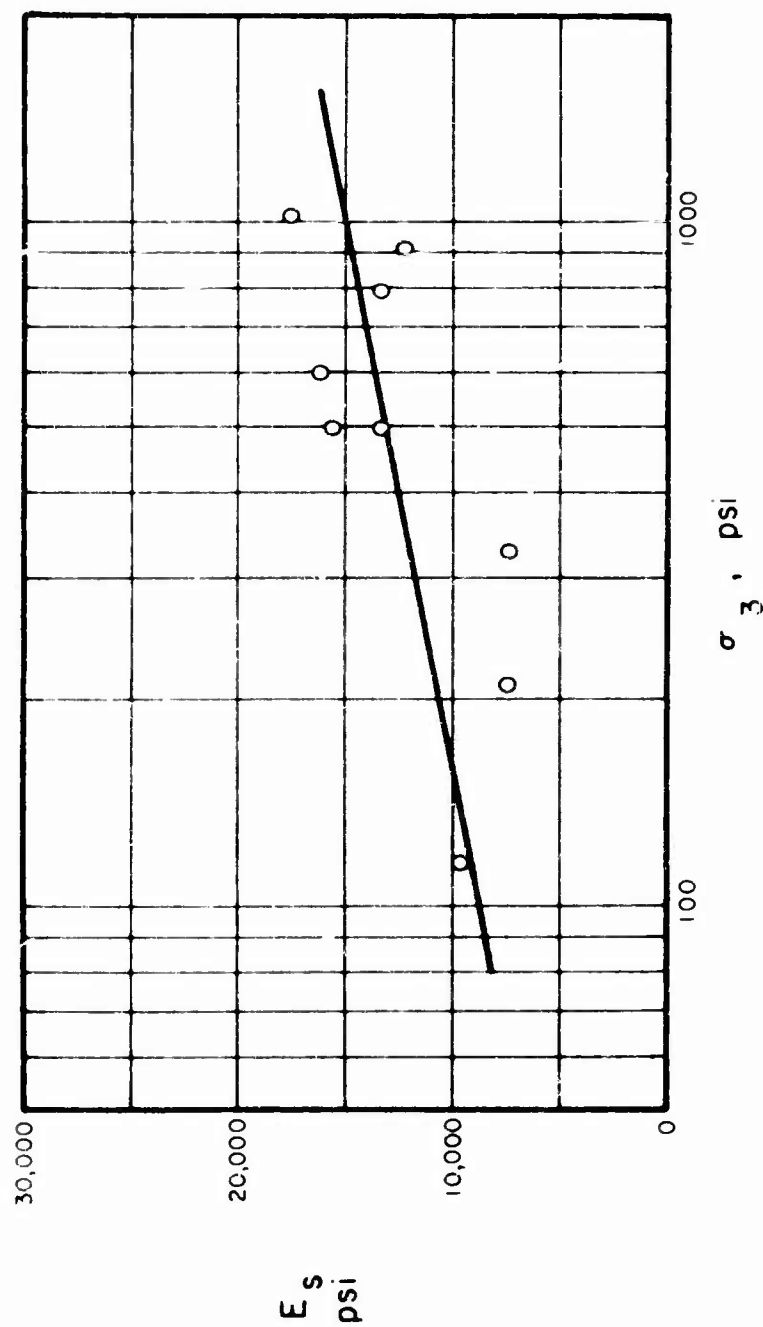


Figure 4.24. Influence of Confining Pressure on the Secant Modulus Defined at Half the Failure Stress for Tests with Times to Failure of 3 to 4 Milliseconds.

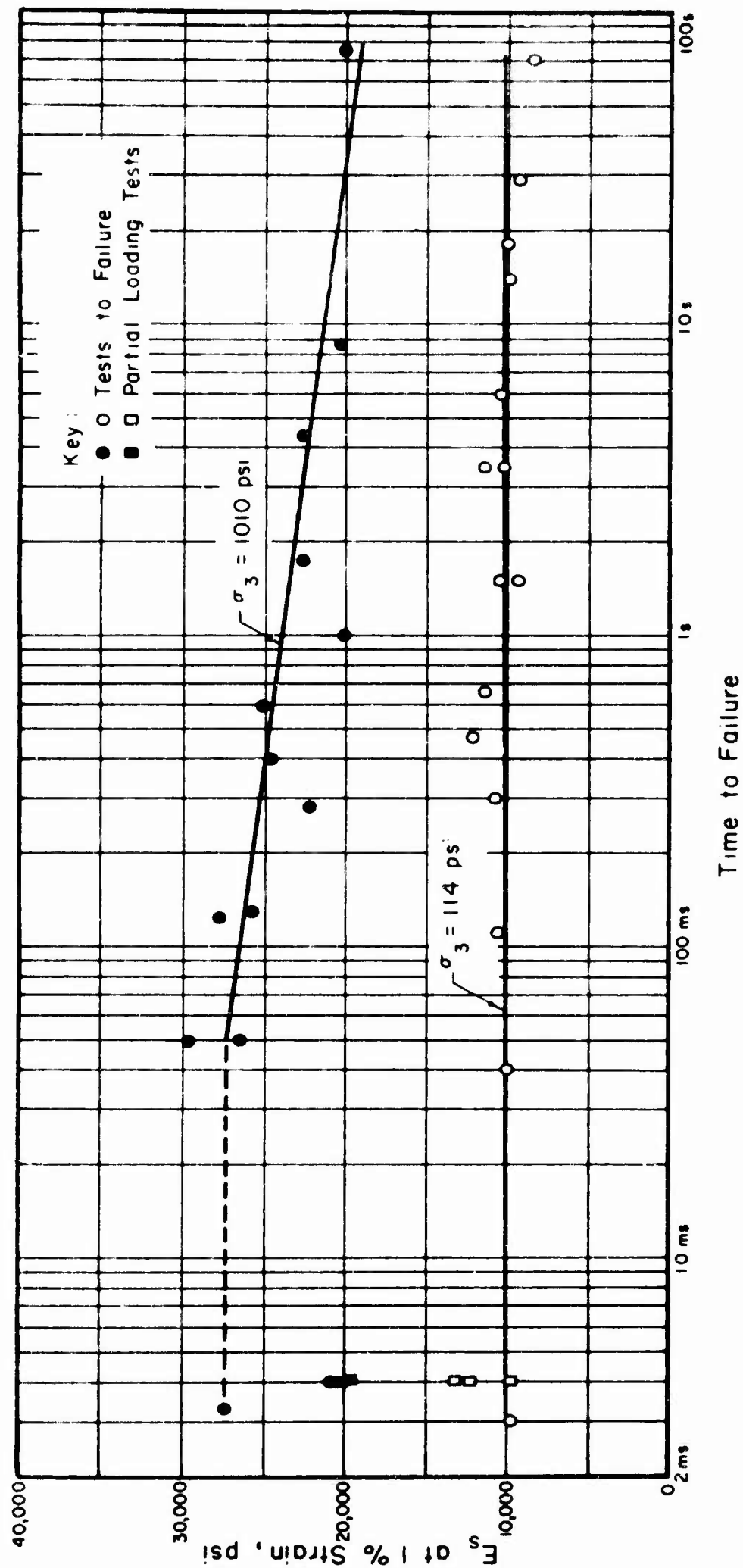


Figure 4.25. Influence of the Rate of Deformation on the Secant Modulus Defined at 1 % Strain in Tests at Confining Pressure of 114 psi and 1010 psi .

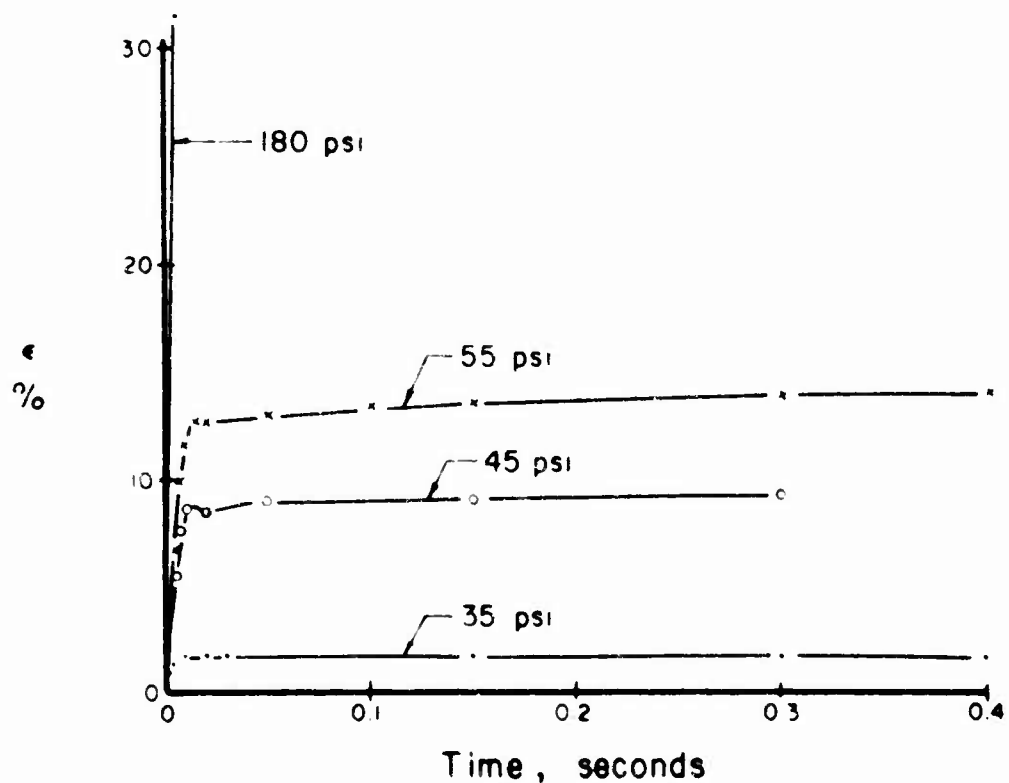
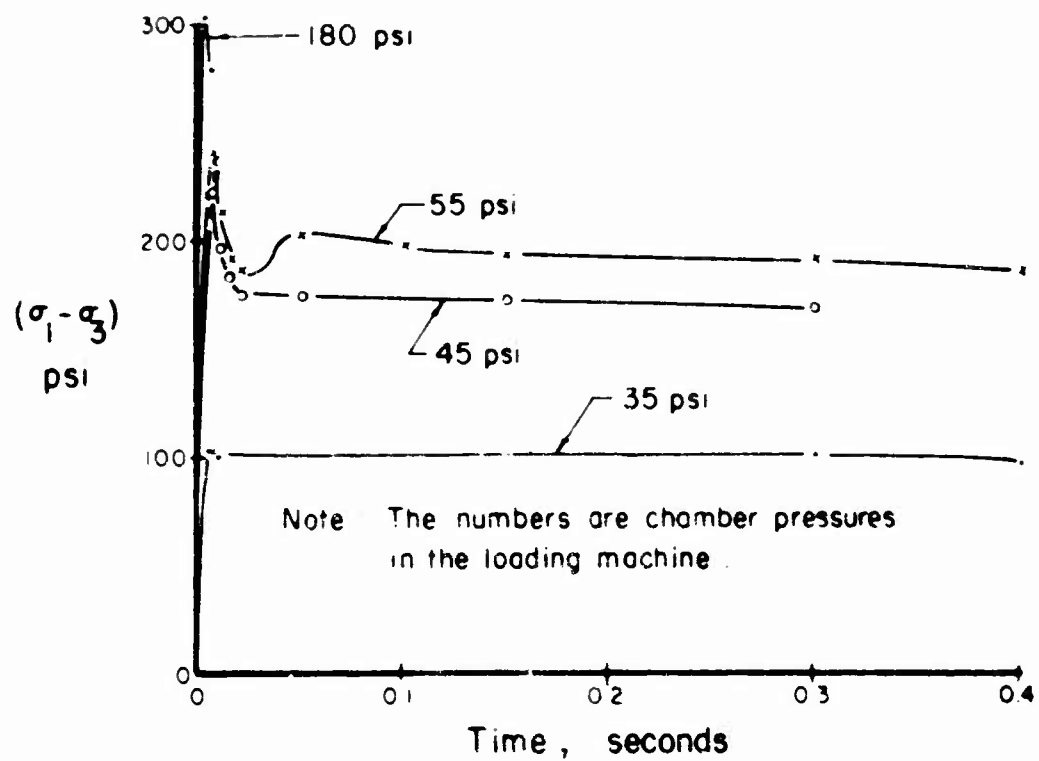


Figure 4.26. "Dynamic" Triaxial Compression Tests at a Cell Pressure of 117 psi.

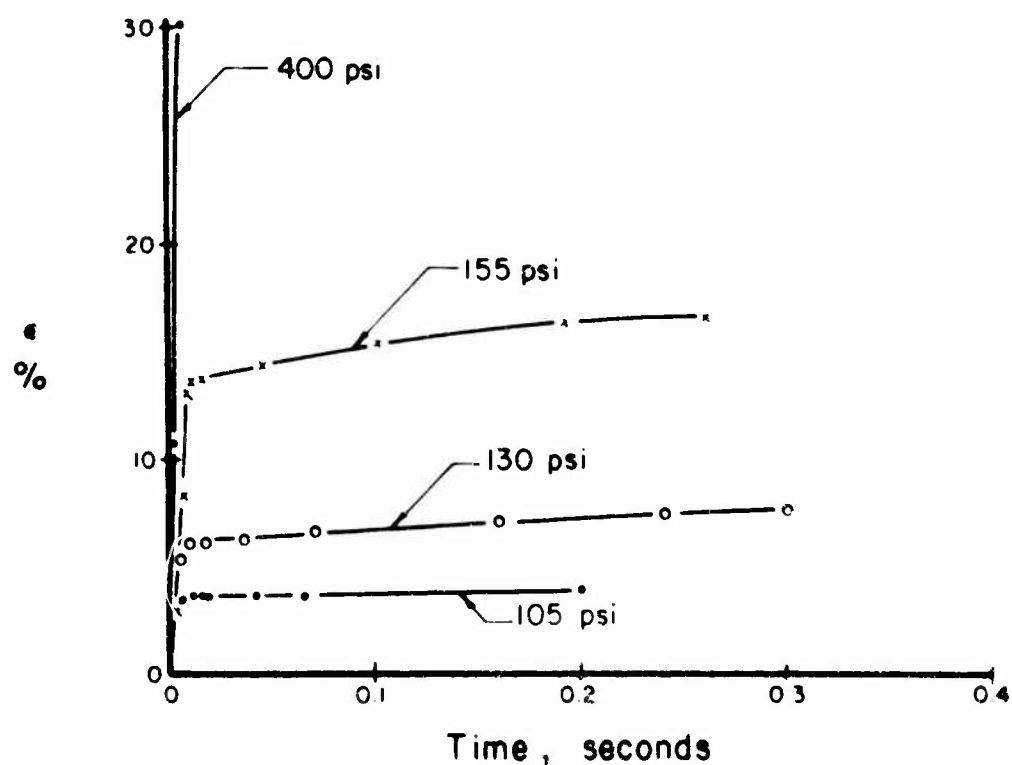
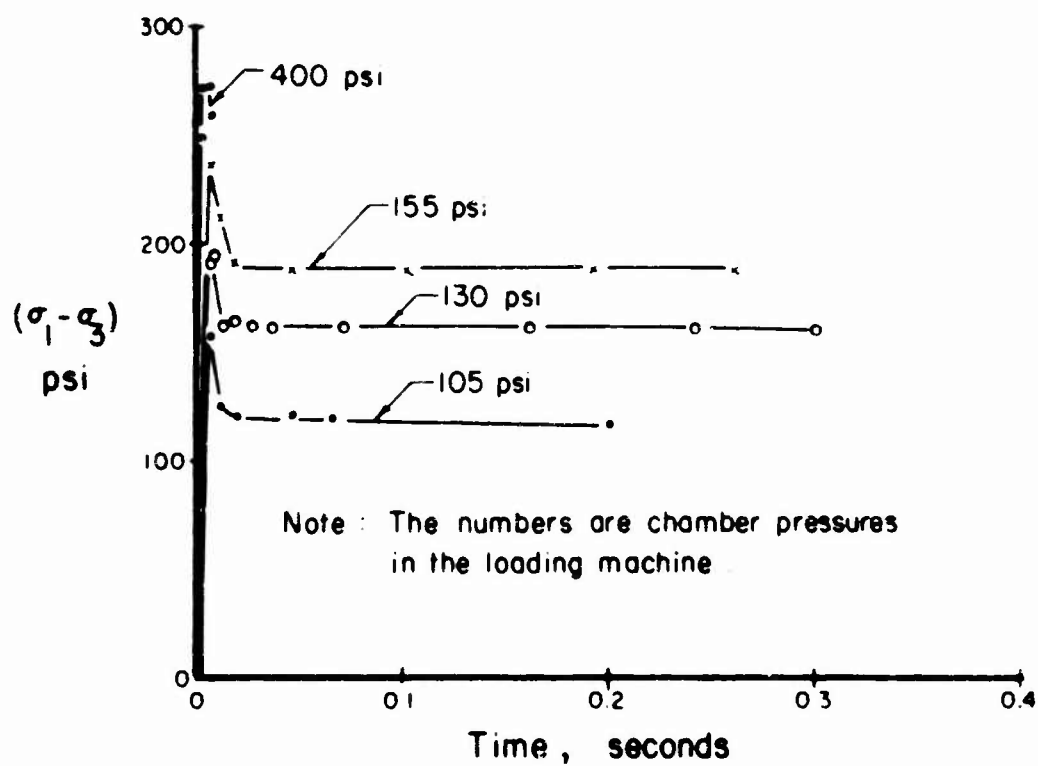


Figure 4.27. "Dynamic" Triaxial Compression Tests at a Cell Pressure of 1010 psi.

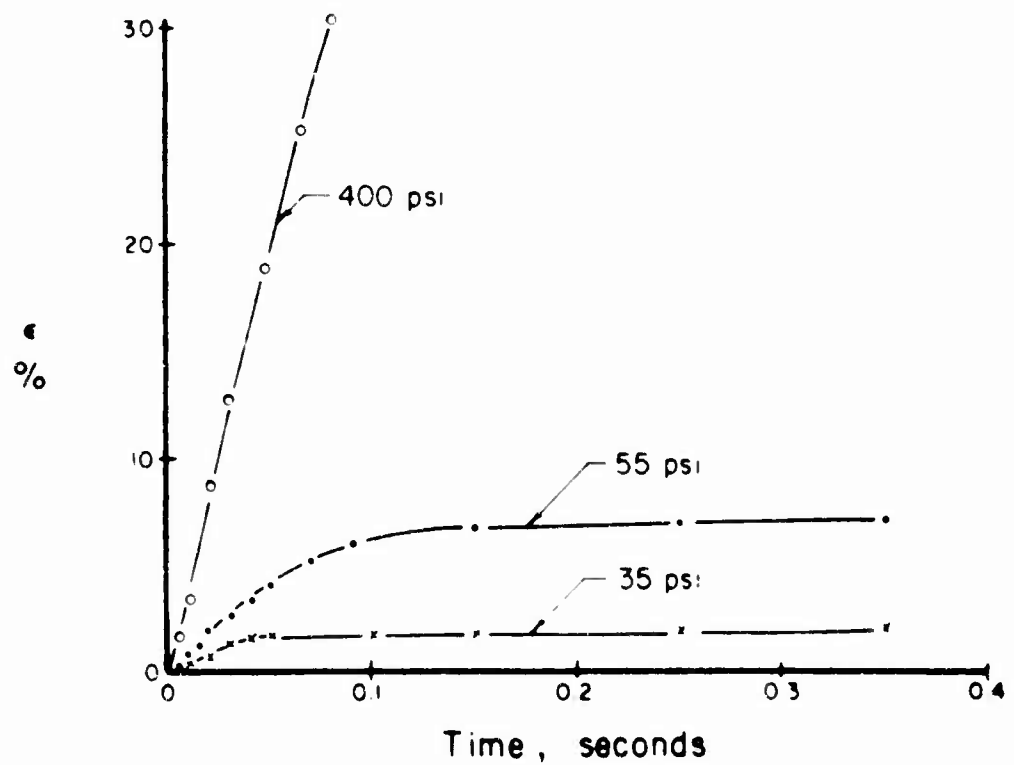
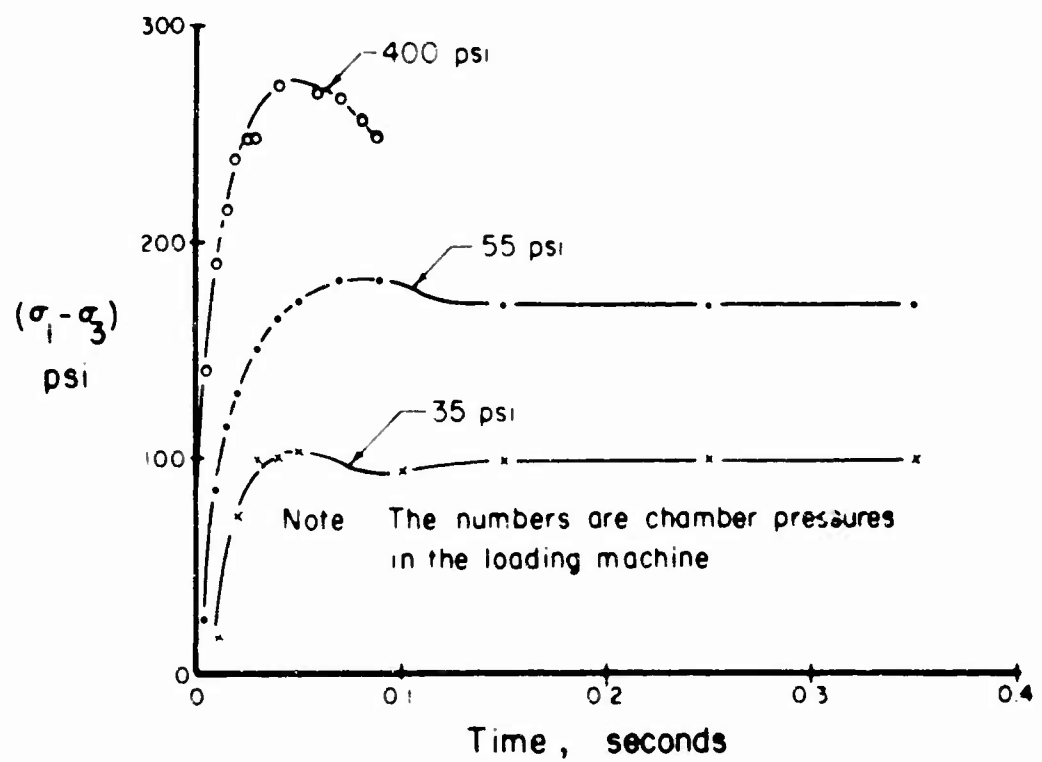


Figure 4.28. Triaxial Compression Tests at a Cell Pressure of 117 psi. and an Oil Valve Setting of 10.

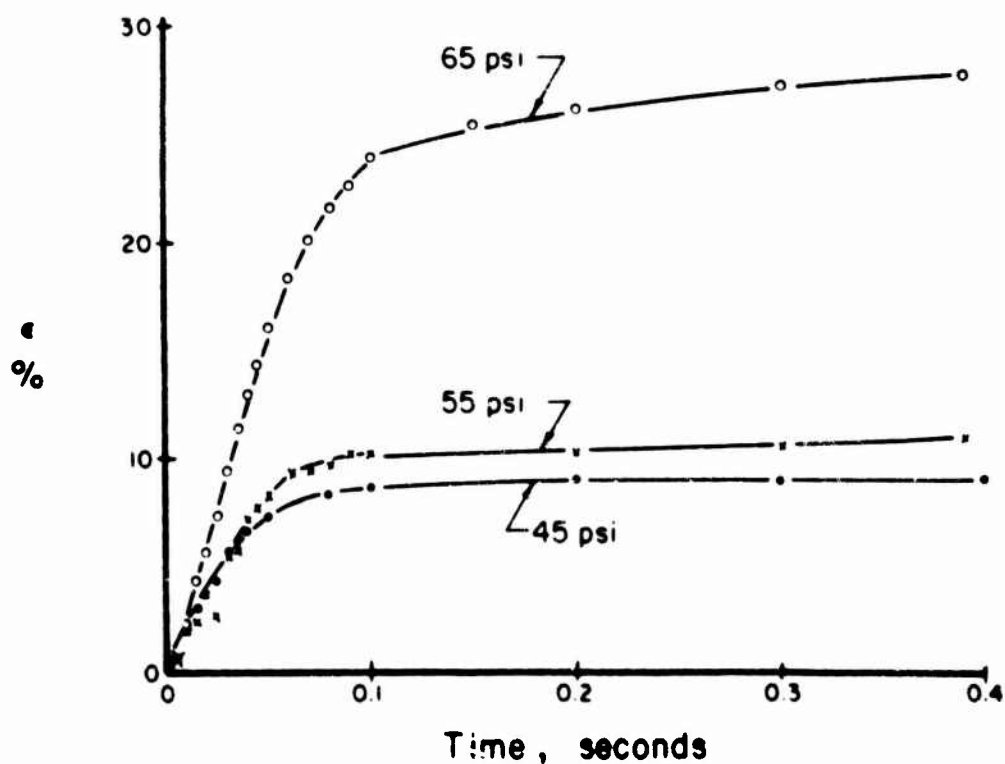
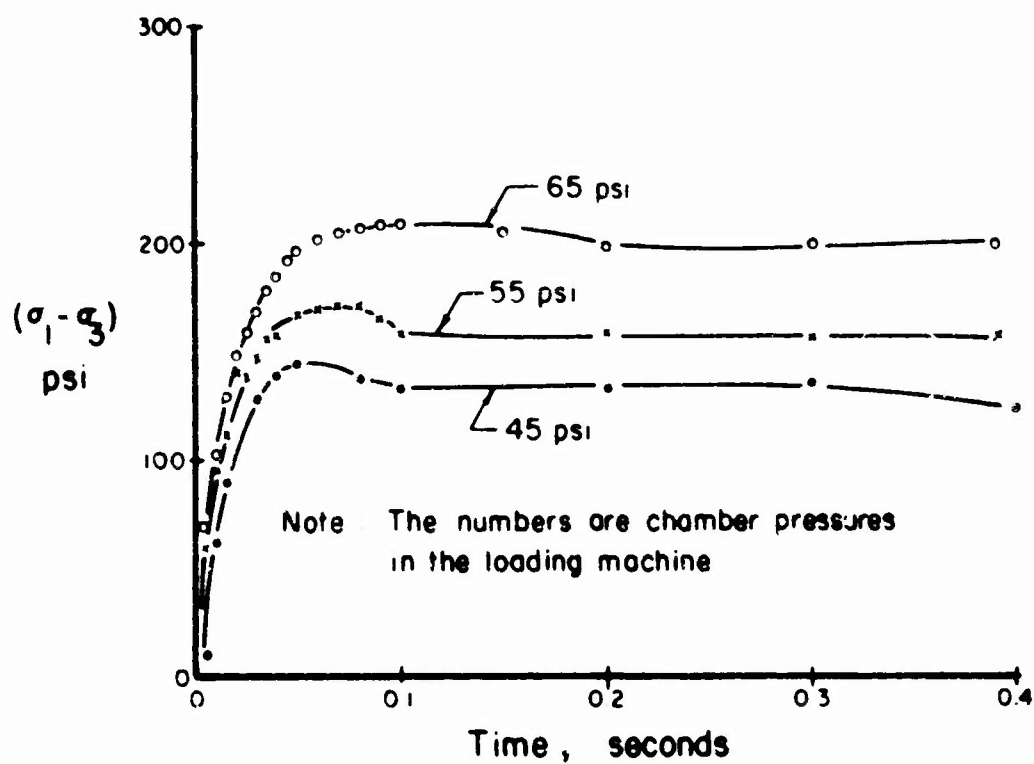


Figure 4.29. Triaxial Compression Tests at a Cell Pressure of 208 psi. and an Oil Valve Setting of 10.

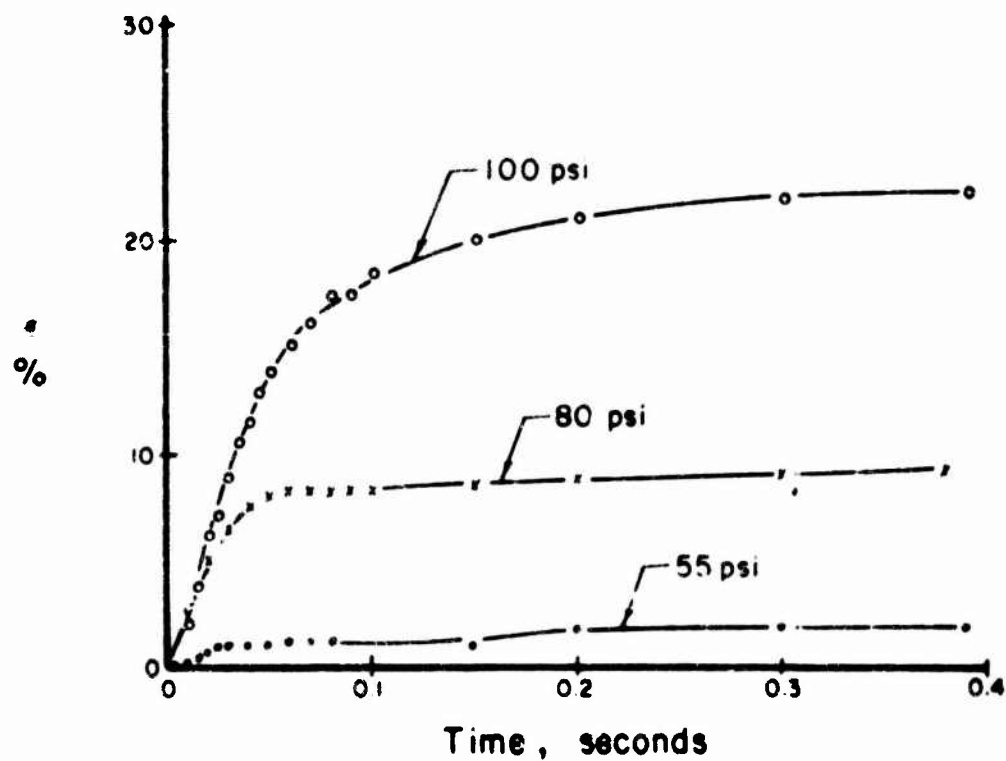
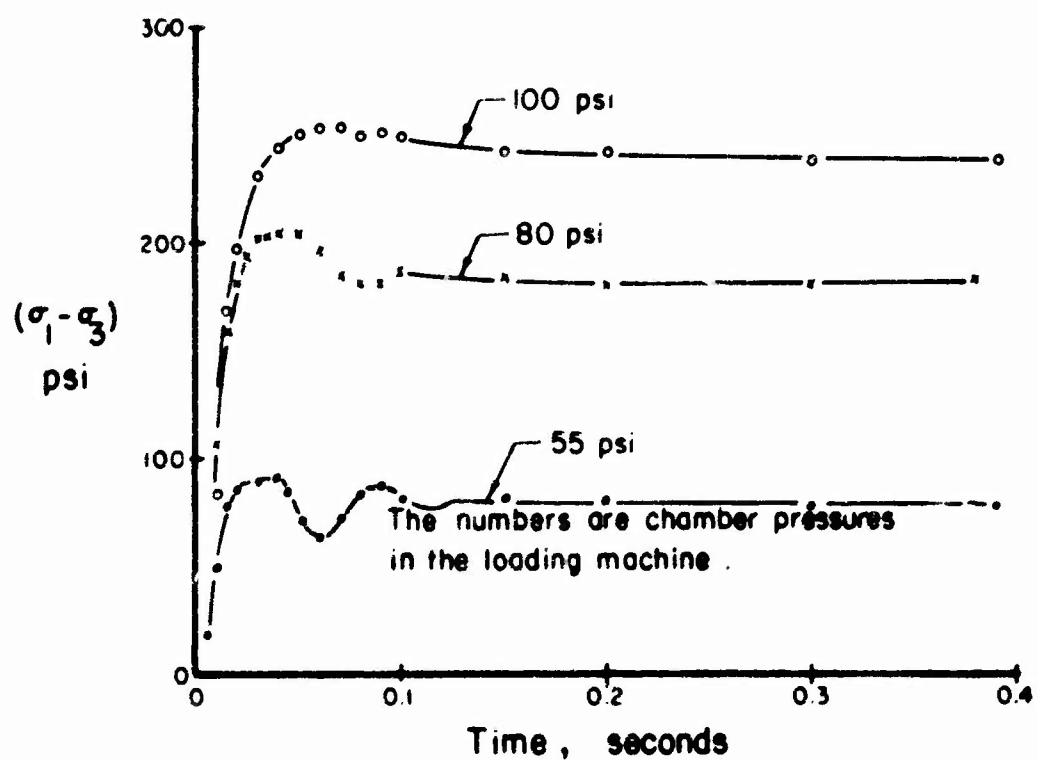


Figure 4.30. Triaxial Compression Tests at a Cell Pressure of 498 psi. and an Oil Valve Setting of 10.

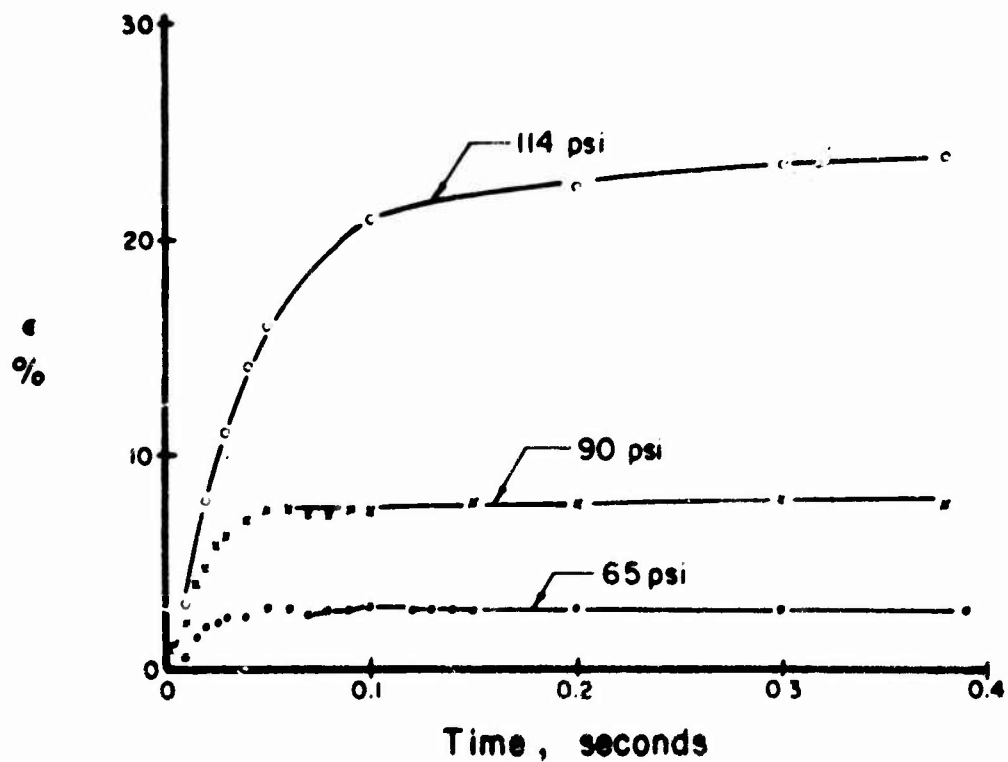
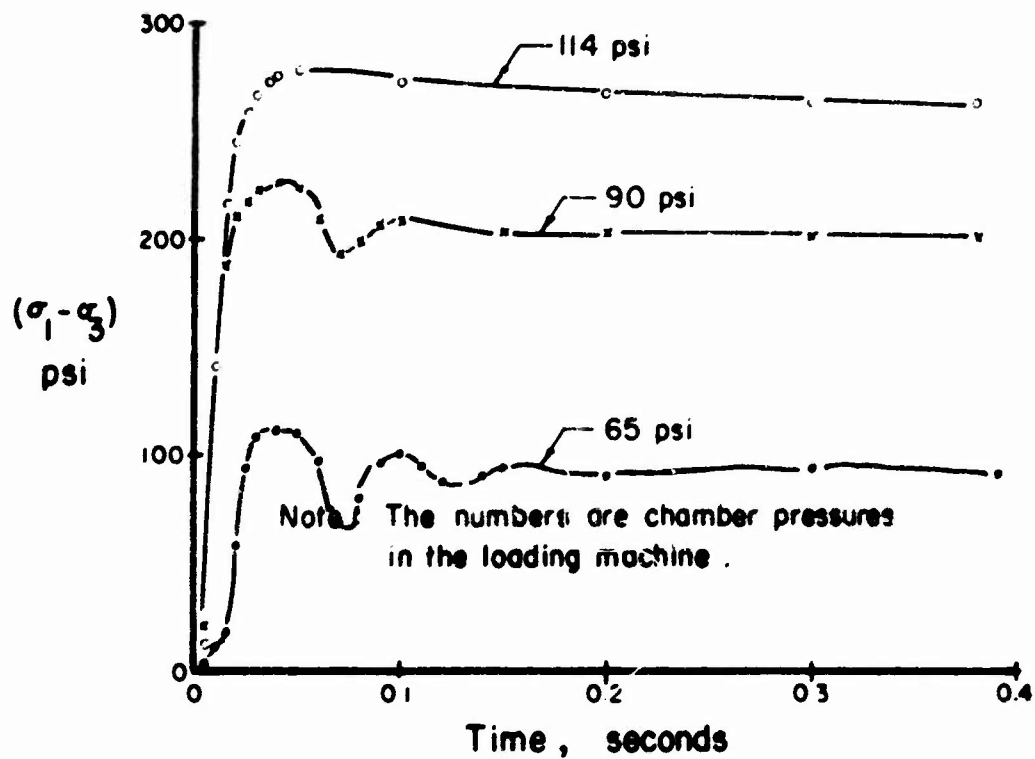


Figure 4.31. Triaxial Compression Tests at a Cell Pressure of 705 psi. and an Oil Valve Setting of 10.

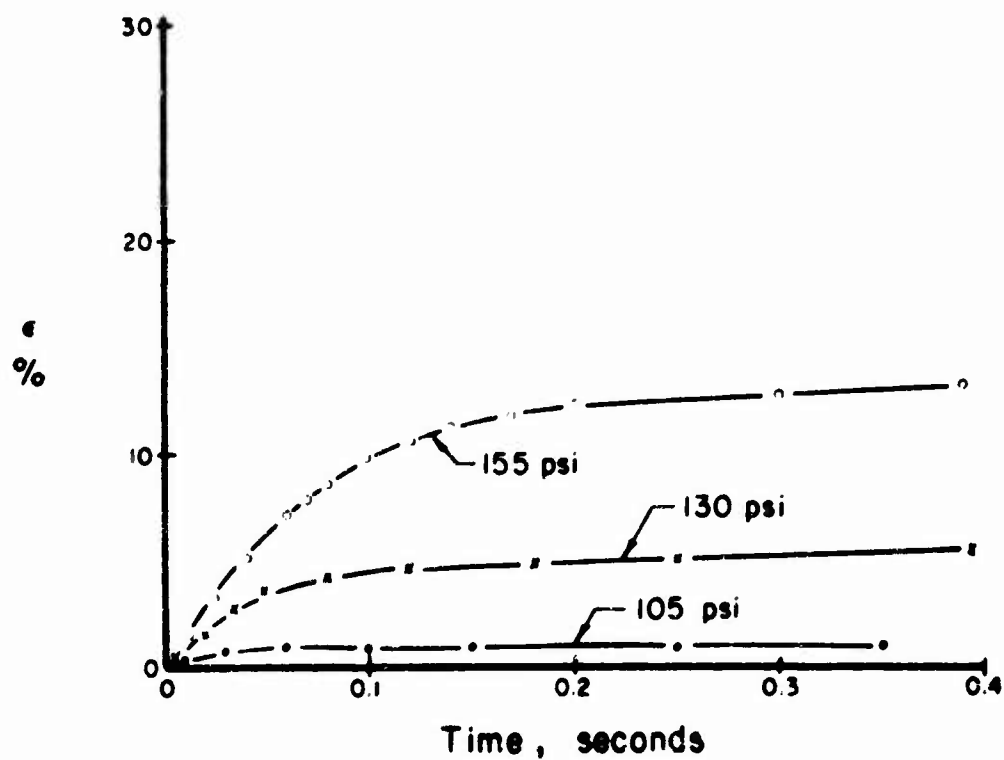
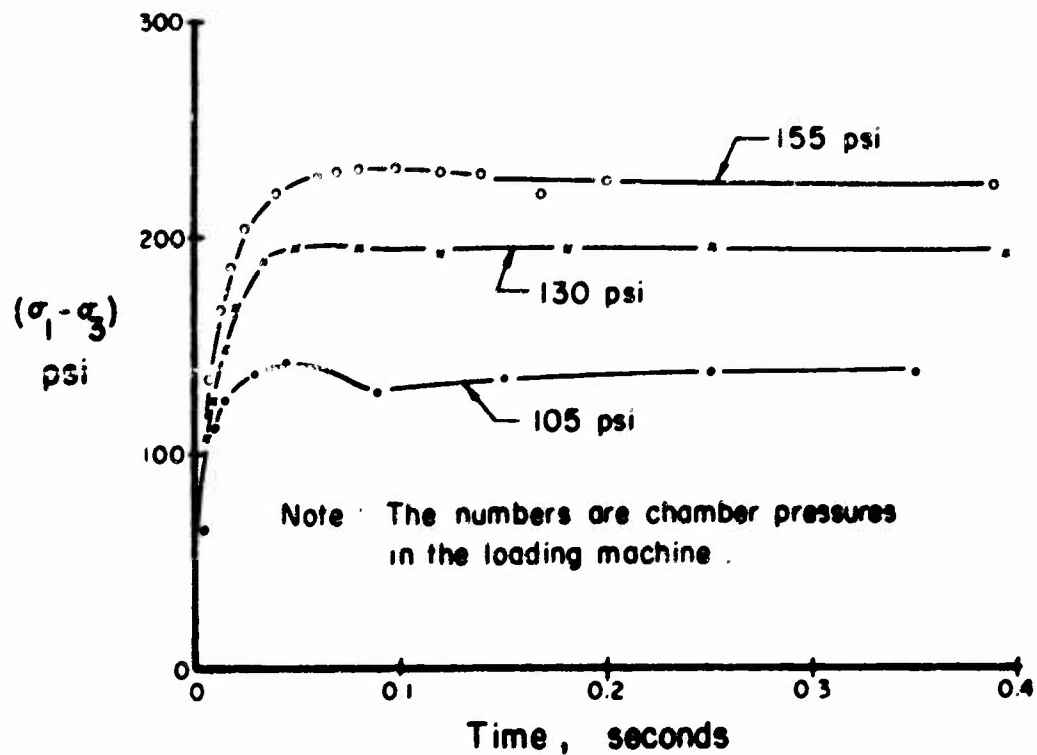


Figure 4.32. Triaxial Compression Tests at a Cell Pressure of 1000psi. and an Oil Valve Setting of 10.

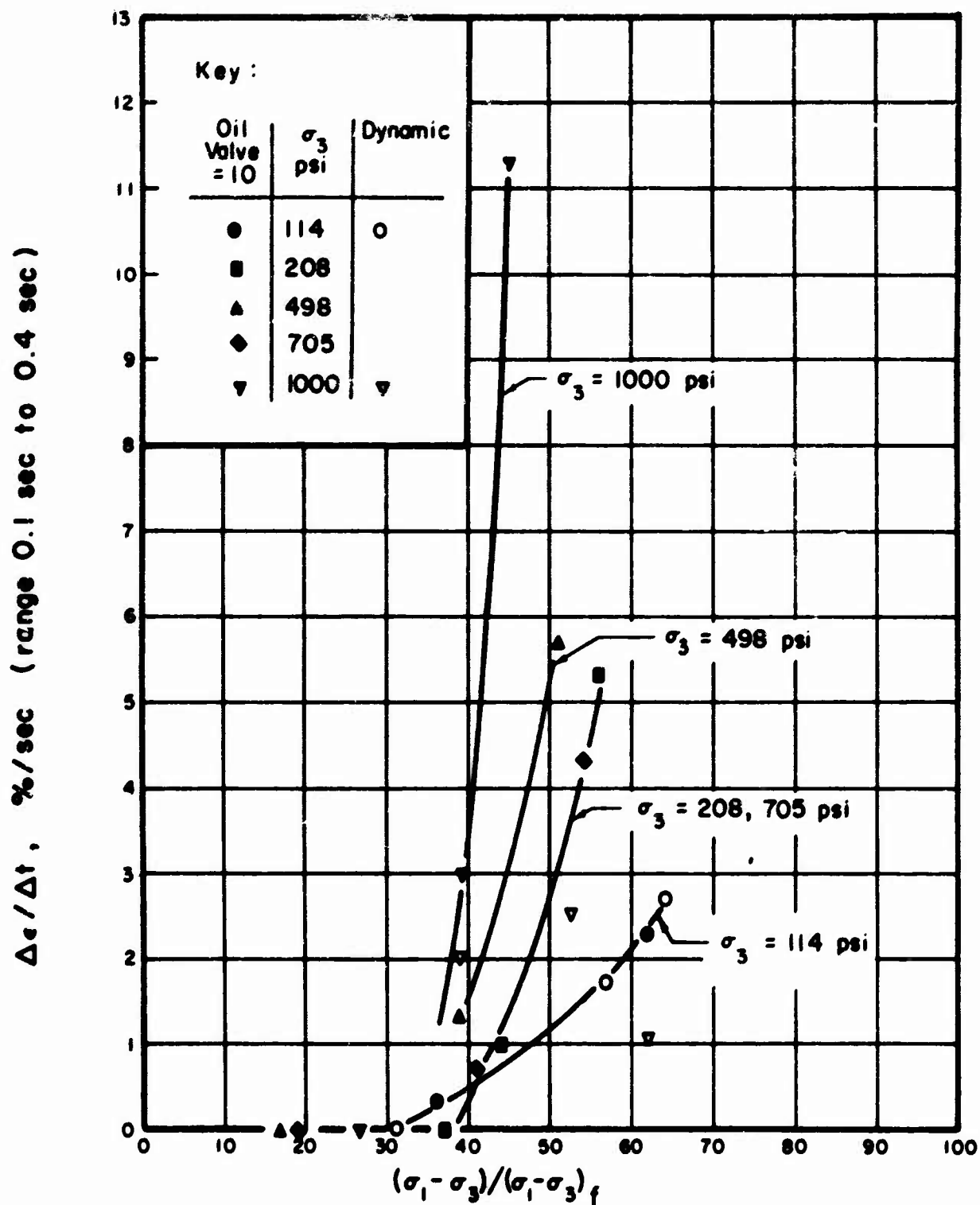


Figure 4.33. Creep Rates for Times Between 0.1 sec. and 0.4 sec., Triaxial Compression Tests.

CHAPTER 5

INTERPRETATION OF ONE-DIMENSIONAL AND TRIAXIAL TEST RESULTS

5.1 HORIZONTAL PRESSURES

If the soil adjacent to a buried structure is subjected to a dynamic vertical loading, horizontal pressures will be exerted on the structure. A knowledge of the magnitude of the horizontal pressures is essential for designing the structure. The ratio of the developed horizontal pressure to the applied vertical pressure, $K = \Delta\sigma_h / \Delta\sigma_v$, depends on the physical properties of the soil, the stress level, the rate of loading, and the conditions of lateral strain imposed on the soil element. The lateral strain in one-dimensional compression is zero; for this condition K is denoted as K_0 . If outward lateral strains are permitted and the lateral stress is constant, the ratio K decreases as the vertical stress increases and attains a minimum value denoted as K_a corresponding to the "active state."

The applied vertical stress and developed horizontal stress are superimposed on the vertical and horizontal stresses existing in situ. The ratio K_0 for the in situ stresses depends on the geological history of the soil deposit and is not generally known. In the subsequent discussion only the increments of stress due to the applied vertical stress are considered. Thus for the one-dimensional compression tests, $\Delta\sigma_h = \sigma_r$ and $\Delta\sigma_v = \sigma_a$, and for the triaxial tests, $\Delta\sigma_h = \sigma_3$ and $\Delta\sigma_v = \sigma_1$.

The one-dimensional and triaxial tests provide data from which values of K_0 and K_a respectively may be determined for dynamic loading.

it should be noted that the character of the loading in the tests differs from that which would be experienced in the field. In the case of the one-dimensional compression test, the dynamic vertical pressure starts from the initial seating load whereas in the field the vertical pressure is superimposed on the existing overburden pressure as previously noted. In the field and in the one-dimensional test the vertical and lateral pressures increase simultaneously. However, in the triaxial test the confining pressure was applied first and then the axial stress was increased dynamically. Thus only a portion of the total axial stress is a dynamic load. The effect of this difference cannot be evaluated at this time; this would be a valuable subject for future research.

The values of K_0 at various stress levels obtained from the one-dimensional tests are given in Table 3.2. On the average, K_0 increases from about 0.4 at low stress levels to 0.9 at an axial stress of about 1500 psi. At this point the soil has been compressed sufficiently to become saturated and stress increments above this level are transmitted almost entirely to the pore water; thus, the lateral stress increases by an amount equal to the increment of vertical stress and K_0 approaches unity. The pressure at which saturation occurs depends upon the initial degree of saturation; if the soil is saturated initially, K_0 will be equal to unity throughout the test. The values of K_0 listed in Table 3.2 have been averaged within the pressure increments 300 psi to 500 psi, 500 psi to 750 psi, and 750 psi to 900 psi. The averages are plotted against the axial stress in Fig. 5.1 and a curve labeled " K_0 " has been drawn to indicate the probable trend of the data. The scatter in the data at stress levels below 1000 psi does not permit a more precise representation.

The failure envelopes for the triaxial tests, Fig. 4.12, may be used to obtain corresponding values of K and vertical stress, $\Delta\sigma_v$, since both $\Delta\sigma_v$ and $\Delta\sigma_h$ are defined for each point on the envelope. These K -values are the minimum values which are possible for a given axial stress and may be denoted as K_a . The relationships between K_a and $\Delta\sigma_v$ obtained from the failure envelopes for the triaxial tests are shown in Fig. 5.1 for two loading rates. K_a increases from about 0.3 for low stress levels to 0.6 or more at an axial stress level of 1500 psi. As discussed in section 4.4, the failure envelopes become horizontal at high stress levels; that is, $(\sigma_1 - \sigma_3)$ becomes constant and independent of σ_1 . K_a can be expressed in the form:

$$K_a = \frac{\sigma_3}{\sigma_1} = \frac{\sigma_1 - (\sigma_1 - \sigma_3)}{\sigma_1} = 1 - \frac{\sigma_1 - \sigma_3}{\sigma_1}$$

Since the stress difference $(\sigma_1 - \sigma_3)$ has an upper limit for unconsolidated-undrained stressing of unsaturated soil (Fig. 4.12) while σ_1 may increase indefinitely, it is apparent that K_a must approach one at large values of σ_1 . Note, however, that large volumetric strains may be required to increase σ_3 to the level required to maintain $(\sigma_1 - \sigma_3)$ at its limiting value.

A relationship between K and $\Delta\sigma_v$ of the type shown in Fig. 5.1 provides a means for estimating the horizontal pressure resulting from a given vertical pressure for different lateral yield conditions. The zone between the one-dimensional and triaxial curves, shown shaded, represents the possible range in K -values. It is important to note that while the upper boundary corresponds to a condition of zero lateral strain, the magnitude of strain at the lower boundary is not defined.

In this respect, it is of interest to study the variation of K and strain during the dynamic triaxial tests as shown in Fig. 5.2. The axial strain in the triaxial tests was taken to be zero when the sample was subjected to the confining pressure only. Point A in Fig. 5.2 represents a sample subjected to an ambient pressure of 114 psi. When the axial stress is increased, K decreases along the curve ABC. Point C represents failure conditions for which $K = K_a$. (The curve labeled K_a in Fig. 5.2 is identical to the curve for K_a with $t_f = 4$ ms in Fig. 5.1.) Curve A'B'C' is similar to ABC but applies to tests with a confining pressure of 1010 psi. The axial strain at failure was approximately 20 percent for all of the triaxial tests; thus the axial strain for curve CC' is 20 percent as shown in the figure. The values of axial stress and K at points B and B' have been determined for an axial strain of one percent.

If it is assumed that the volume changes are negligible during the dynamic portion of the tests, the lateral strain will be equal to one-half the axial strain. Thus a lateral strain of only 0.5 percent will cause K to decrease from unity to the values given by curve BB' while an additional lateral strain of 9.5 percent is required to achieve the minimum K -values. It is important to note that the condition of zero lateral strain in the triaxial test is different from that in the one-dimensional test because zero lateral strain is defined differently for the two tests. As a result the K_0 -curve in Fig. 5.1 cannot be compared with the triaxial zero-lateral-strain line, line AA', in Fig. 5.2. The K_0 -curve actually corresponds roughly with curve BB' instead. Therefore an estimate of the lateral strain required to cause a reduction from K_0 to K_a may be inferred from the difference in lateral

strain between curves BB' and CC'. On this basis, it is estimated that a lateral strain of approximately 9 percent to 10 percent will cause a reduction in horizontal pressure from $K_0 \Delta \sigma_v$ to $K_a \Delta \sigma_v$.

5.2 STRESS-STRAIN RELATIONS

The stress-strain relationship for a given soil under an axially symmetrical state of stress is primarily a function of the degree of confinement provided in the radial direction. This fact is demonstrated in Fig. 5.3 where representative stress-strain curves for a one-dimensional compression test (No. 9) and for a triaxial test (No. 27) are shown. The vertical scale represents the increase in axial stress; for the one-dimensional test this is the total axial stress whereas for the triaxial test it is equal to $(\sigma_1 - \sigma_3)$. Both tests were conducted at comparable strain rates. Direct numerical comparisons of the test results are difficult because of the differences in densities and degrees of saturation between the two samples. However, a comparison of the moduli when the lateral stresses in the two tests are equal is of interest. The constrained tangent moduli at radial stresses of 500 psi and 1000 psi (for example, at point A in Fig. 5.3) are listed in Table 5.1. In Table 5.2, the minimum, average, and maximum constrained tangent moduli are compared with the secant moduli at one percent strain from the triaxial tests with $t_f = 4$ ms. The latter values, as shown in Fig. 4.23, are 18,000 psi and 22,000 psi for lateral pressures of 500 psi and 1000 psi respectively. Because of the difficulty in measuring the small strains during the fastest triaxial tests, it is possible that a better value for the lateral pressure of 1000 psi may be given by extrapolating from the

moduli for the slower tests. In this case, E_s is found to be 35,000 psi (Fig. 4.25). The ratio M_{ct}/E_s for the average M_{ct} -values increase from 2.25 for a lateral pressure of 500 psi to 3.37 or 4.59 for a lateral pressure of 1000 psi. The difference between the moduli at a given lateral pressure is believed to be largely the result of differing conditions of lateral restraint and, to a lesser extent, the result of differences in average density and degree of saturation.

If it is assumed that the moduli at a given lateral pressure are related in the same manner as the constrained modulus and the modulus of elasticity for an elastic material, then the following relation holds:

$$\frac{M_{ct}}{E_s} = \frac{1-\nu}{(1+\nu)(1-2\nu)} \dots \dots \dots (5.1)$$

in which M_{ct} = constrained tangent modulus
 E_s = triaxial secant modulus
 ν = Poisson's ratio

For an elastic material,

$$K_o = \frac{\nu}{1-\nu} \dots \dots \dots (5.2)$$

The relation between K_o and M_{ct}/E_s may be found by eliminating ν from Eq. (5.1) and (5.2) or, more simply, it can be expressed graphically as shown in Fig. 5.4. Measured values of K_o and M_{ct}/E_s may be plotted on Fig. 5.4 for comparison with the elastic curve. This has been done for confining pressures of 500 psi and 1000 psi using the values of K_o and M_{ct}/E_s listed in Table 5.2. The K_o -values in Table 5.2 were obtained from the K_o -curve in Fig. 5.1. The scatter in M_{ct}/E_s in Fig. 5.4 does not permit definite conclusions to be drawn from the comparison. The

proximity of the average values and the theoretical curve, however, implies that K_0 , the constrained tangent modulus, and the triaxial secant modulus at one percent strain may be related, for a given lateral stress, by Eq. (5.1) and (5.2).

5.3 DESIGN IMPLICATIONS FOR HIGH PRESSURE LEVELS

Limitations

The one-dimensional test results may be used to draw several conclusions regarding the interaction of a compacted soil with a relatively rigid structure at high pressure levels. These conclusions are of a general nature and may assist in making estimates of the soil properties for design purposes. They are limited to silty clays (CL under the Unified Classification System) which are compacted to about 95 percent of the maximum dry density obtained from the Modified AASHO compaction test and which have a degree of saturation of 80 percent to 85 percent. These conditions are not uncommon in practice so that the limitations are not severe.

Constrained Secant Modulus

The variation of the constrained secant modulus with axial stress was shown in Fig. 3.22. The modulus decreases to a minimum value at an axial pressure of 500 psi to 1000 psi and then increases linearly for pressures above 1000 psi, which is the pressure level at which the soil becomes essentially saturated. On the basis of the rapid test results shown in Fig. 3.22, the value of this modulus is

$$M_{cs} = 25000 + 15\sigma_a$$

where σ_a is the axial stress. This equation will give approximate M_{cs} -values for σ_a greater than 1000 psi and less than 10,000 psi. The influence of the rate of loading is not clear from the test results but the indication is that under very fast rates of loading the value of M_{cs} may be, on the average, 50 percent greater than that given by the above equation. Thus both the stress level and the rate of loading have a significant influence on the constrained modulus.

A similar series of one-dimensional tests was conducted on Playa silt from the Nevada Test Site (Hendron and Davisson¹). The constrained secant modulus for static and rapid tests was found to be approximately

$$M_{cs} = 4000 + 3\sigma_a$$

or about one-fifth of the value obtained for the Goose Lake Clay. At an axial stress of 5000 psi, for example, the moduli are 19,000 psi and 100,000 psi for the Playa Silt and Goose Lake Clay respectively. The difference in moduli may be largely the result of the difference in initial degree of saturation, which was about 30 percent for the Playa Silt compared with 80 percent for the Goose Lake Clay.

The dynamic modulus for the Playa Silt was found to be approximately 1.85 times the rapid modulus (rise times greater than 35 ms) whereas this factor is, on the average, 1.5 for the Goose Lake Clay. The range in dynamic moduli (rise times less than 35 ms) at an axial stress of 5000 psi was 26,000 psi to 40,000 psi for the Playa Silt. For the same axial stress, the moduli for the Goose Lake Clay ranged from 80,000 psi to 200,000 psi. Thus the dynamic modulus is significantly greater than

the static or rapid modulus even when the initial degree of saturation is as great as 80 percent. Because of this difference, it is probable that the dynamic modulus can be determined only on the basis of dynamic tests for degrees of saturation lower than 80 percent.

Ratio of Horizontal to Vertical Soil Pressures

The variation of K_0 with axial stress for the one-dimensional tests has been presented in Fig. 5.1. Though a scatter in the measurements exists, on the average K_0 increases from about 0.4 at low stress levels to about 0.9 at an axial stress level of about 1500 psi. It is of interest to compare these values with the values listed in the Air Force Design Manual² for various soil types. The samples of Goose Lake Clay which were tested may be classified as cohesive soils of a hard consistency. The Air Force Design Manual lists the following dynamic K_0 -values for stress up to 1000 psi:

| | <u>Dynamic K_0</u> |
|---|---------------------------------|
| Unsaturated Cohesive Soils of Very Stiff to Hard Consistency | 1/3 |
| Saturated Cohesive Soils of Very Soft to Hard Consistency | 1 |

The measured K_0 -values fall within these rather broad limits, but it is clear that the Goose Lake Clay, with a degree of saturation of approximately 80 percent, agrees more closely with the "saturated" rather than the "unsaturated" classification. For design in this type of material with stresses up to 1000 psi or 2000 psi a K_0 -value of 0.9 would be reasonable.

REFERENCES

1. Hendron, A. J., Jr., and M. T. Davisson (1963), "Static and Dynamic Behavior of a Playa Silt in One-Dimensional Compression," Report to AFWL, Kirtland Air Force Base, New Mexico on Contracts AF 29(601)-6107 and AF 29(601)-63-5577, September 1963.
2. Air Force Design Manual (1962), "Principles and Practices for Design of Hardened Structures," Technical Documentary Report No. AFSWC-TDR-62-138, Kirtland Air Force Base, New Mexico, December 1962.

TABLE 5.1
CONSTRAINED TANGENT MODULI FOR ONE-DIMENSIONAL TESTS

| Test No. | M_{ct} | |
|----------|------------------------|-------------------------|
| | @ $\sigma_r = 500$ psi | @ $\sigma_r = 1000$ psi |
| | ksi | ksi |
| 1 | (150) | 180 |
| 2 | 50 | 75 |
| 3 | 40 | 100 |
| 4 | 60 | 100 |
| 5 | 50 | 180 |
| 6 | 45 | 60 |
| 7 | 25 | 50 |
| 8 | 75 | 125 |
| 9 | 40 | 100 |
| 10 | 35 | 90 |
| 11 | 20 | 80 |
| 12 | 40 | -- |
| 13 | 35 | 70 |
| 14 | 70 | 180 |
| 15 | 30 | 70 |
| 16 | 45 | 80 |
| 17 | 25 | -- |
| 18 | 30 | -- |
| 19 | 20 | 80 |
| 20 | 15 | -- |
| 21 | (135) | (400) |
| 22 | 50 | 90 |
| 23 | -- | -- |
| 24 | -- | -- |
| 25 | 50 | 90 |
| Range | 15 to 75 | 50 to 180 |
| Average | 40.5 | 101 |

Note: Values in parentheses are not included in Range and Average

TABLE 5.2

COMPARISON OF ONE-DIMENSIONAL AND TRIAXIAL MODULI

| $\frac{\sigma_3}{\text{psi}}$ | $\frac{K_o}{}$ | $\frac{E_s^a}{\text{psi}}$ | $\frac{\text{Tangent } M_{ct}}{\text{psi}}$ | $\frac{M_{ct}}{E_s}$ |
|-------------------------------|----------------|----------------------------|---|----------------------|
| 500 | 0.63 | 18000 ^b | min. 15,000 | 0.83 |
| | | | av. 40,500 | 2.25 |
| | | | max. 75,000 | 4.27 |
| 1000 | 0.78 | 22000 ^b | min. 50,000 | 2.27 |
| | | | av. 101,000 | 4.59 |
| | | | max. 180,000 | 8.17 |
| | | 35000 ^c | min. 50,000 | 1.43 |
| | | | av. 101,000 | 3.37 |
| | | | max. 180,000 | 5.15 |

^a Triaxial secant modulus at 1% strain for $t_f = 4$ ms

^b Measured (Fig. 4.23)

^c Extrapolated from measurements with slower times-to-failure (Fig. 4.25)

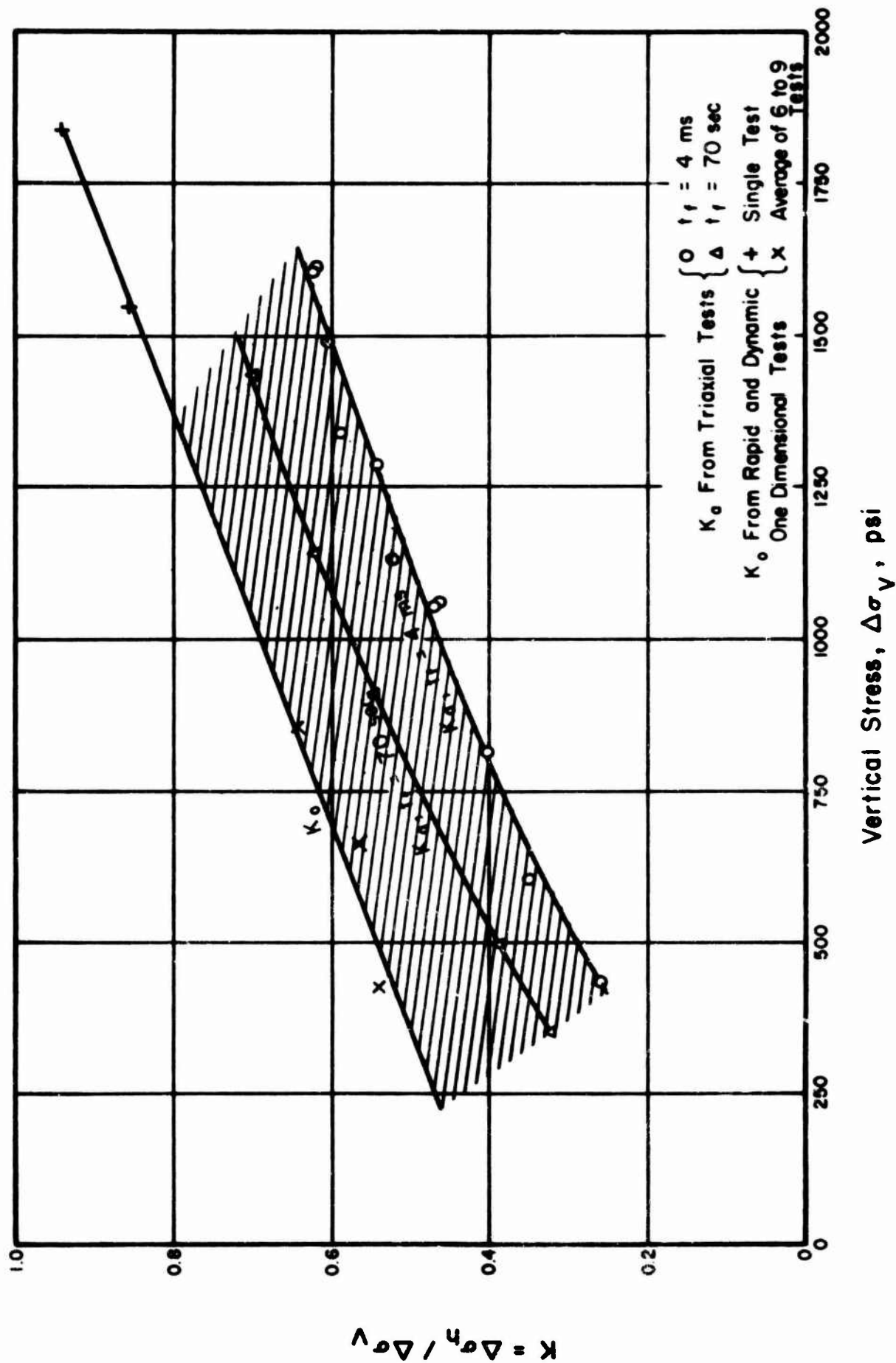


FIGURE 5.1. RELATIONSHIP BETWEEN K AND $\Delta\sigma_v$ FOR ONE-DIMENSIONAL AND TRIAXIAL TESTS ON GOOSE LAKE CLAY .

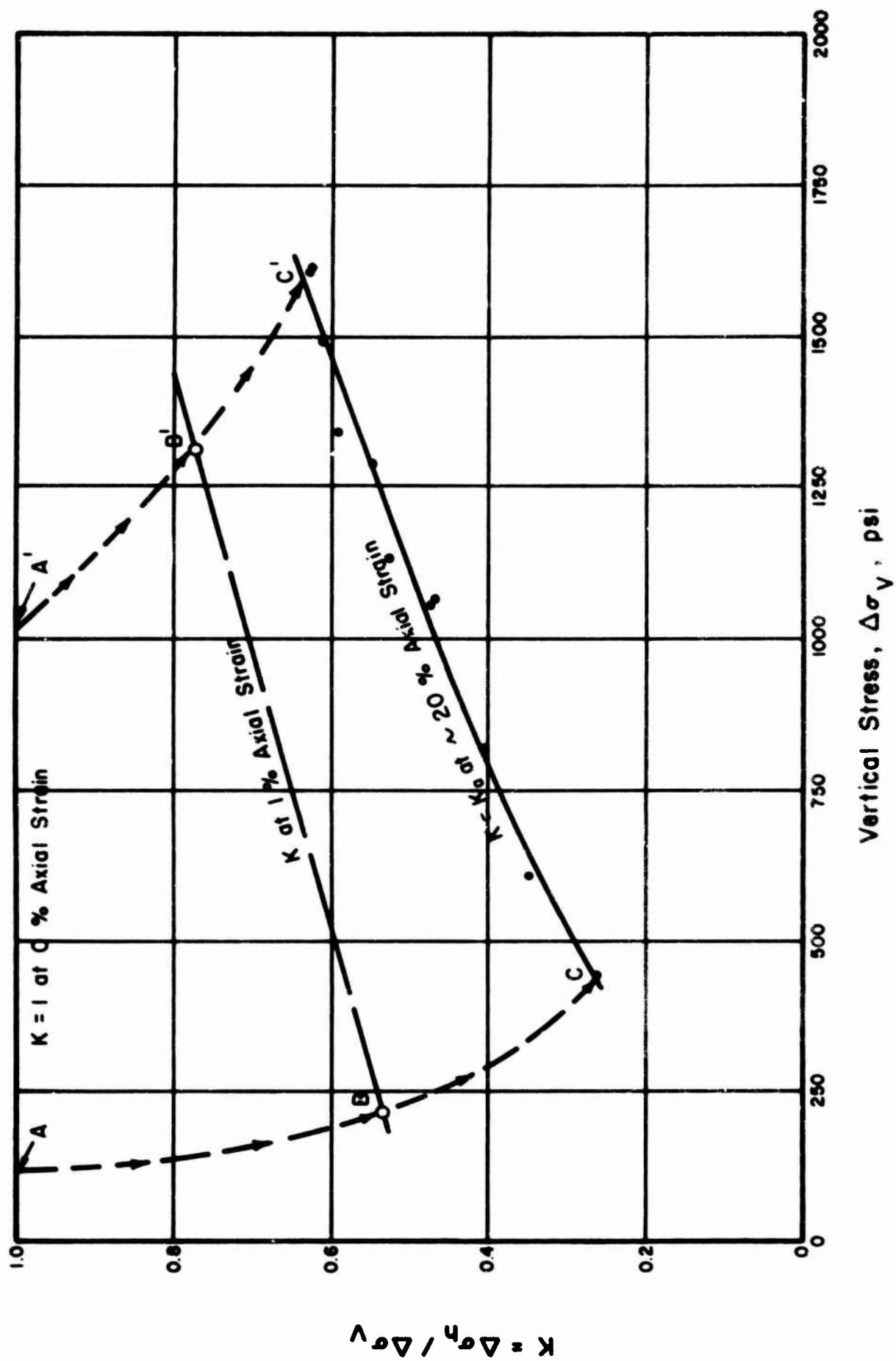


FIGURE 5.2. RELATIONSHIP AMONG K , $\Delta\sigma_v$, AND AXIAL STRAIN FOR TRIAXIAL TESTS ON GOOSE LAKE CLAY.

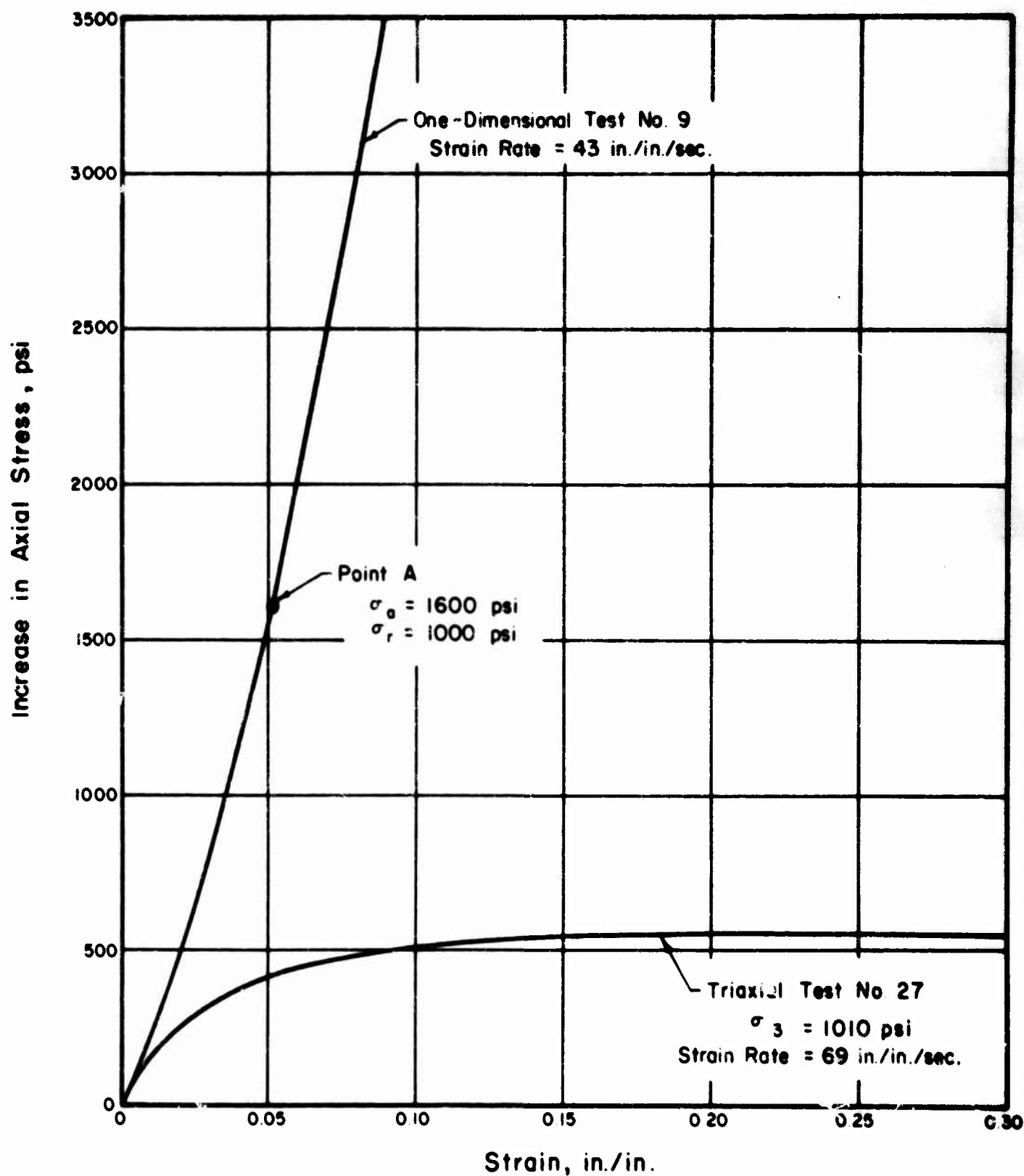


FIGURE 5.3. COMPARISON OF ONE-DIMENSIONAL AND TRIAXIAL STRESS-STRAIN CURVES.

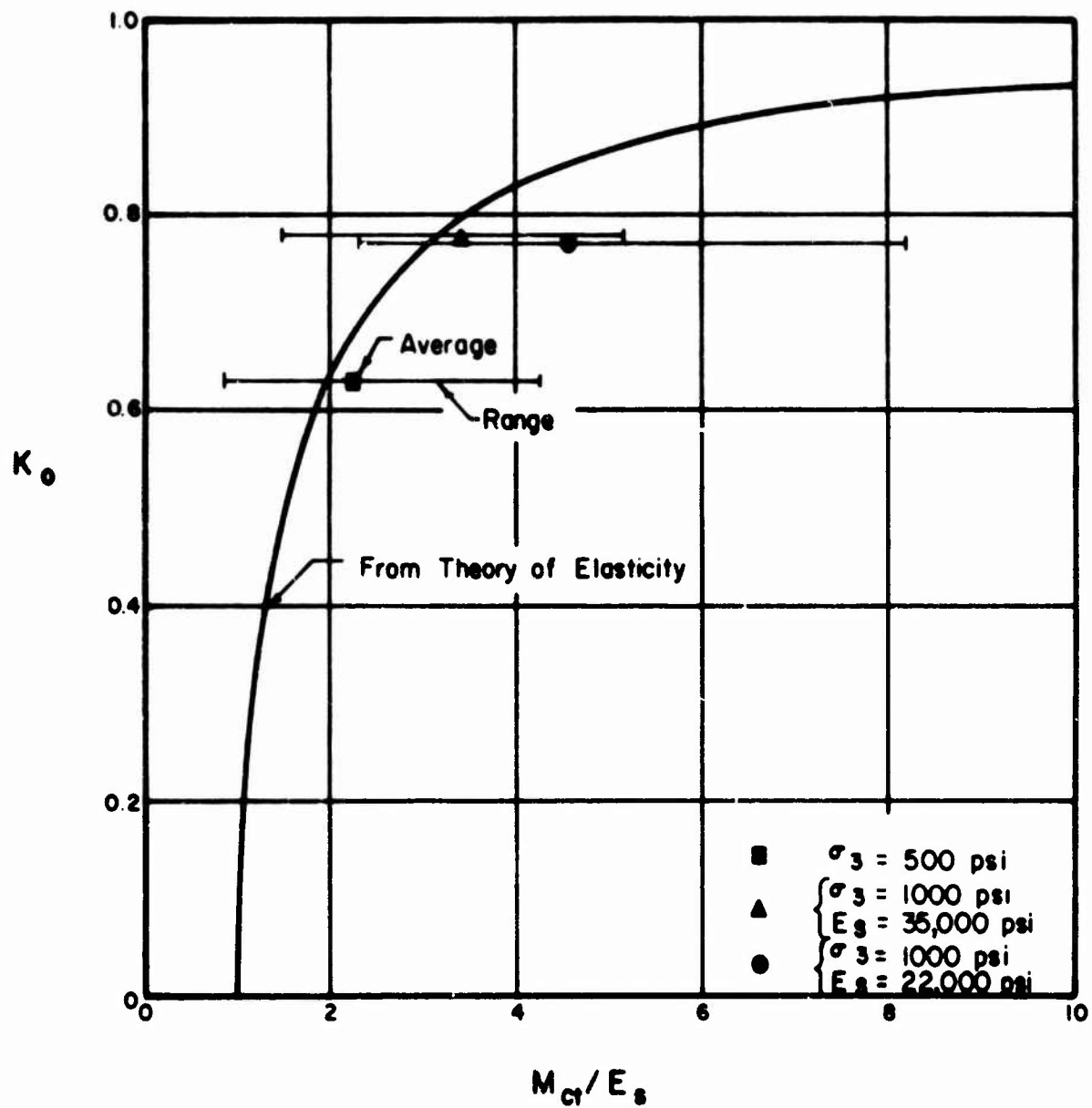


FIGURE 5.4. RELATION BETWEEN K_0 AND M_{ct}/E_s .

CHAPTER 6

SUMMARY, CONCLUSIONS, AND RECOMMENDATIONS

6.1 SUMMARY OF TESTING PROGRAM

Equipment

A series of dynamic, high pressure triaxial and one-dimensional tests has been conducted to expand our current knowledge of the behavior of soils under this type of loading. The development of special testing machines for the tests required a major portion of the time available for this work. The capabilities of these machines are summarized below.

Dynamic and rapid one-dimensional devices:

| | |
|---------------------|--|
| Sample diameter | 4 in. |
| Sample height | 1 in. |
| Peak axial pressure | 10,000 psi |
| Minimum rise time | |
| to peak pressure | 2 milliseconds (dynamic loading machine) |
| | 35 milliseconds (rapid loading machine) |
| Dwell time | controlled |

Triaxial device:

| | |
|-------------------------|----------------|
| Sample diameter | 1.5 in. |
| Sample height | 3 in. |
| Maximum cell pressure | 1500 psi |
| Minimum time to failure | 3 milliseconds |
| Dwell time | controlled |

One-Dimensional Compression Tests

Twenty-five one-dimensional compression tests were run on compacted samples of Goose Lake Clay. The average initial dry density of the test specimens was 121.1 pcf and the water contents averaged 11.6 percent. The degree of saturation was slightly less than 80 percent on the average. The peak pressures ranged from 620 psi to 11,300 psi with rise times to the peak pressure of 1.9 milliseconds to 1625 milliseconds. The dwell time and rate of decay were also varied.

Triaxial Compression Tests

Forty-four triaxial compression tests to failure were performed. Cell pressures from 100 psi to 1010 psi were used with times-to-failure varying from 3 milliseconds to 100 seconds. In addition, 20 partial loading tests were performed with the same range in cell pressures. In these tests, the applied axial stress varied from 20 percent to 60 percent of the stress required to cause failure and the sum of the rise time and dwell time was about 400 milliseconds. The average density and water content for all the test specimens were 117.3 pcf and 11.3 percent respectively.

6.2 CONCLUSIONS

Dynamic Compressive Strength

The Mohr-Coulomb failure envelopes (Fig. 4.12) are concave downward and approach a zero slope at high pressures. This type of envelope is common for unconsolidated-undrained compression tests on unsaturated soil and is the result of the "pressure saturation" of the soil under high ambient total stress.

The compressive strength increased about 50 percent as the time-to-failure was reduced from 100 seconds to 3 milliseconds. This relationship was similar for both the upper and lower ranges of cell pressure used in this project (Figs. 4.10 and 4.11).

Ratio of Lateral to Axial Pressures

The ratio of lateral stress to axial stress in the one-dimensional compression tests, designated as K_0 , varied on the average from 0.4 at low axial stress levels to 0.9 or 1.0 at axial stresses over 1500 psi (Fig. 5.1). The rate of loading did not appear to influence K_0 significantly. A study of the change in the ratio of lateral to axial pressures which results when lateral yield is permitted indicates that a lateral strain of the order of 10 percent will reduce the ratio from K_0 to the minimum value, K_a (Figs. 5.1 and 5.2).

Stress-Strain Relations

The triaxial secant modulus at one-percent strain, E_s , was found to be relatively independent of the loading rate for samples subjected to a confining pressure of 114 psi but the modulus increased with decreasing times-to-failure at a confining pressure of 1010 psi (Fig. 4.25). This difference in behavior is attributed to the effect of the prestress which resulted from the kneading compaction procedure. The secant modulus at one-percent strain increased from 10,000 psi to more than 20,000 psi as the confining pressure increased from 114 psi to 1010 psi (Fig. 4.23).

The constrained secant moduli for the rapid one-dimensional tests ($t_r > 35$ ms.) decreased to a minimum value at an axial pressure

of 500 psi and then increased nearly linearly with the axial stress (Fig. 3.22). Above 1000 psi, the modulus is given approximately by the equation

$$M_{cs} = 25000 + 15 \sigma_a$$

The constrained secant moduli for the dynamic tests ($t_r < 35$ ms.) averaged 50 percent greater than those for the rapid tests, but the range in dynamic moduli overlapped the moduli from the rapid tests (Fig. 3.22).

A study summarized in Fig. 5.4 implies that, for a given lateral pressure, the constrained tangent modulus, the triaxial secant modulus at one-percent strain, and K_0 may be related by equations for an elastic material. However no conclusions to this effect are warranted at this time.

Residual Strains and Creep

The residual strains due to one-dimensional loading were about 3 percent for axial stresses between 500 psi and 1000 psi, and from 3 percent to 5 percent for stresses from 1000 psi to 10,000 psi (Fig. 3.21). The residual strains for the rapid and dynamic tests were similar.

In the one-dimensional tests, little or no creep occurred under steady load after the peak stress was applied, possibly as a result of stress overshoot. In the triaxial test series, in which lateral strains were not controlled, the partial loading tests demonstrated that the creep rate under constant load is a function of the stress level, expressed as a ratio of the stress required to cause failure, and of

the cell pressure. The prestress caused by stress overshoot was found to reduce the creep rate. No creep was observed for stresses less than 35 percent of the failure stress.

6.3 RECOMMENDATIONS FOR FUTURE RESEARCH EFFORTS

Static Soil Properties

To provide a basis for the interpretation of dynamic test results the static soil properties at various densities and water contents should be established. To this end, static unconsolidated-undrained triaxial tests, with volume change measurements, at cell pressures from 10 psi to 1000 psi are required. Effective stress data should be obtained from samples pressure saturated in the same pressure range.

Triaxial Compression Tests

Because of time limitations, the density and degree of saturation were not varied in this study. In future efforts, consolidated-undrained tests at confining pressures between 10 psi and 1000 psi should be performed using various densities, water contents, consolidation pressures, and strain rates.

One-Dimensional Compression Tests

To improve the accuracy of strain measurements for highly compacted specimens, a sample height of 2 inches with a floating-type confining ring may be required. The strain due to the seating load in the dynamic tests complicated the interpretation of the strain measurements. Efforts should be directed towards improving the method of accounting for these strains.

The most interesting changes in the constrained modulus take place below a stress level of 2000 psi. This stress range should be investigated more thoroughly with equipment having a higher sensitivity at low stress levels than that used for the high pressure tests.

APPENDIX A

ONE-DIMENSIONAL TEST RESULTS

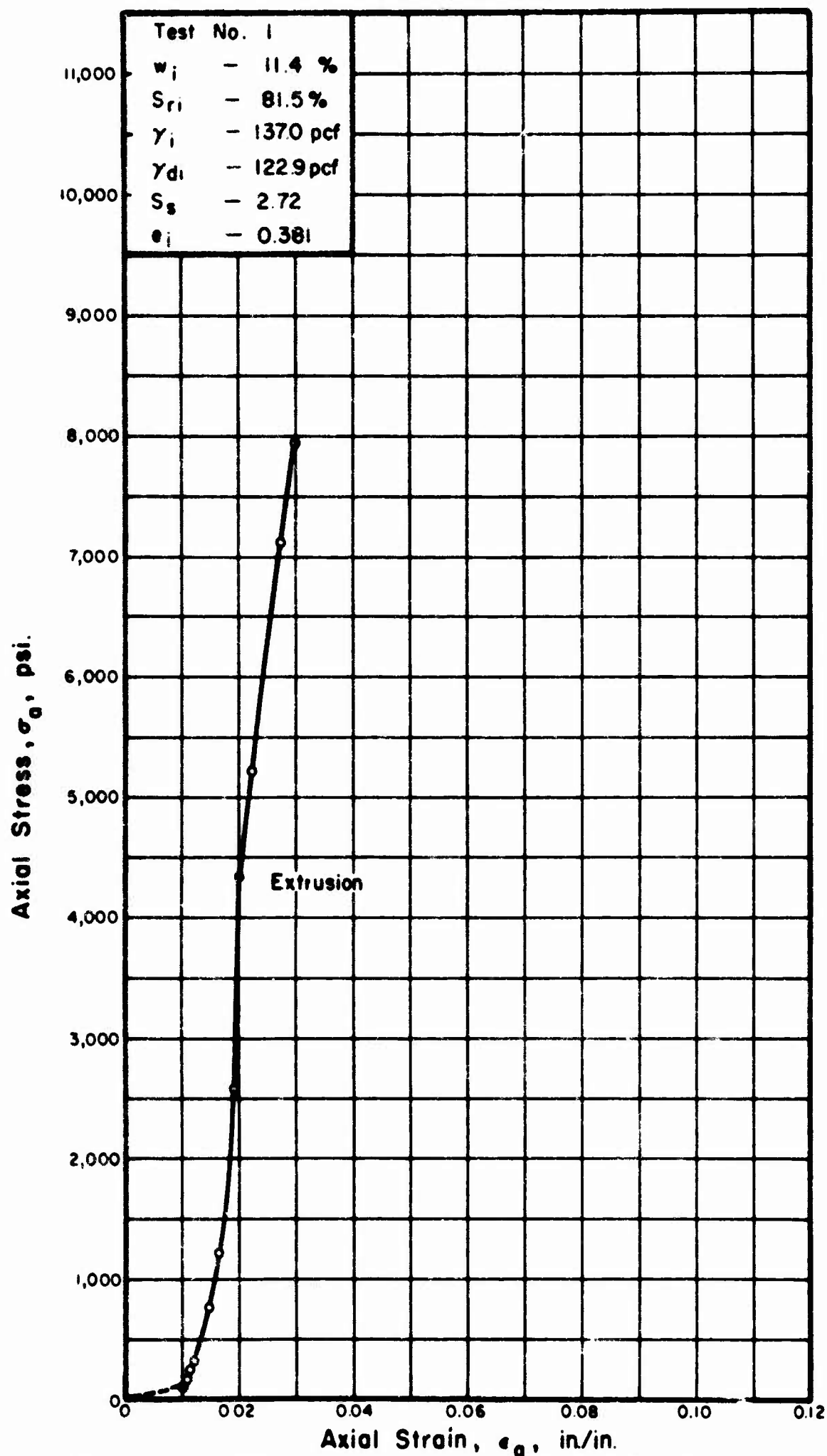


FIGURE A. 1. STRESS-STRAIN CURVE FOR GOOSE LAKE CLAY IN ONE-DIMENSIONAL COMPRESSION.

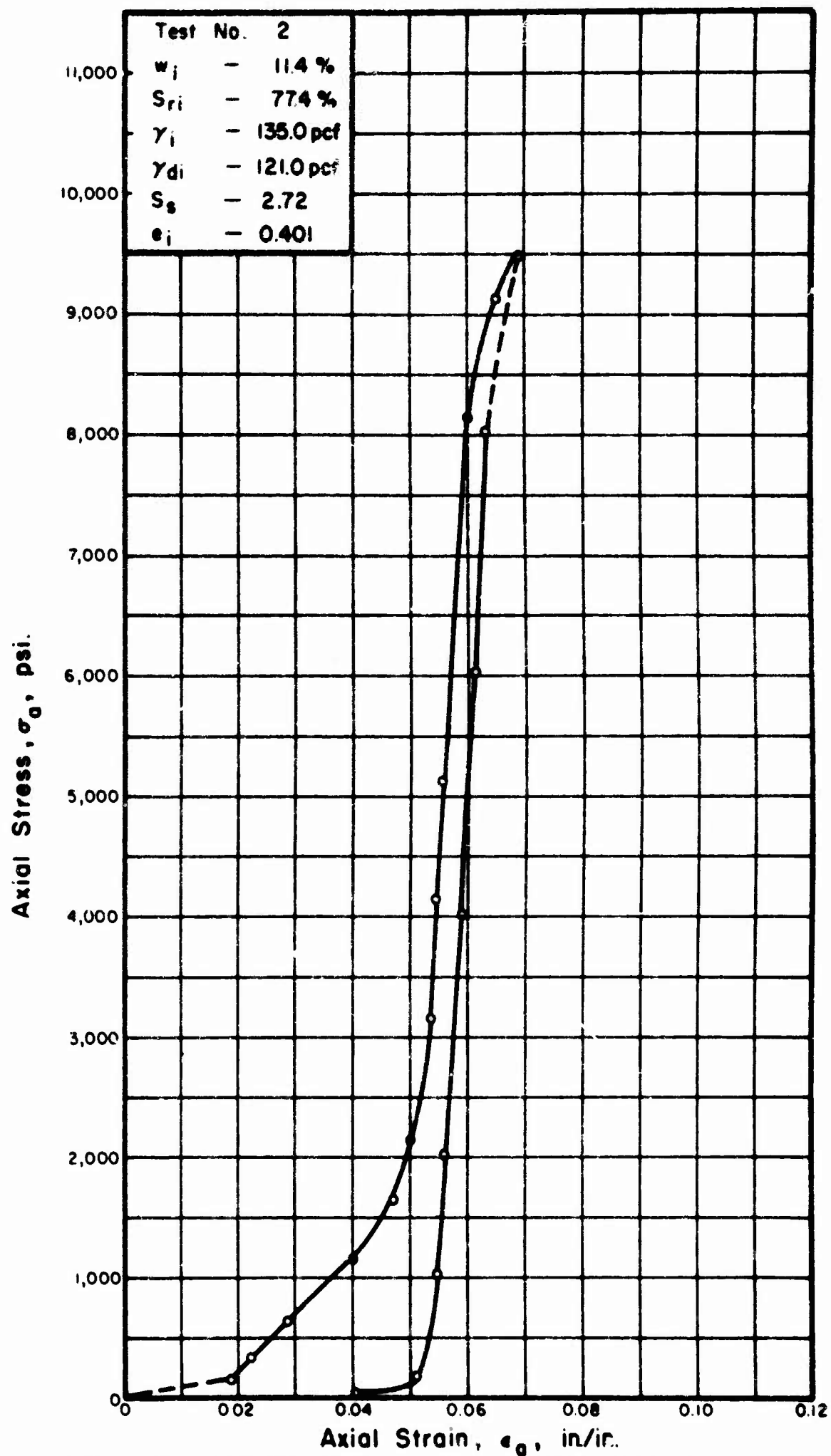


FIGURE A. 2. STRESS-STRAIN CURVE FOR GOOSE LAKE CLAY IN ONE-DIMENSIONAL COMPRESSION.

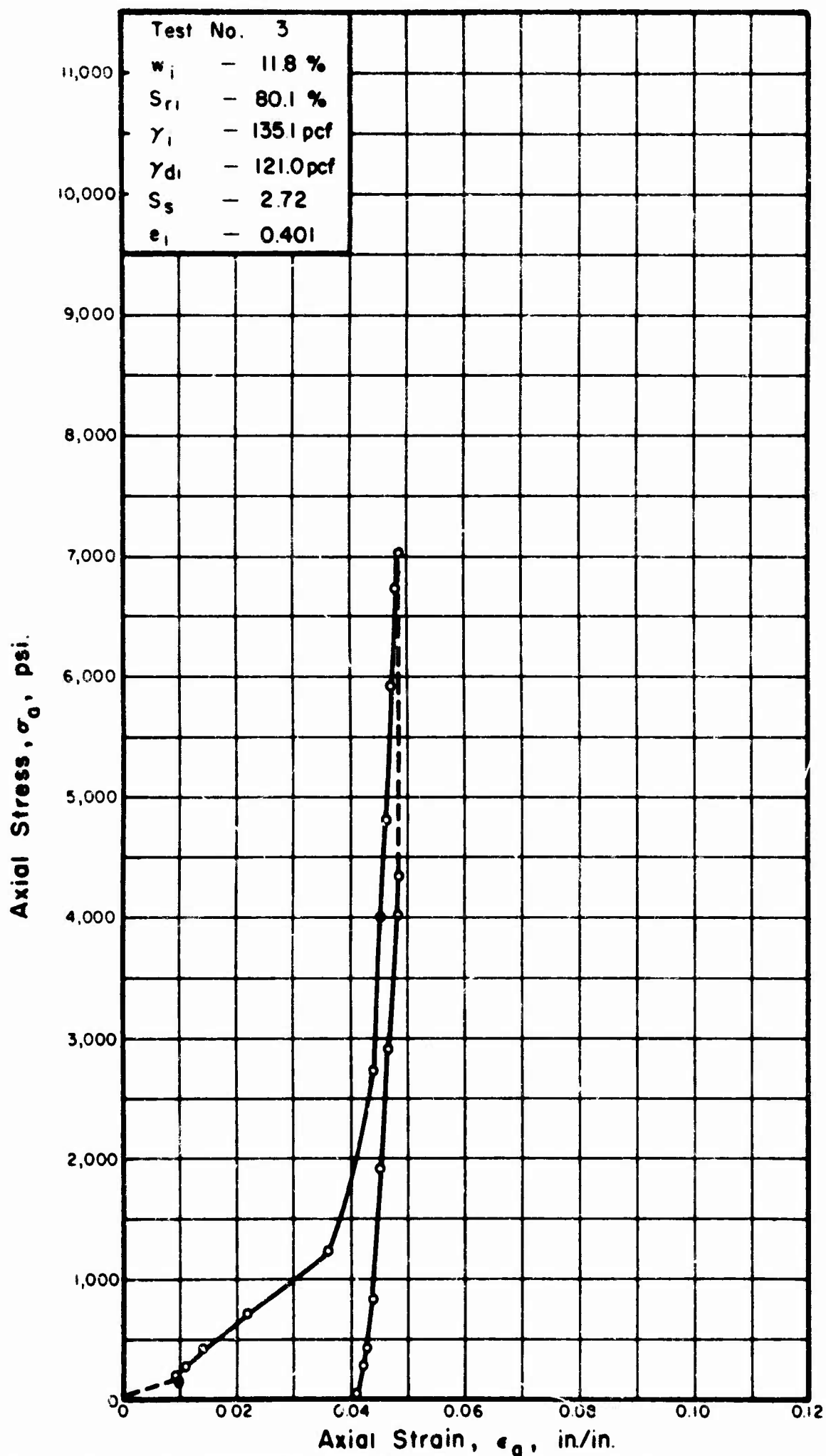


FIGURE A.3. STRESS-STRAIN CURVE FOR GOOSE LAKE CLAY IN ONE-DIMENSIONAL COMPRESSION.

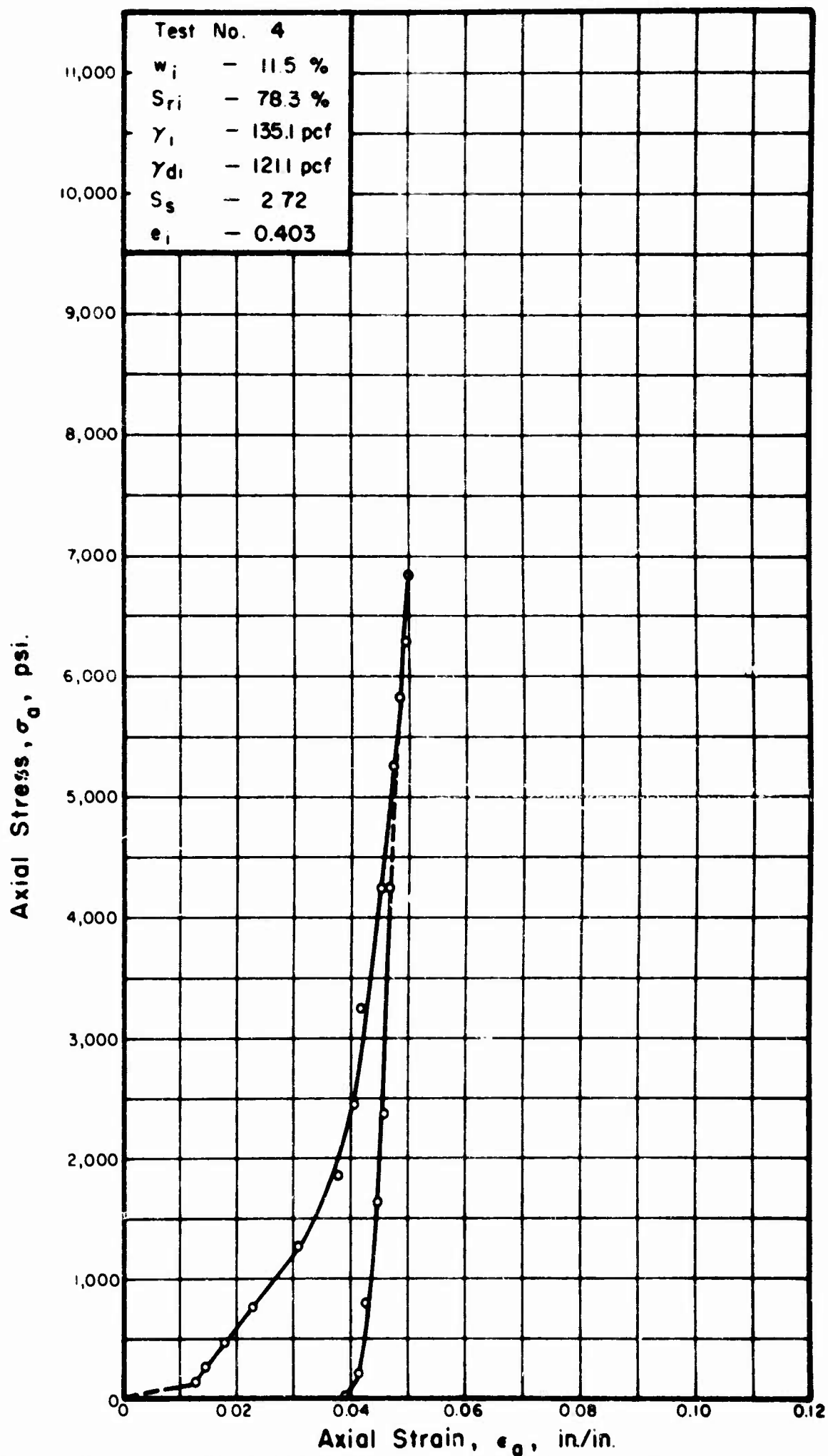


FIGURE A. 4 . STRESS-STRAIN CURVE FOR GOOSE LAKE CLAY
IN ONE-DIMENSIONAL COMPRESSION .

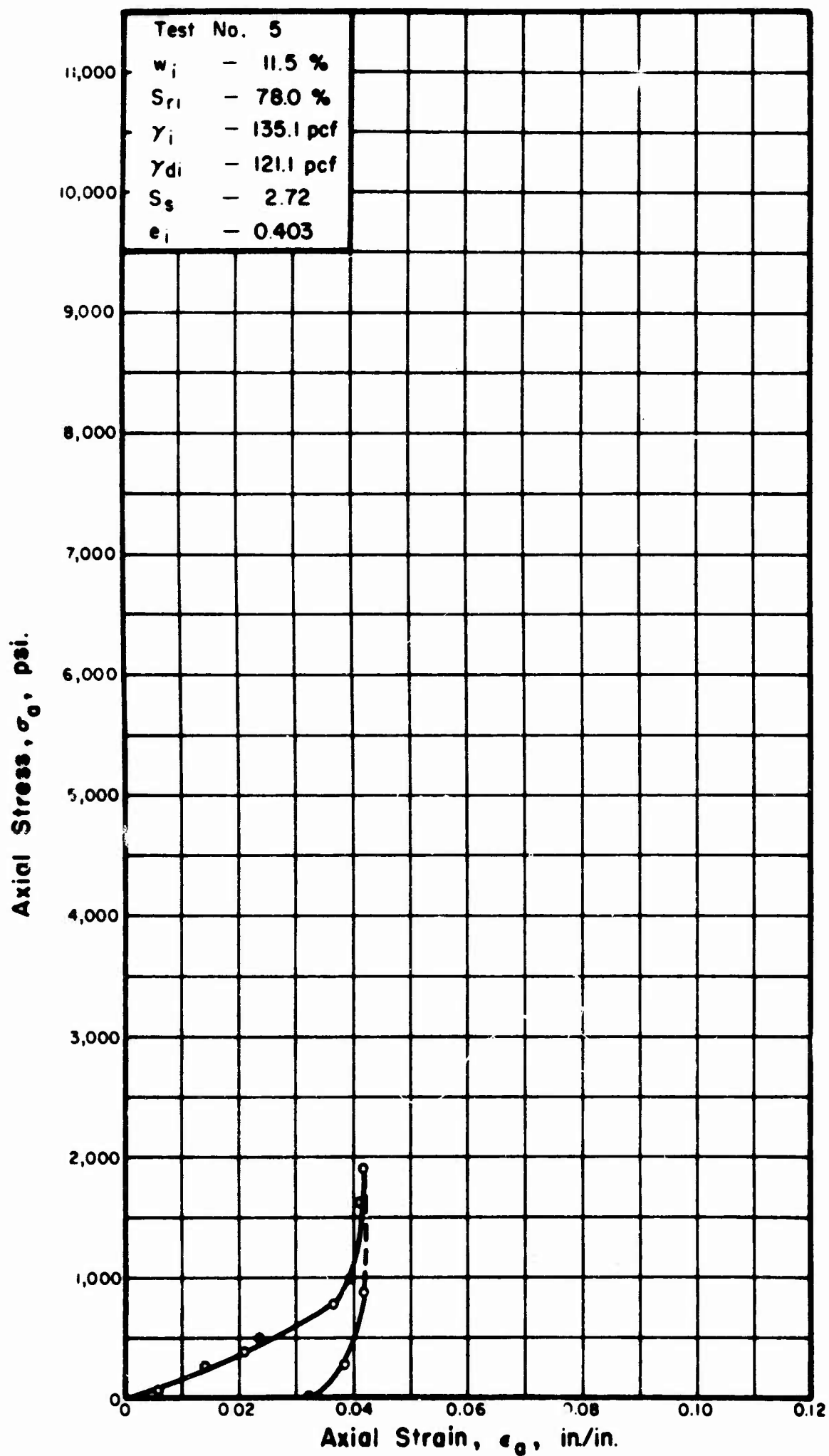
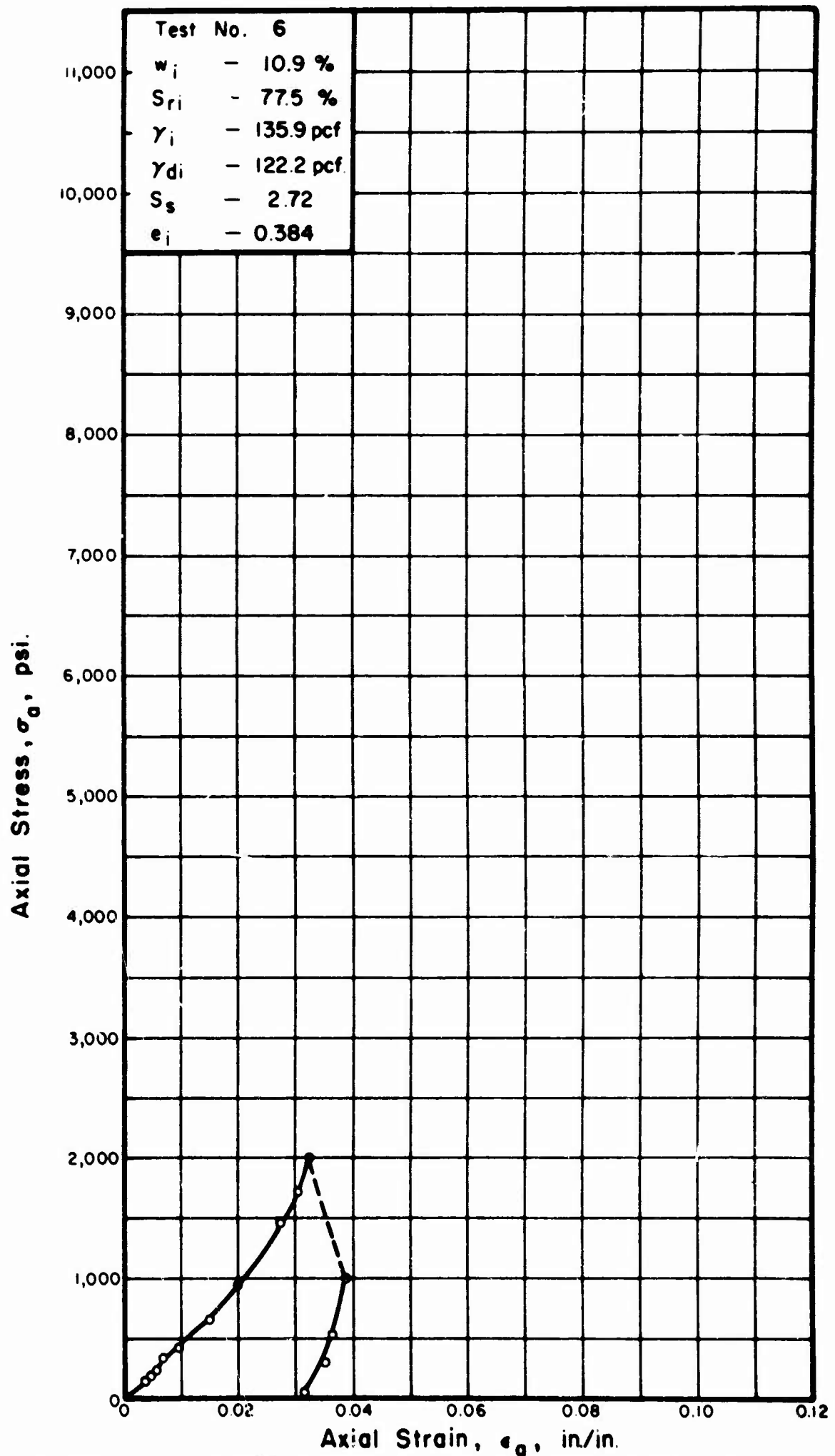


FIGURE A. 5. STRESS-STRAIN CURVE FOR GOOSE LAKE CLAY IN ONE-DIMENSIONAL COMPRESSION.



**FIGURE A.6 . STRESS-STRAIN CURVE FOR GOOSE LAKE CLAY
IN ONE-DIMENSIONAL COMPRESSION .**

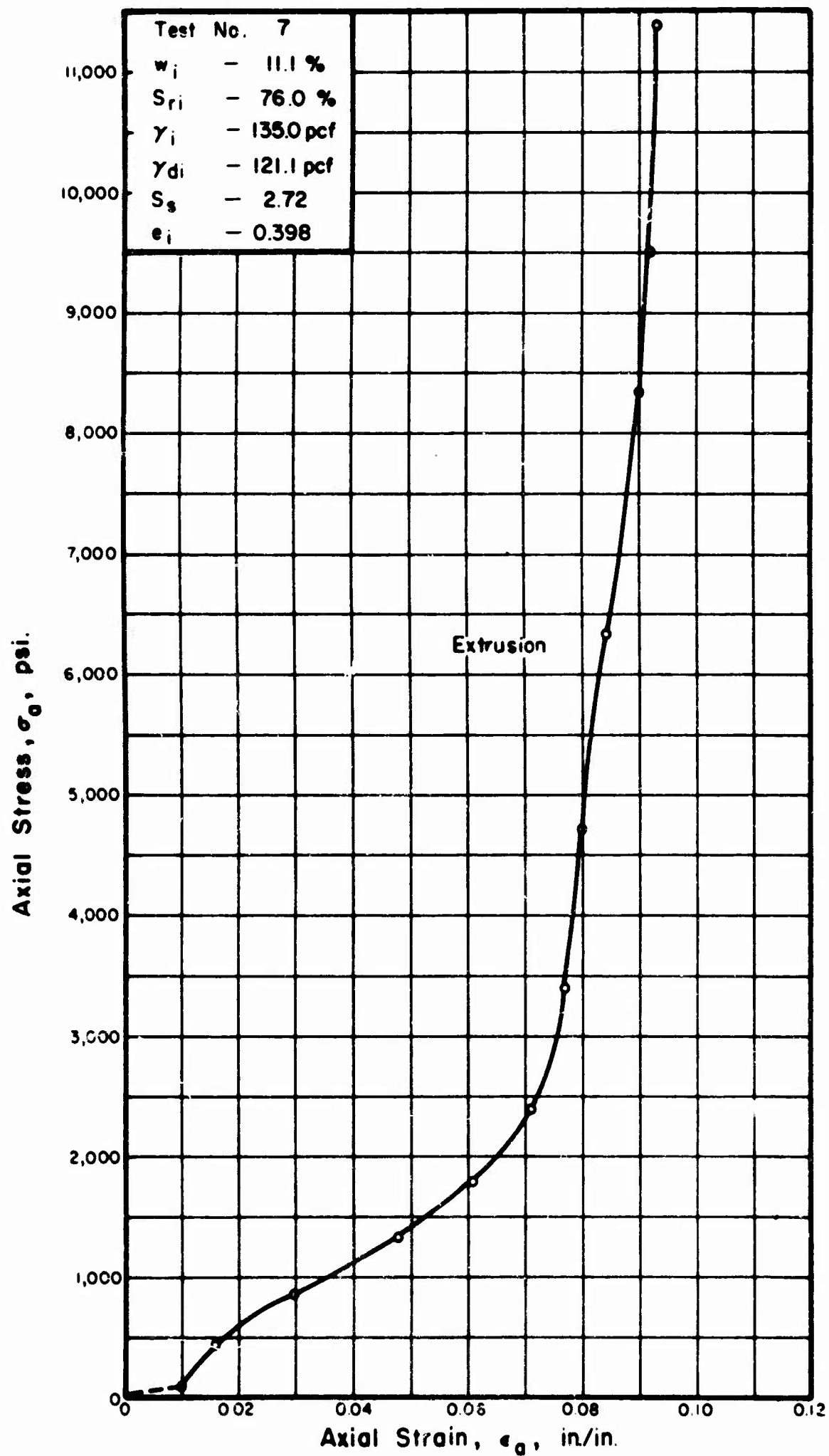


FIGURE A.7. STRESS-STRAIN CURVE FOR GOOSE LAKE CLAY IN ONE-DIMENSIONAL COMPRESSION.

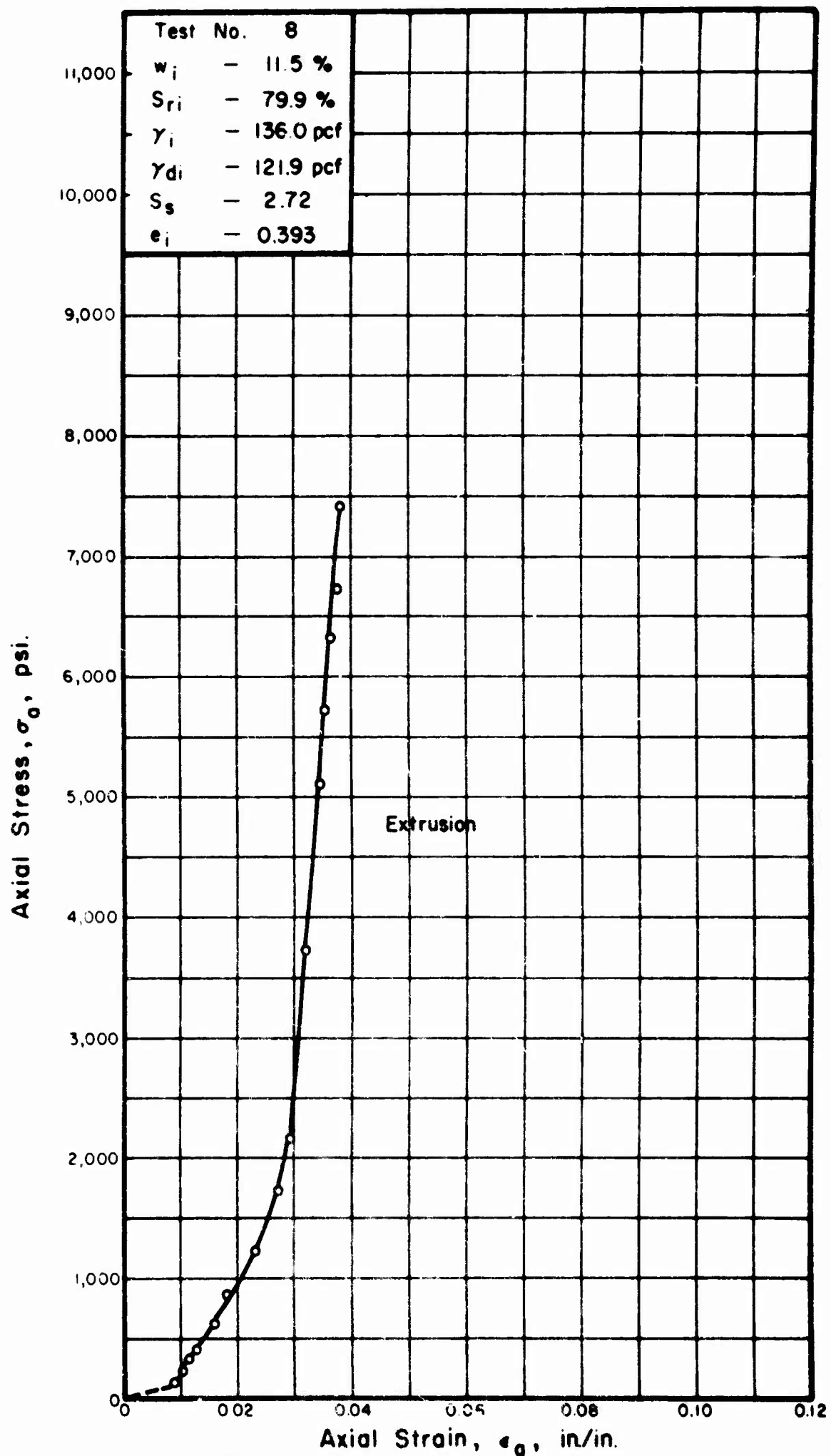


FIGURE A.8. STRESS-STRAIN CURVE FOR GOOSE LAKE CLAY IN ONE-DIMENSIONAL COMPRESSION.

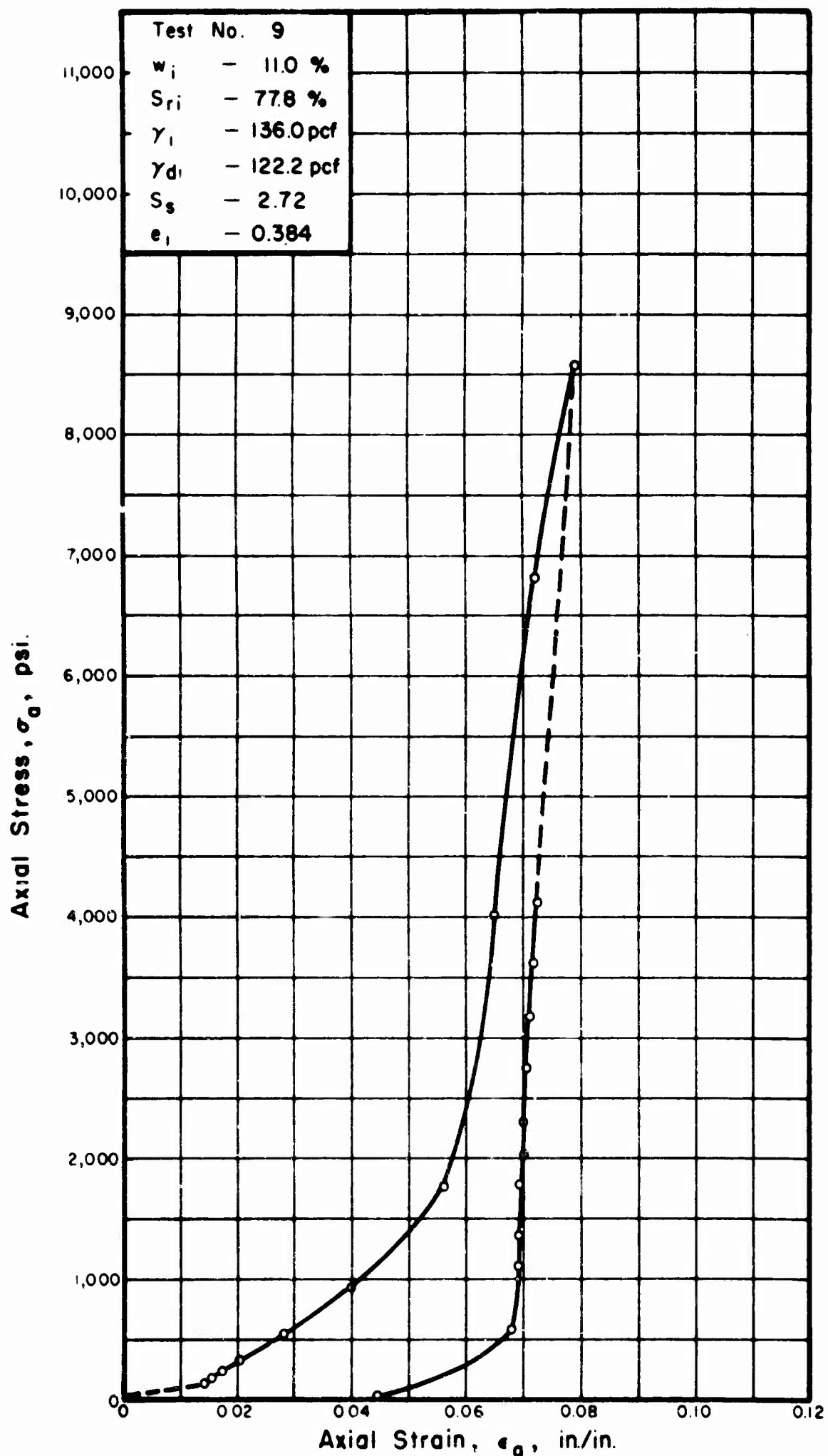
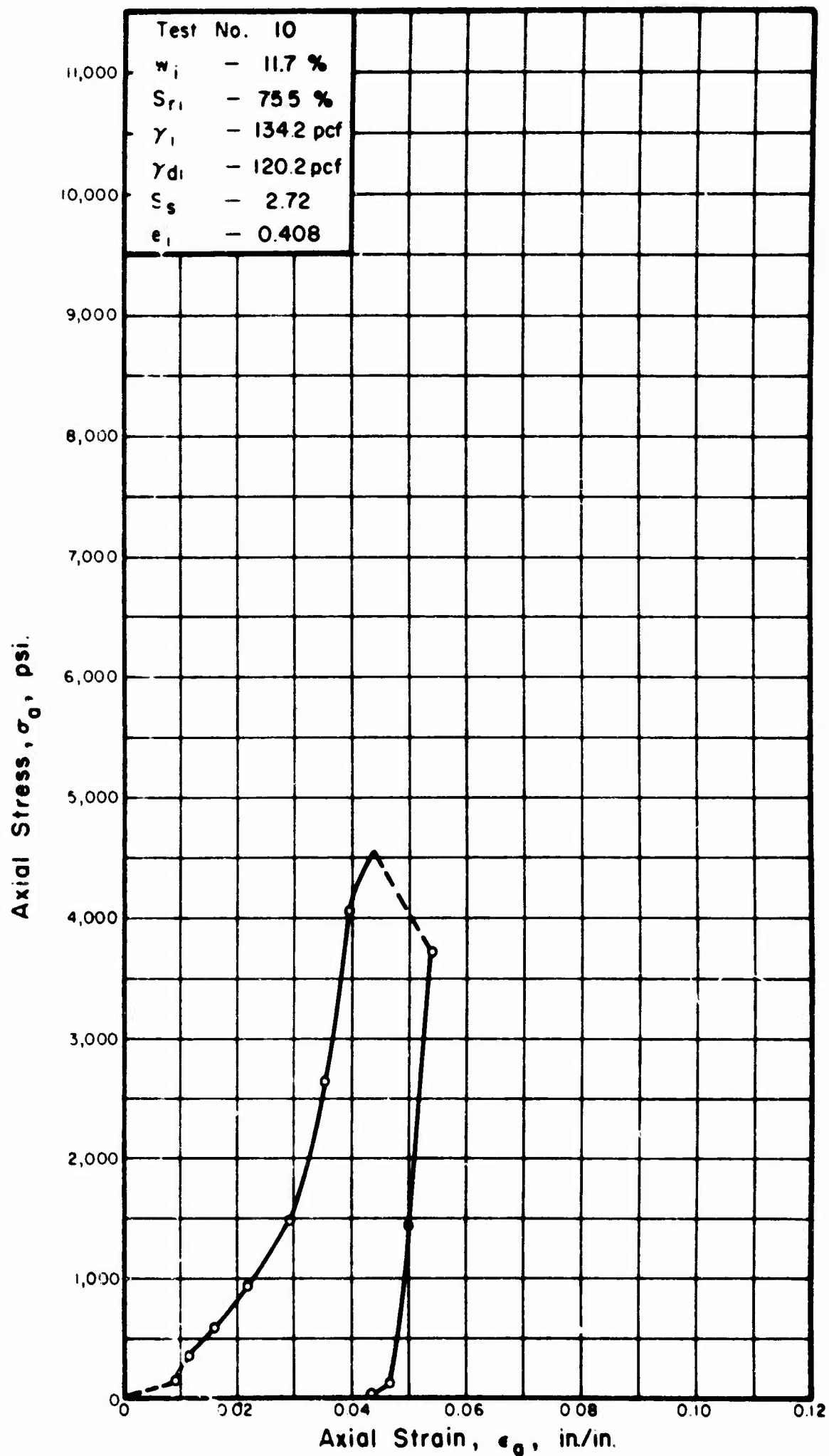


FIGURE A. 9. STRESS-STRAIN CURVE FOR GOOSE LAKE CLAY IN ONE-DIMENSIONAL COMPRESSION.



**FIGURE A.10 STRESS-STRAIN CURVE FOR GOOSE LAKE CLAY
IN ONE-DIMENSIONAL COMPRESSION.**

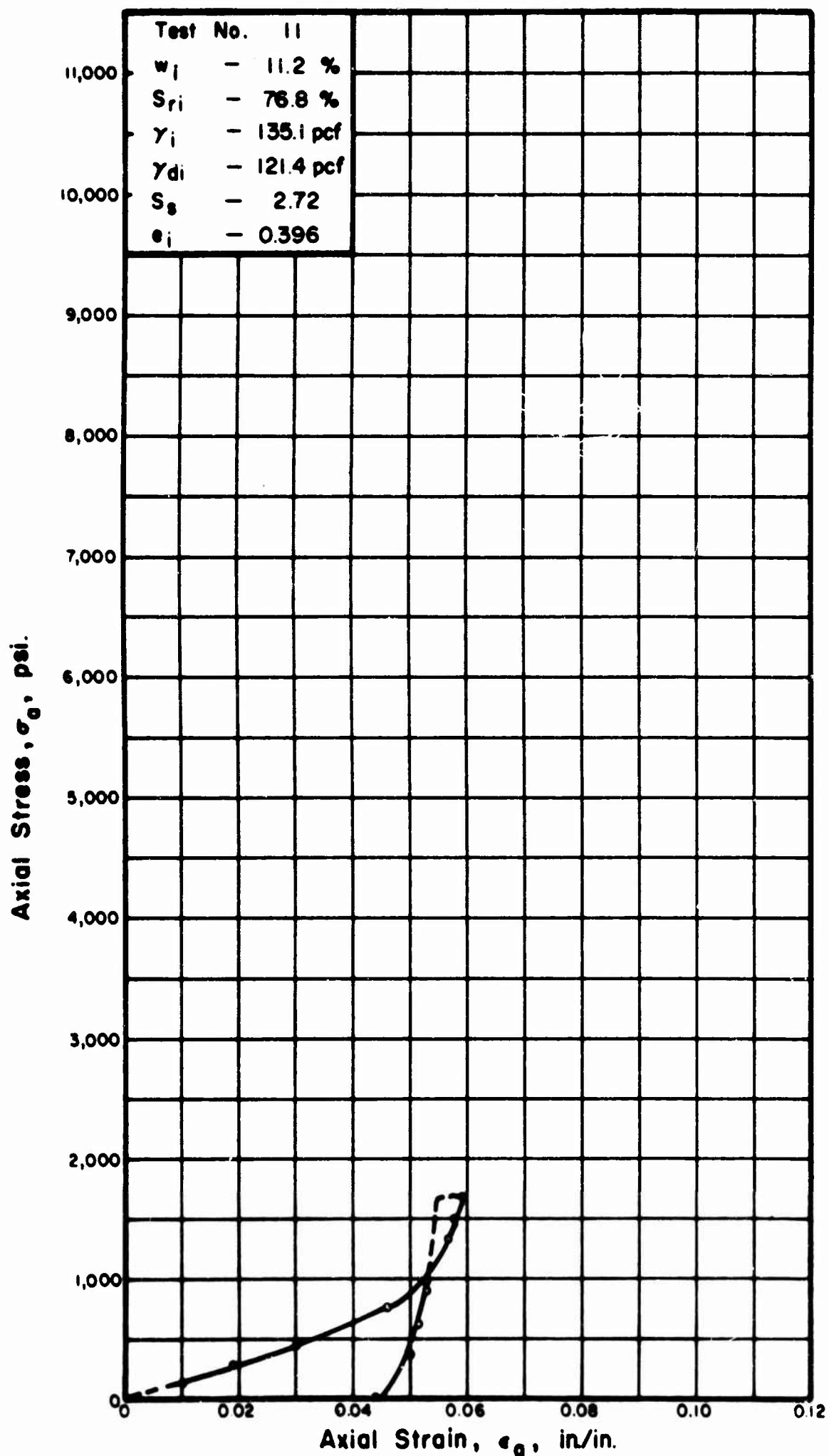


FIGURE A.11. STRESS-STRAIN CURVE FOR GOOSE LAKE CLAY IN ONE-DIMENSIONAL COMPRESSION.

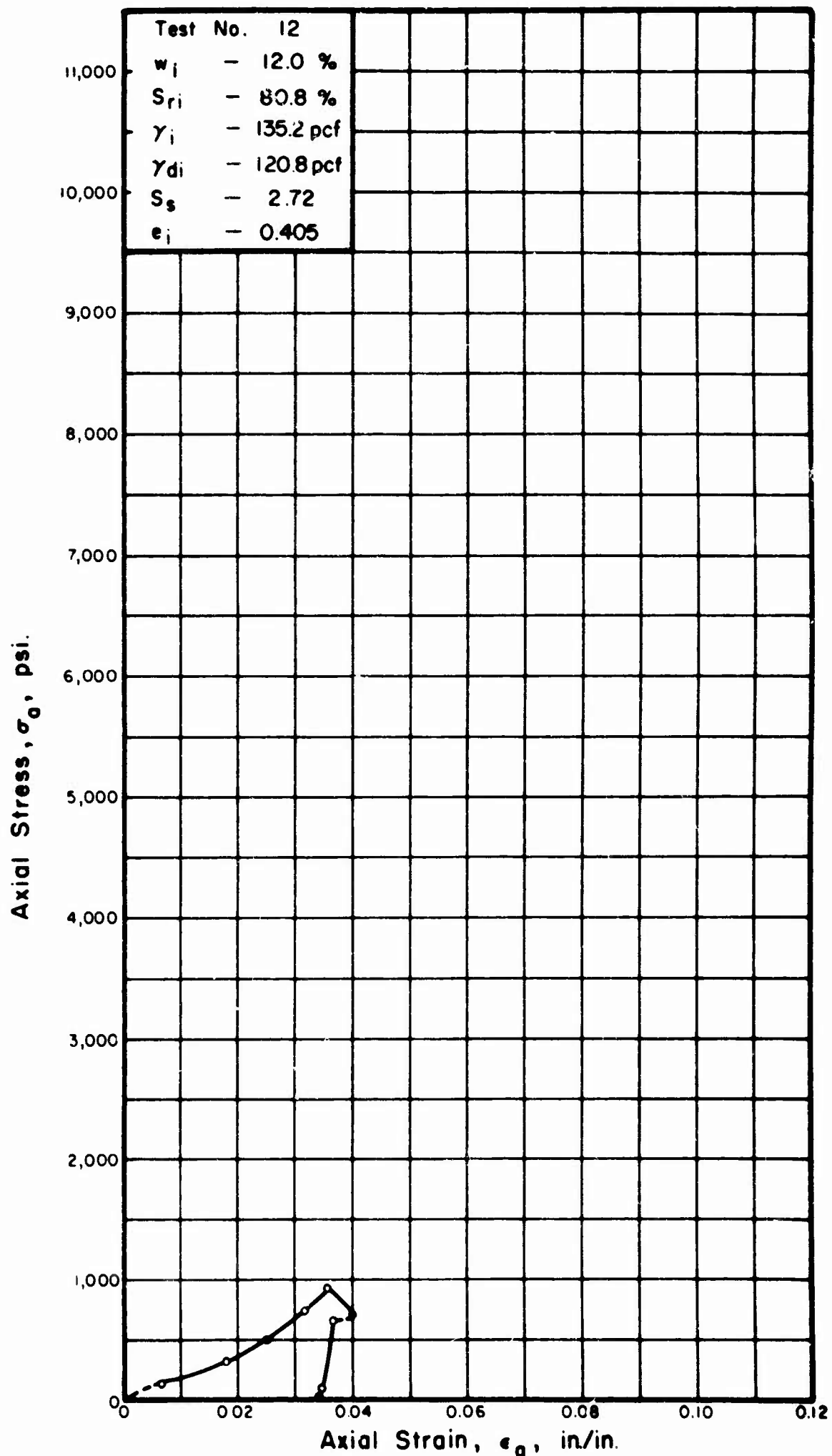


FIGURE A.12. STRESS-STRAIN CURVE FOR GOOSE LAKE CLAY IN ONE-DIMENSIONAL COMPRESSION.

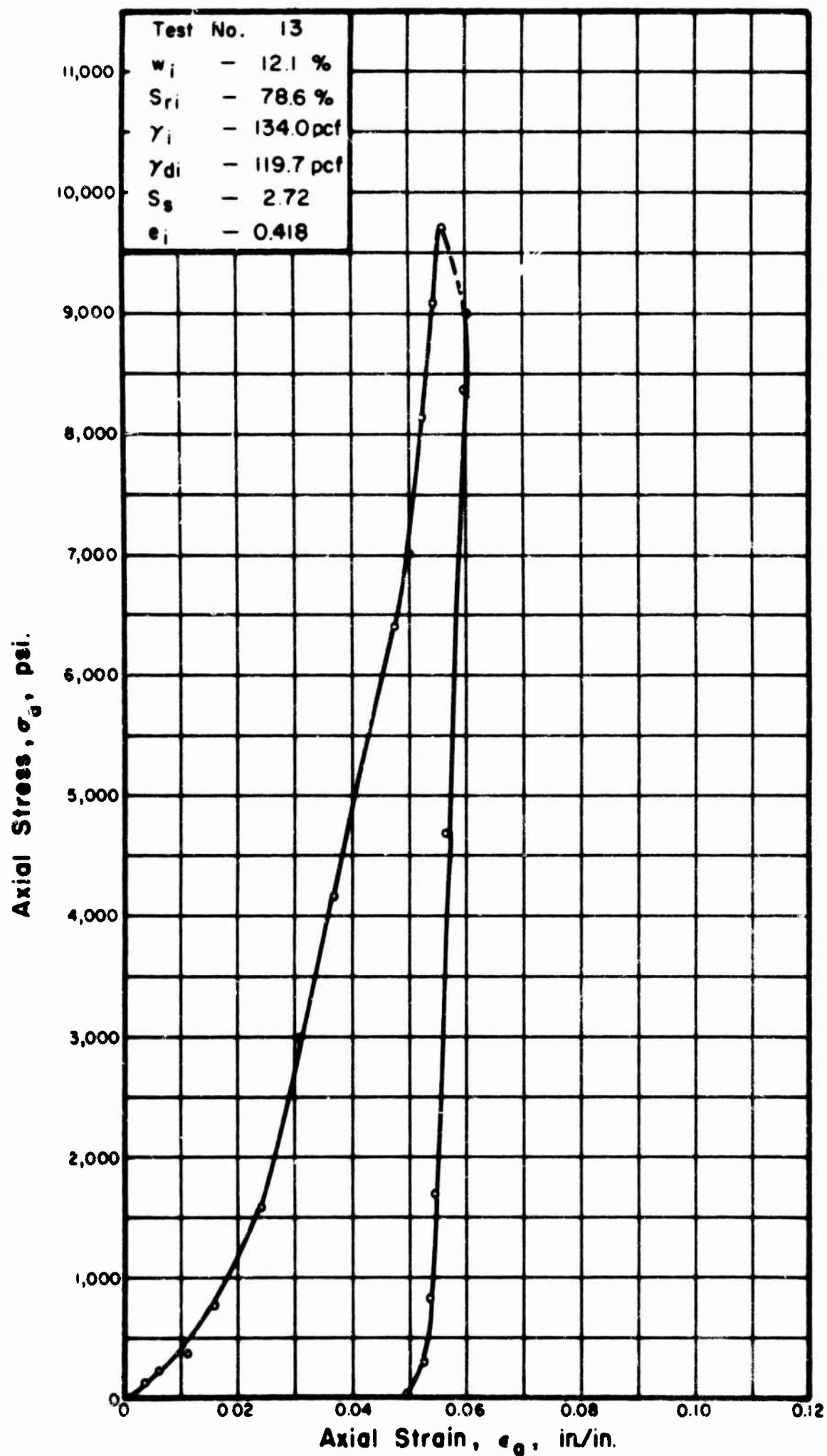


FIGURE A.13. STRESS-STRAIN CURVE FOR GOOSE LAKE CLAY IN ONE-DIMENSIONAL COMPRESSION.

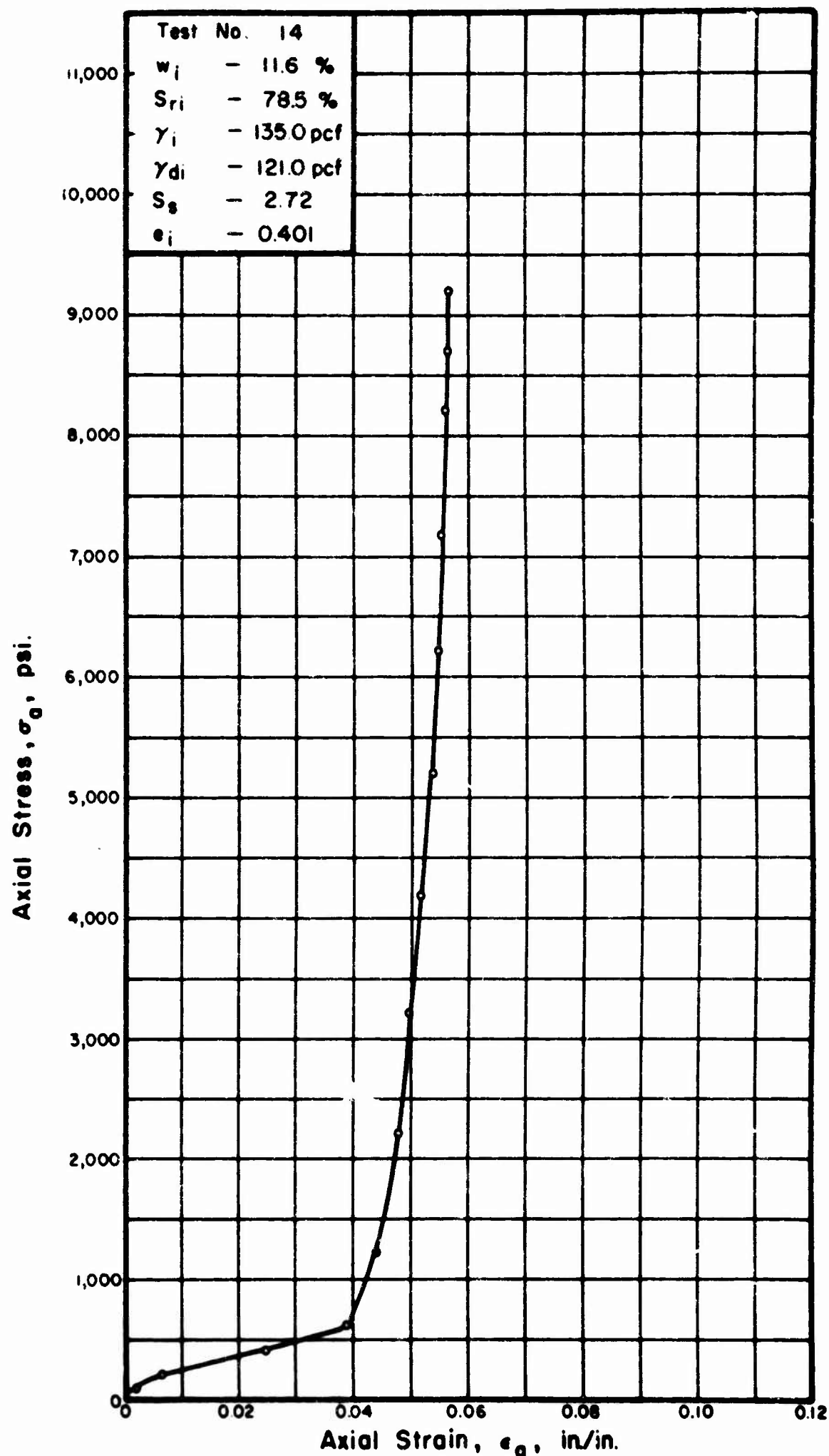


FIGURE A.14. STRESS-STRAIN CURVE FOR GOOSE LAKE CLAY IN ONE-DIMENSIONAL COMPRESSION.

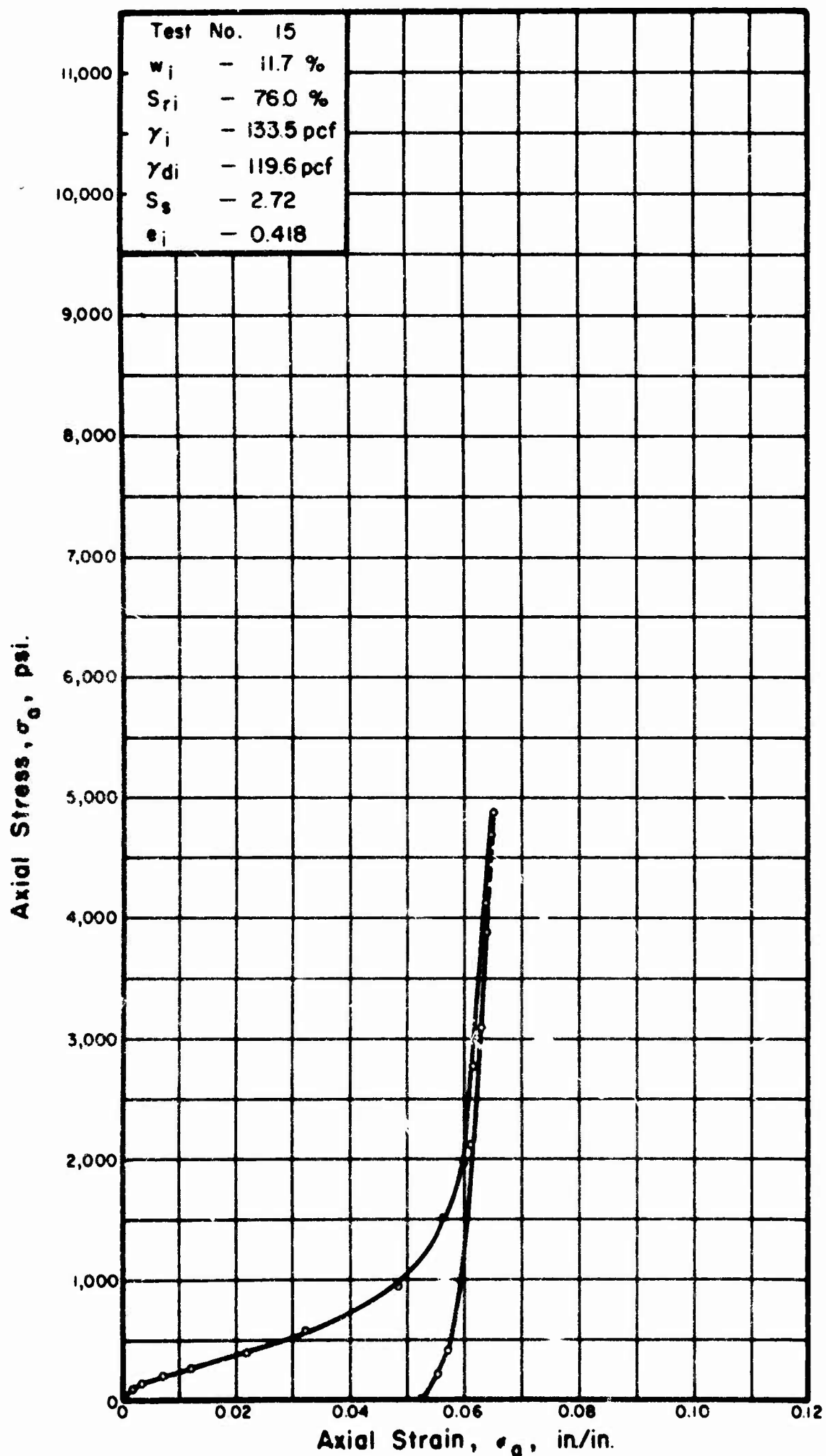


FIGURE A.15. STRESS-STRAIN CURVE FOR GOOSE LAKE CLAY IN ONE-DIMENSIONAL COMPRESSION.

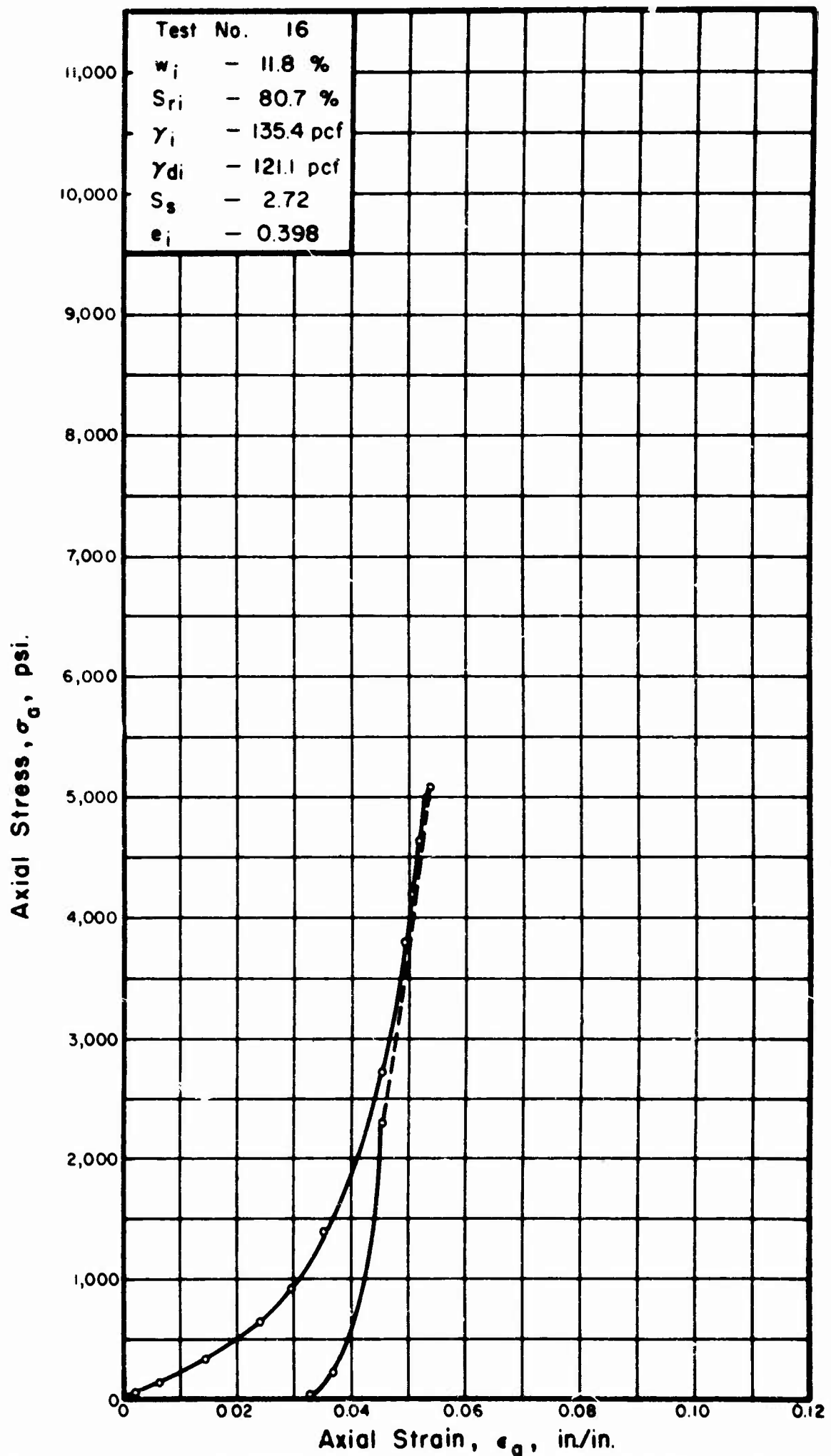


FIGURE A.16. STRESS-STRAIN CURVE FOR GOOSE LAKE CLAY IN ONE-DIMENSIONAL COMPRESSION.

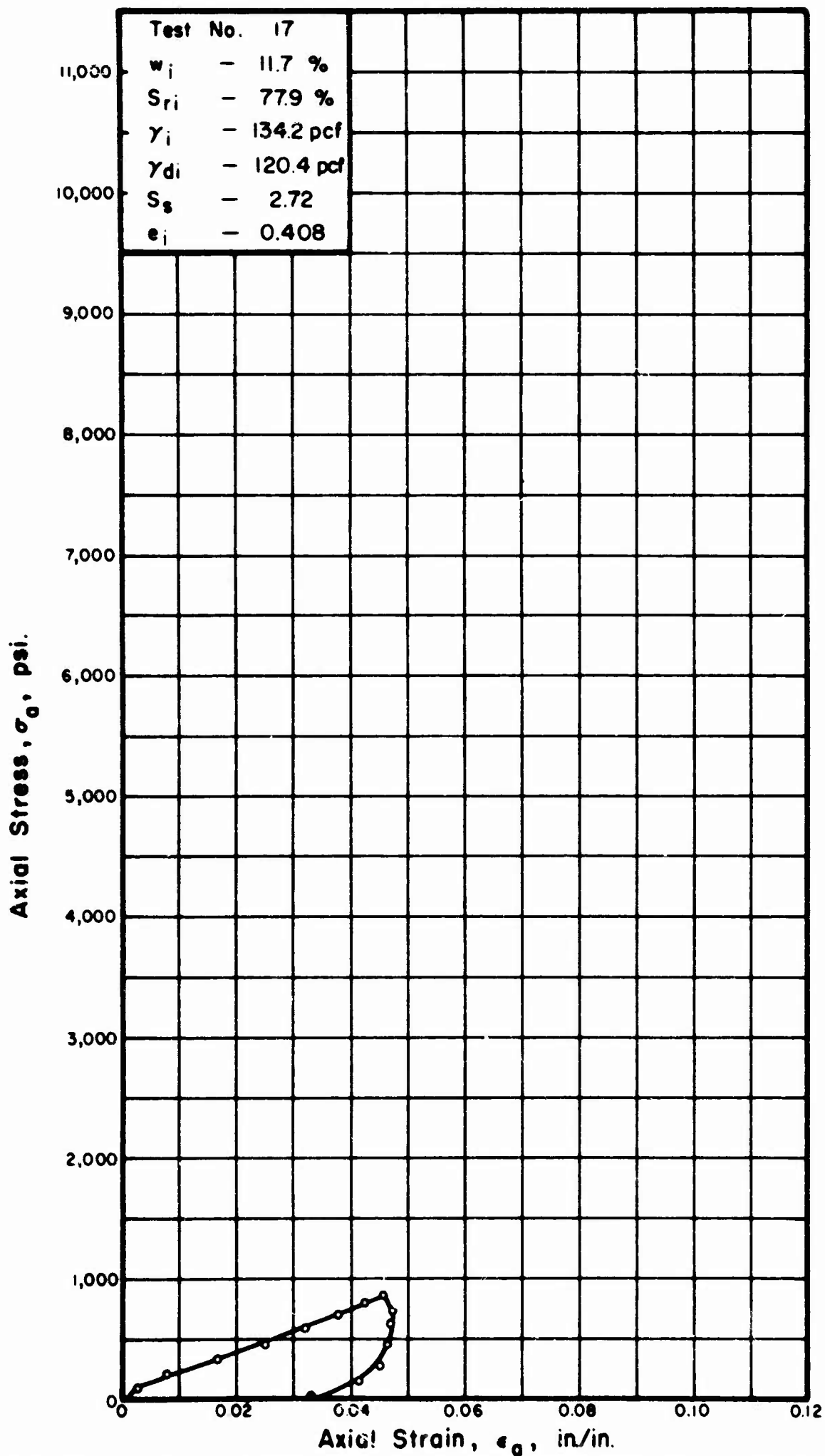


FIGURE A.17. STRESS-STRAIN CURVE FOR GOOSE LAKE CLAY IN ONE-DIMENSIONAL COMPRESSION.

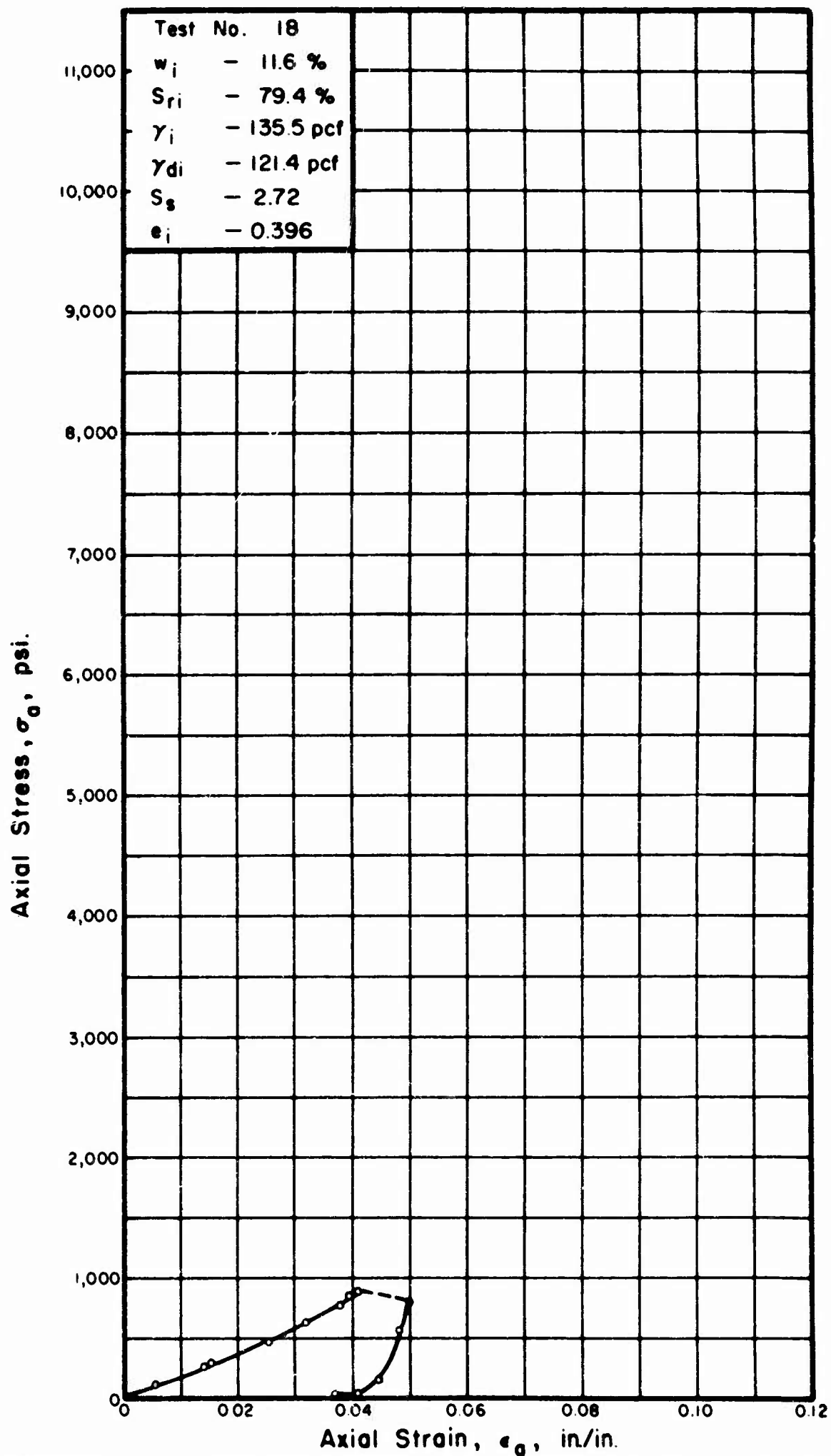


FIGURE A.18. STRESS-STRAIN CURVE FOR GOOSE LAKE CLAY IN ONE-DIMENSIONAL COMPRESSION.

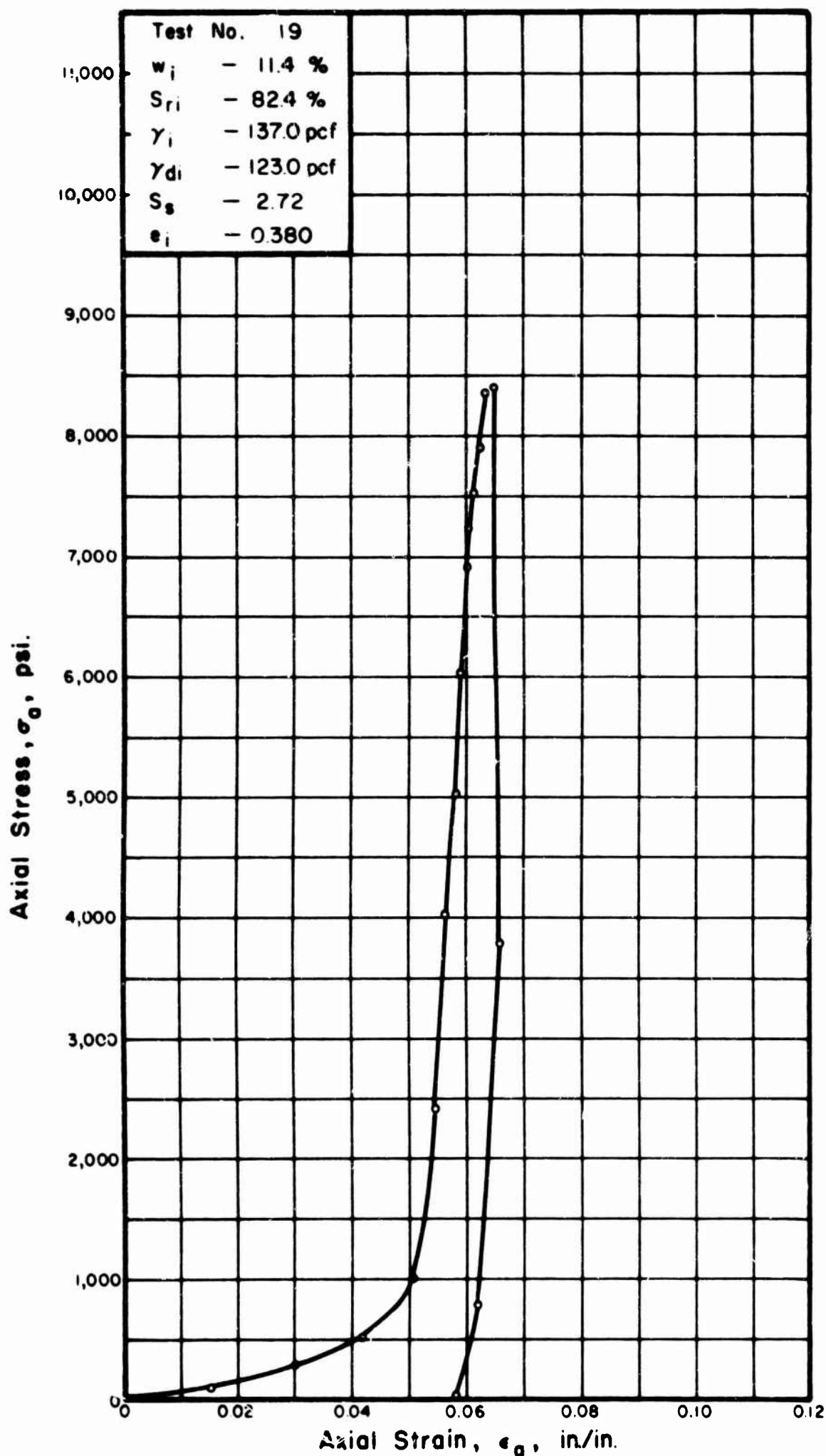


FIGURE A.19. STRESS-STRAIN CURVE FOR GOOSE LAKE CLAY IN ONE-DIMENSIONAL COMPRESSION.

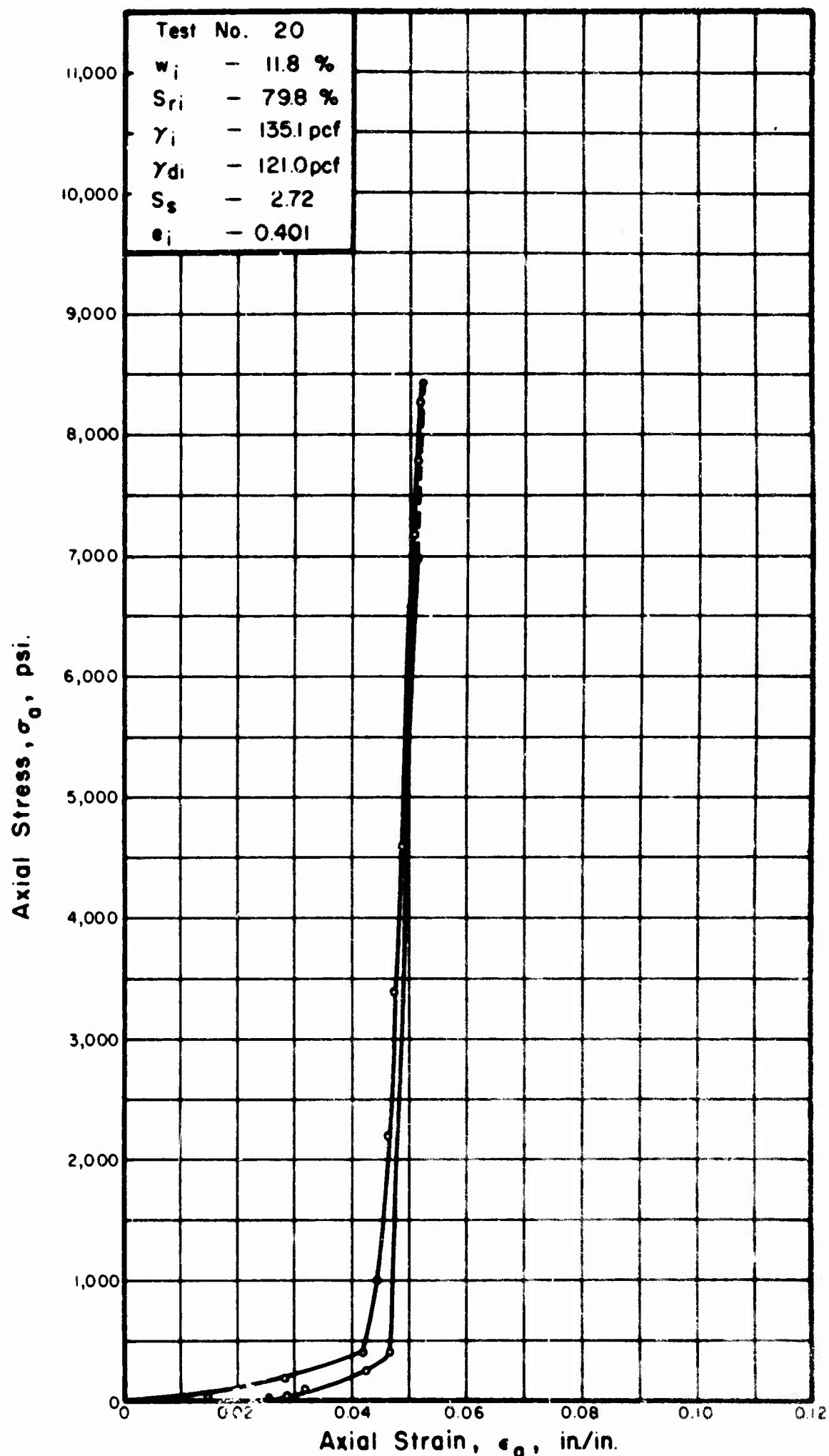


FIGURE A.20. STRESS-STRAIN CURVE FOR GOOSE LAKE CLAY IN ONE-DIMENSIONAL COMPRESSION.

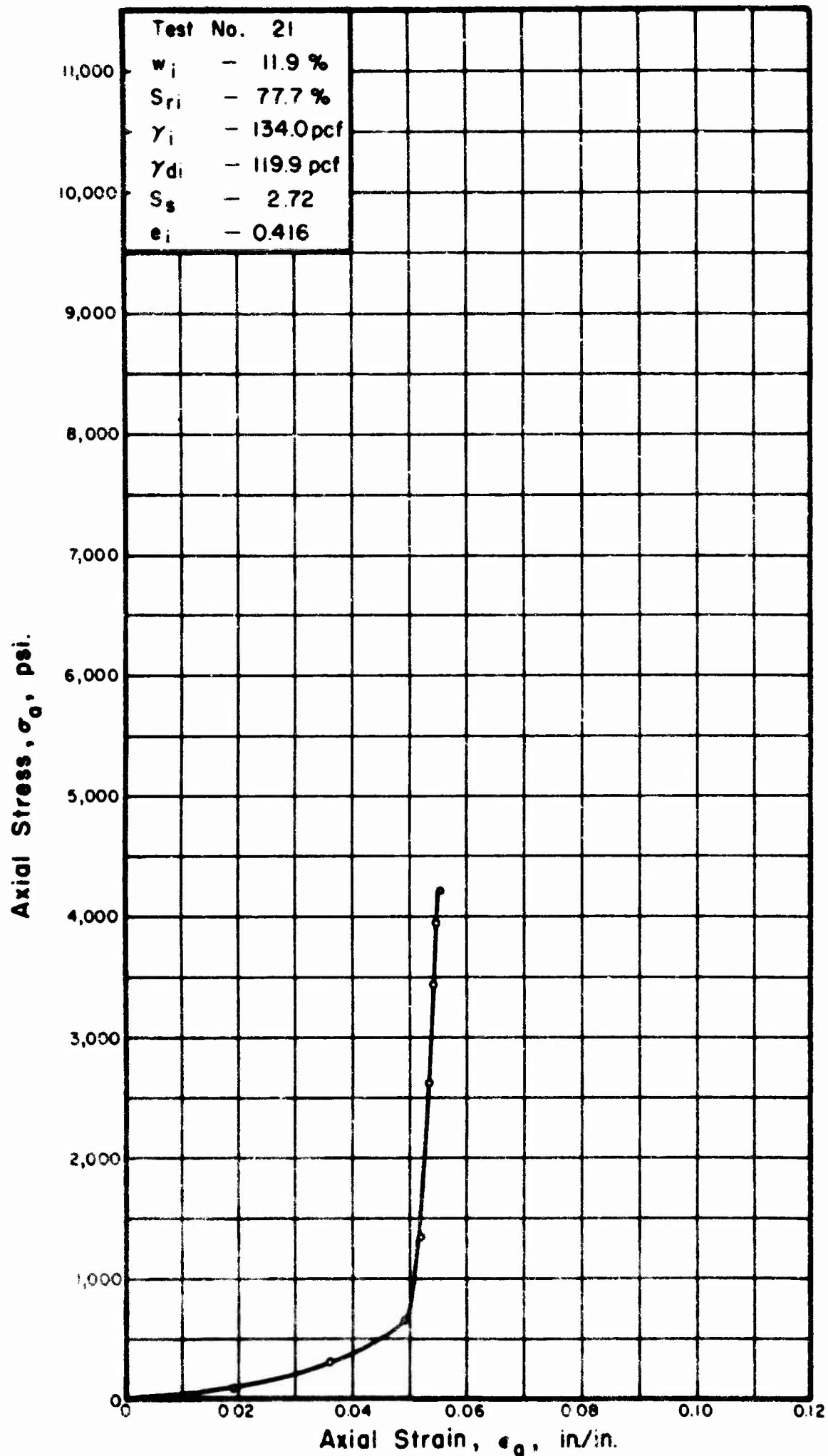


FIGURE A.21. STRESS-STRAIN CURVE FOR GOOSE LAKE CLAY IN ONE-DIMENSIONAL COMPRESSION.

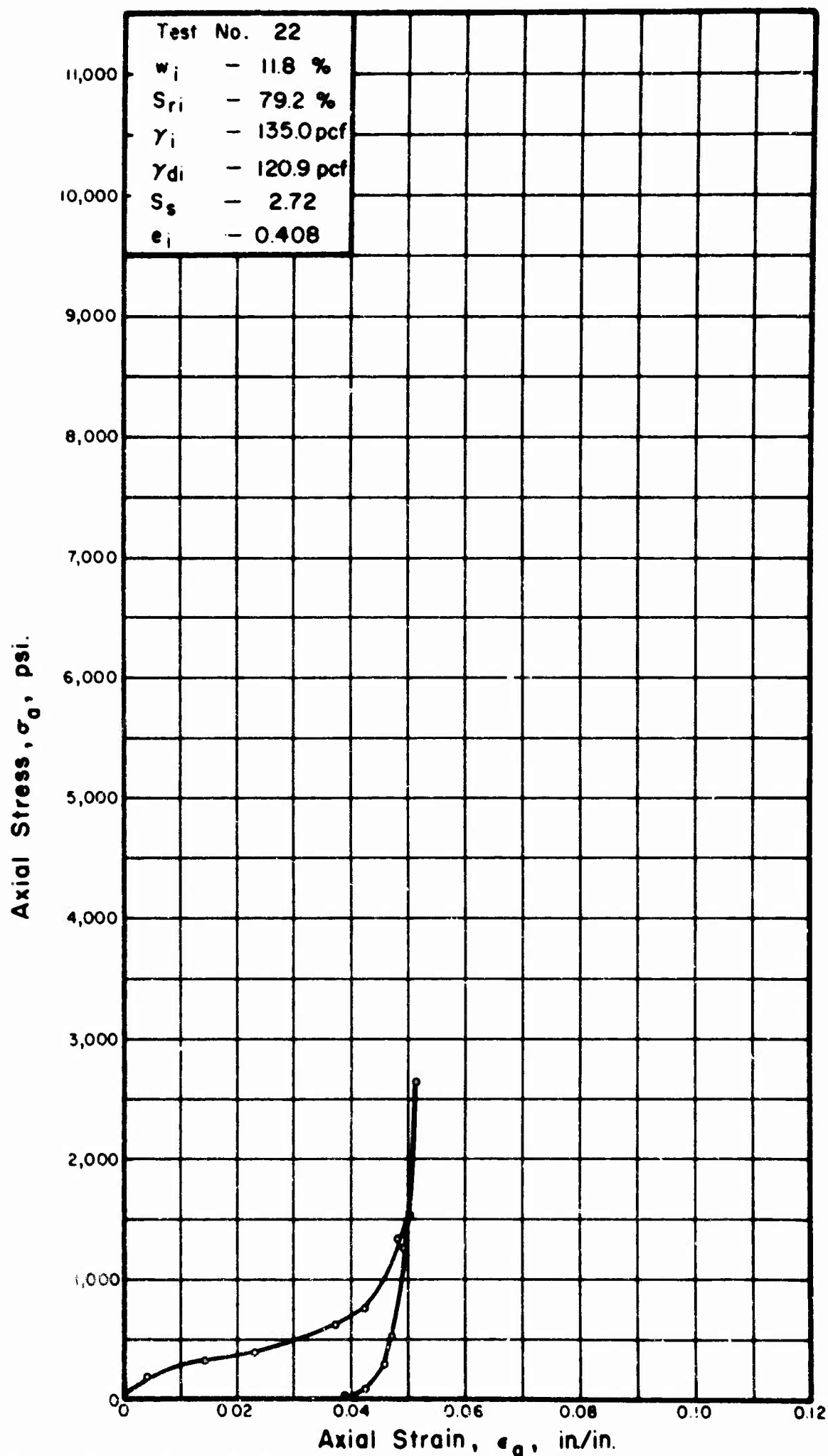


FIGURE A.22. STRESS-STRAIN CURVE FOR GOOSE LAKE CLAY IN ONE-DIMENSIONAL COMPRESSION.

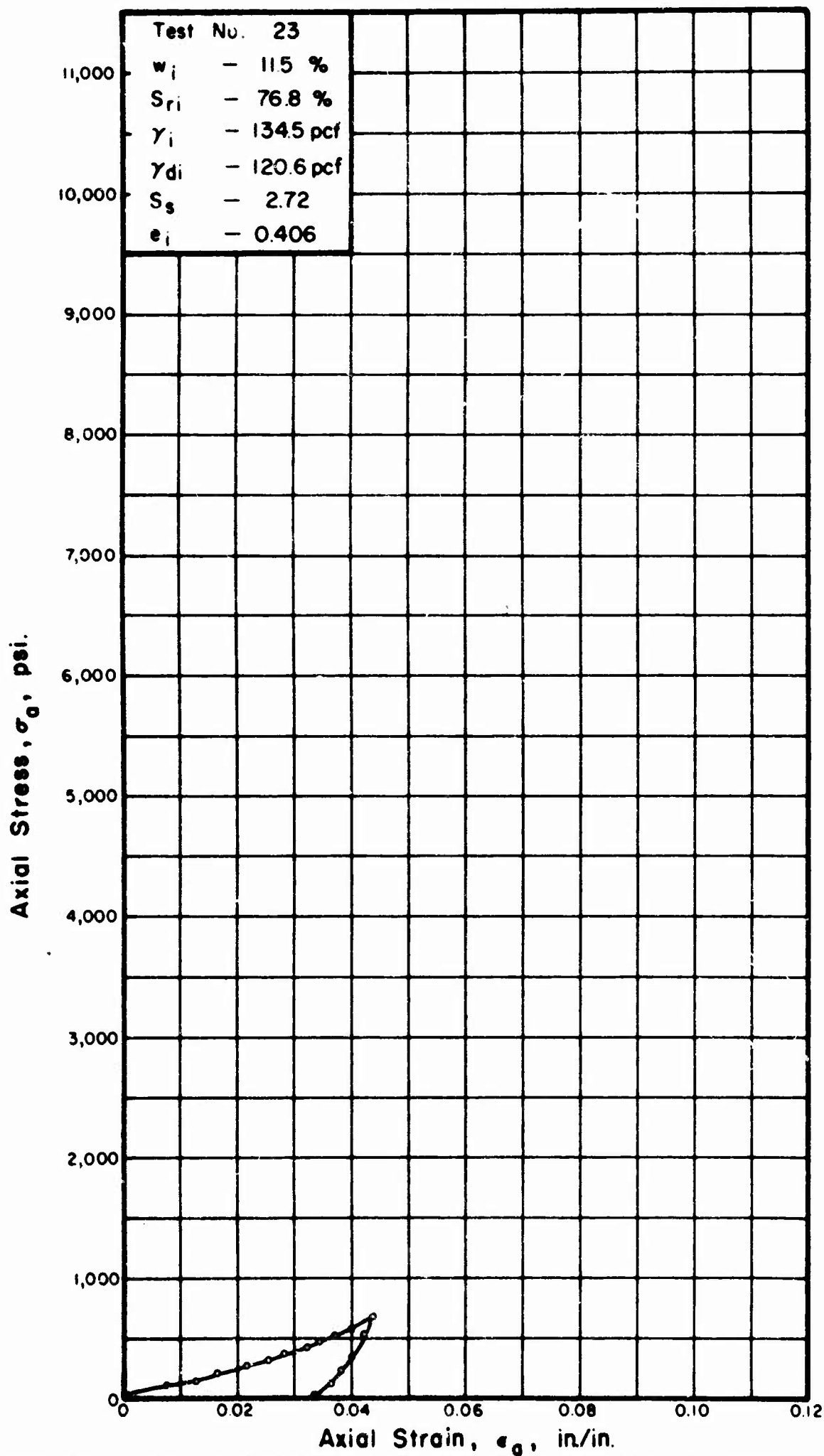


FIGURE A.23. STRESS-STRAIN CURVE FOR GOOSE LAKE CLAY IN ONE-DIMENSIONAL COMPRESSION.

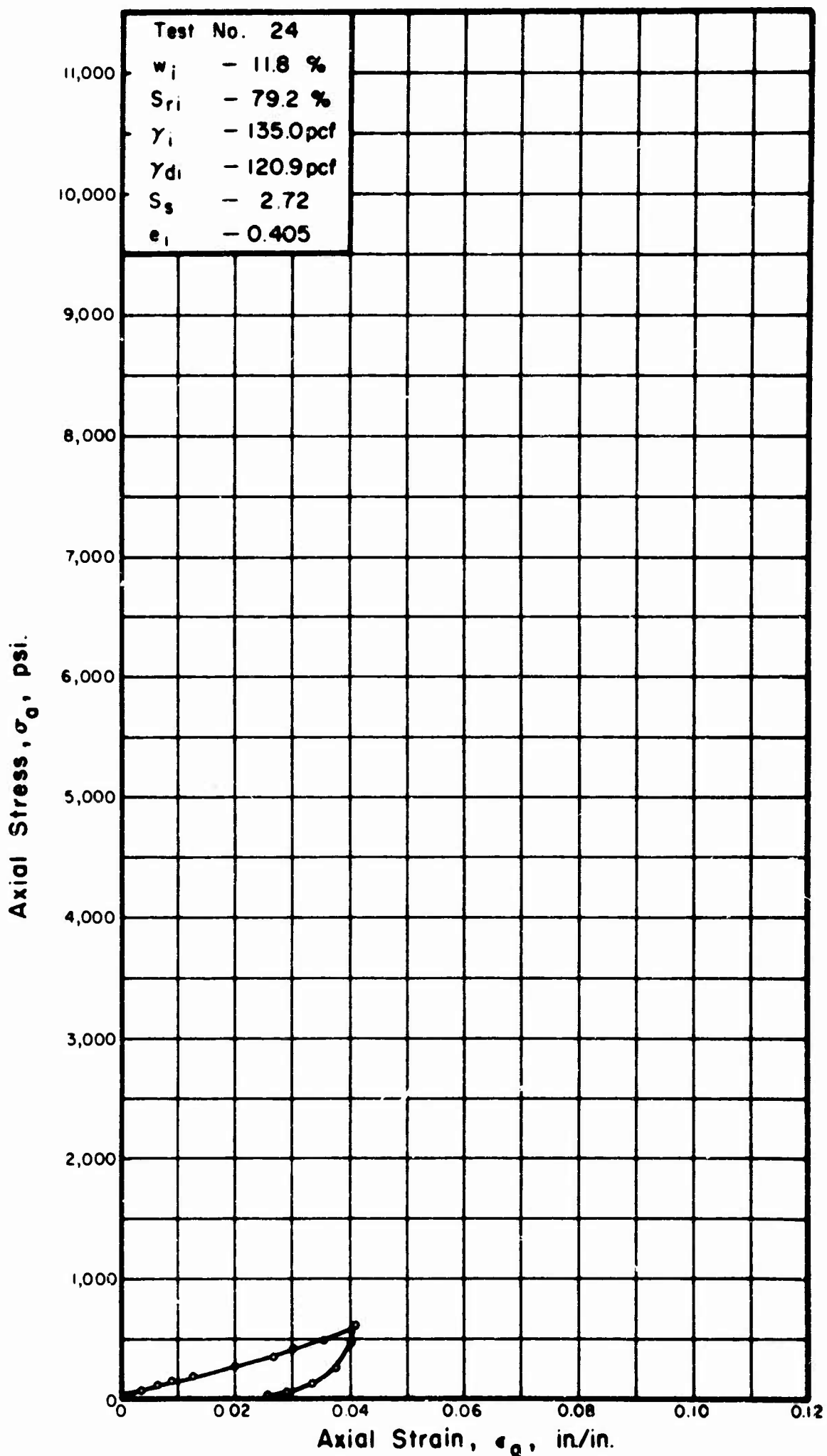


FIGURE A.24. STRESS-STRAIN CURVE FOR GOOSE LAKE CLAY IN ONE-DIMENSIONAL COMPRESSION.

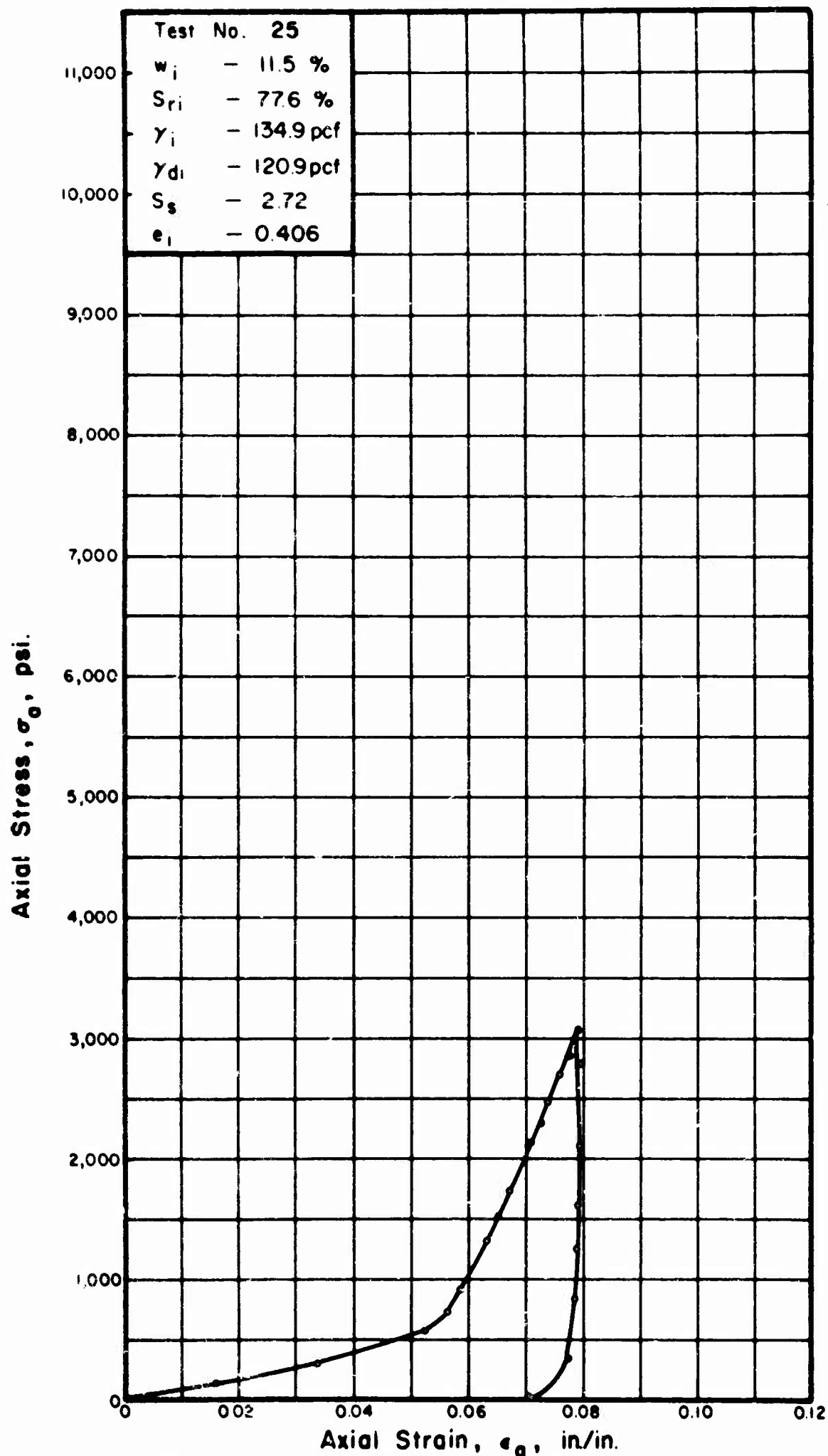


FIGURE A.25. STRESS-STRAIN CURVE FOR GOOSE LAKE CLAY IN ONE-DIMENSIONAL COMPRESSION.

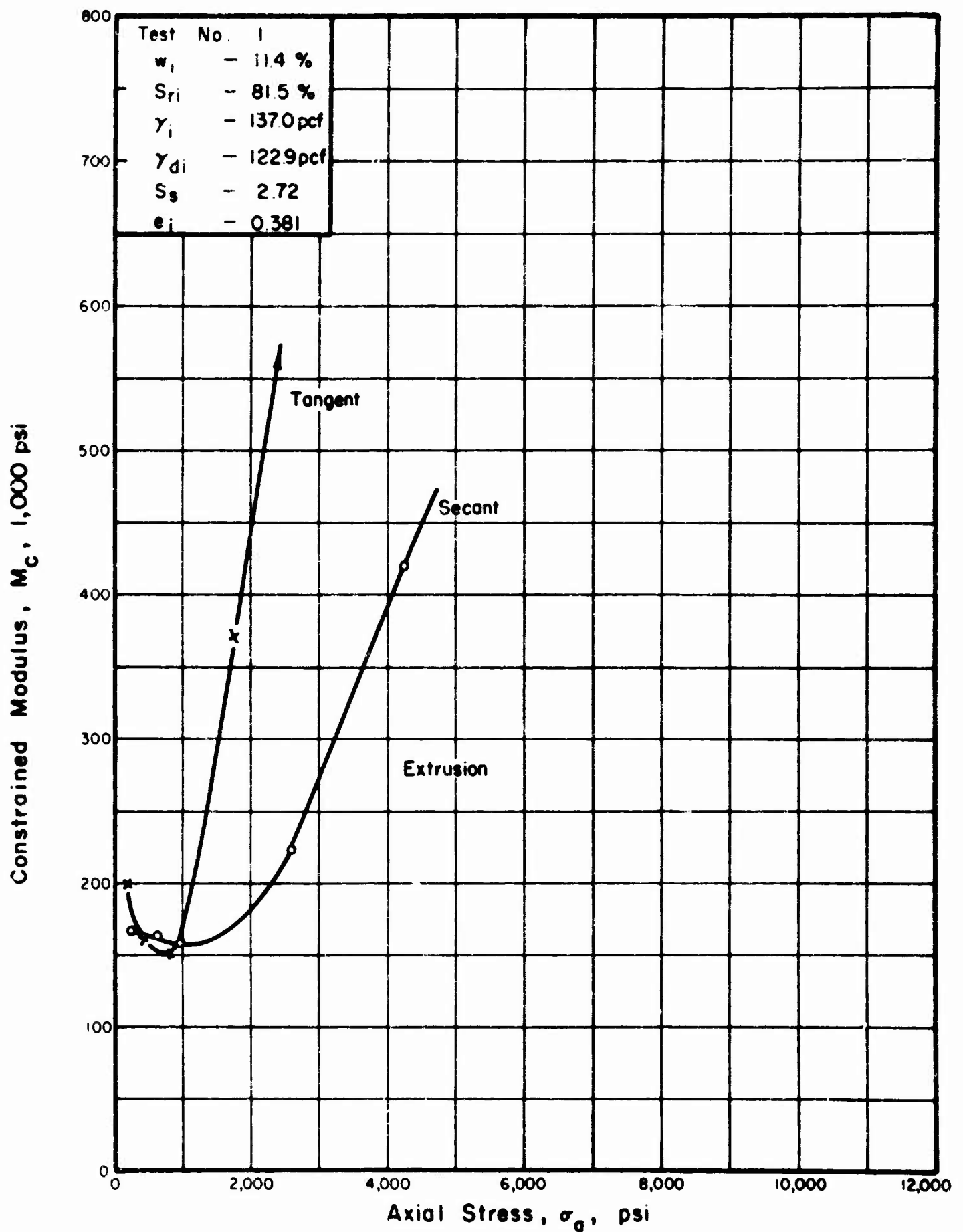


FIGURE A.26. RELATIONSHIP BETWEEN CONSTRAINED MODULUS AND AXIAL STRESS FOR GOOSE LAKE CLAY IN ONE DIMENSIONAL COMPRESSION.

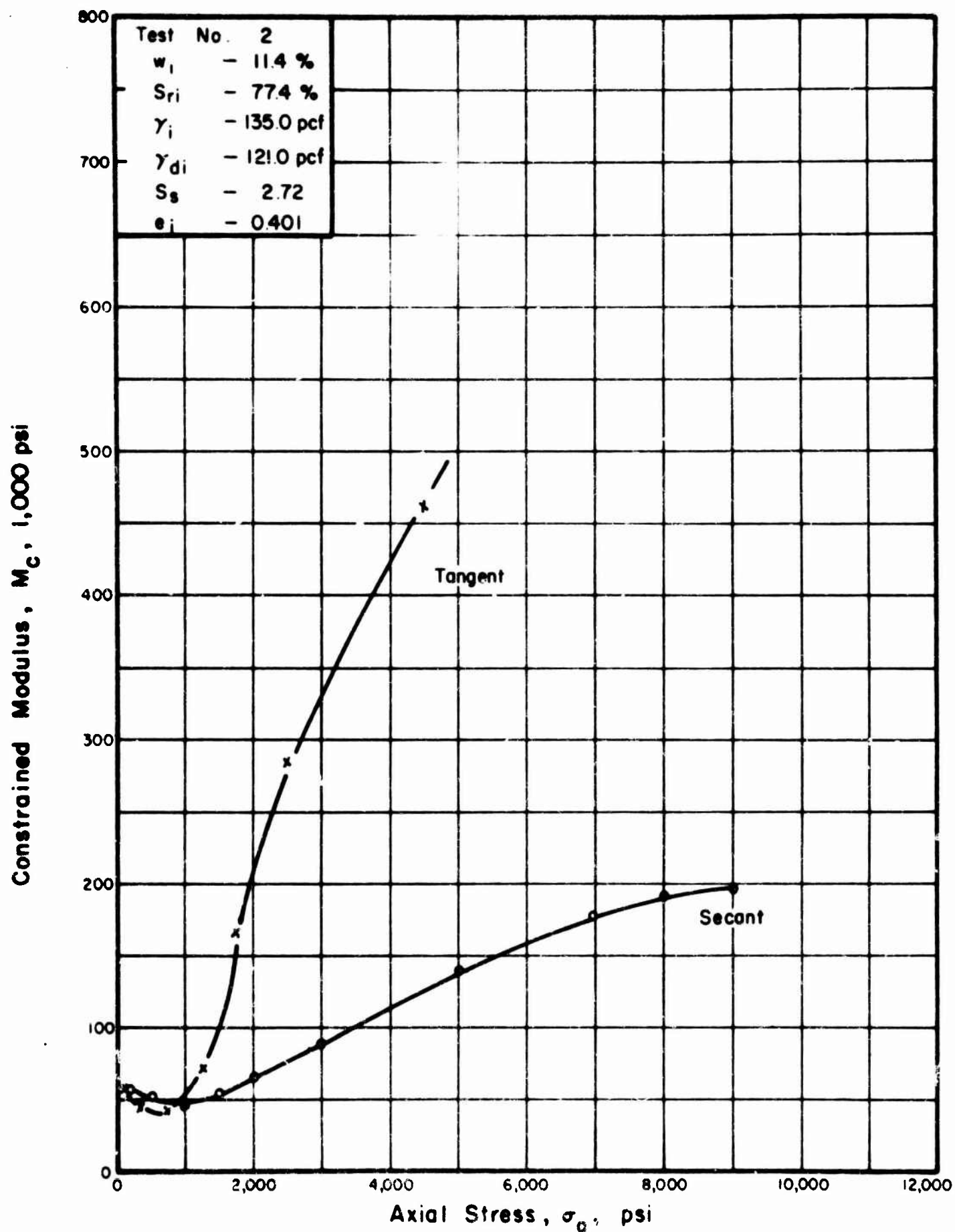


FIGURE A.27. RELATIONSHIP BETWEEN CONSTRAINED MODULUS AND AXIAL STRESS FOR GOOSE LAKE CLAY IN ONE DIMENSIONAL COMPRESSION.

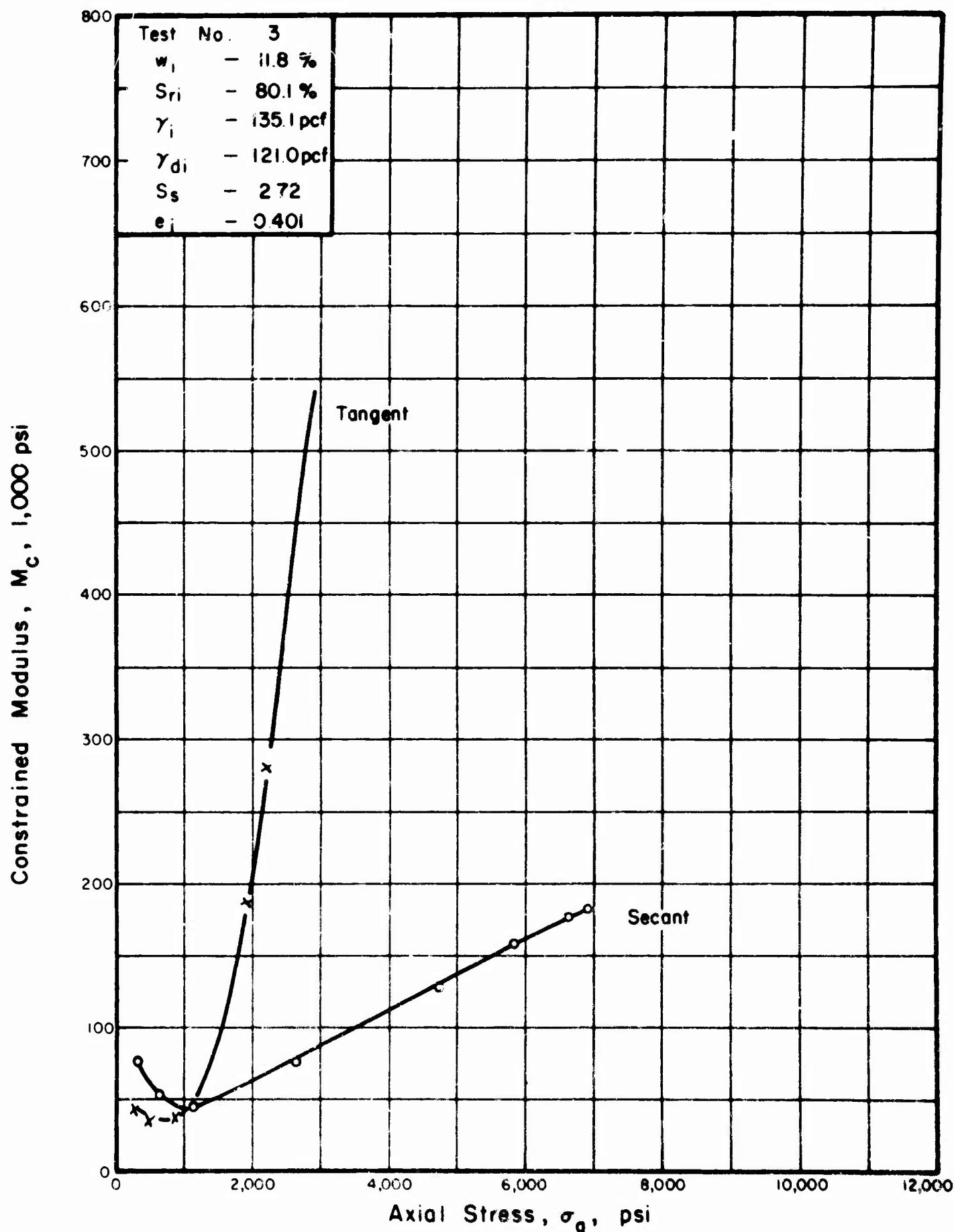


FIGURE A.28. RELATIONSHIP BETWEEN CONSTRAINED MODULUS AND AXIAL STRESS FOR GOOSE LAKE CLAY IN ONE DIMENSIONAL COMPRESSION.

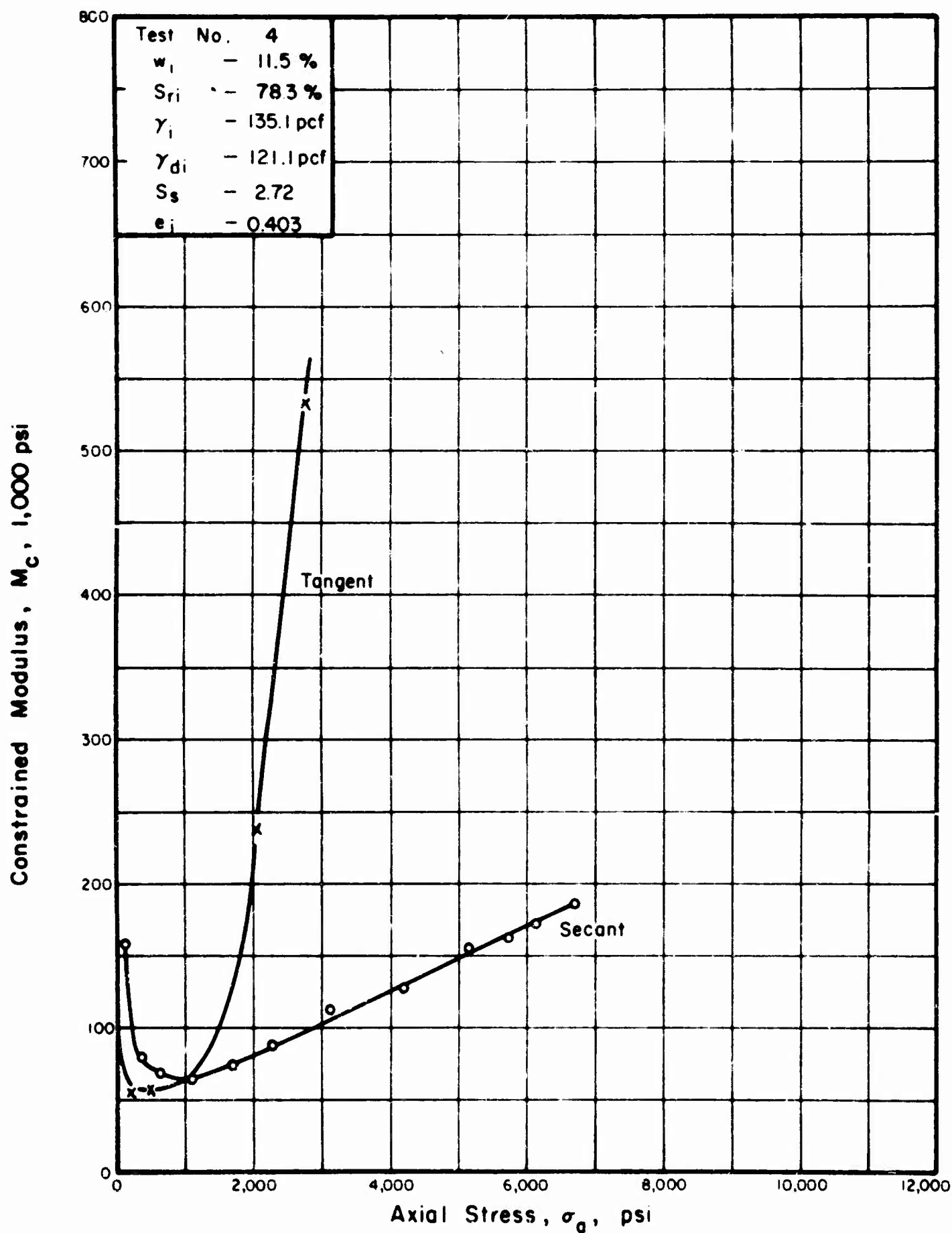


FIGURE A.29. RELATIONSHIP BETWEEN CONSTRAINED MODULUS AND AXIAL STRESS FOR GOOSE LAKE CLAY IN ONE DIMENSIONAL COMPRESSION.

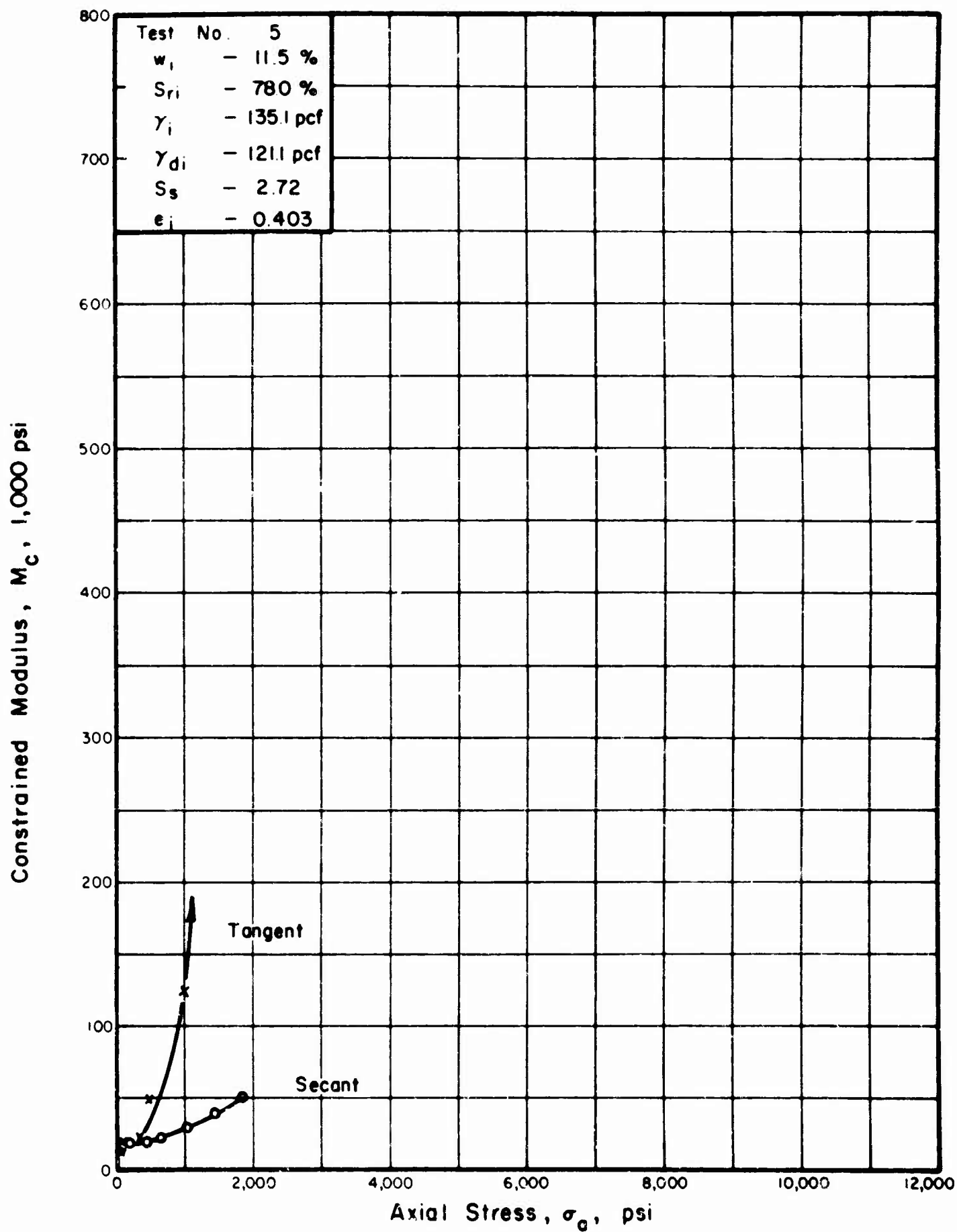


FIGURE A.30. RELATIONSHIP BETWEEN CONSTRAINED MODULUS AND AXIAL STRESS FOR GOOSE LAKE CLAY IN ONE DIMENSIONAL COMPRESSION.

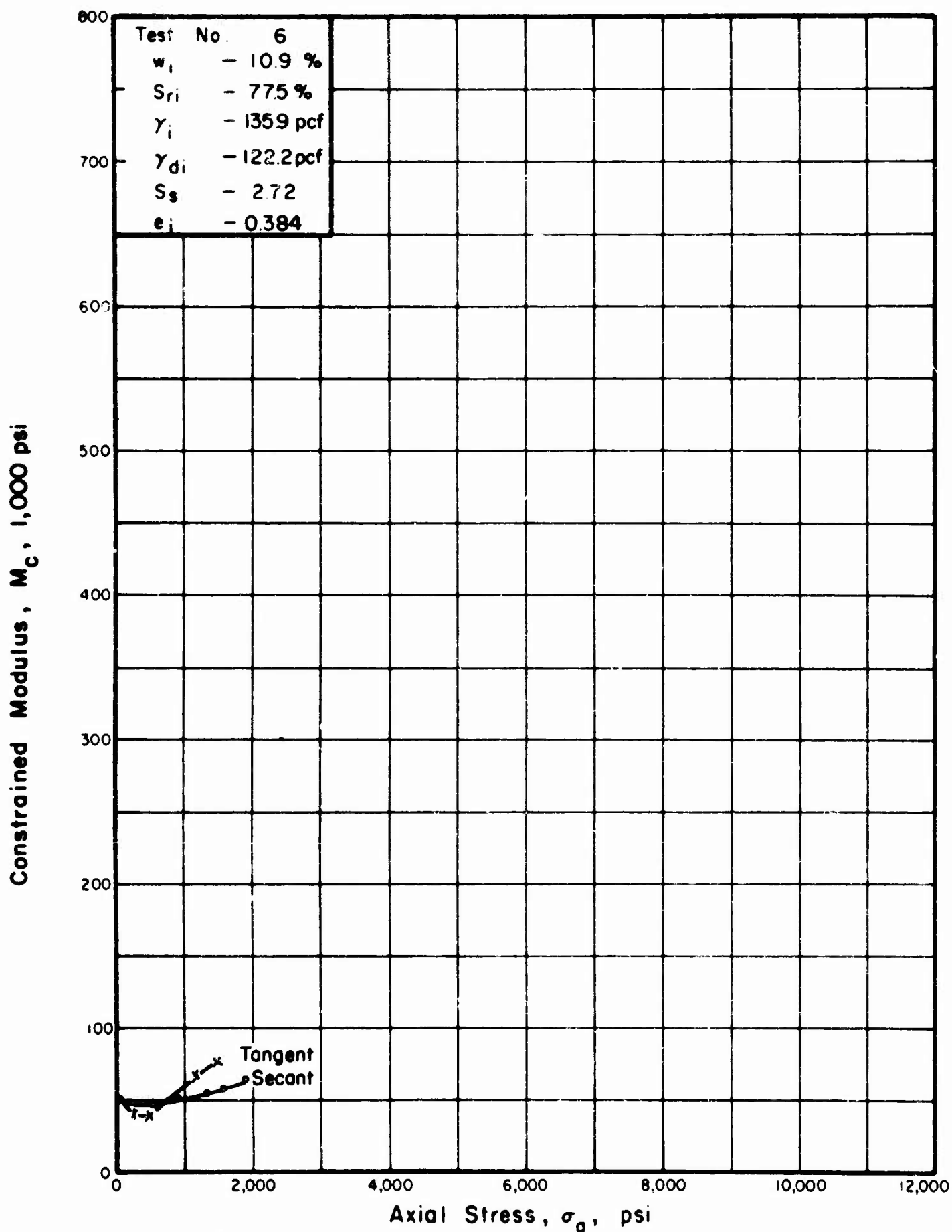


FIGURE A.31. RELATIONSHIP BETWEEN CONSTRAINED MODULUS AND AXIAL STRESS FOR GOOSE LAKE CLAY IN ONE DIMENSIONAL COMPRESSION.

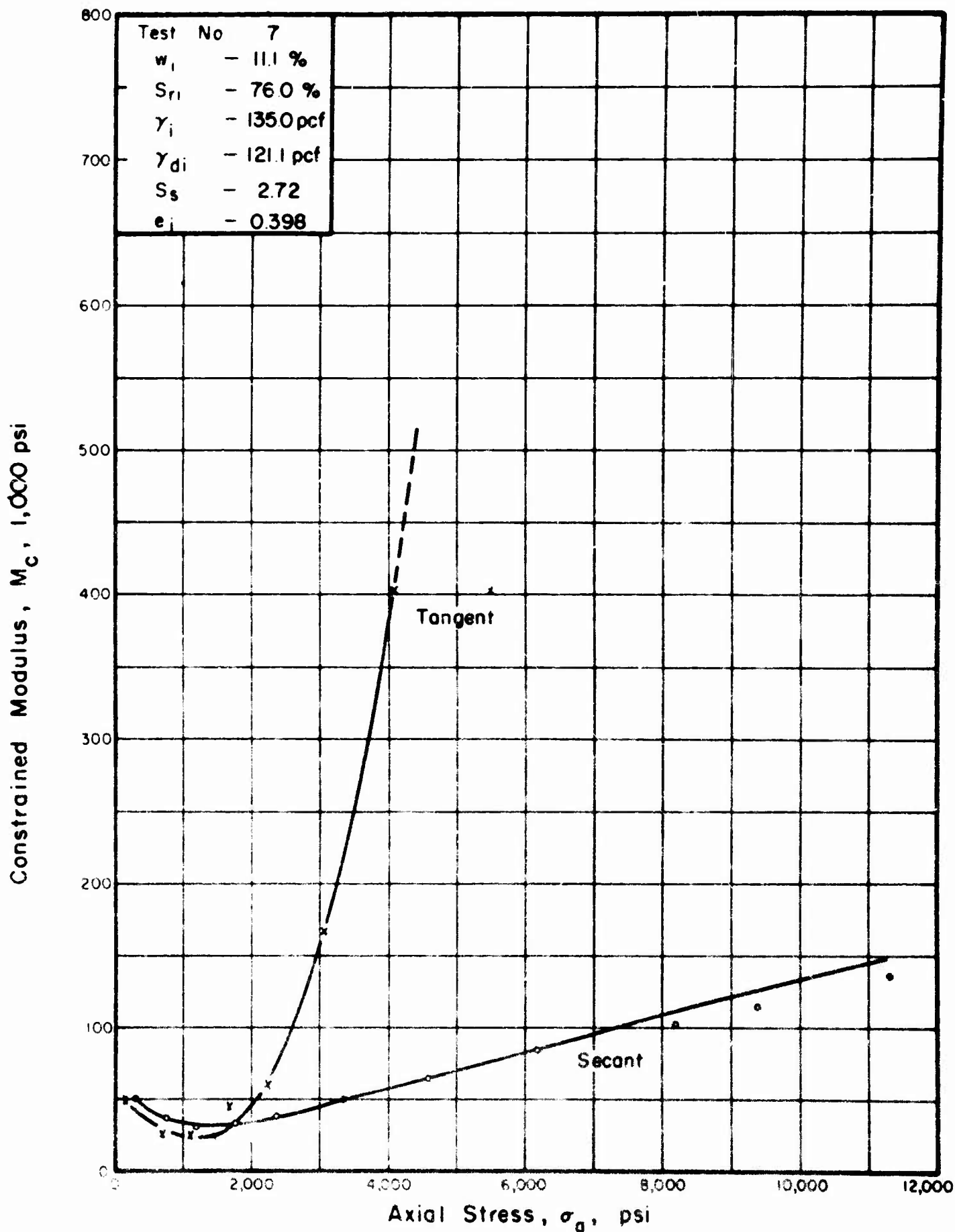


FIGURE A.32. RELATIONSHIP BETWEEN CONSTRAINED MODULUS AND AXIAL STRESS FOR GOOSE LAKE CLAY IN ONE DIMENSIONAL COMPRESSION.

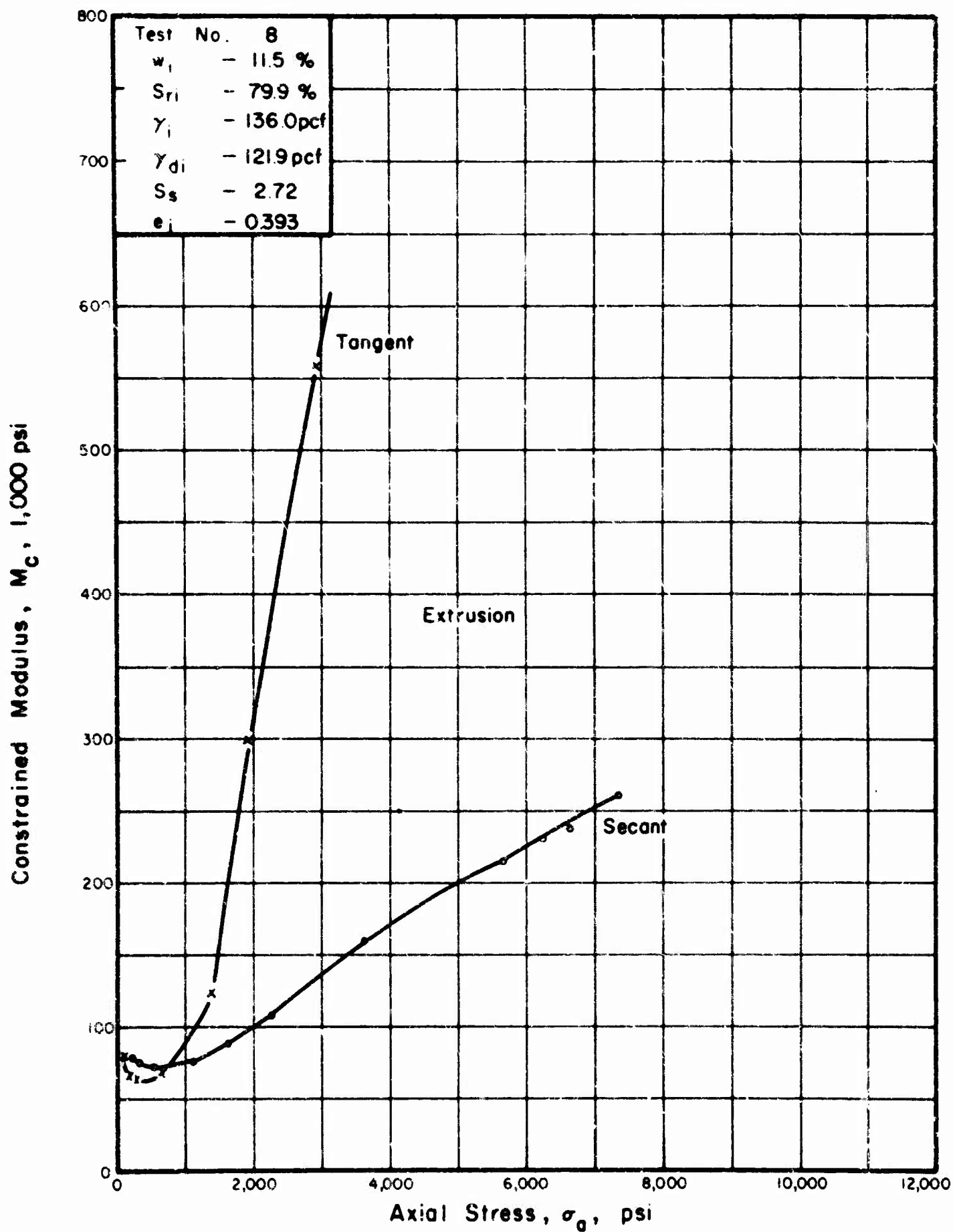


FIGURE A.33. RELATIONSHIP BETWEEN CONSTRAINED MODULUS AND AXIAL STRESS FOR GOOSE LAKE CLAY IN ONE DIMENSIONAL COMPRESSION.

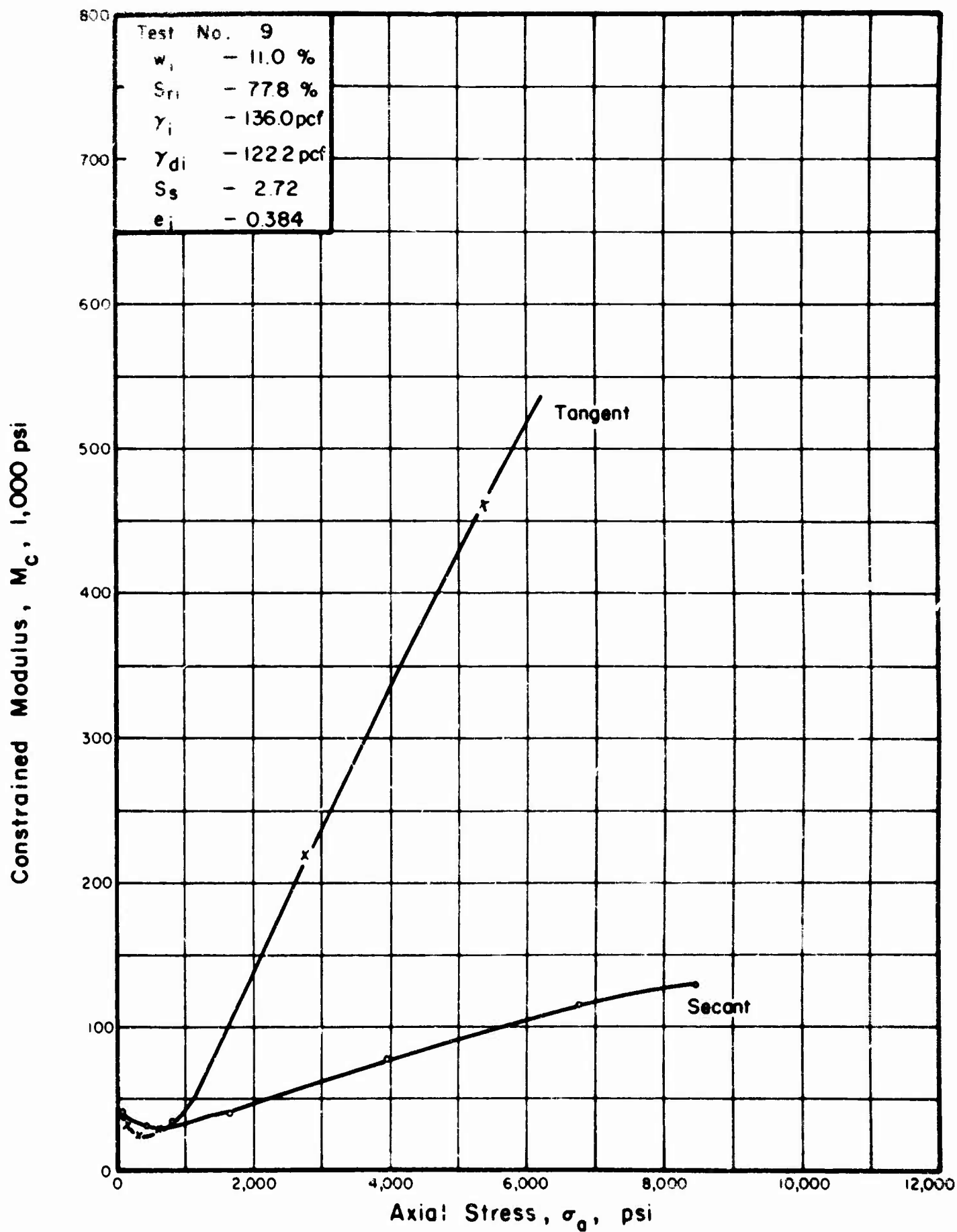


FIGURE A.34. RELATIONSHIP BETWEEN CONSTRAINED MODULUS AND AXIAL STRESS FOR GOOSE LAKE CLAY IN ONE DIMENSIONAL COMPRESSION.

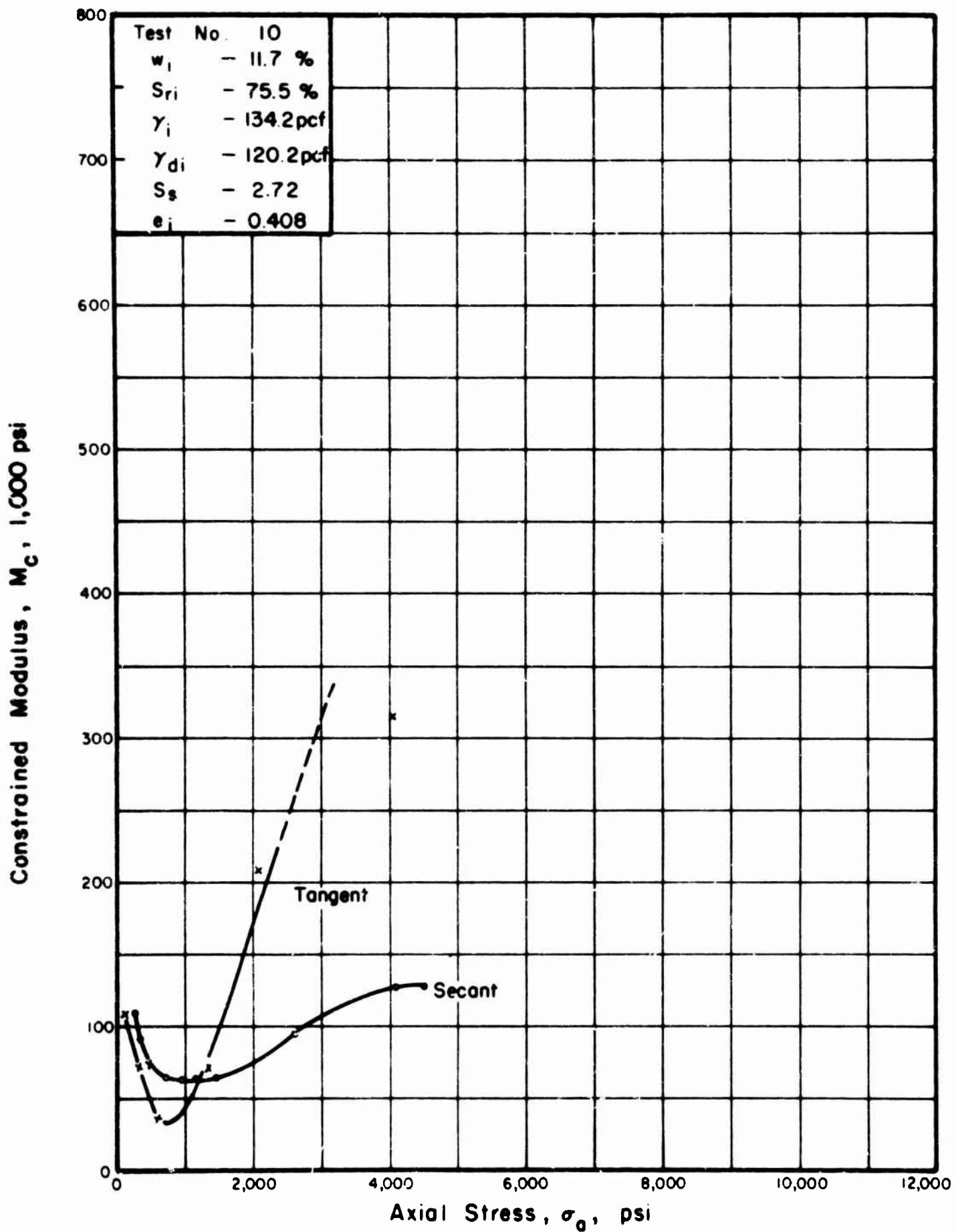


FIGURE A.35. RELATIONSHIP BETWEEN CONSTRAINED MODULUS AND AXIAL STRESS FOR GOOSE LAKE CLAY IN ONE DIMENSIONAL COMPRESSION.

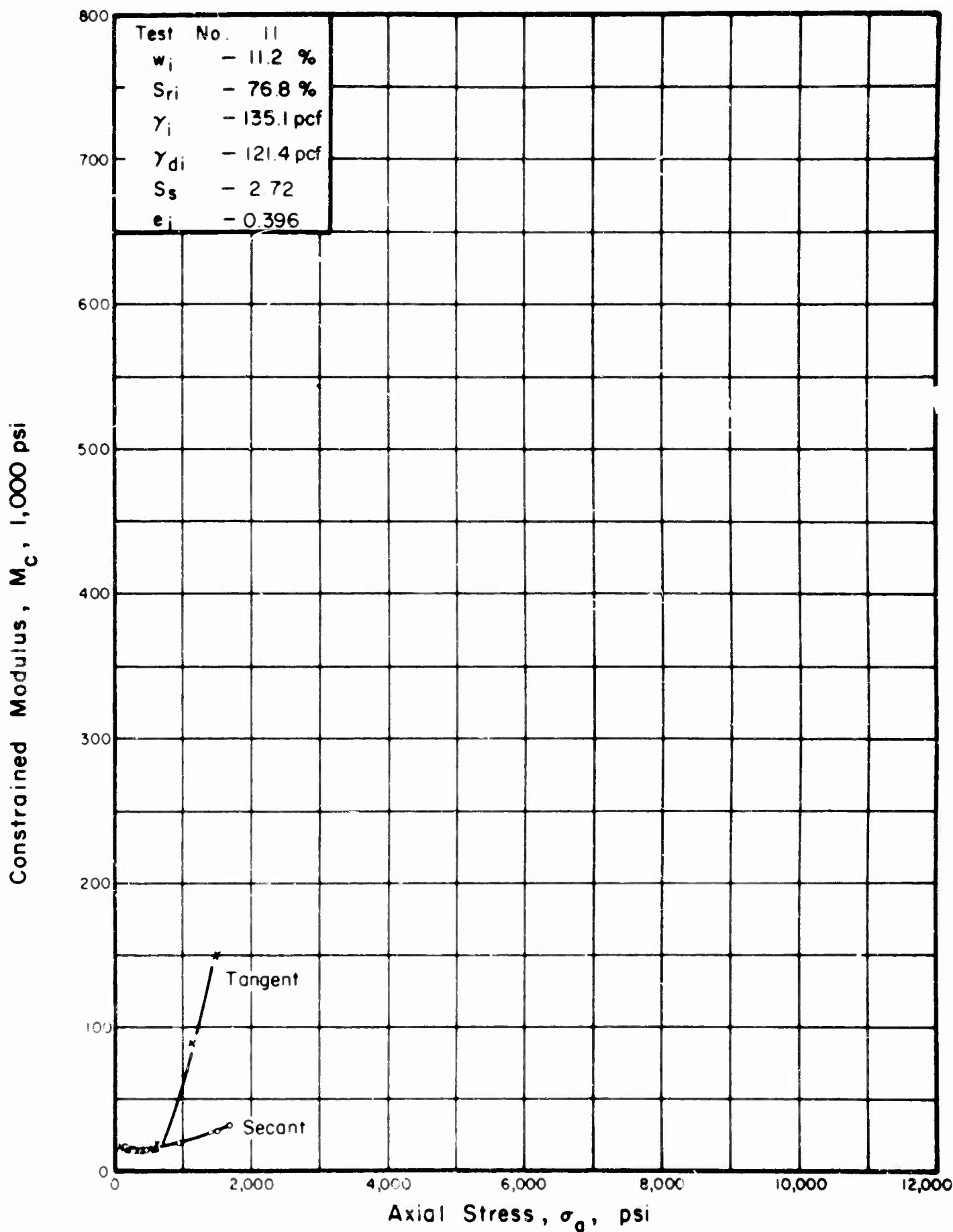


FIGURE A.36. RELATIONSHIP BETWEEN CONSTRAINED MODULUS AND AXIAL STRESS FOR GOOSE LAKE CLAY IN ONE DIMENSIONAL COMPRESSION .

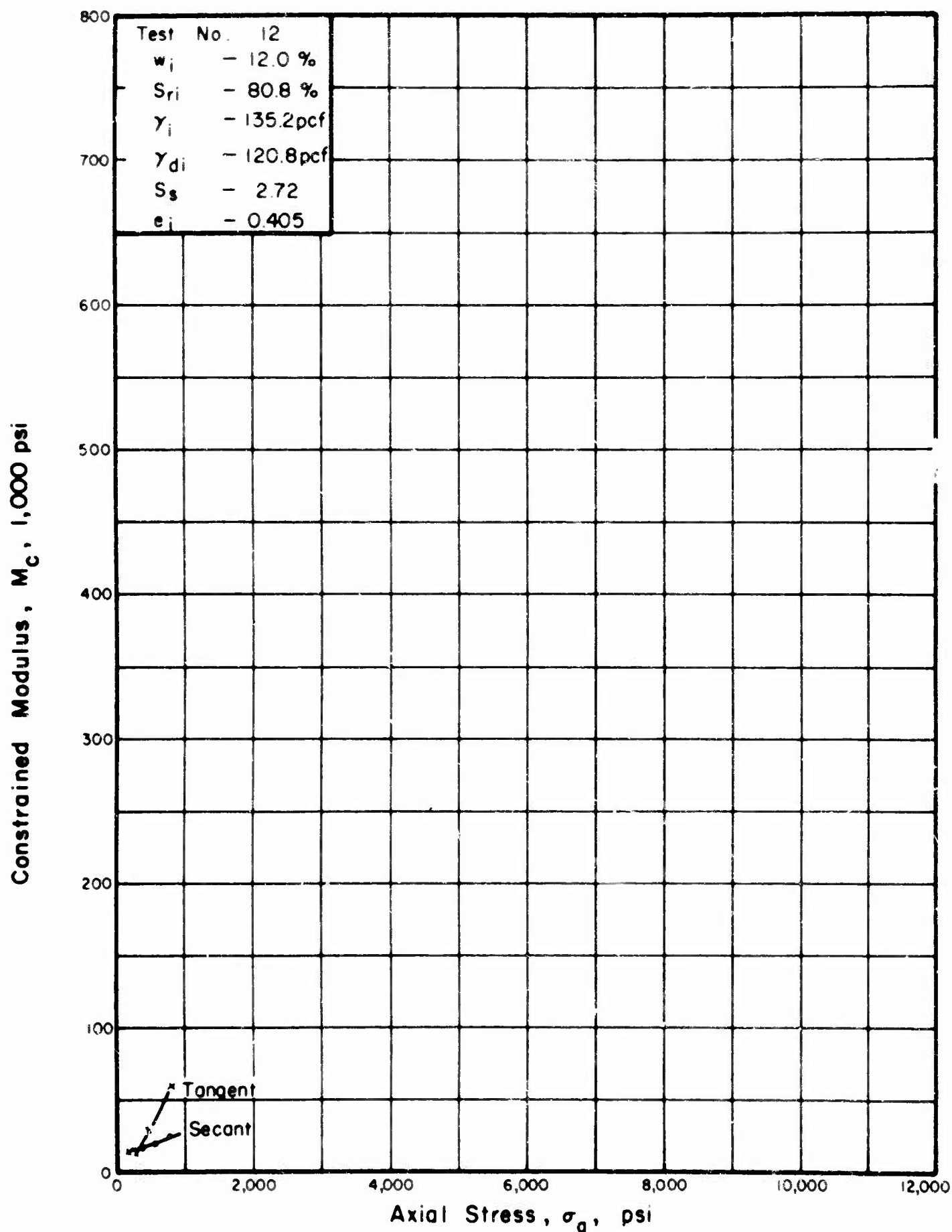


FIGURE A.37. RELATIONSHIP BETWEEN CONSTRAINED MODULUS AND AXIAL STRESS FOR GOOSE LAKE CLAY IN ONE DIMENSIONAL COMPRESSION.

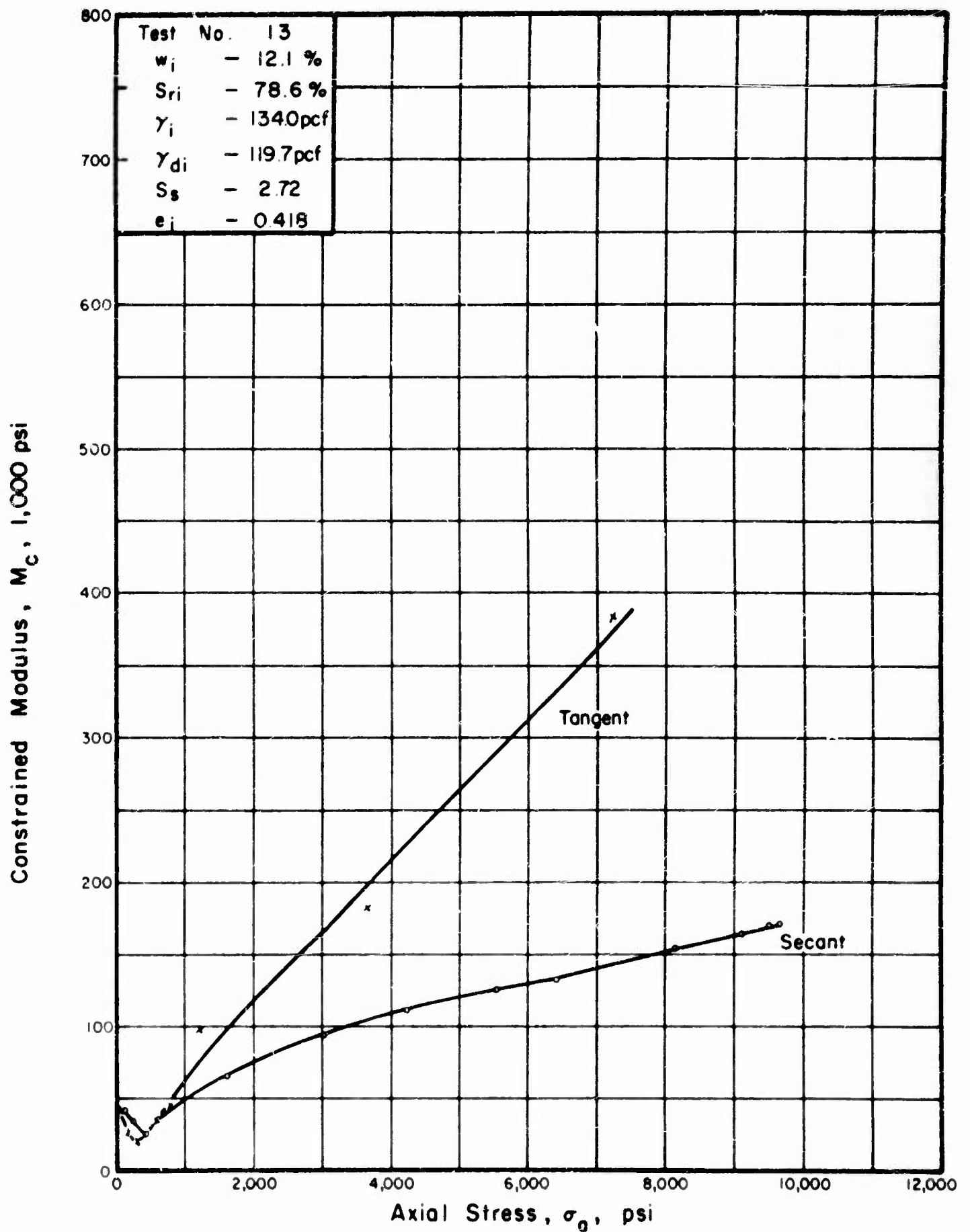


FIGURE A.38. RELATIONSHIP BETWEEN CONSTRAINED MODULUS AND AXIAL STRESS FOR GOOSE LAKE CLAY IN ONE DIMENSIONAL COMPRESSION.

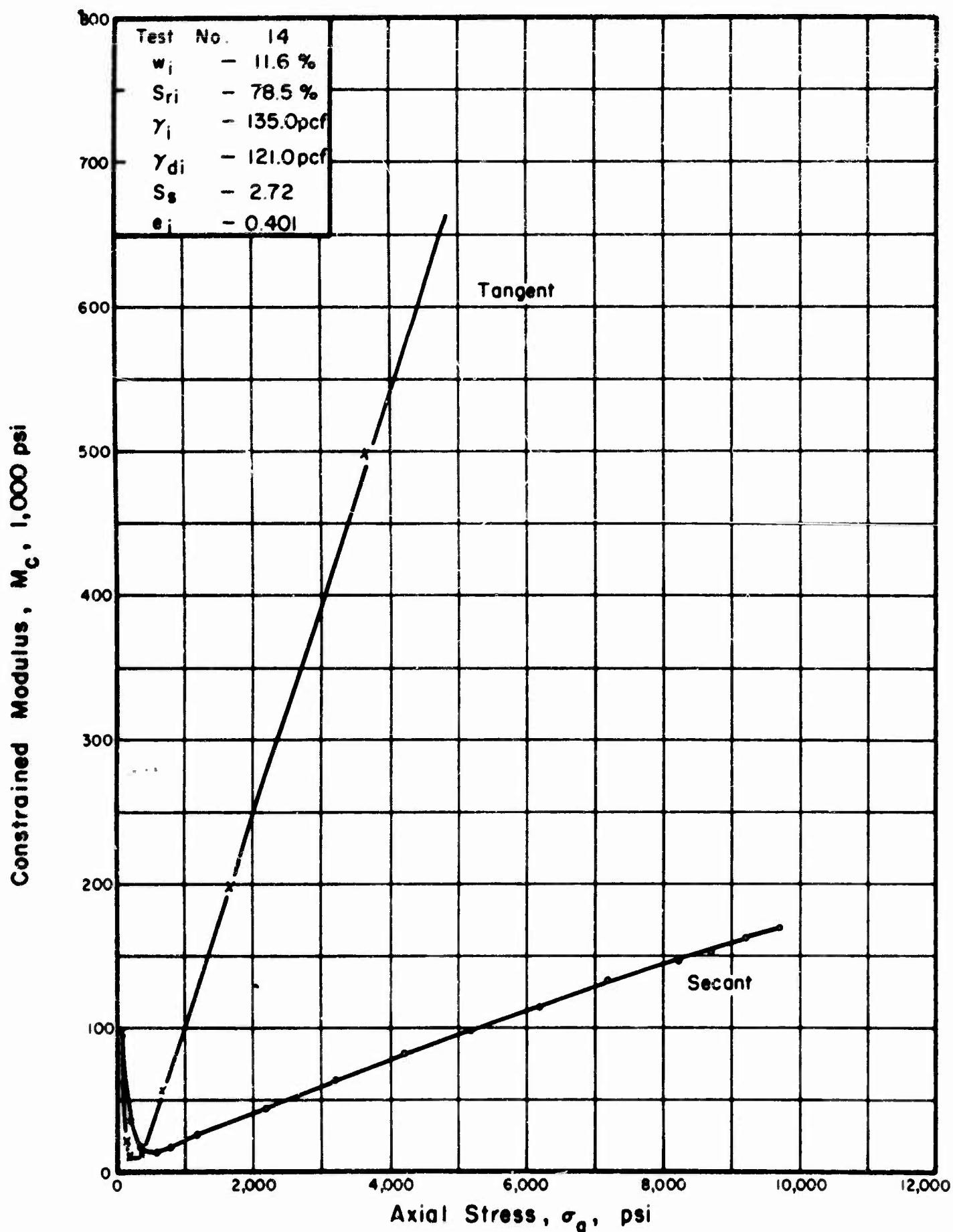


FIGURE A.39. RELATIONSHIP BETWEEN CONSTRAINED MODULUS AND AXIAL STRESS FOR GOOSE LAKE CLAY IN ONE DIMENSIONAL COMPRESSION.

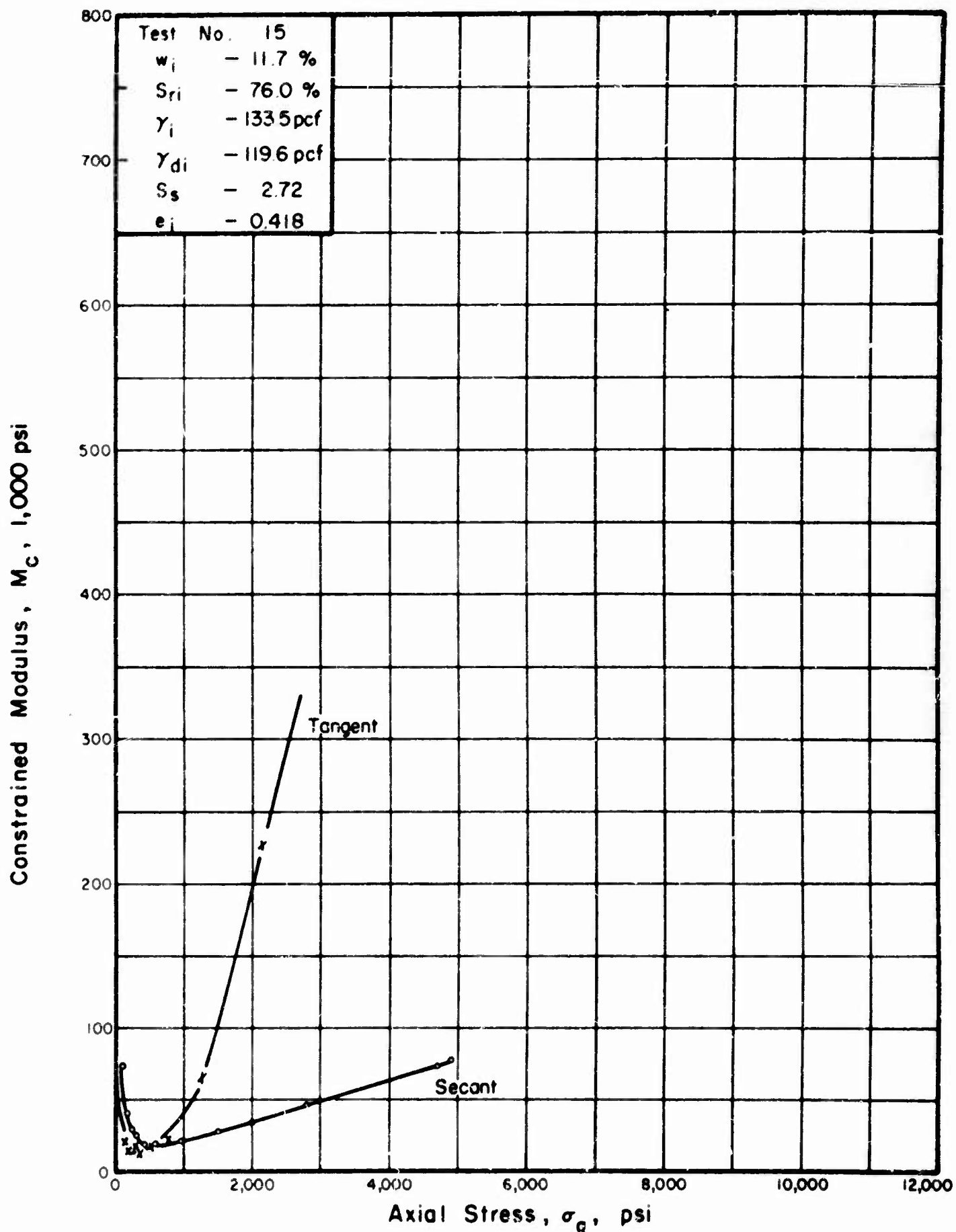


FIGURE A.40. RELATIONSHIP BETWEEN CONSTRAINED MODULUS AND AXIAL STRESS FOR GOOSE LAKE CLAY IN ONE DIMENSIONAL COMPRESSION.

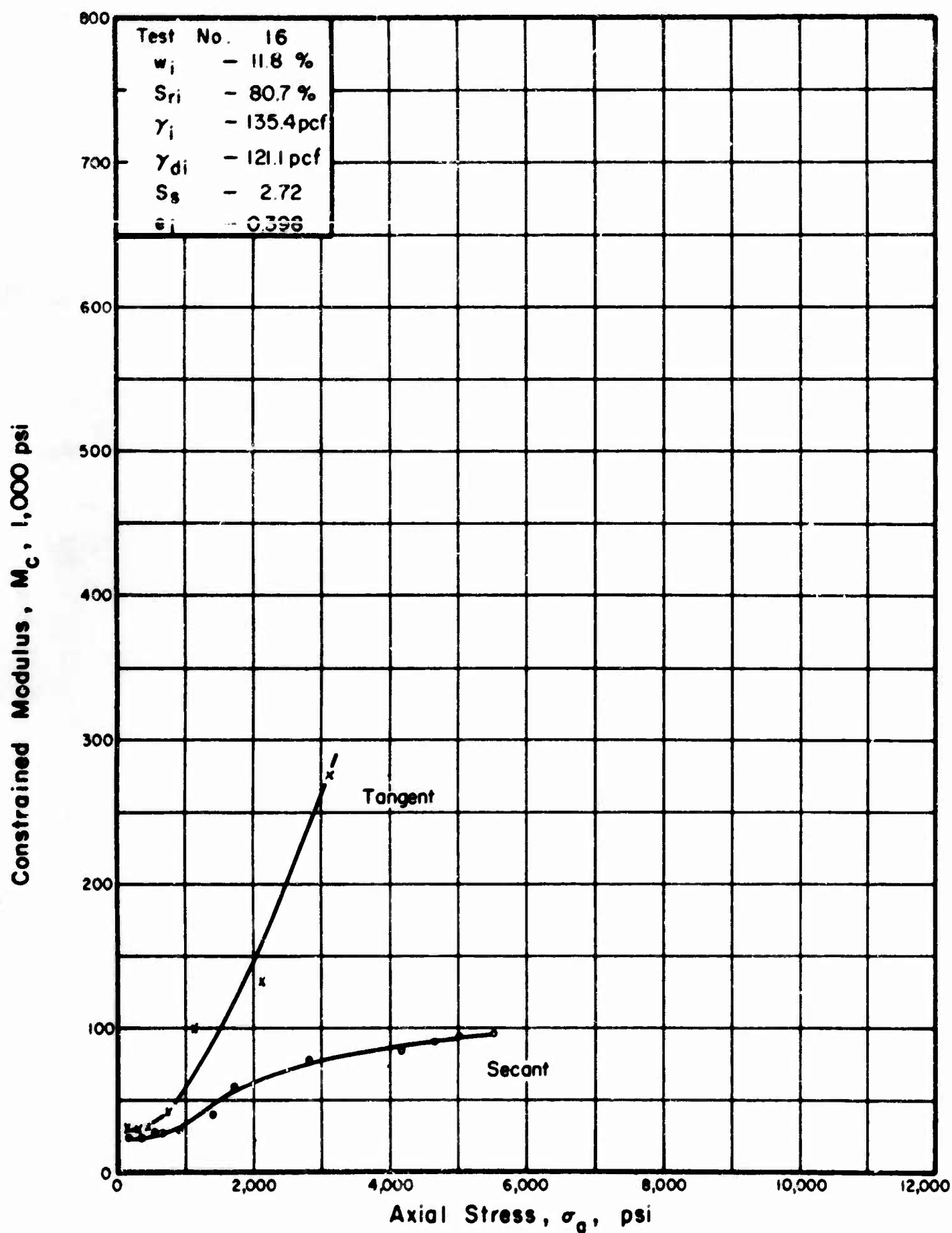


FIGURE A.41. RELATIONSHIP BETWEEN CONSTRAINED MODULUS AND AXIAL STRESS FOR GOOSE LAKE CLAY IN ONE DIMENSIONAL COMPRESSION.

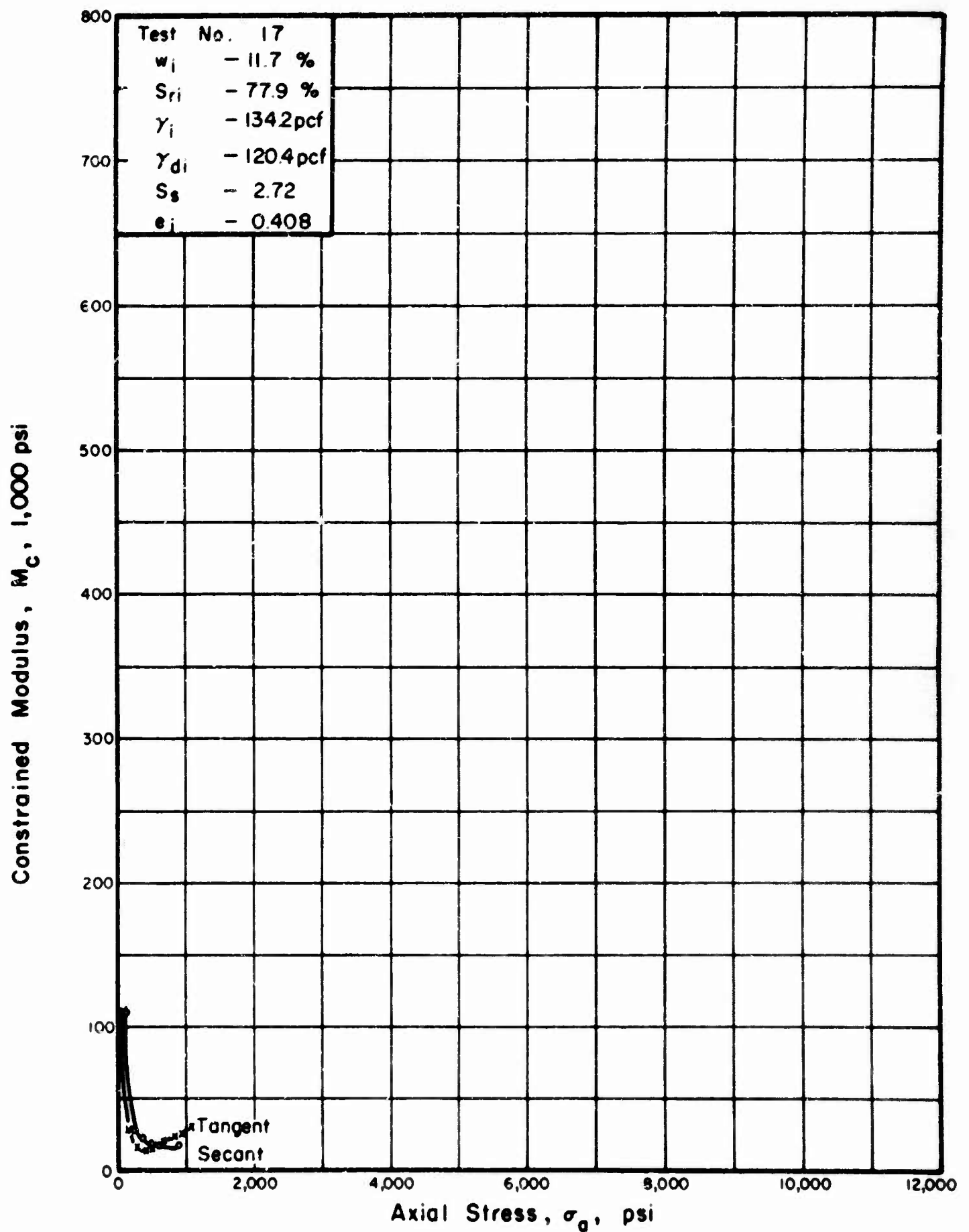


FIGURE A.42. RELATIONSHIP BETWEEN CONSTRAINED MODULUS AND AXIAL STRESS FOR GOOSE LAKE CLAY IN ONE DIMENSIONAL COMPRESSION.

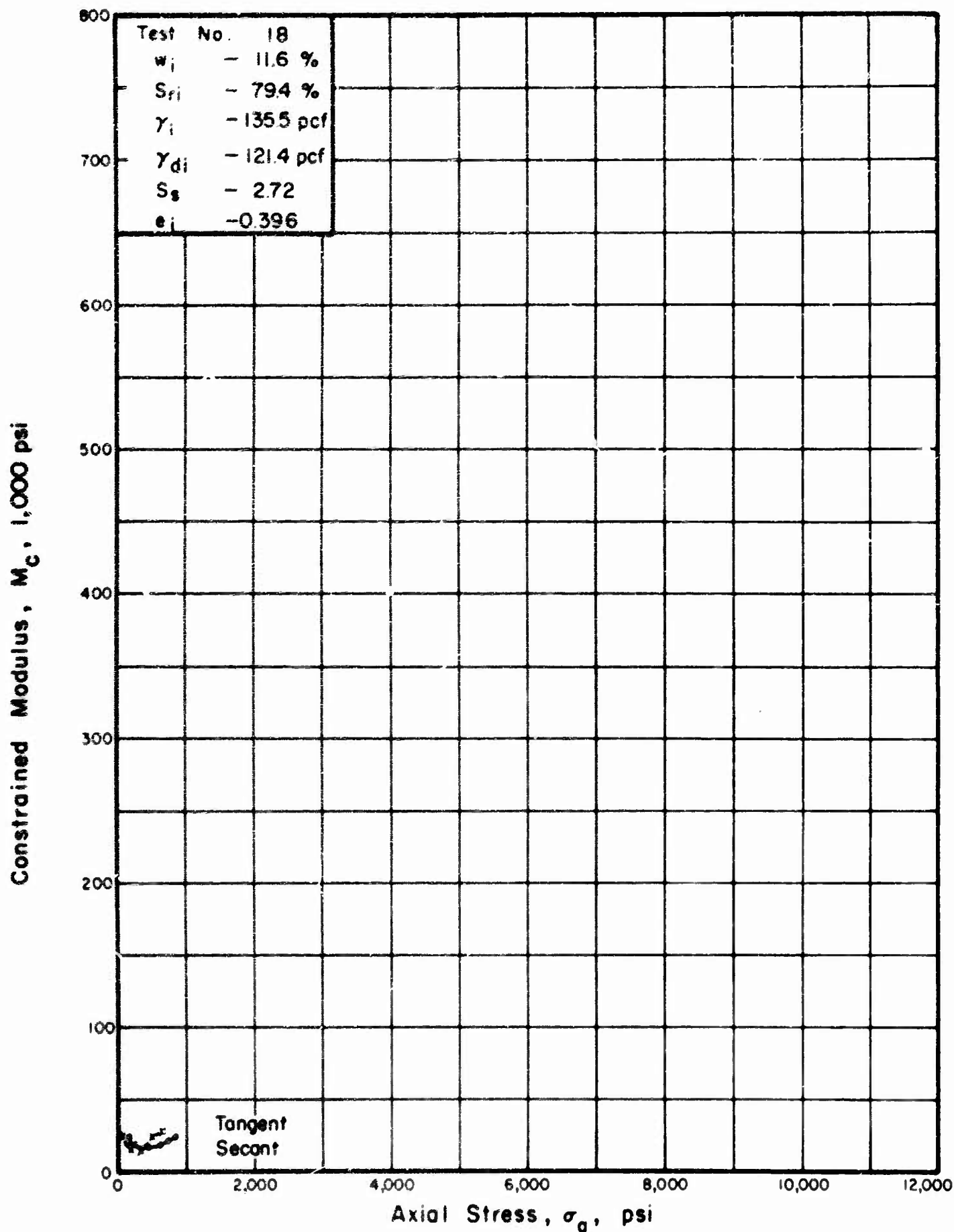


FIGURE A.43. RELATIONSHIP BETWEEN CONSTRAINED MODULUS AND AXIAL STRESS FOR GOOSE LAKE CLAY IN ONE DIMENSIONAL COMPRESSION.

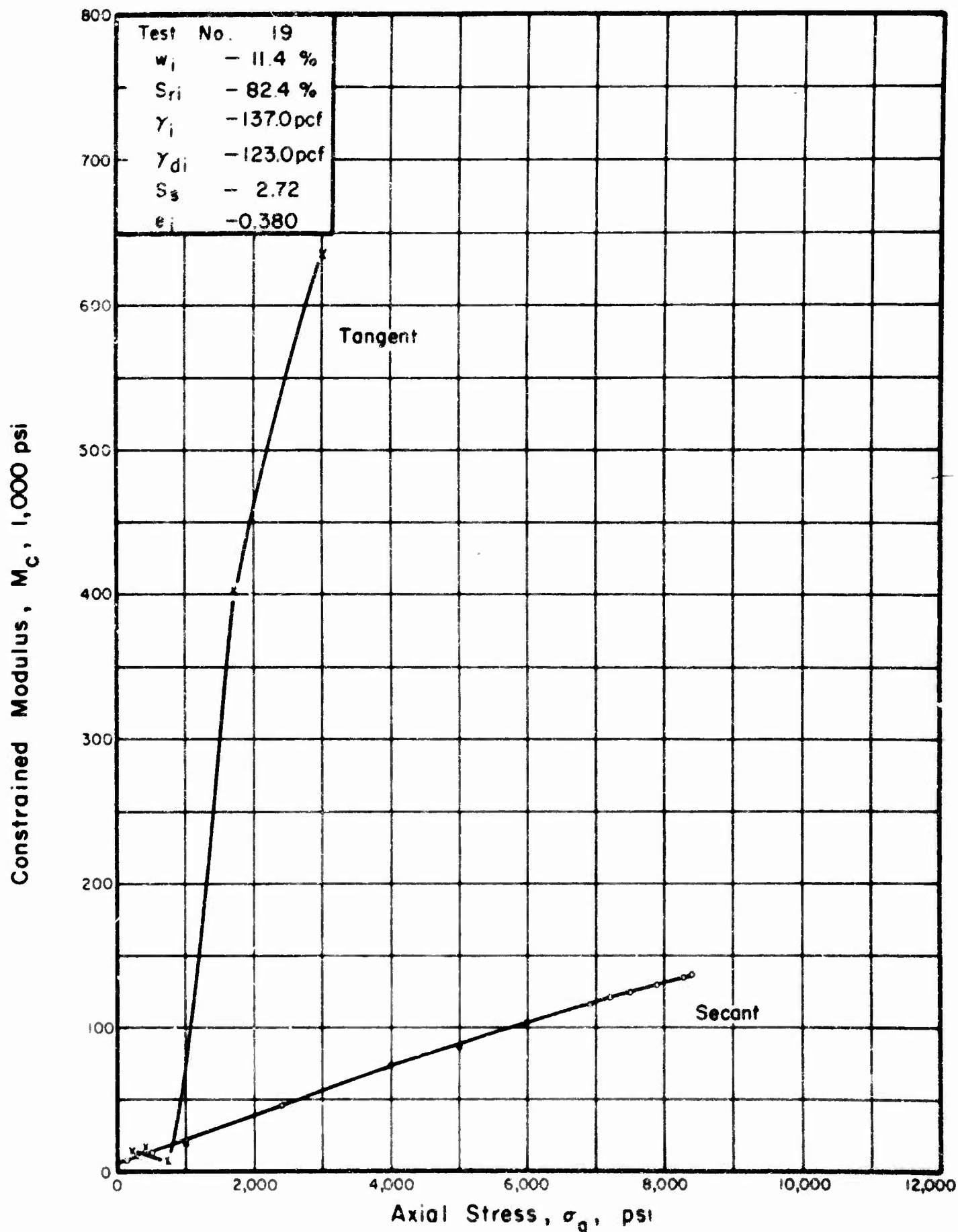


FIGURE A.44. RELATIONSHIP BETWEEN CONSTRAINED MODULUS AND AXIAL STRESS FOR GOOSE LAKE CLAY IN ONE DIMENSIONAL COMPRESSION.

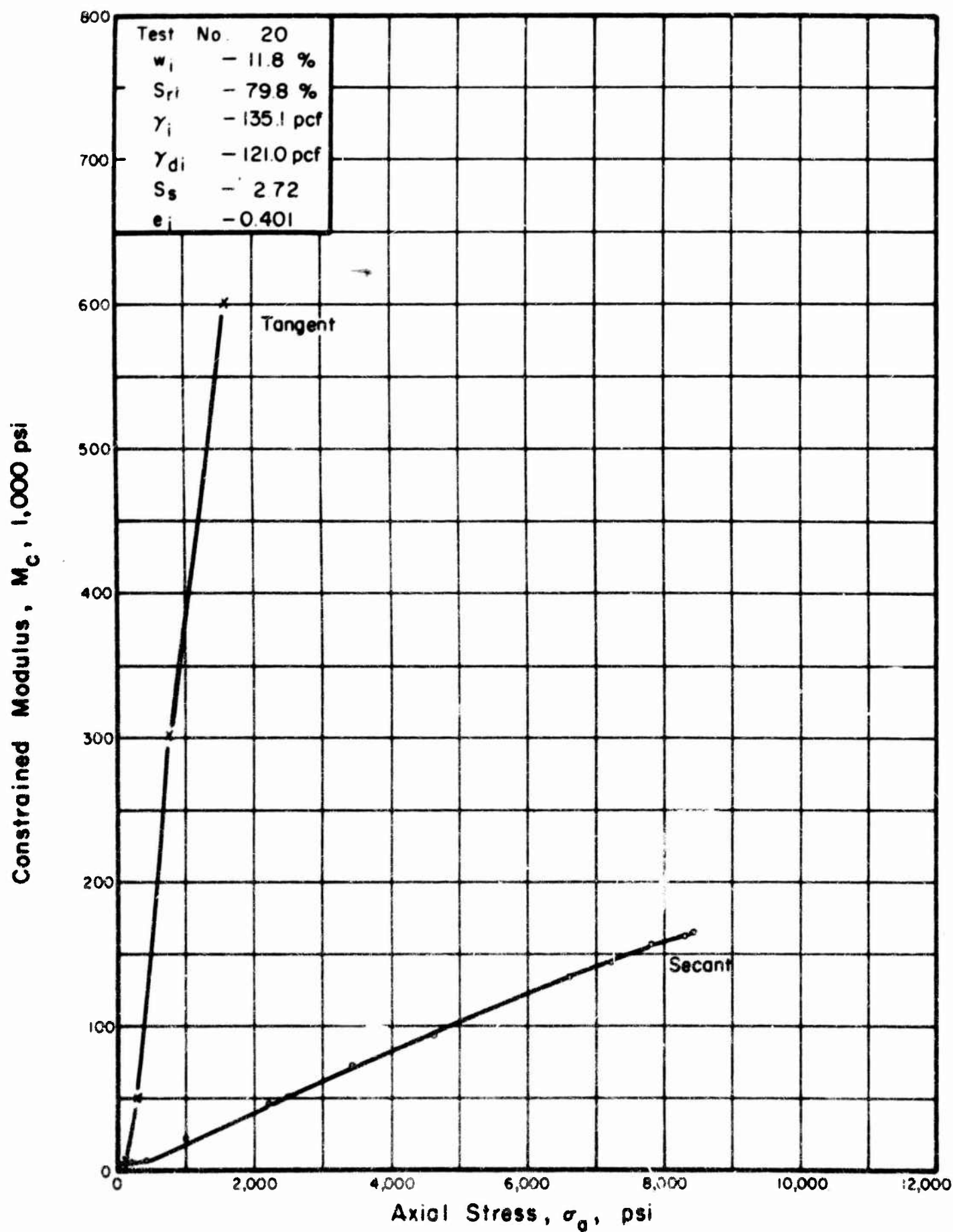


FIGURE A.45. RELATIONSHIP BETWEEN CONSTRAINED MODULUS AND AXIAL STRESS FOR GOOSE LAKE CLAY IN ONE DIMENSIONAL COMPRESSION.

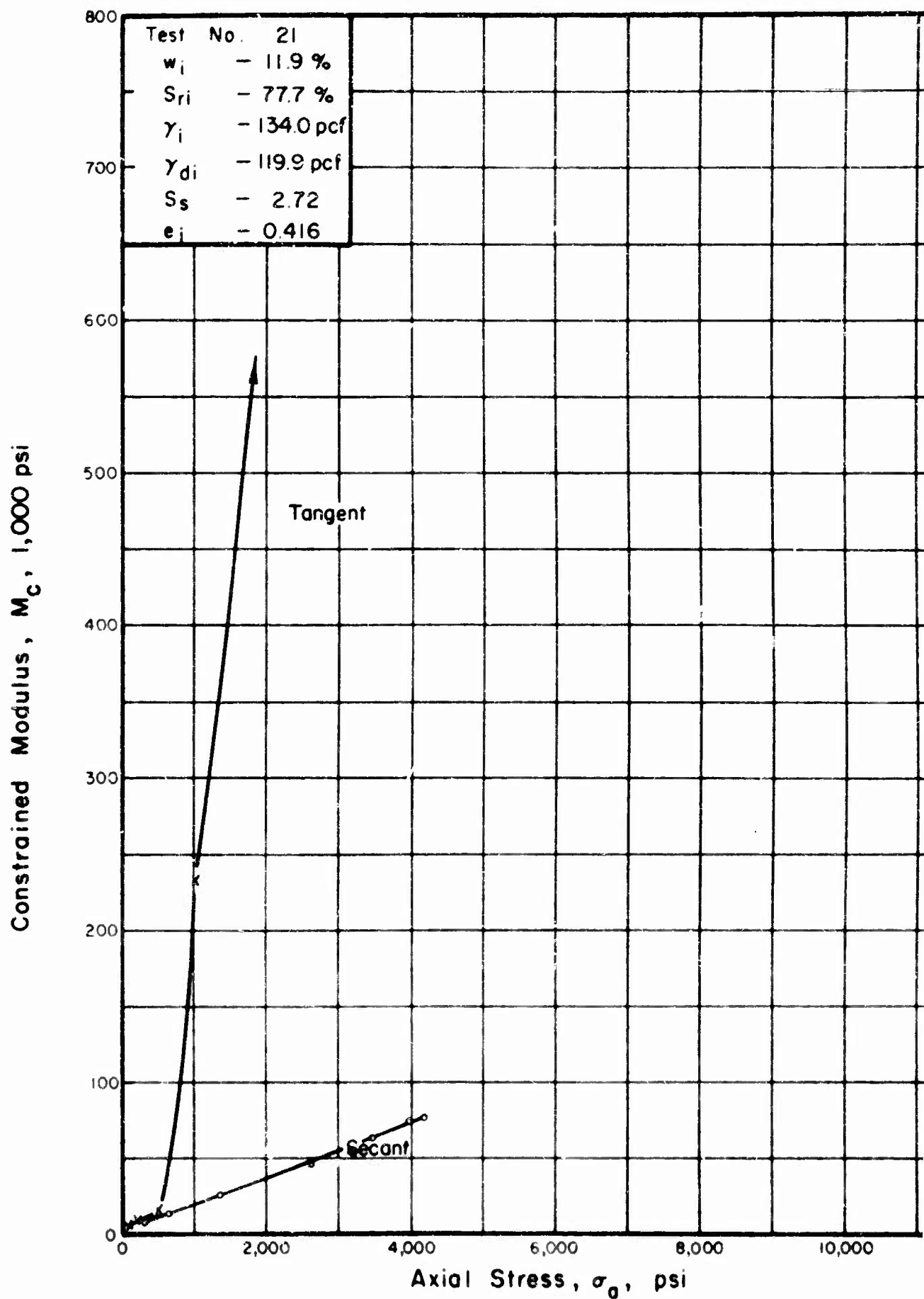


FIGURE A.46. RELATIONSHIP BETWEEN CONSTRAINED MODULUS AND AXIAL STRESS FOR GOOSE LAKE CLAY II IN ONE DIMENSIONAL COMPRESSION.

Constrained Modulus, M_c , 1,000 psi

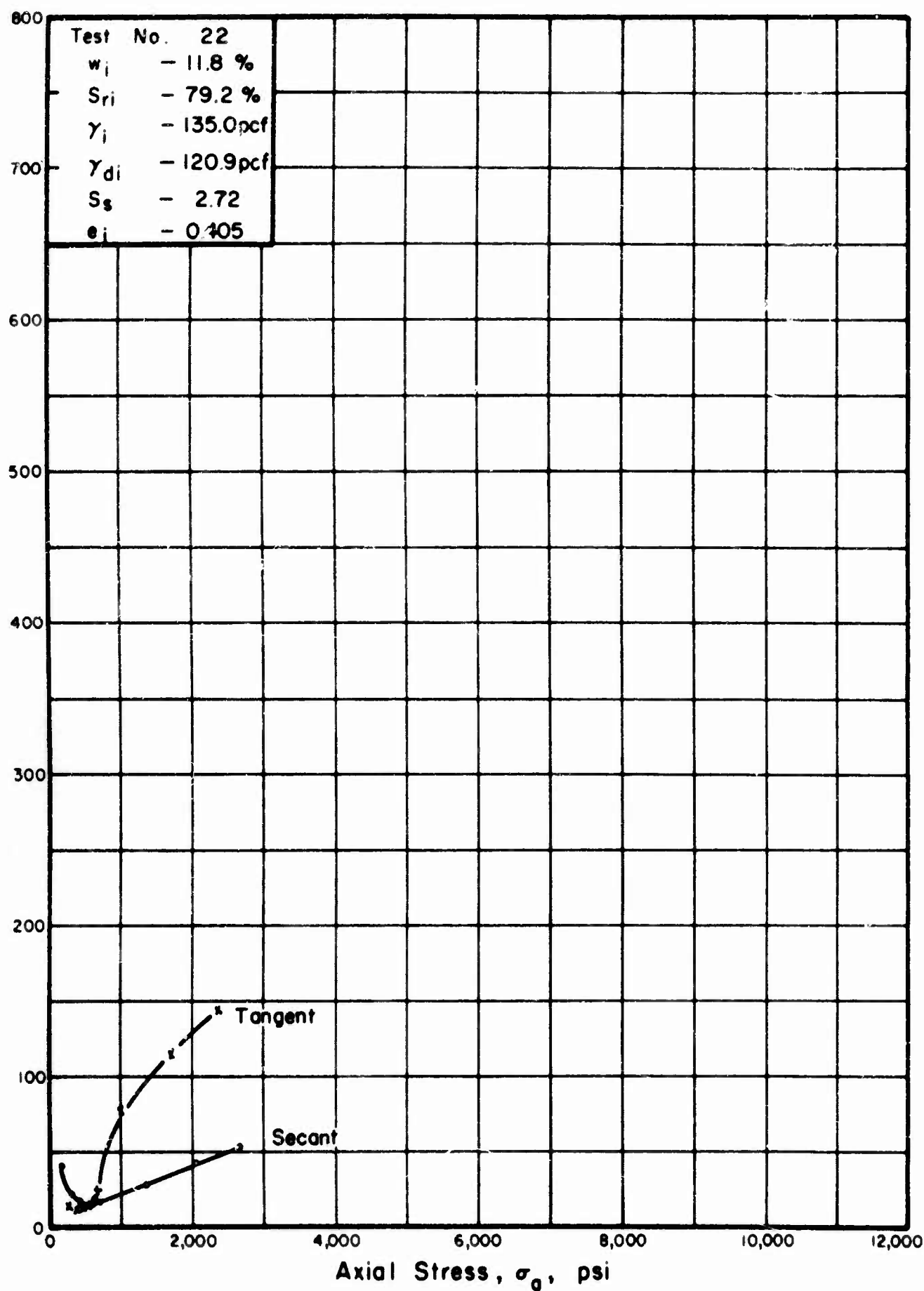


FIGURE A.47. RELATIONSHIP BETWEEN CONSTRAINED MODULUS AND AXIAL STRESS FOR GOOSE LAKE CLAY IN ONE DIMENSIONAL COMPRESSION.

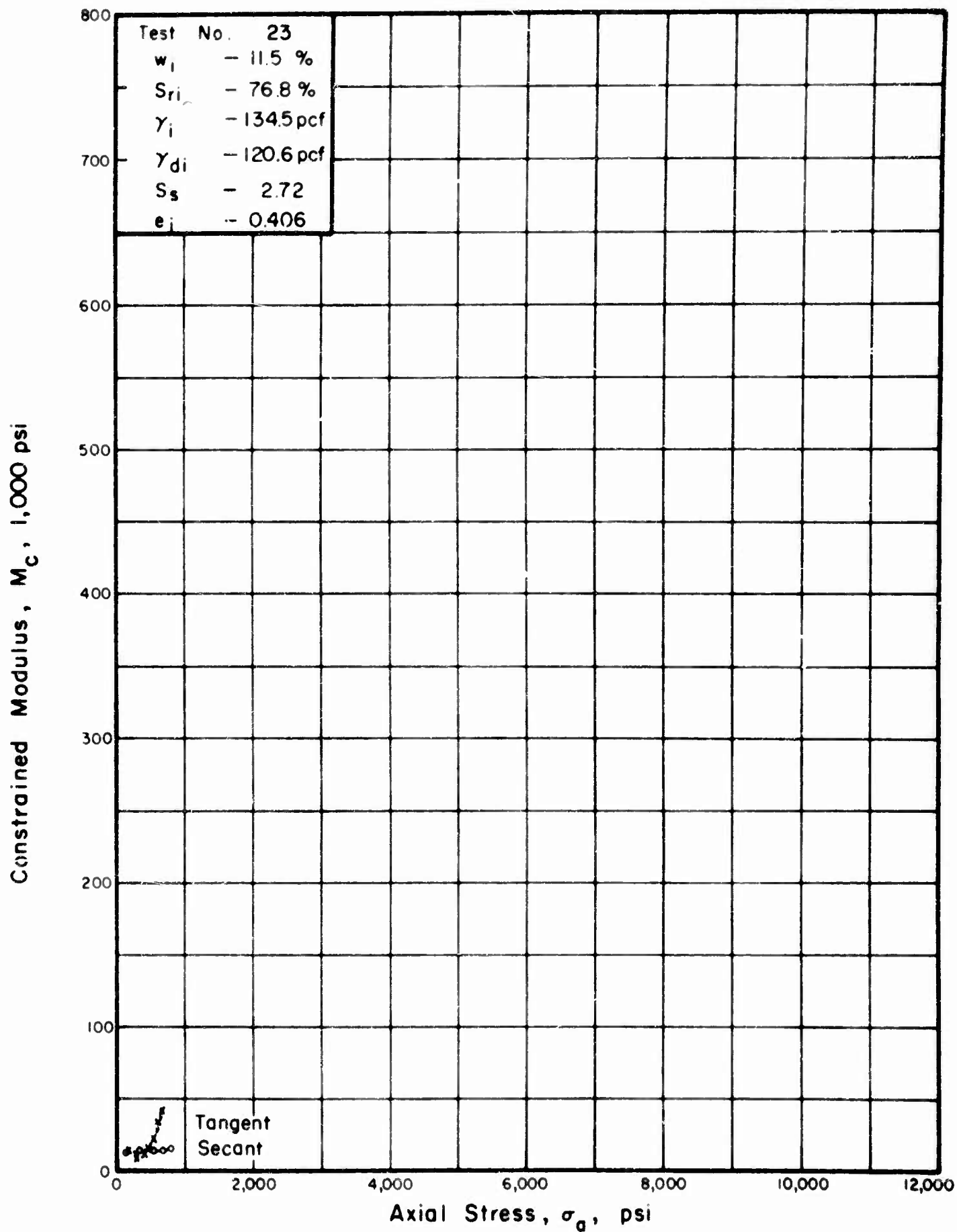


FIGURE A.48. RELATIONSHIP BETWEEN CONSTRAINED MODULUS AND AXIAL STRESS FOR GOOSE LAKE CLAY IN ONE DIMENSIONAL COMPRESSION.

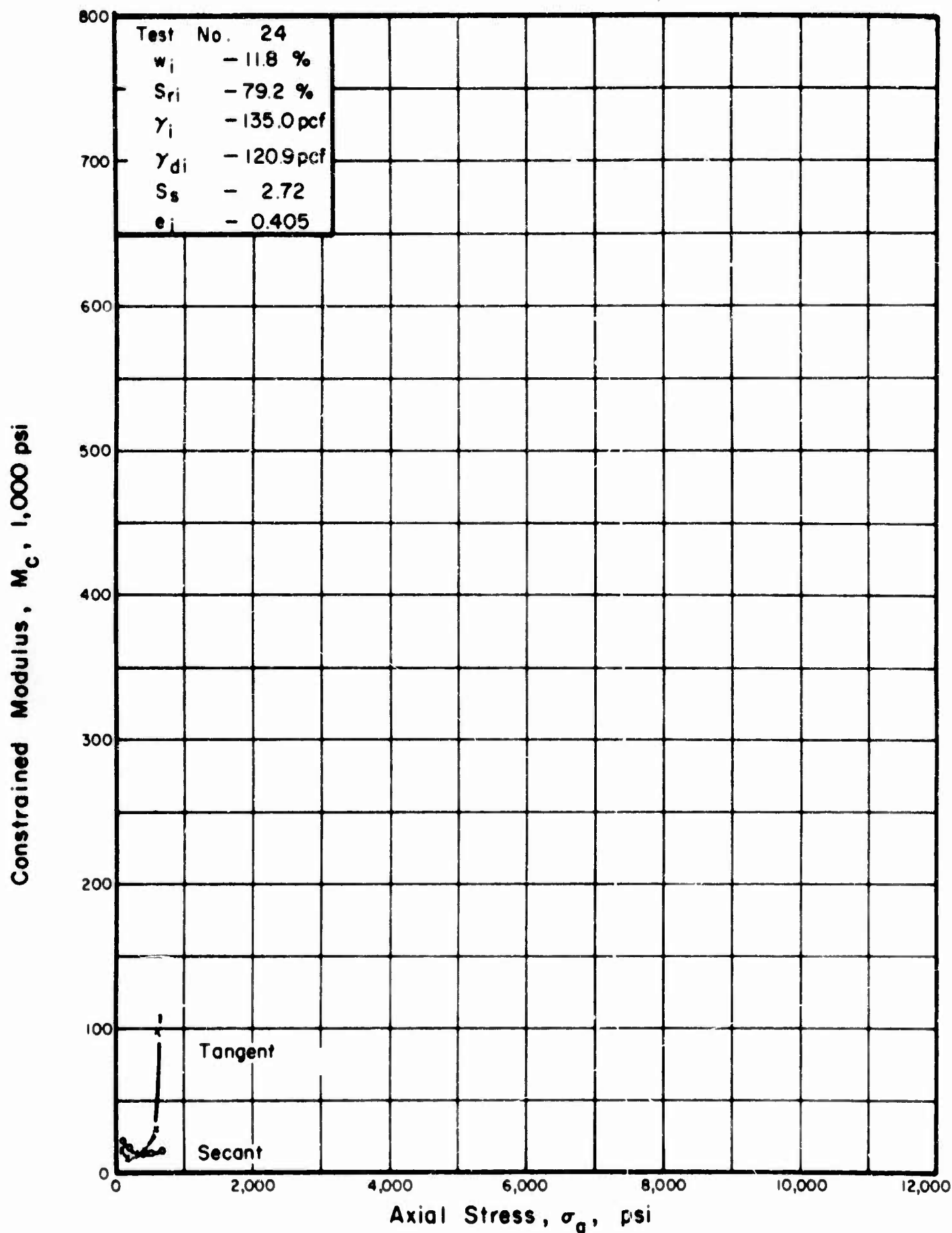


FIGURE A.49. RELATIONSHIP BETWEEN CONSTRAINED MODULUS AND AXIAL STRESS FOR GOOSE LAKE CLAY IN ONE DIMENSIONAL COMPRESSION.

Constrained Modulus, M_c , 1,000 psi

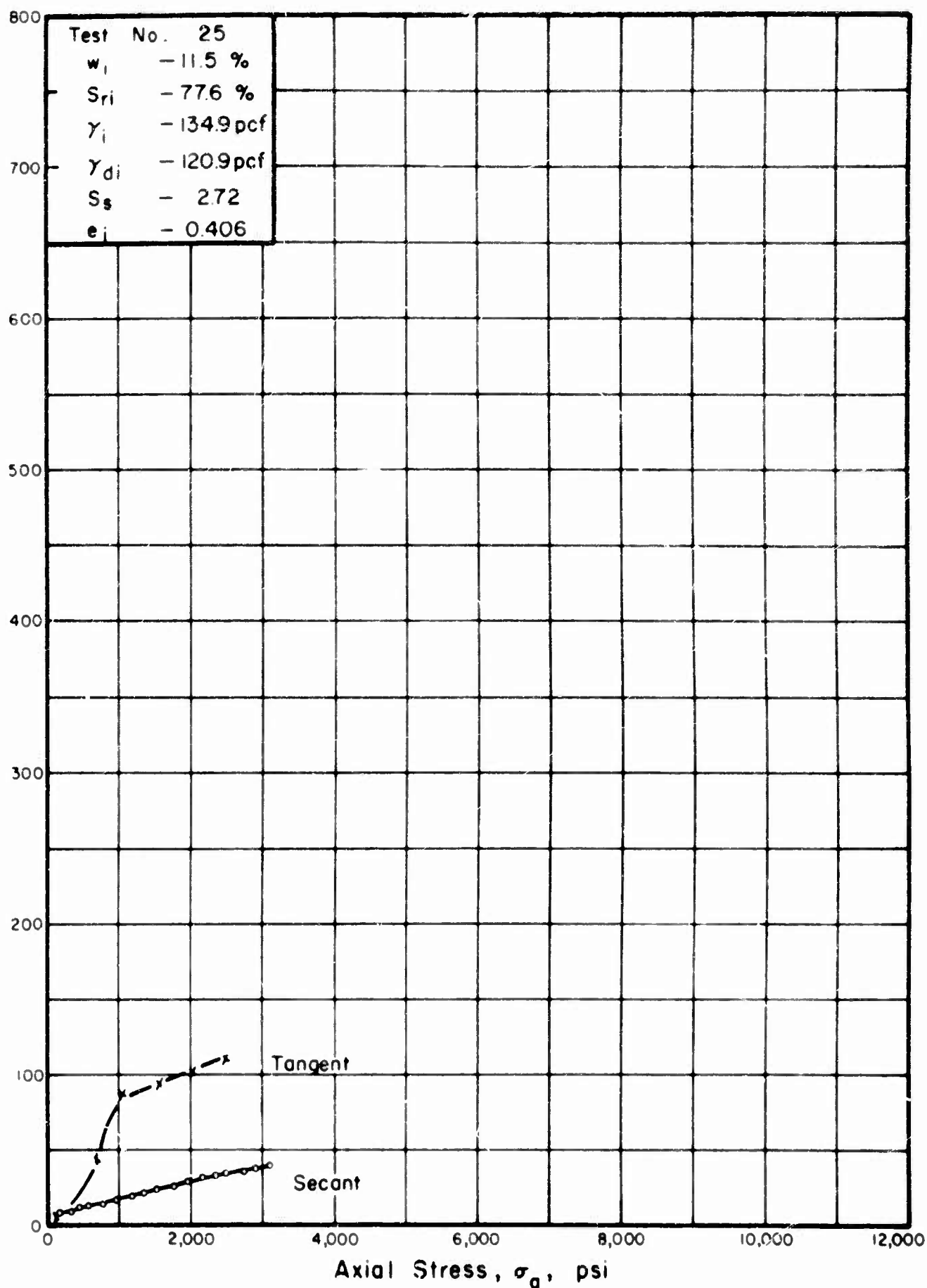


FIGURE A.50. RELATIONSHIP BETWEEN CONSTRAINED MODULUS AND AXIAL STRESS FOR GOOSE LAKE CLAY IN ONE DIMENSIONAL COMPRESSION.

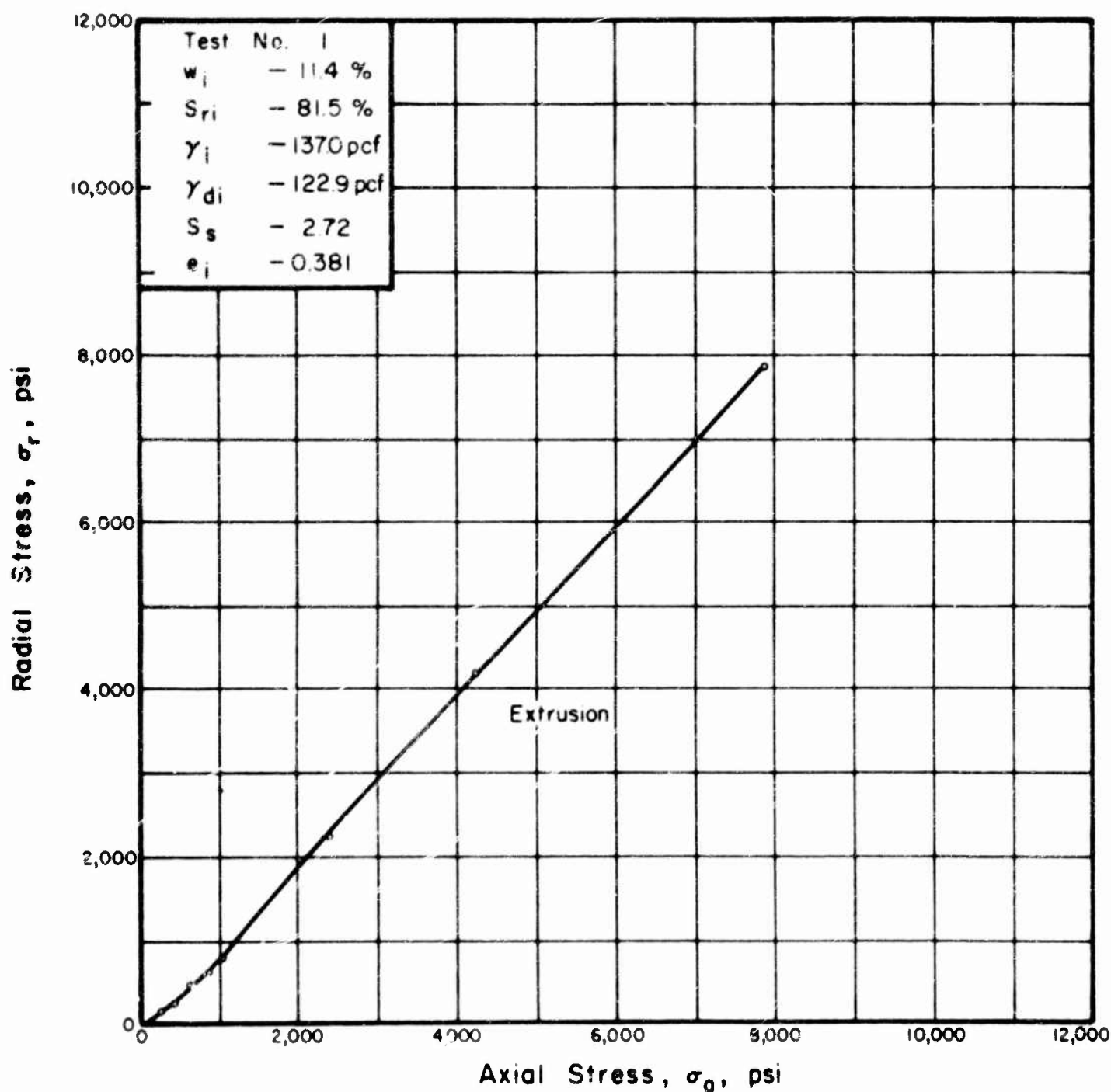


FIGURE A.51. RELATIONSHIP BETWEEN AXIAL AND RADIAL STRESS FOR GOOSE LAKE CLAY IN ONE-DIMENSIONAL COMPRESSION .

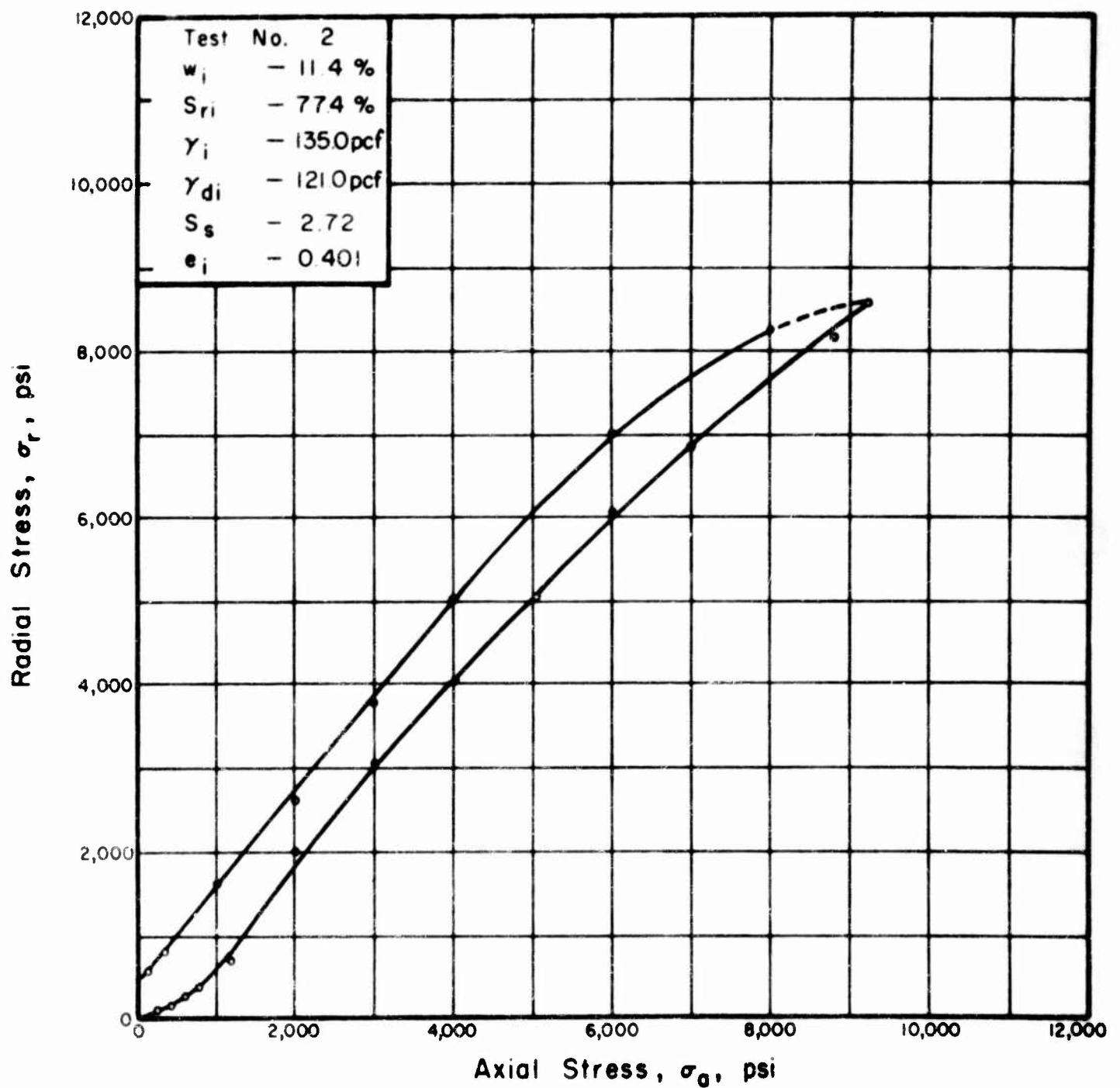


FIGURE A.52. RELATIONSHIP BETWEEN AXIAL AND RADIAL STRESS FOR GOOSE LAKE CLAY IN ONE-DIMENSIONAL COMPRESSION.

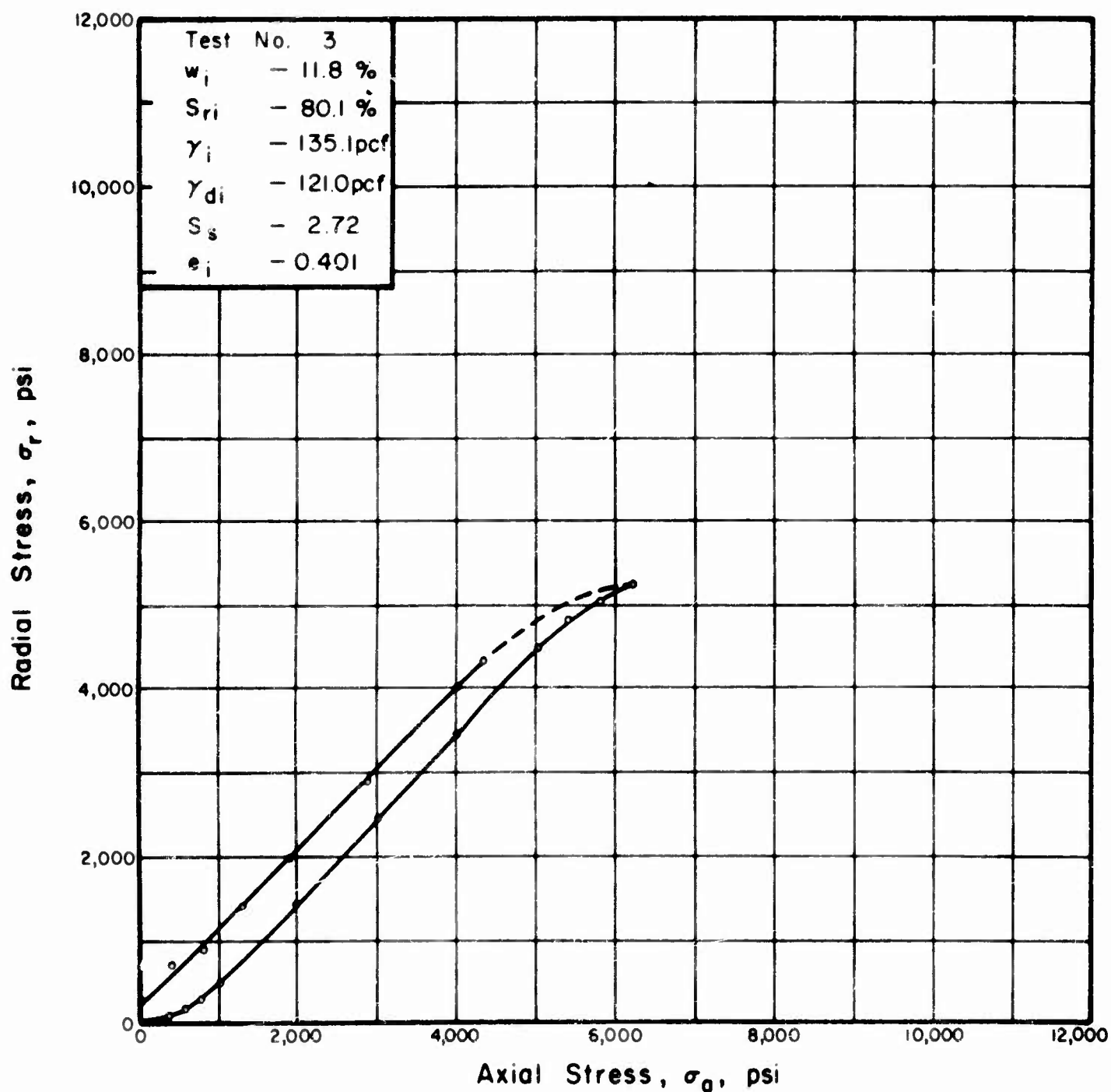


FIGURE A.53. RELATIONSHIP BETWEEN AXIAL AND RADIAL STRESS FOR GOOSE LAKE CLAY IN ONE-DIMENSIONAL COMPRESSION.

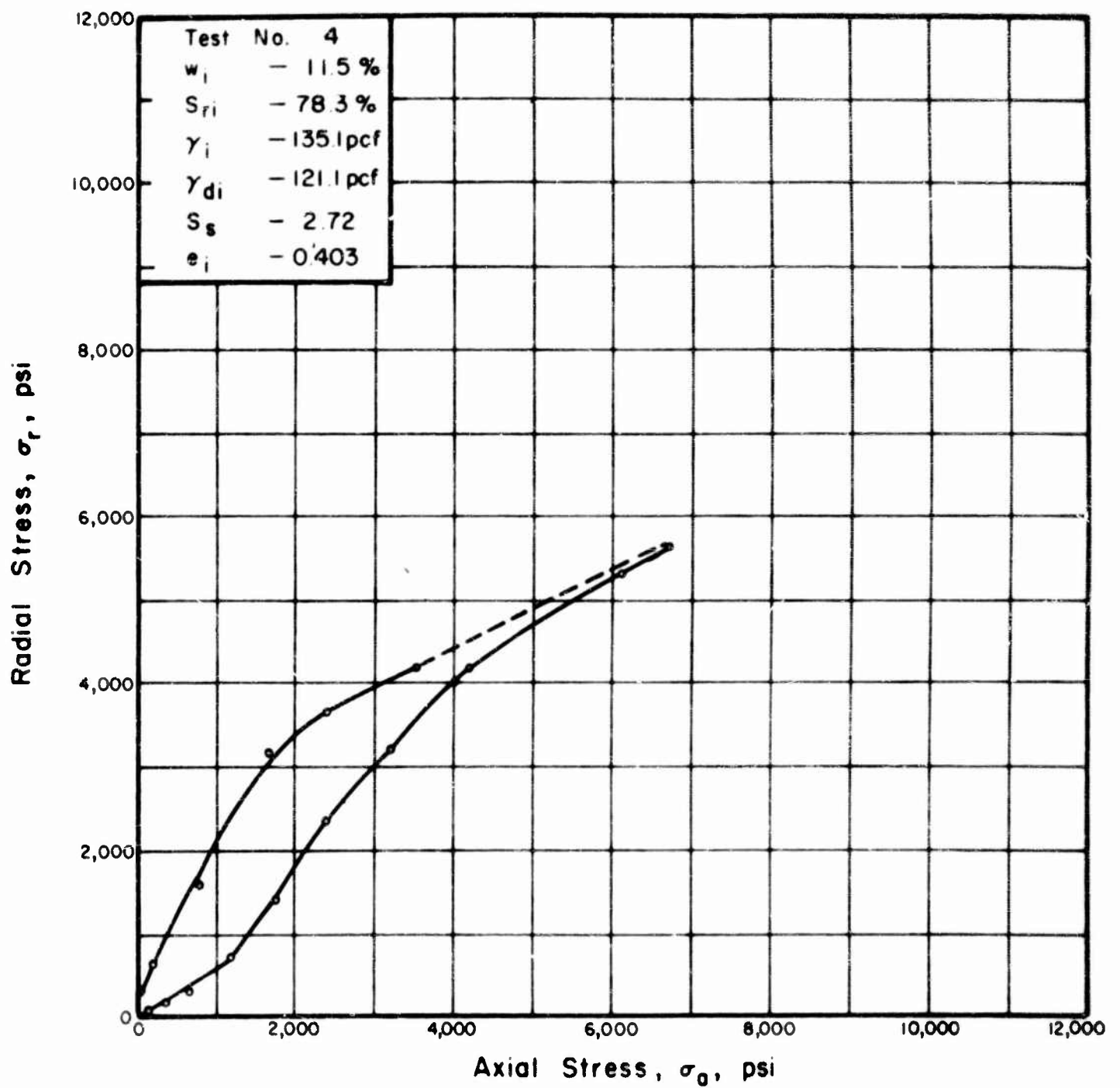


FIGURE A.54. RELATIONSHIP BETWEEN AXIAL AND RADIAL STRESS FOR GOOSE LAKE CLAY IN ONE-DIMENSIONAL COMPRESSION.

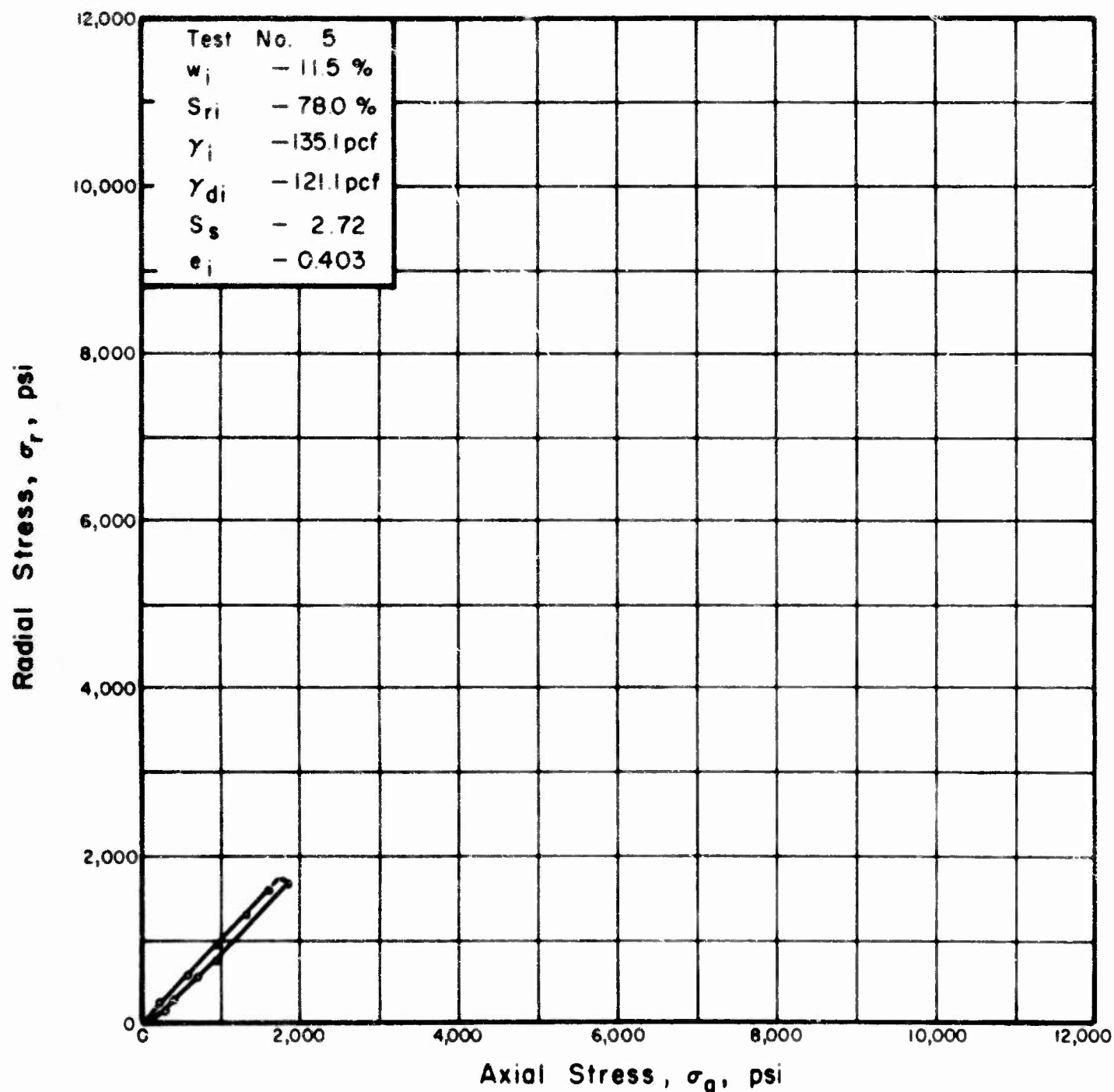


FIGURE A.55. RELATIONSHIP BETWEEN AXIAL AND RADIAL STRESS FOR GOOSE LAKE CLAY IN ONE-DIMENSIONAL COMPRESSION .

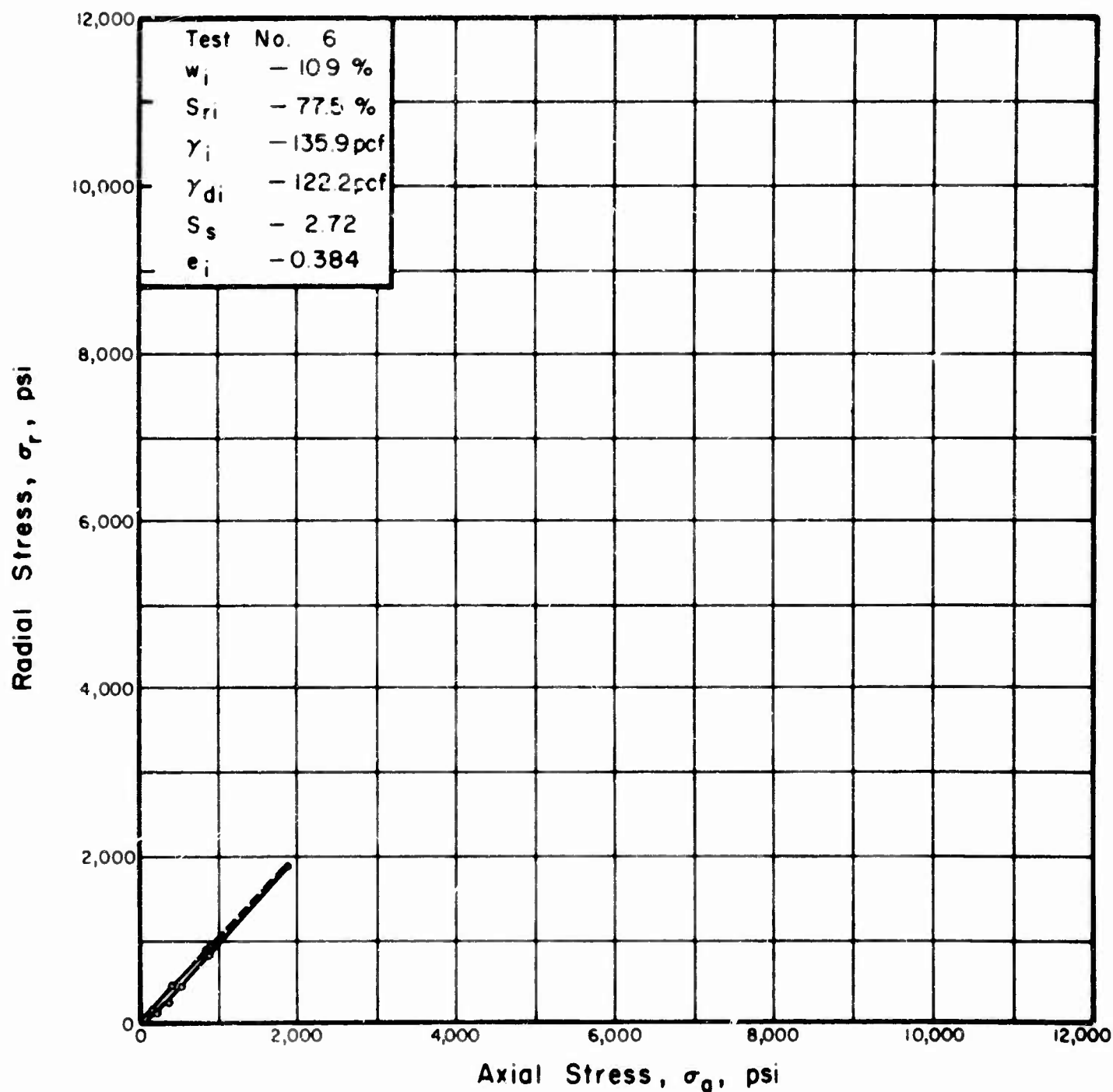


FIGURE A.56. RELATIONSHIP BETWEEN AXIAL AND RADIAL STRESS FOR GOOSE LAKE CLAY IN ONE-DIMENSIONAL COMPRESSION.

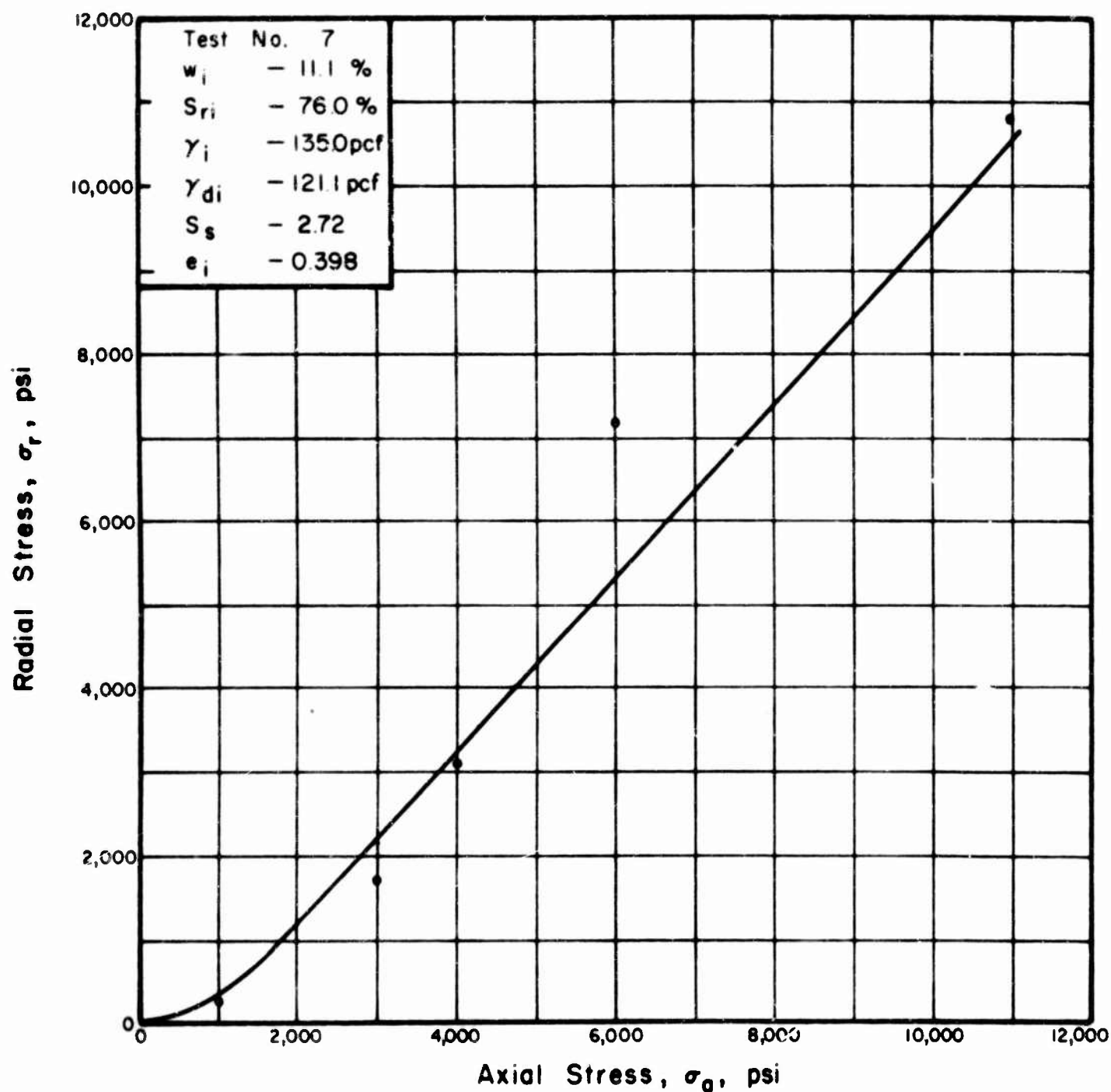


FIGURE A.57. RELATIONSHIP BETWEEN AXIAL AND RADIAL STRESS FOR GOOSE LAKE CLAY IN ONE-DIMENSIONAL COMPRESSION .

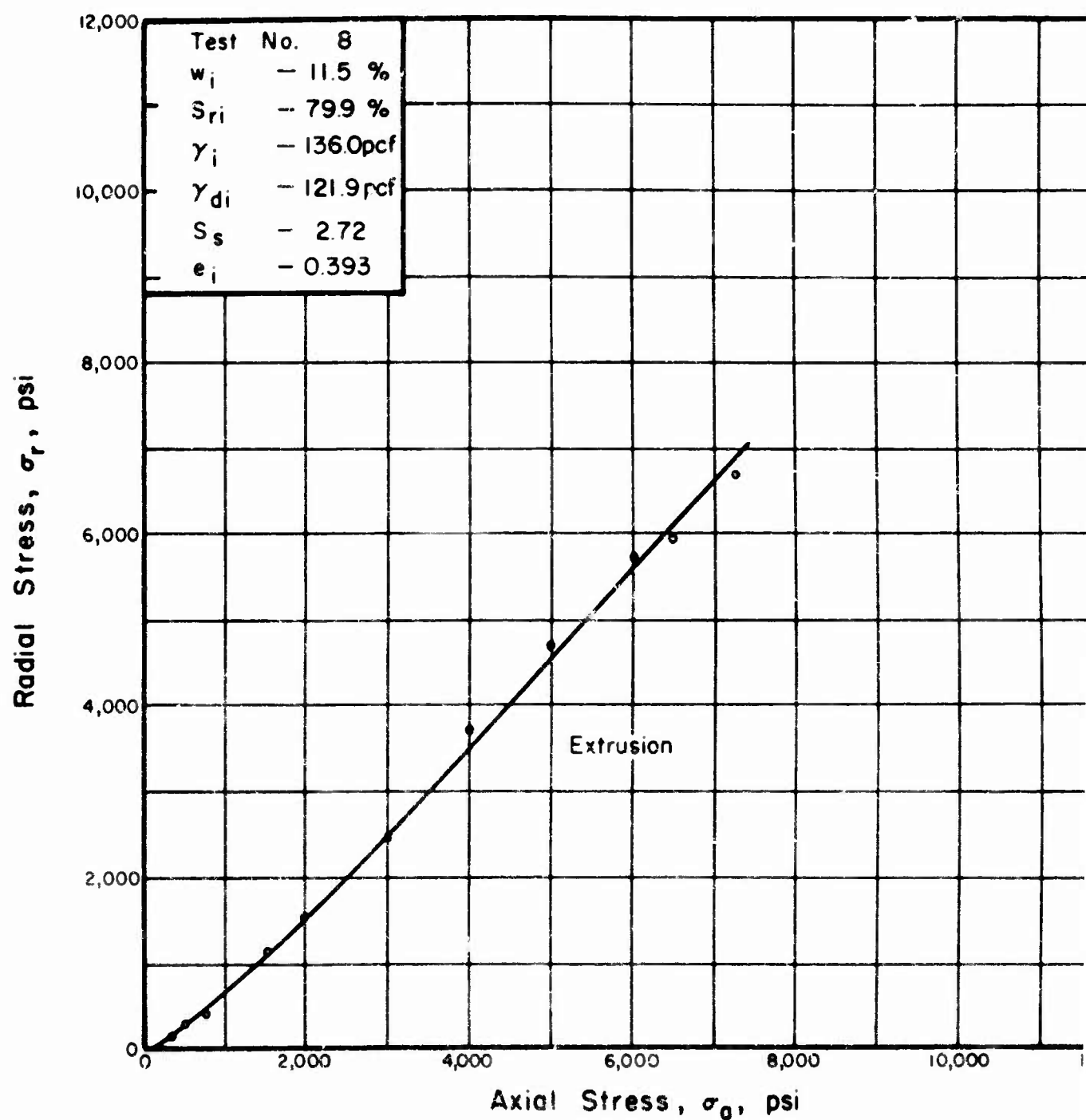


FIGURE A.58. RELATIONSHIP BETWEEN AXIAL AND RADIAL STRESS FOR GOOSE LAKE CLAY IN ONE-DIMENSIONAL COMPRESSION.

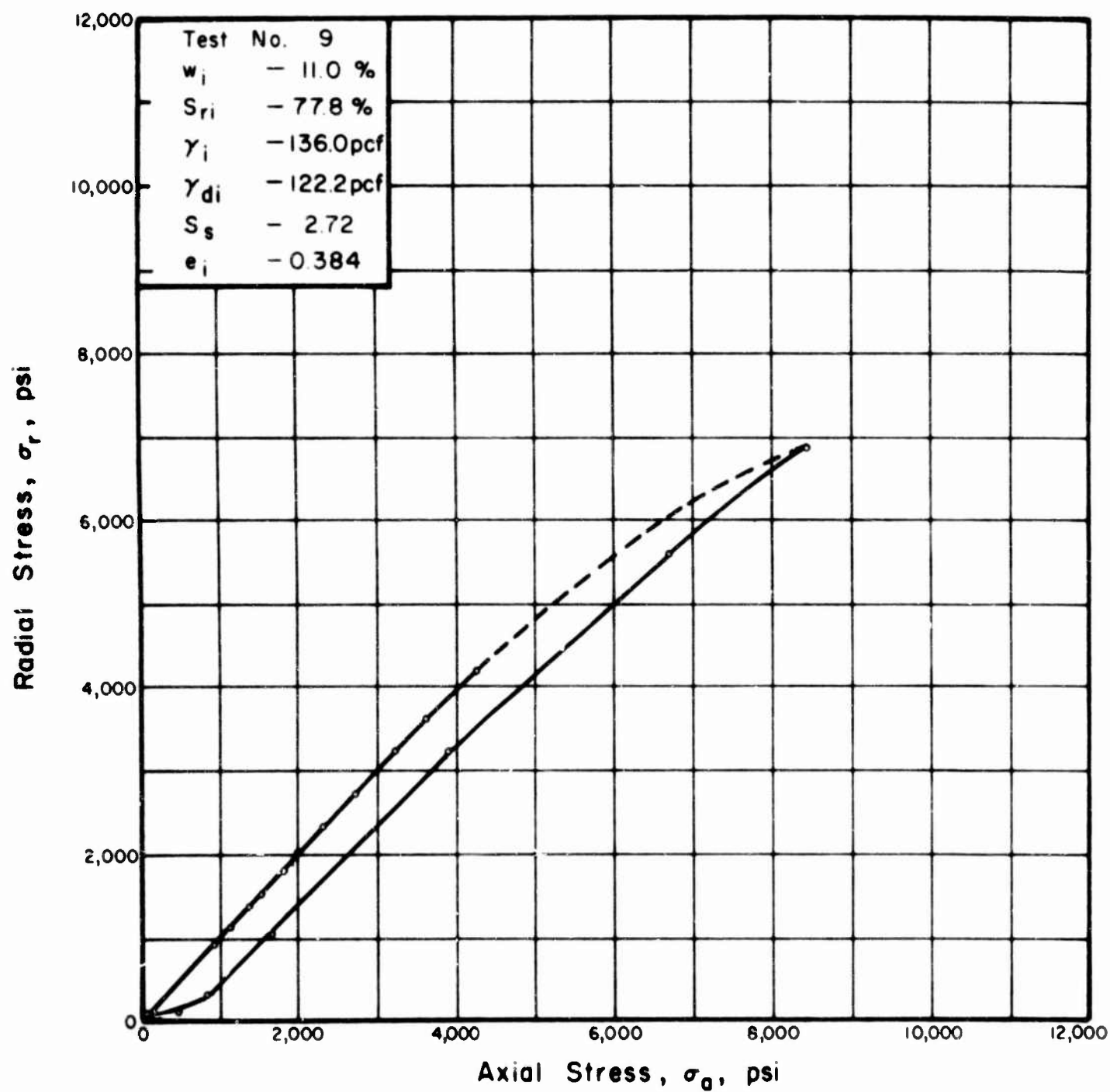


FIGURE A.59. RELATIONSHIP BETWEEN AXIAL AND RADIAL STRESS FOR GOOSE LAKE CLAY IN ONE-DIMENSIONAL COMPRESSION .

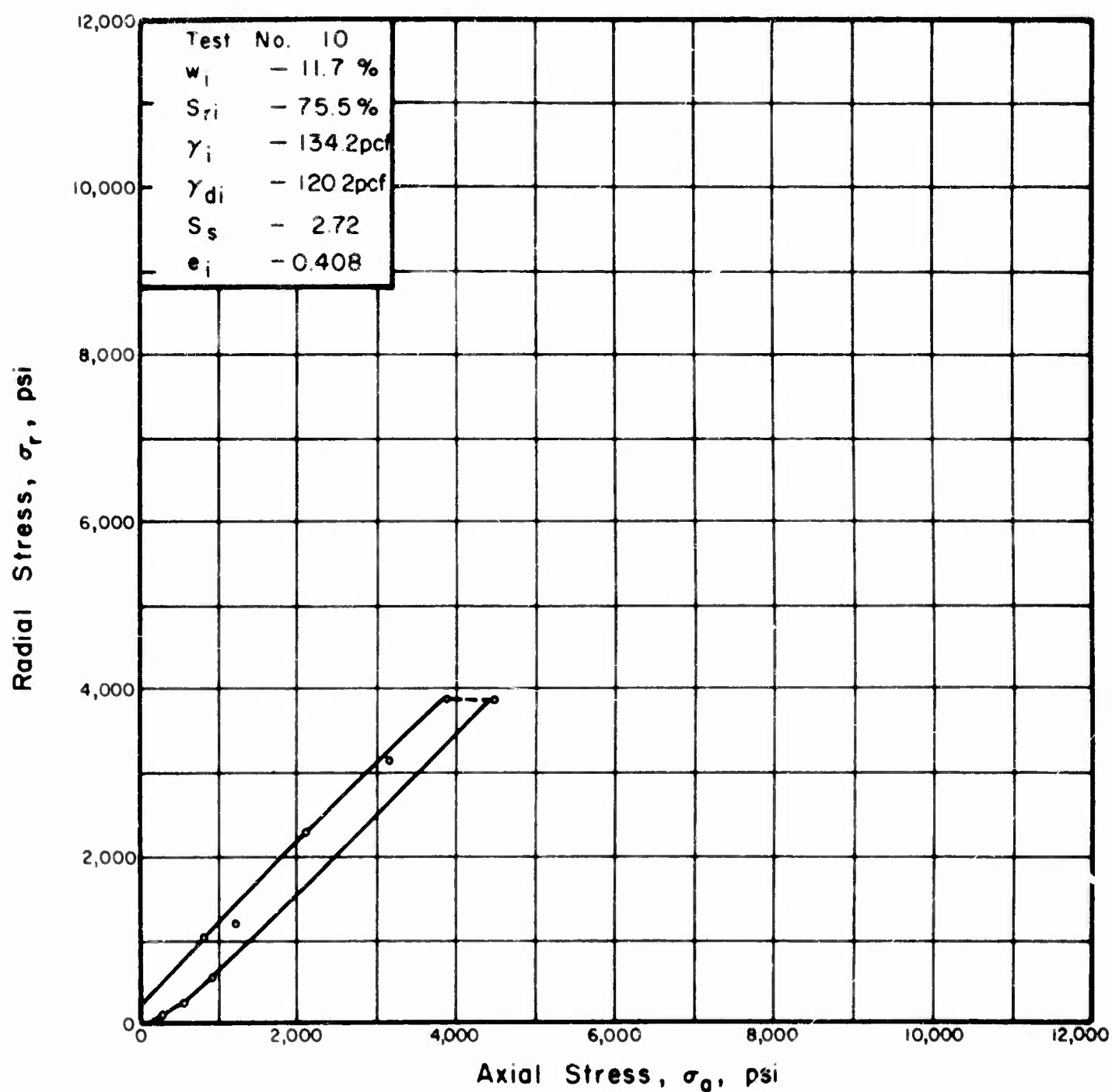


FIGURE A.60. RELATIONSHIP BETWEEN AXIAL AND RADIAL STRESS FOR GOOSE LAKE CLAY IN ONE-DIMENSIONAL COMPRESSION .

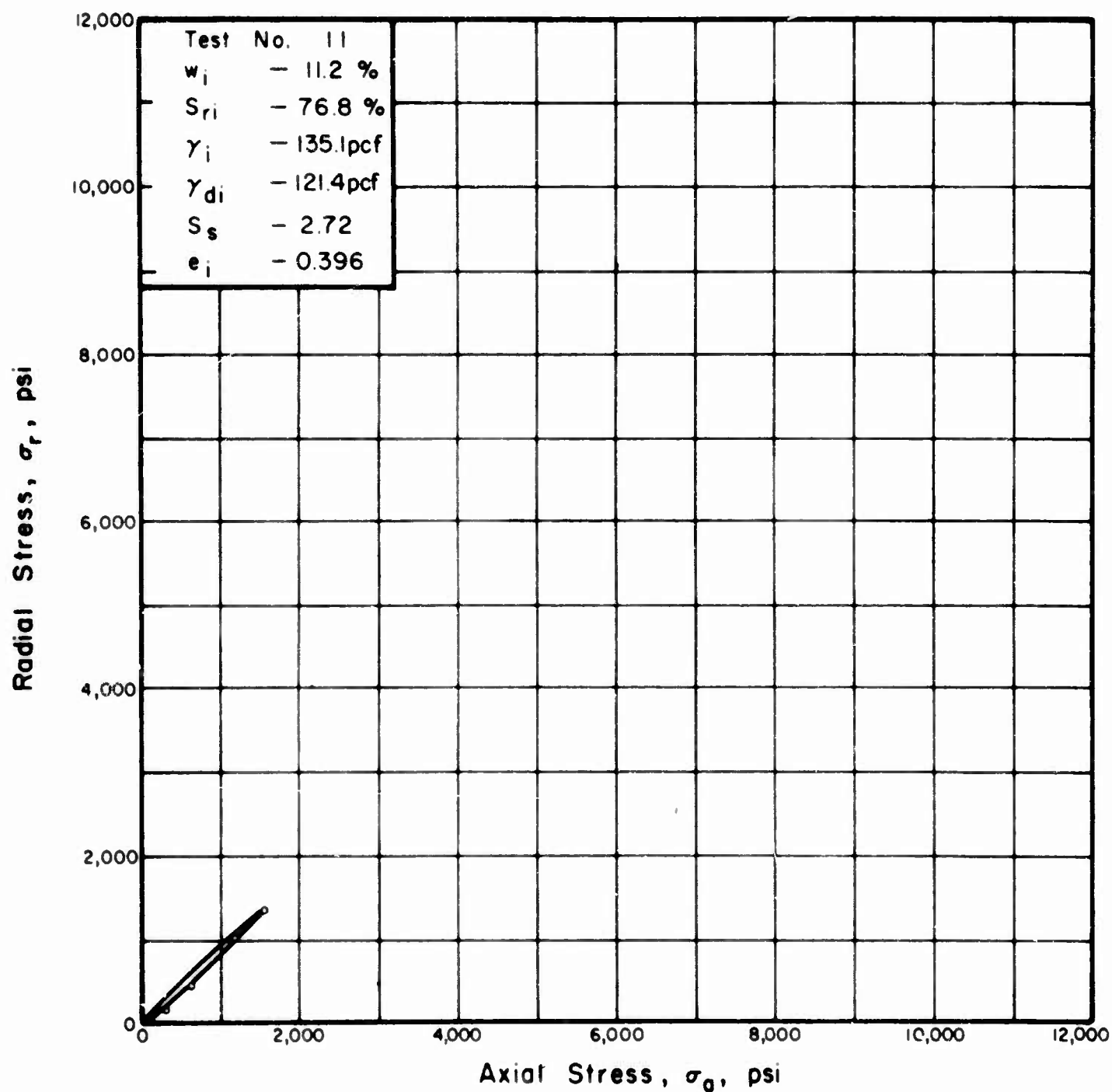


FIGURE A.61. RELATIONSHIP BETWEEN AXIAL AND RADIAL STRESS FOR GOOSE LAKE CLAY IN ONE-DIMENSIONAL COMPRESSION .

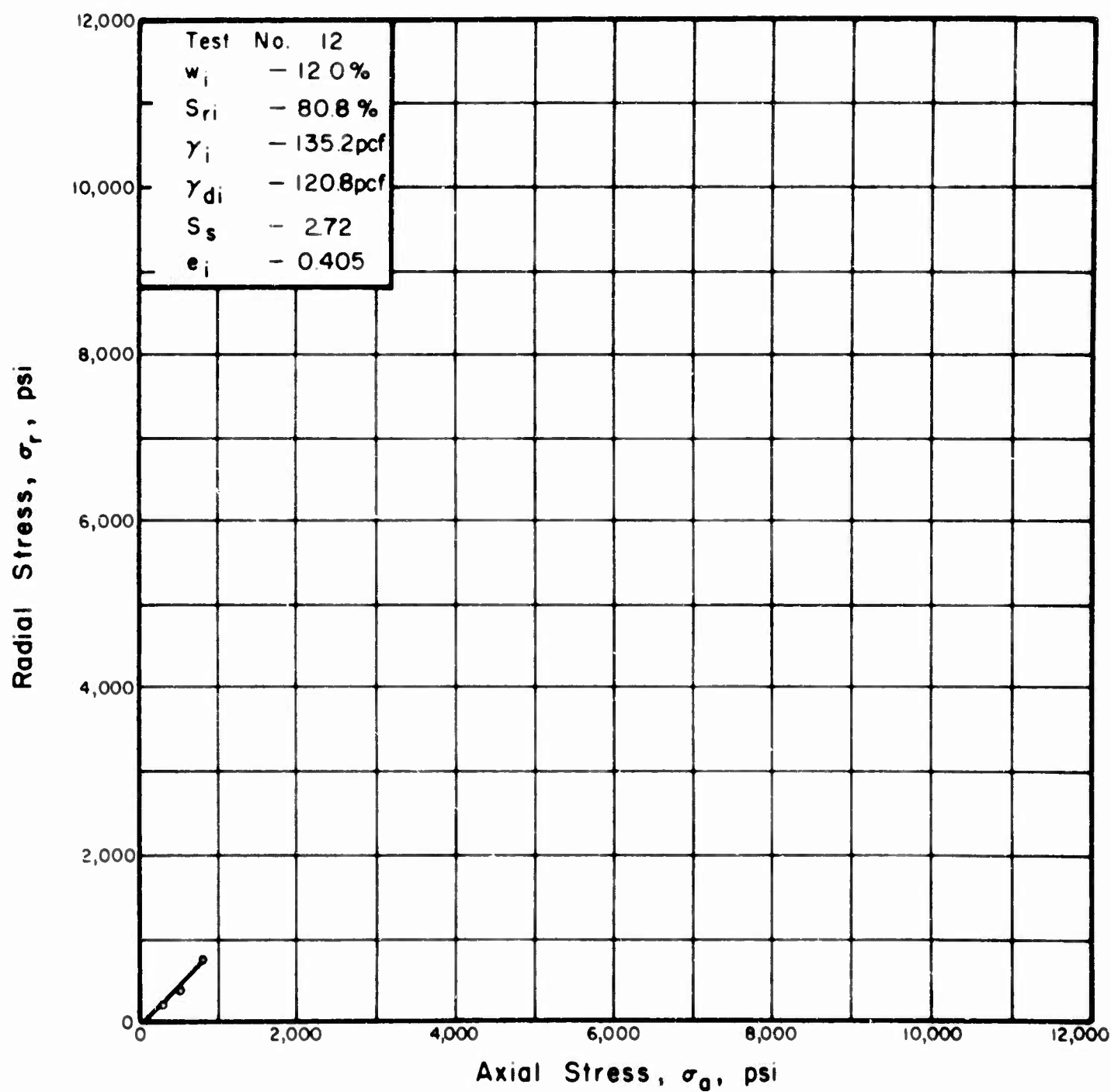


FIGURE A.62. RELATIONSHIP BETWEEN AXIAL AND RADIAL STRESS FOR GOOSE LAKE CLAY IN ONE-DIMENSIONAL COMPRESSION.

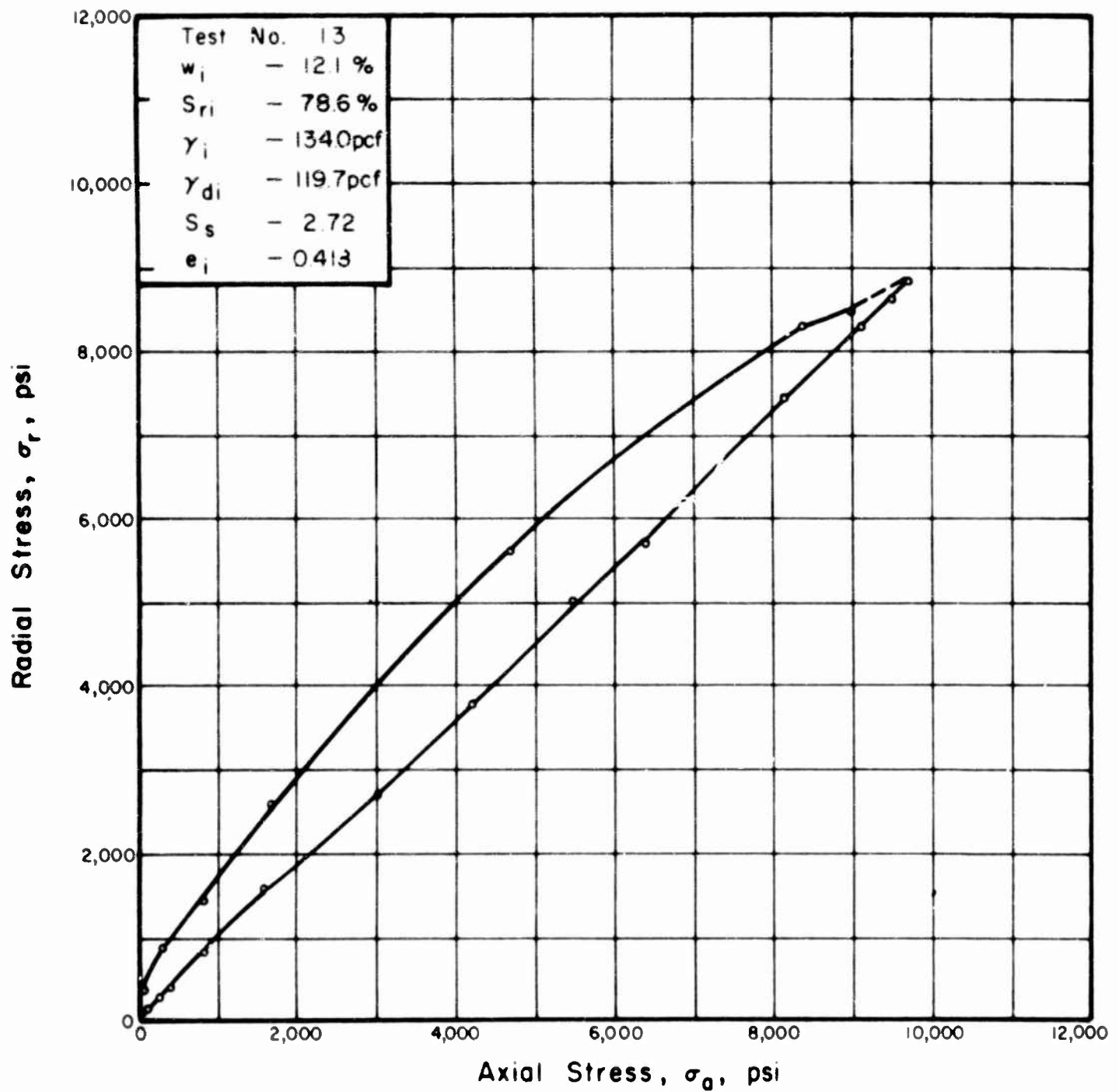


FIGURE A.63. RELATIONSHIP BETWEEN AXIAL AND RADIAL STRESS FOR GOOSE LAKE CLAY IN ONE-DIMENSIONAL COMPRESSION .

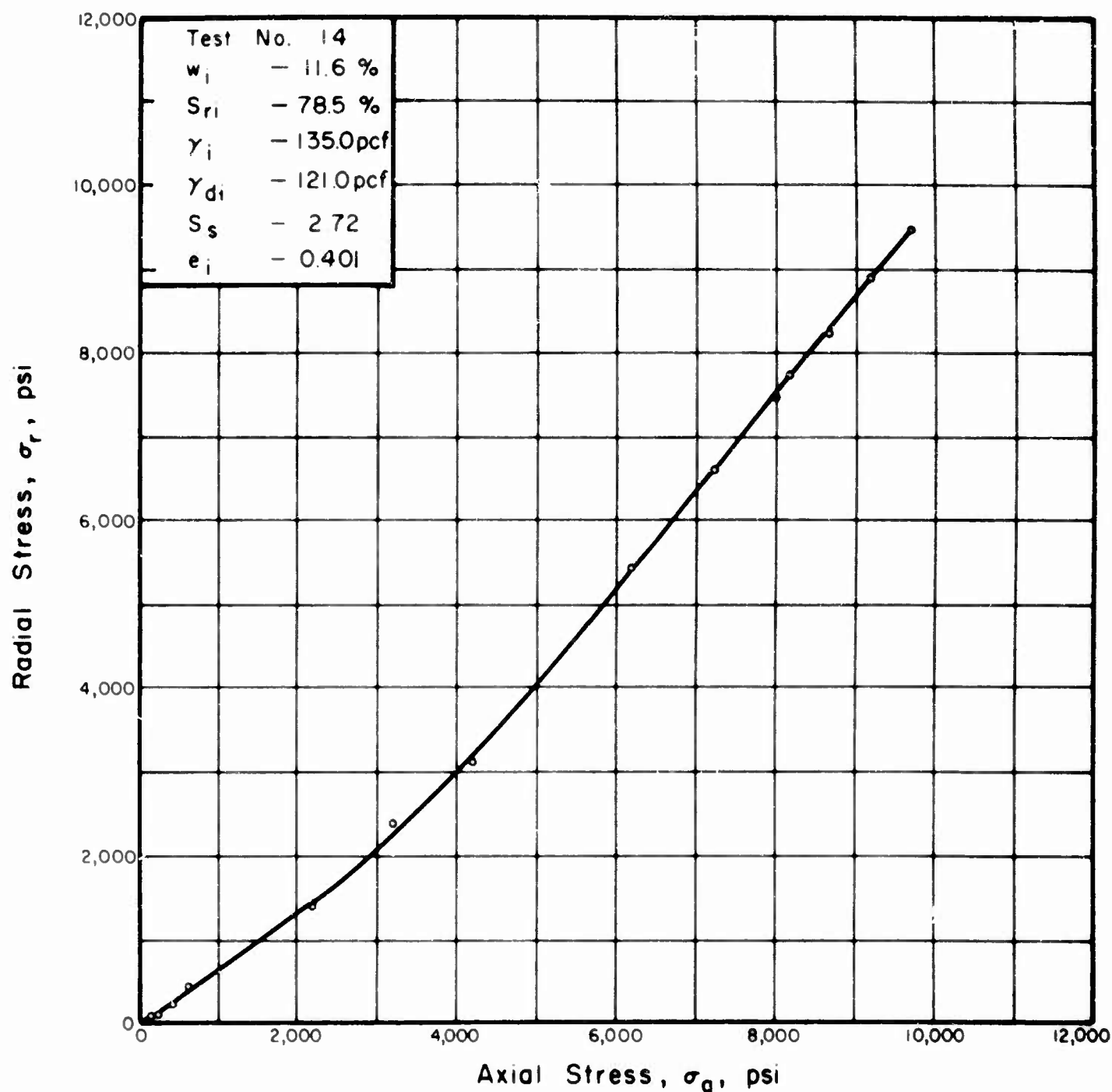


FIGURE A.64. RELATIONSHIP BETWEEN AXIAL AND RADIAL STRESS FOR GOOSE LAKE CLAY IN ONE-DIMENSIONAL COMPRESSION .

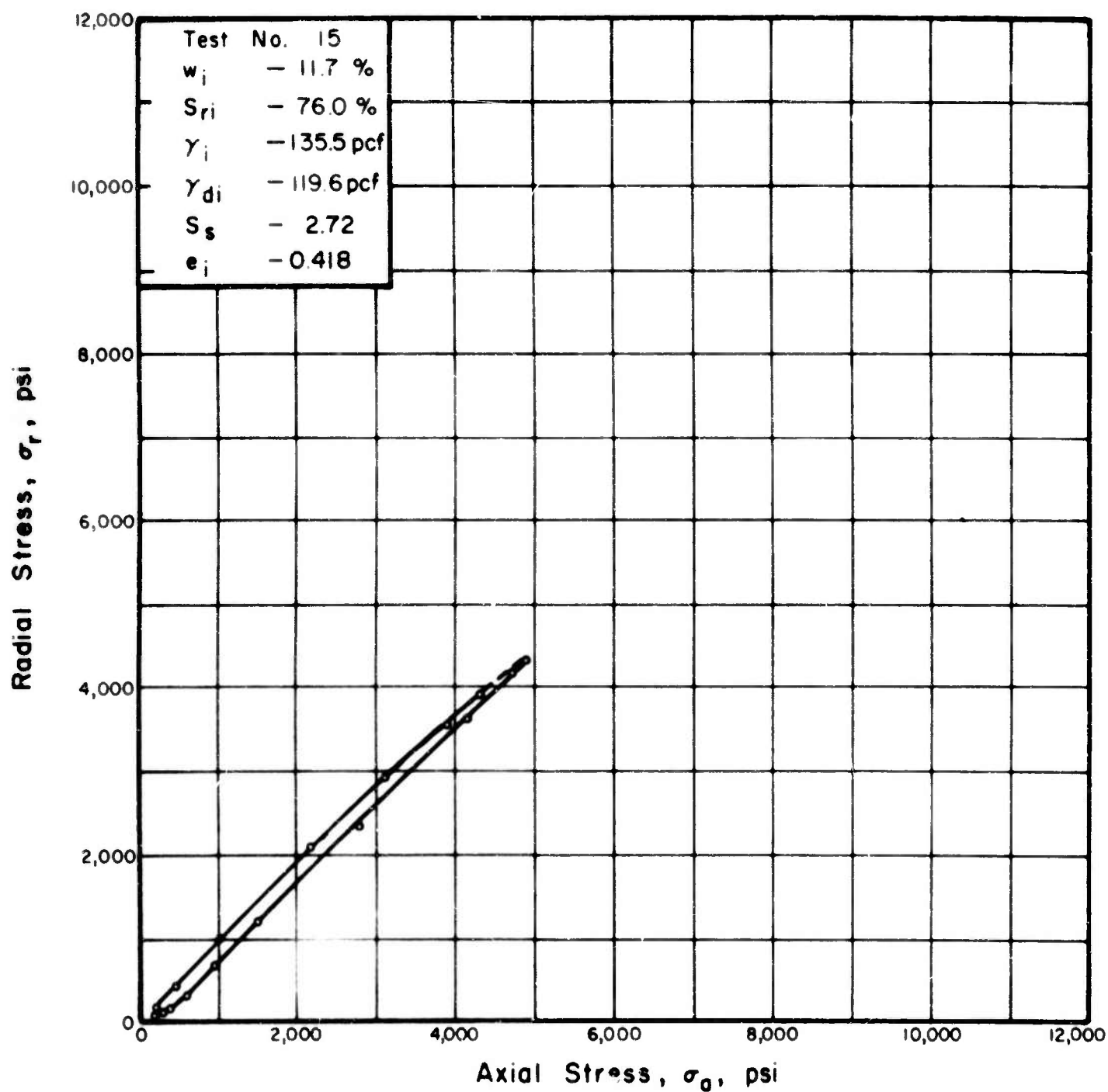


FIGURE A.65. RELATIONSHIP BETWEEN AXIAL AND RADIAL STRESS FOR GOOSE LAKE CLAY IN ONE-DIMENSIONAL COMPRESSION .

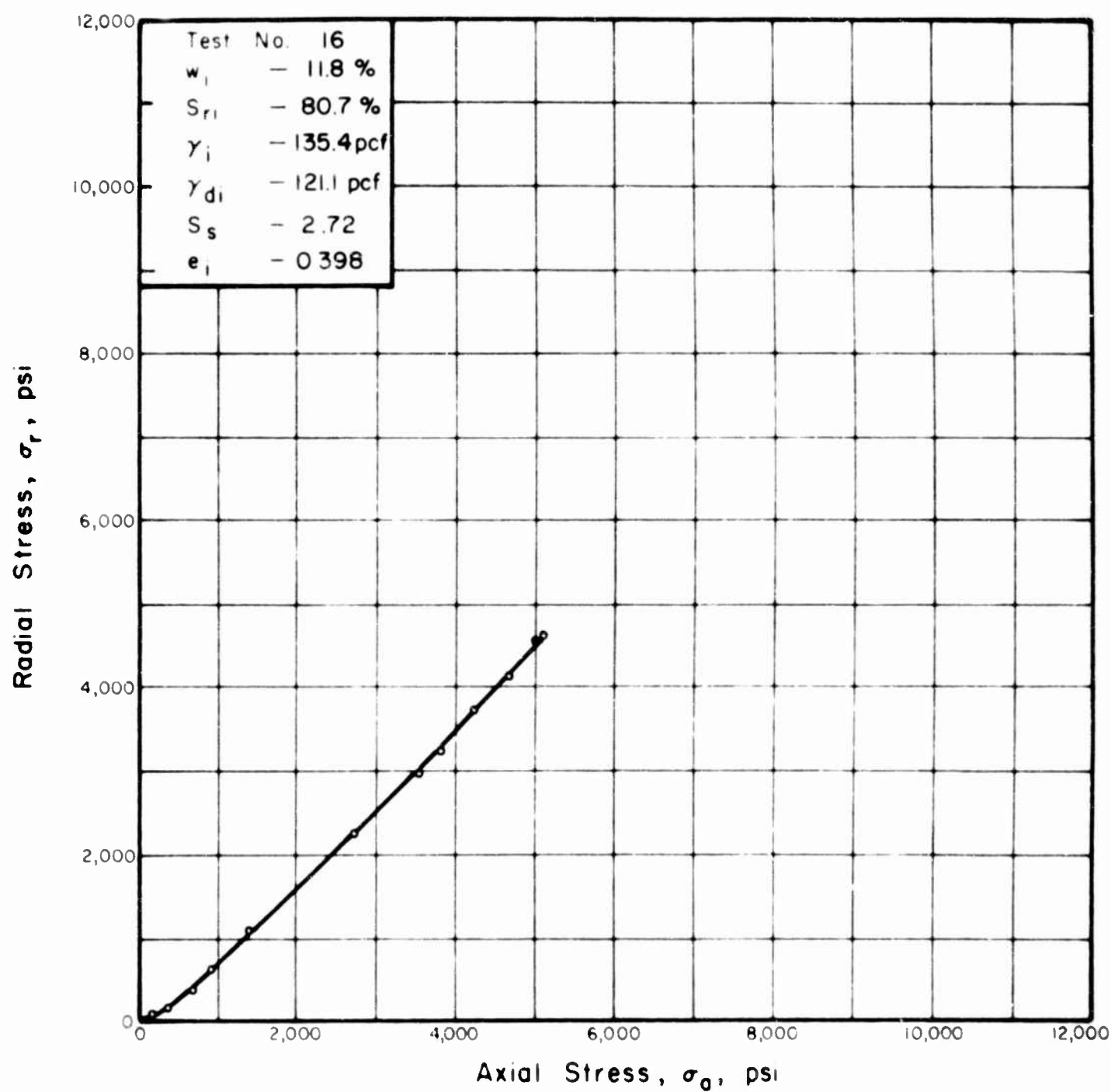


FIGURE A.66. RELATIONSHIP BETWEEN AXIAL AND RADIAL STRESS FOR GOOSE LAKE CLAY IN ONE-DIMENSIONAL COMPRESSION.

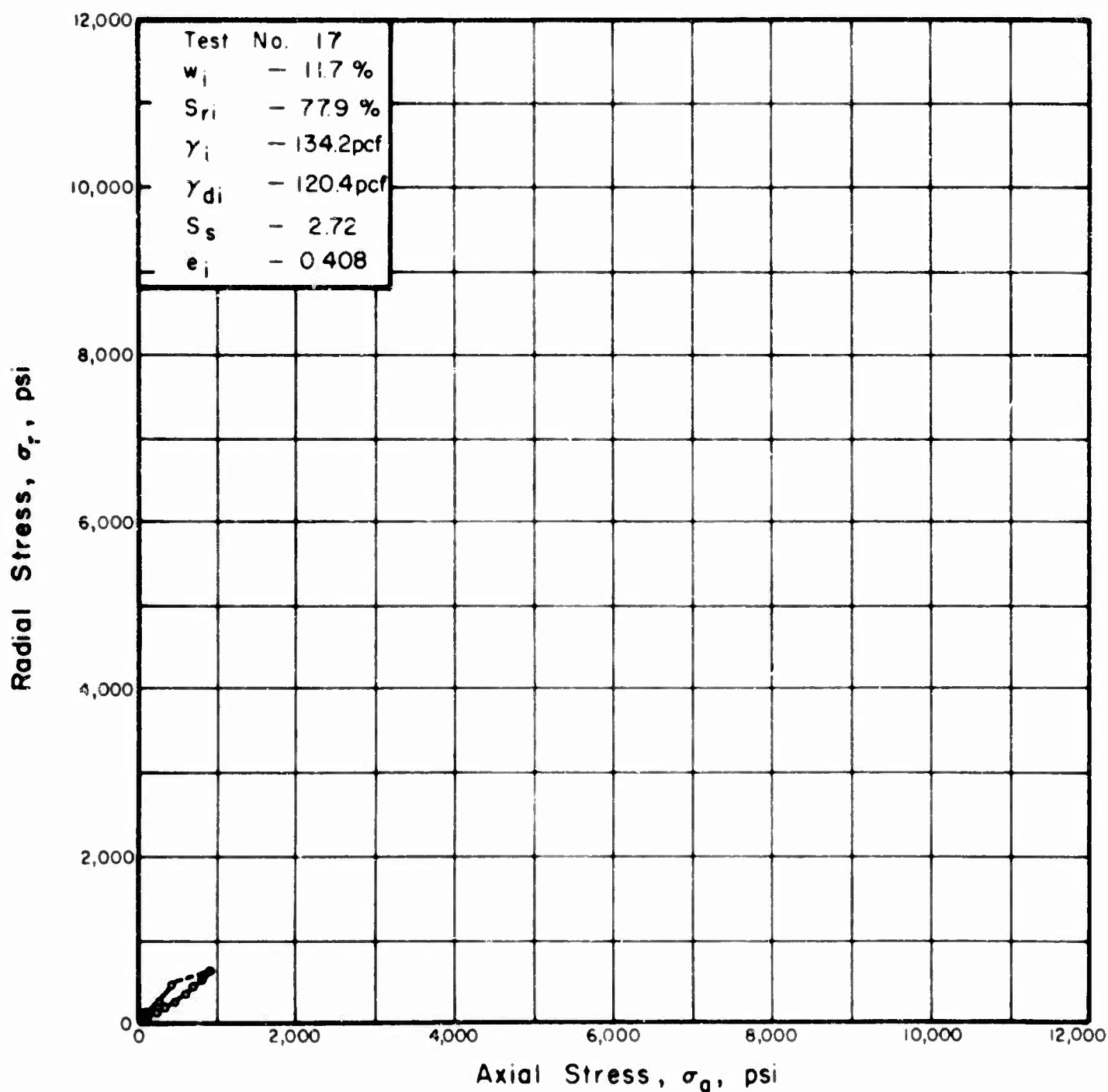


FIGURE A.67. RELATIONSHIP BETWEEN AXIAL AND RADIAL STRESS FOR GOOSE LAKE CLAY IN ONE-DIMENSIONAL COMPRESSION.

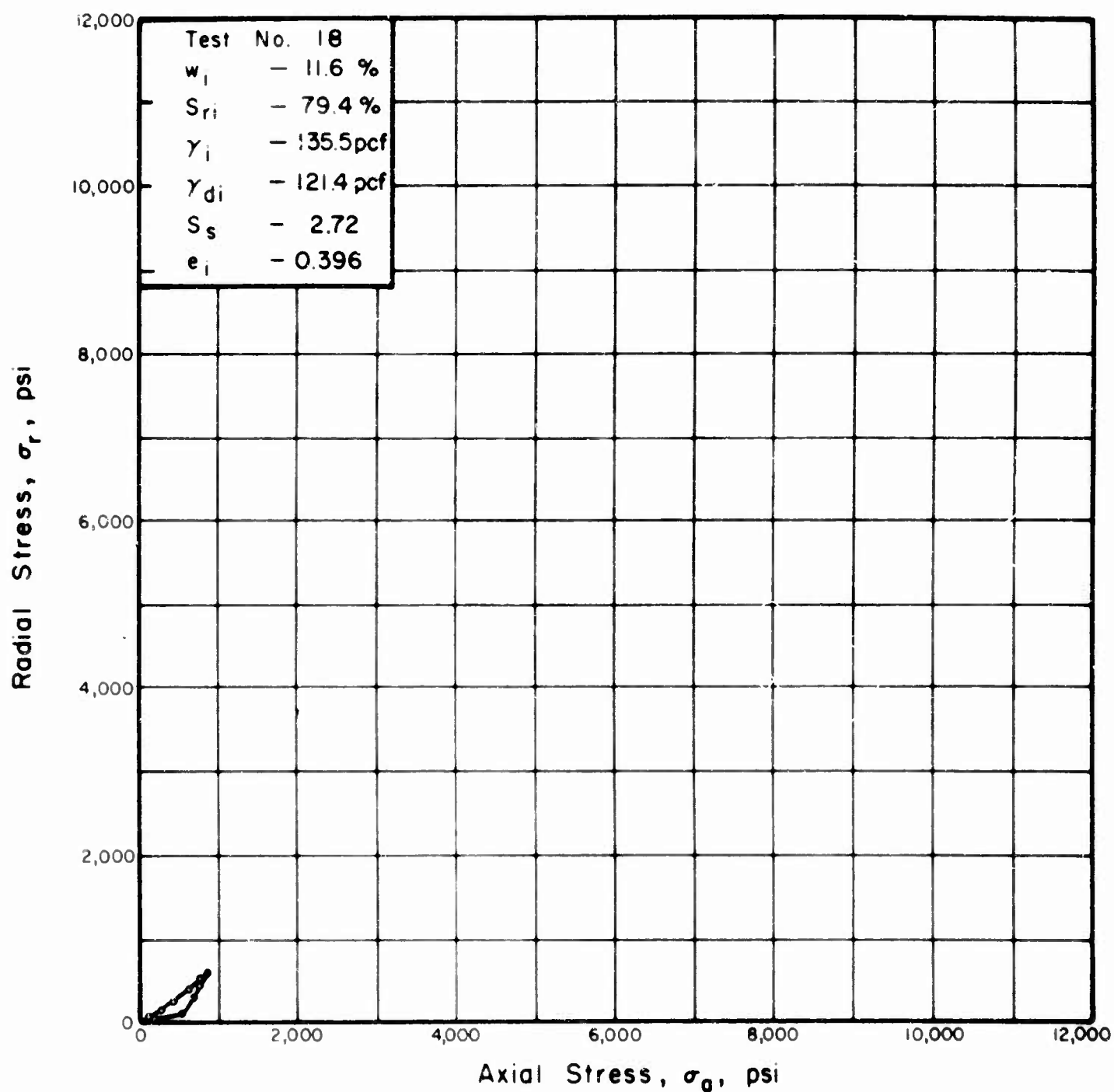


FIGURE A.68. RELATIONSHIP BETWEEN AXIAL AND RADIAL STRESS FOR GOOSE LAKE CLAY IN ONE-DIMENSIONAL COMPRESSION .

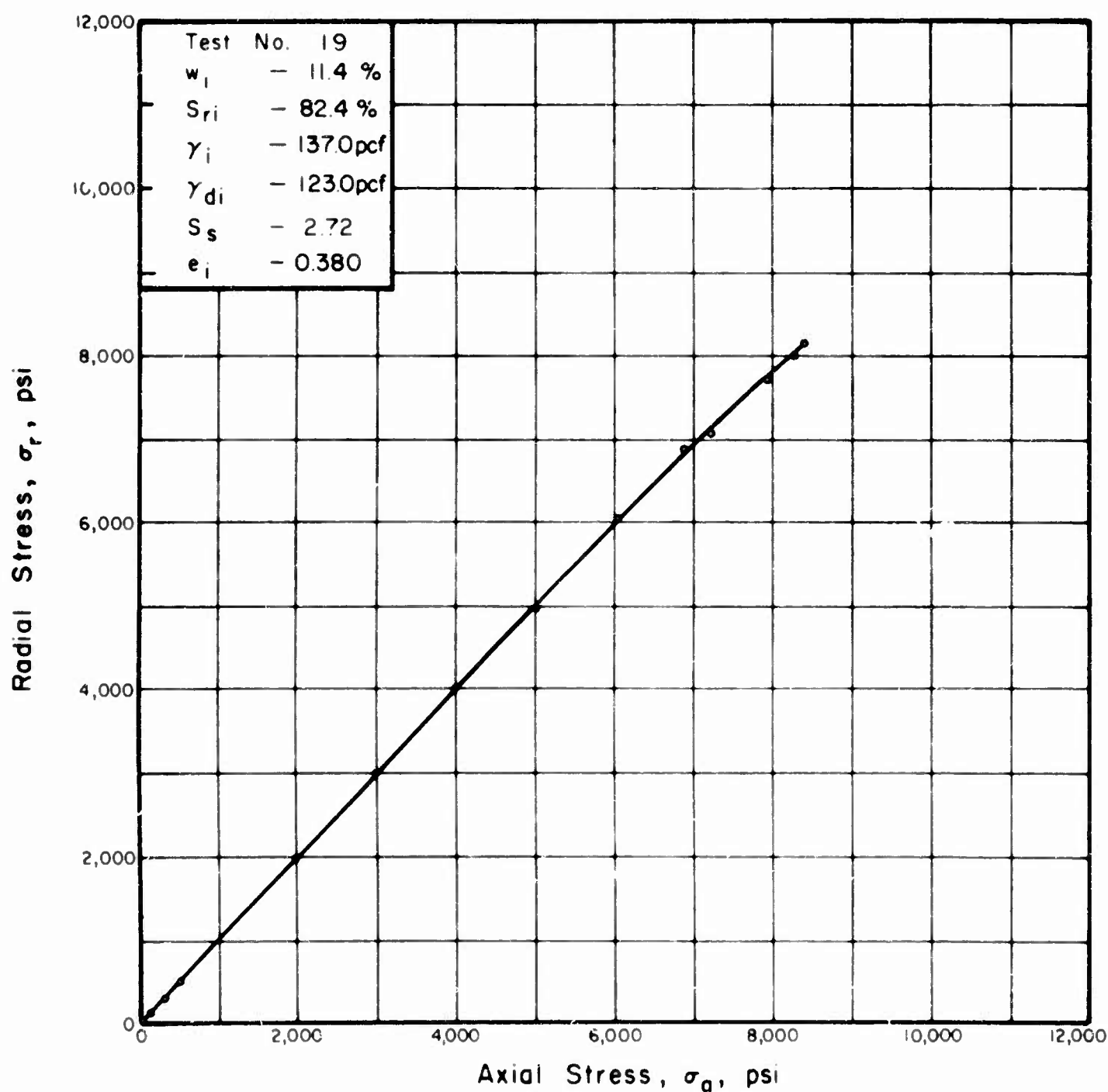


FIGURE A.69. RELATIONSHIP BETWEEN AXIAL AND RADIAL STRESS FOR GOOSE LAKE CLAY IN ONE-DIMENSIONAL COMPRESSION.

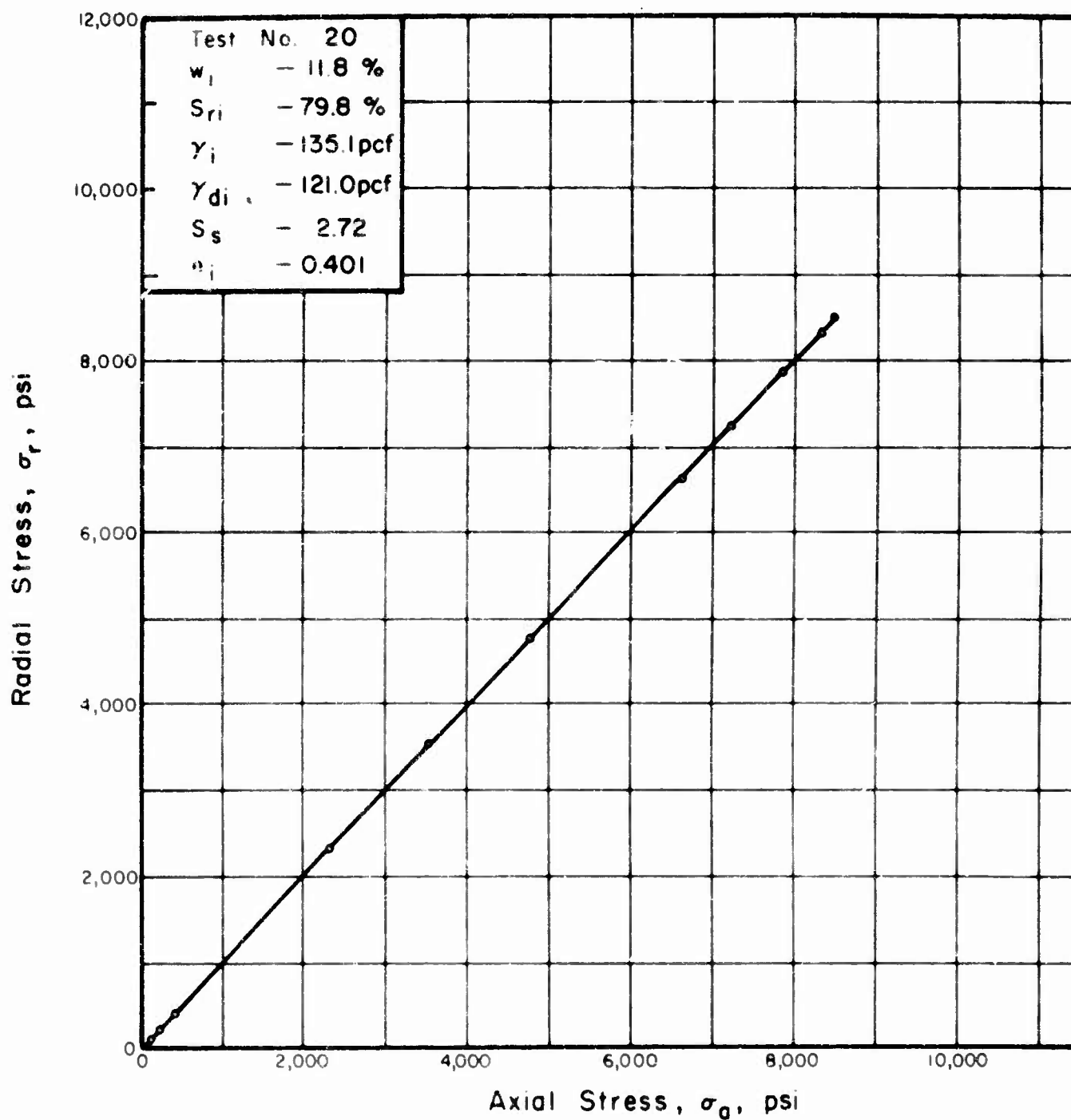


FIGURE A.70. RELATIONSHIP BETWEEN AXIAL AND RADIAL STRESS FOR GOOSE LAKE CLAY IN ONE-DIMENSIONAL COMPRESSION.

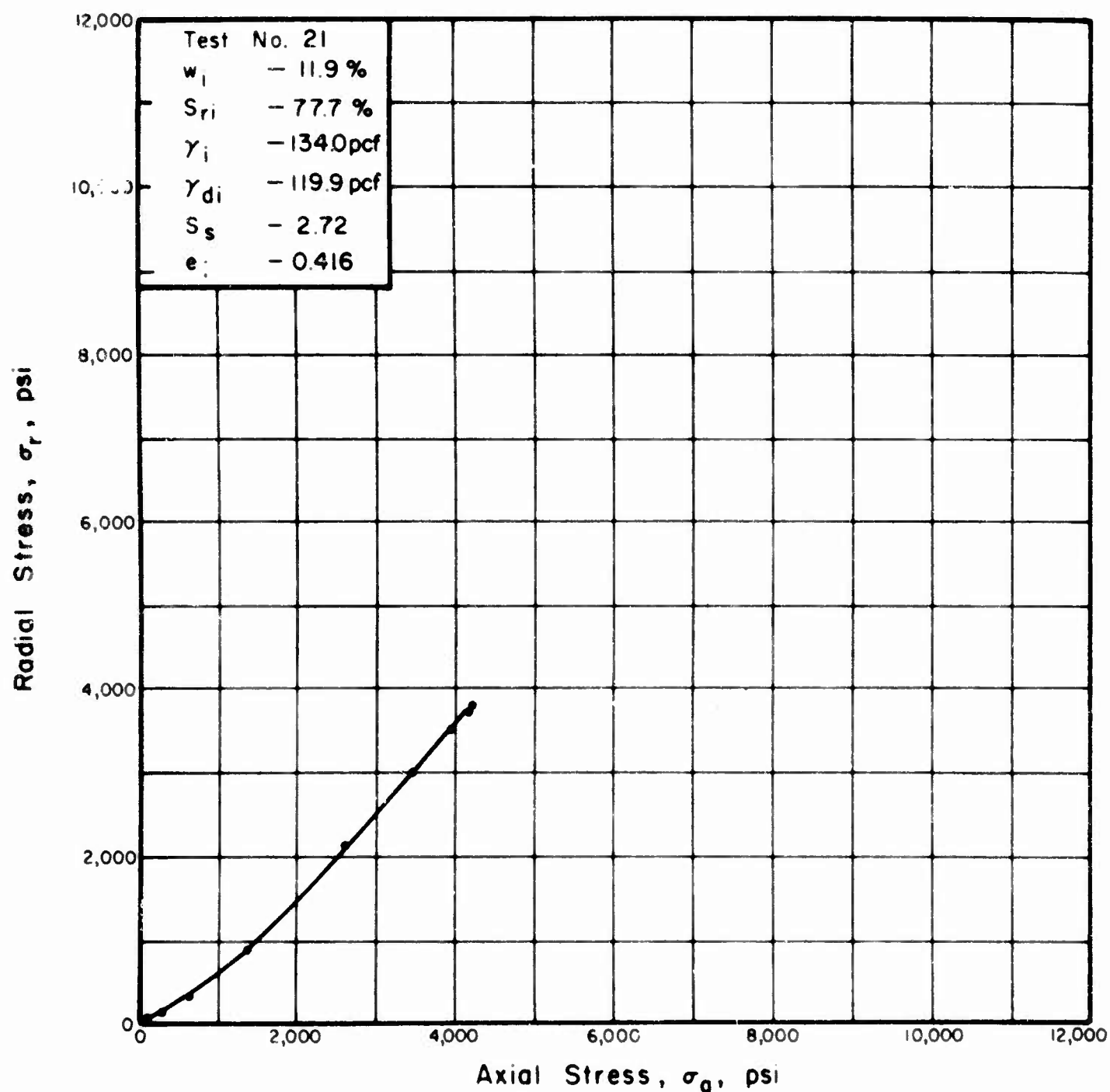


FIGURE A.71. RELATIONSHIP BETWEEN AXIAL AND RADIAL STRESS FOR GOOSE LAKE CLAY IN ONE-DIMENSIONAL COMPRESSION.

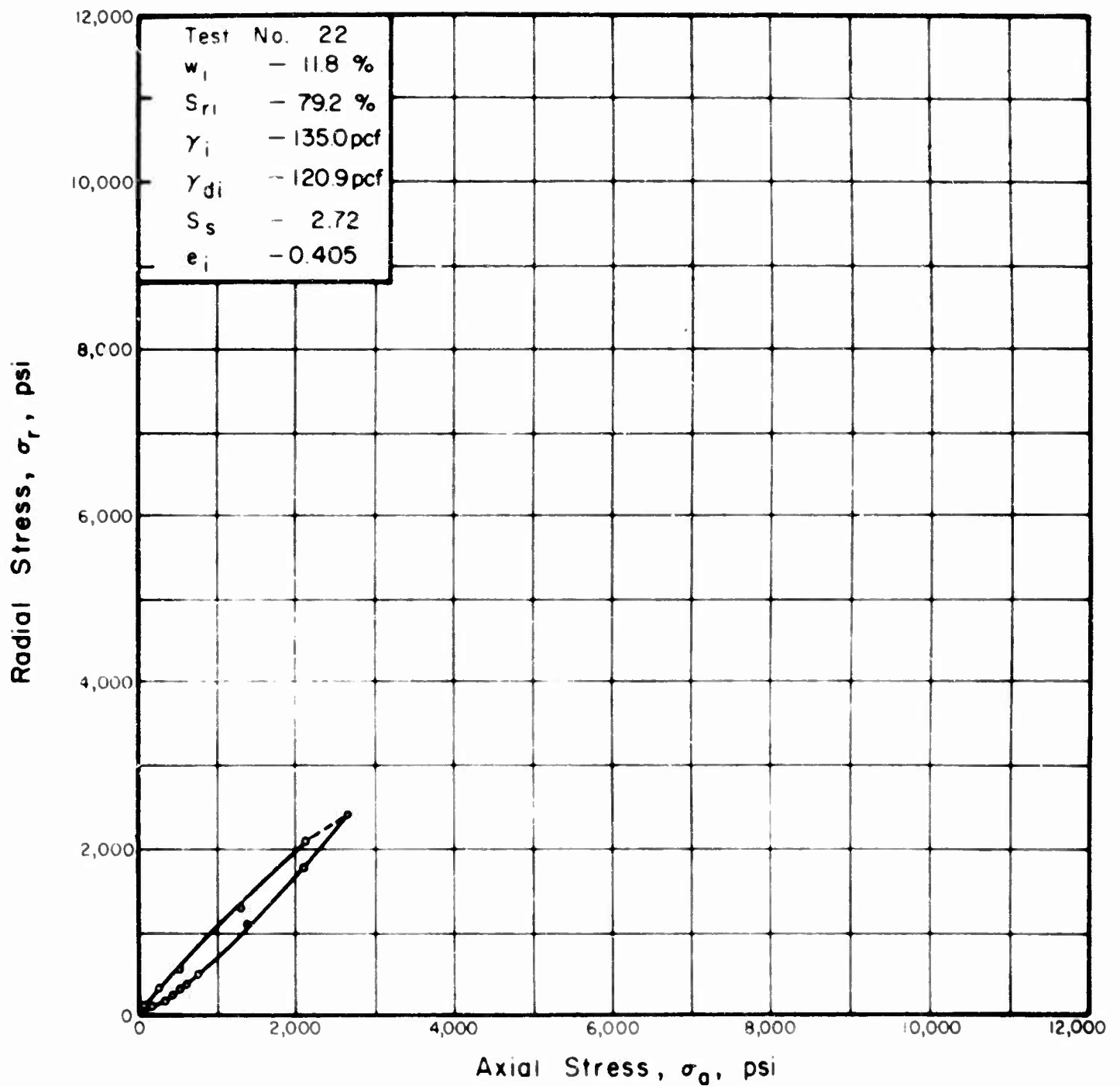


FIGURE A.72. RELATIONSHIP BETWEEN AXIAL AND RADIAL STRESS FOR GOOSE LAKE CLAY IN ONE-DIMENSIONAL COMPRESSION .

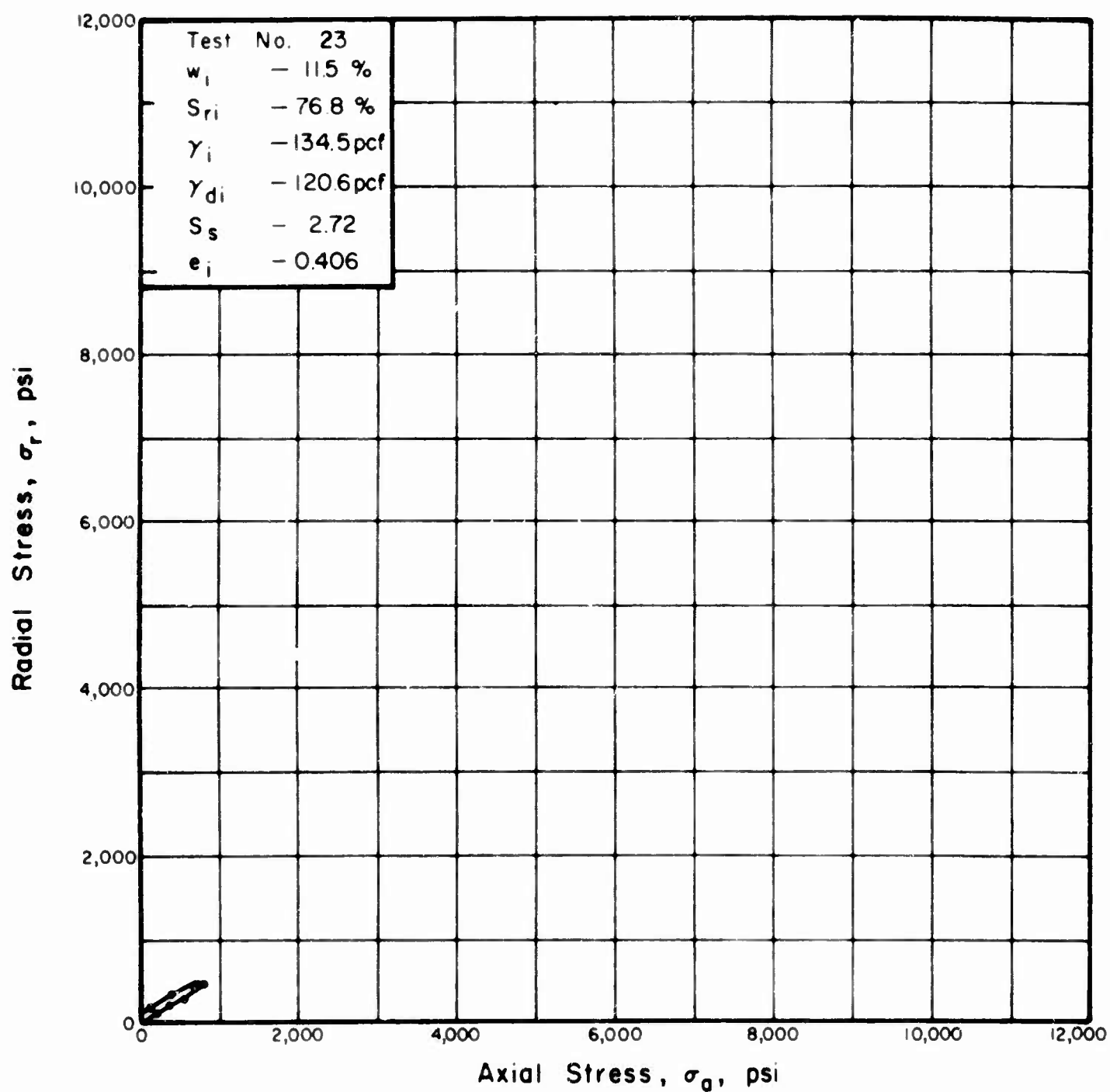


FIGURE A.73. RELATIONSHIP BETWEEN AXIAL AND RADIAL STRESS FOR GOOSE LAKE CLAY IN ONE-DIMENSIONAL COMPRESSION .

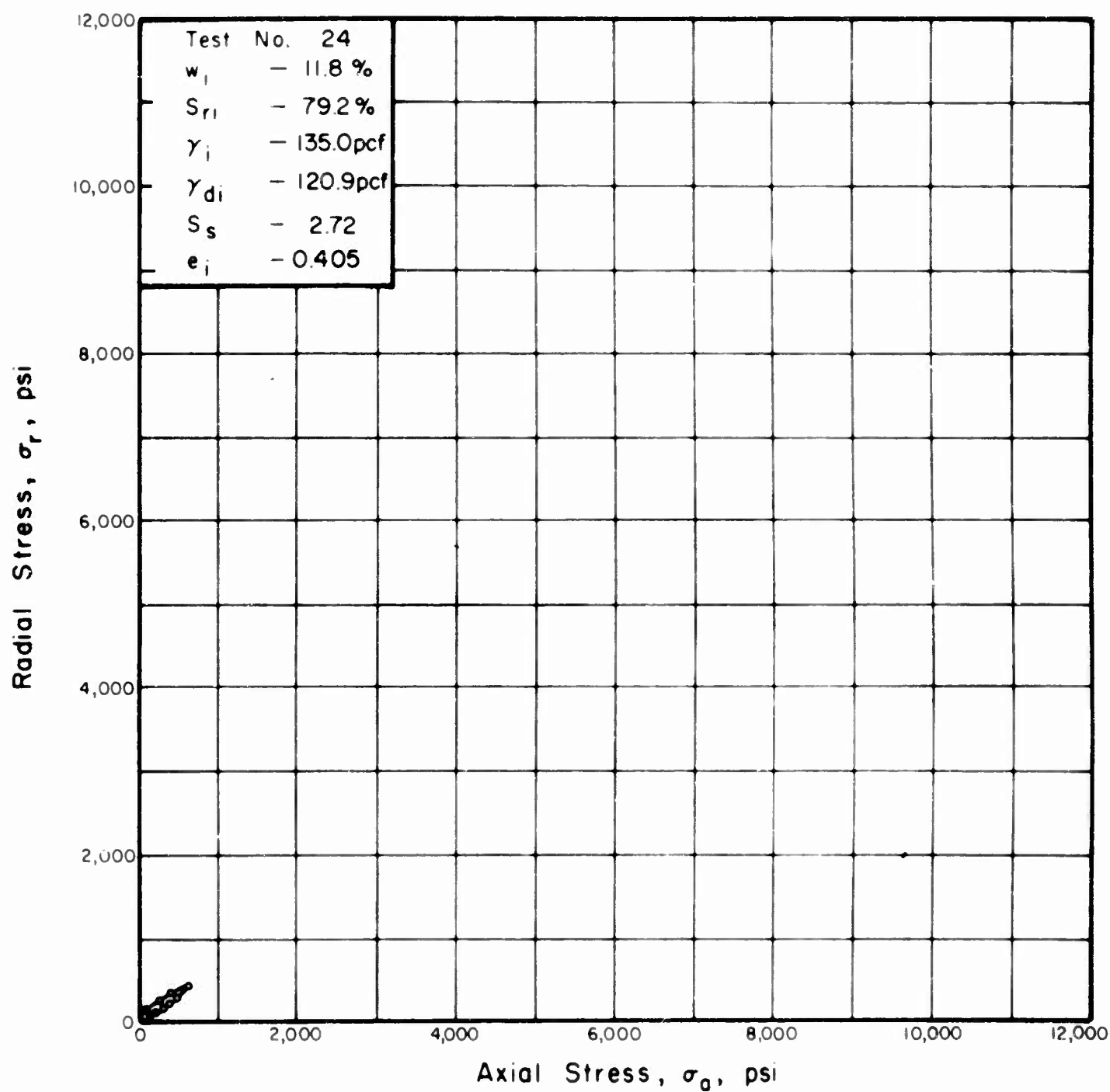


FIGURE A.74. RELATIONSHIP BETWEEN AXIAL AND RADIAL STRESS FOR GOOSE LAKE CLAY IN ONE-DIMENSIONAL COMPRESSION .

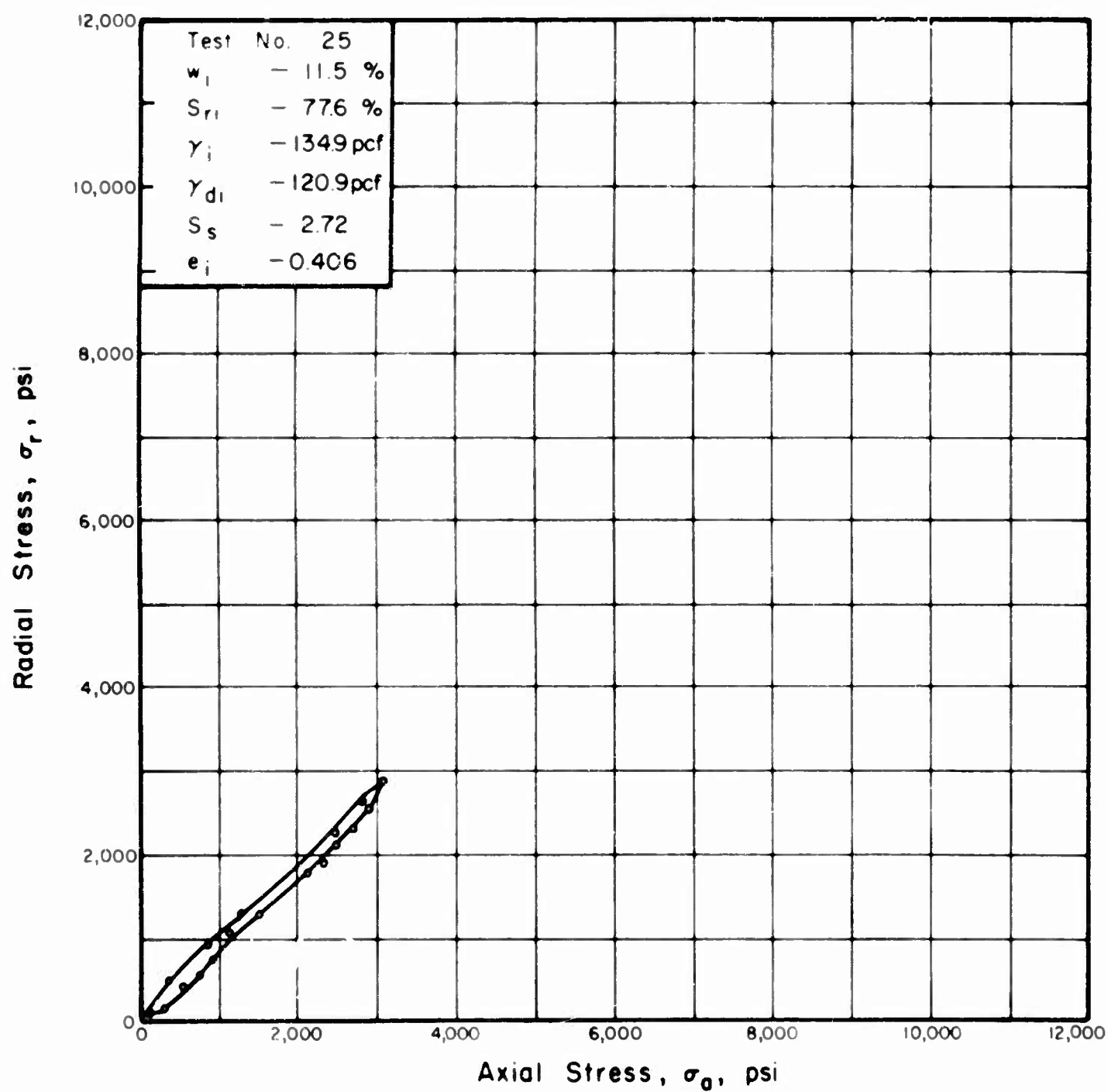


FIGURE A.75. RELATIONSHIP BETWEEN AXIAL AND RADIAL STRESS FOR GOOSE LAKE CLAY IN ONE-DIMENSIONAL COMPRESSION.

APPENDIX B

SYMBOLS

| | |
|--------------|---|
| a | = constant |
| b | = constant |
| C_a | = velocity of air blast shock front |
| C_s | = stress wave velocity in soil |
| c_Q | = cohesion intercept of total stress failure envelope for unconsolidated-undrained shear (psi) |
| E_s | = secant modulus (psi) |
| e_i | = initial void ratio |
| K | = ratio of developed horizontal pressure to applied vertical pressure |
| K_a | = coefficient of active earth pressure |
| K_o | = ratio of radial stress to axial stress for one-dimensional compression |
| M_c | = constrained modulus (psi) |
| M_{cs} | = constrained secant modulus (psi) |
| M_{ct} | = constrained tangent modulus (psi) |
| N_B | = number of blows per layer |
| N_L | = number of compacted layers |
| n | = constant |
| p | = nominal pressure on compaction foot (psi) |
| R_ϵ | = ratio of strain to strain at failure |
| R_σ | = ratio of stress difference to stress difference at failure |
| S_r | = degree of saturation (percent) |

| | |
|---------------|---|
| S_{ri} | = initial degree of saturation (percent) |
| S_s | = specific gravity of solids |
| t | = time (milliseconds or seconds) |
| t_f | = time-to-failure (milliseconds or seconds) |
| t_r | = rise time to peak pressure (milliseconds) |
| w | = water content (percent) |
| w_i | = initial water content (percent) |
| γ_d | = dry density (pcf) |
| γ_{di} | = initial dry density (pcf) |
| Δ | = increment (used as prefix) |
| ϵ | = axial strain in triaxial compression test (percent) |
| ϵ_a | = axial strain in one-dimensional compression test (in./in.) |
| ϵ_f | = axial strain at failure in triaxial test (percent) |
| ϵ_r | = radial strain in one-dimensional compression test (in./in.) |
| ν | = Poisson's ratio |
| σ | = standard deviation |
| σ_1 | = major principal stress (psi) |
| σ_3 | = minor principal stress (psi) |
| σ_a | = axial stress (psi) |
| σ_h | = horizontal stress (psi) |
| σ_r | = radial stress (psi) |
| σ_v | = vertical stress (psi) |
| ϕ_Q | = slope of total stress failure envelope for unconsolidated-undrained shear (degrees) |